POLITECNICO DI TORINO
Repository ISTITUZIONALE

Mild Hybrid Electric Vehicles: Powertrain Optimization for Energy Consumption, Driveability and Vehicle Dynamics Enhancements

Publisher copyright

(Article begins on next page)

04 August 2020

Doctoral Dissertation

Doctoral Program in Mechanical Engineering (29^{th}cycle)

Mild Hybrid Electric Vehicles: Powertrain Optimization for Energy Consumption, Driveability and Vehicle Dynamics Enhancements

By

Luca Castellazzi
******

Supervisor(s):
Prof. Andrea Tonoli, Supervisor

Doctoral Examination Committee:
Prof. Luigi Garibaldi, PhD Course Coordinator, Politecnico di Torino
Prof. Bruce Minaker, Referee, University of Windsor
Prof. Subhash Rakheja, Referee, Concordia University of Montreal
Prof. Nicola Amati, Committee Member, Politecnico di Torino
Prof. Massimiliano Gobbi, Committee Member, Politecnico di Milano
Prof. Stefano D'Ambrosio, Committee Member, Politecnico di Torino

Politecnico di Torino
2017

Declaration

I hereby declare that, the contents and organization of this dissertation constitute my own original work and does not compromise in any way the rights of third parties, including those relating to the security of personal data.

Luca Castellazzi
2017

* This dissertation is presented in partial fulfillment of the requirements for **Ph.D. degree** in the Graduate School of Politecnico di Torino (ScuDo).

Acknowledgements

At the end of my doctoral studies I feel the need to thank many people that helped me in different ways.

I am extremely grateful with my supervisor Prof. Andrea Tonoli for continuously guiding me towards the science of road vehicles, supervising my research activity and demonstating his faith in me. I can clearly say that the results I have been able to achieve are directly correlated to the numberless things that he was able to teach me during our discussions. I really hope that, in future, somehow our ways will meet again.

I am really thankful with Prof. Nicola Amati, who assisted me during several activities, always providing me important suggestions for increase the scientific level of my research works.

I would like to thank also my thesis reviewers, Prof. Bruce Minaker and Prof. Subhash Rakheja, for providing me extremely important feedbacks and comments. Their availability to review my thesis has been really appreciated, and their opinions about my research work constituted important key points for the production of a higher quality document.

During the time spent in the Mechatronics Laboratory of Politecnico di Torino (LIM) I had the opportunity to meet fantastic people with which I could spend three exciting years.

I am really grateful with Sanjarbek Ruzimov for assisting me in several ways and providing me numberless of advices and recommendations regarding mechanical systems analysis and design. I started to work with him when I was a master student thesist, and I am glad that he wanted to keep our cooperations active. During the last three years we continuously interfaced about several subjects, and he always had the will to teach me how to analyze several kind of issues. For all of this, your kindness, knowledge and support will never be forgotten, thank you.

With Jyotishman Ghosh I spent most of my doctoral studies discussing about automotive systems. His passion for cars and control systems really stimulated me in improving my knowledge in such field. Also, we shared the management of Squadra Corse together, an experience that improved our skills from many different points of view. I am very glad

to say that Jyoti has not been only a work colleague, but also a very good friend. I hope to meet you again in future and continue our left discussions!

A special thanks goes also to Renato Galluzzi and Joaquim Girardello Detoni, two post doc researchers which I shared really a lot of time with, that had always the will to give extremely useful advices, sharing their knowledge about mechatronic systems with me. Thank you guys, our friendship really meant a lot to me.

A big thank you to Maria di Napoli for her kindness and support both from the technical and from the human point of view. Final thanks to Mirko De Giuseppe, Gianluca Dara, Dario Gandini, Gabriele Ermacora, Antonio Toma, Raffaele Saggese, Enrico Gasparin, Angelo Bonfitto, Fabrizio Impinna, Lester Daniel Suarez Cabrera, Gianluca Botto, Quingwen Cui, Yijun Xu, Mario Silvagni, Javier Eduardo Pereira Rivas, Stefano Di Donato and Simone Natoli for the inspirational times spent together.

Finally I would like to thank my friends from my hometown Trino and my university classmates, who have always been able to give me funny moments and times when I just needed to laugh and distract myself. A big thank to my family for their moral support and for always believing in me.

Last but not least, a special thank you goes to Giulia. If I have been able to reach such a goal is also because of her continuous support. Her kindness, sweetness and strenght always helped me in good and bad times to become a better man. It wouldn't have been the same thing without you, and I'll be there by your side in our future.

Abstract

This thesis deals with the modeling, the design and the control of mild hybrid electric vehicles. The main goal is to develop accurate design tools and methodologies for preliminary system and component level analysis.

Particular attention is devoted to the configuration in which an electric machine is mounted on the rear axle of a passenger car. The use of such a machine in parallel with the internal combustion engine allows one to exploit different functionalities that are able to reduce the overall fuel consumption of the vehicle. In addition, the indirect coupling between the thermal and the electric machine, realized *through the road* and not by means of mechanical couplers, together with the position of the latter in the overall vehicle chassis system, enables such an architecture to be efficient both from the energy recovery and the full electric driving point of view.

Chapter 1 introduces the problem of fuel consumption and emissions reduction in the overall world context and presents the main hybrid architectures available.

Chapter 2 is devoted to the study of the influence of the electric machine position in the powertrain regarding the regenerative braking potentialities concerned. The model considered for the analysis will be described on each of its subcomponents. The braking performance of the vehicle in electric mode is presented considering no losses in the electric powertrain (electric motor, battery, inverter).

Chapter 3 is dedicated to the design of an electric machine for a rear axle powertrain. The specifications of such machine are optimized considering both the vehicle and the application under analysis. The design takes into account analytical techniques for the computation of electrical parameters (such as phase and DC currents) and the torque - speed map, as well as numerical ones for its thermal behavior.

In Chapter 4 the electrical and thermal characteristics of the designed electric motor are implemented in the model presented in Chapter 2. The overall vehicle model is therefore used both to assess a simple torque split strategy between thermal and electric machine

and to perform an optimal sizing of the battery considering all the limitations imposed by the electric powertrain (e. g. maximum currents, maximum temperatures).

Chapter 5 makes a step forward and analyzes the different implications that the use of the rear axle electric motor to brake the vehicle has on the vehicle dynamics. Open loop analysis will present a degradation of the vehicle handling comfort caused by the introduction of an oversteering moment to the vehicle. Through the use of a simplified vehicle model, the introduced oversteering yaw moment is evaluated, while a control strategy based on a new stability detector will show how to find a trade off between handling comfort and regenerable energy.

At last, Chapter 6 deals with the problem of longitudinal driving comfort. Drivelines and chassis are lightly damped systems and the application of an impulsive torque imposed by the driver can cause the vehicle longitudinal acceleration (directly perceived by the driver) to be oscillating and non smooth. A sensitivity analysis on a conventional powertrain is presented demonstrating which of the different components are more influential in the different modes of vibration, and possible solutions to improve the driveability are proposed. One of these relates to the use of the rear axle electric machine in order to give more responsiveness to the vehicle.

Finally, concluding remarks are given in Chapter 7.

Contents

List of Figures

List of Tables

Chapter 1

Introduction

1.1 Background

The current trend of reducing fuel consumption and emissions in both passenger, light and heavy duty vehicles is motivated by several factors which are, by the way, continuously changing.

In 2010 ([1], [2]) the urban population represented 51 % of the world population while in 2014 represented 54 %. Forecasts expect that this percentage is going to increase until 70 % in about 30 years. The major growth is going to occur in the Asiatic - Pacific area.

More people in urban areas mean more circulating vehicles (for personal mobility) and more freight circulation. It is clear that transport systems will play a consistent role in the overall energy consumption. As a matter of fact, a percentage between 30 and 35 % of the overall consumption of energy in Europe is addressed to transport systems (road, maritime, air, railway) [3]. It is easy to imagine which would be their primary source: black oil (96 % in Europe, 2011). In addition, in the aforementioned 30 - 35 % of energy used for transport, a percentage about 80 - 85 % is used for road transport, while air transport account for 10 - 13 % [4].

These few percentages give a general overview of how and how much the overall energy produced is then used, but are enough to demonstrate that more circulating vehicles mean more energy consumed for transport systems and, therefore, a larger use of black oil. The continuous increase of people living in urban areas are forcing the existing transportation systems to move towards more efficient technologies to reduce the environmental impacts related to any kind of emissions (e.g. CO_2, PMs, CO, HC, NO_x).
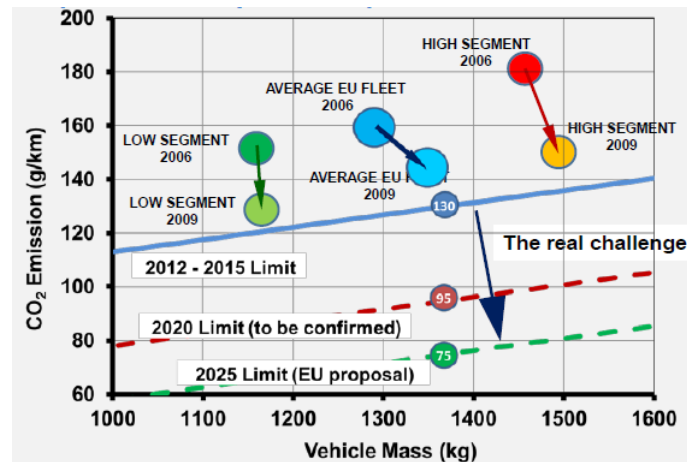
Fig. 1.1 CO_2 Emissions as a function of the vehicle mass for different years regulations.

Such a large dependence on black oil has driven the development of passenger, light and heavy duty vehicles based on internal combustion engines. Although a very well established technology, these machines have a low efficiency and, especially in urban driving, are used in their lower efficiency working points.

For these reasons, regulations have been introduced to force the manufacturers to reduce the emissions of their vehicles. At the moment, the fleet average to be achieved by all cars in the European Union (EU) is 130 gCO_2/km, but this value is going to decrease to 95 gCO_2/km (2020) until 68 - 78 gCO_2/km (2025), with penalties of 95 Euros per each exceeding gCO_2/km for each vehicle sold (from 2019) [5]. Such limits are very stringent as also shown in Fig. 1.1, in which the emissions limitations are presented, plotted as a function of the vehicles mass [6].

The reduction of CO_2 emissions (and consequently of the fuel consumption) regarding ICE driven vehicles can be oriented to improvements related to the engine itself (e.g. advanced injection systems, downsizing, aftertreatment, advanced cooling, advanced combustion techniques, switch to alternative fuels) or to the vehicle (tires rolling resistance reduction, aerodynamic drag reduction, weight reduction, powertrain improved efficiency).

In the following, the focus is set on powertrain efficiency improvements. Particularly speaking, the attention will be devoted to hybrid electric vehicles (HEVs), architectures which make use of more than one source of energy (in this case thermal and electric) in order to improve the overall vehicle efficiency, minimizing fuel consumption and emissions.

1.2 Hybrid Electric Vehicles

Hybrid electric vehicles are promising technologies that make use of two sources of energy substantially different to each other [7]. The main one is typically a chemical fuel with a high storage capacity, while the secondary one, having a lower storage capacity, can function as an energy buffer with the capabilities of kinetic energy recovery. Typically can be of the electrochemical kind.

The spelling between a high - capacity storage (the conventional fuel) powering the main energy converter (the ICE), together with an energy storage system coupled with an energy converter able to realize bi - directional power flows, results in a high level of flexibility translated into the following possible tasks:

- Allow the less efficient energy converter (the ICE) to operate close to its maximum efficiency working points;

- Switch off the ICE whenever the vehicle is at standstill (zero output power) to avoid idle fuel consumption;

- Downsize the ICE because less power is required due to the presence of a second energy converter;

which allow reductions of the fuel consumption in the order of 10 - 30 % with respect to conventional vehicles [8]. Additionally, depending on the architecture under consideration, the following functions can also be accomplished:

- Advanced Start&Stop systems. Conventional starter motors can be substituted with more efficient and controllable electric machines.

- Regenerative braking. The vehicle's kinetic energy during the braking phases can be recovered and not dissipated by the friction brakes, charging the battery and allowing electric traction;

- Full electric traction. Depending on the secondary energy storage power installed on board, the vehicle can travel for a limited range of distance (especially in urban driving cycles) without switching on the engine.

- Engine assist. The secondary energy converter can support the engine in several conditions.

The classification of HEVs can be done based on the topology, on the size of the electric powertrain and, going more in depth, based on the position of the secondary energy converter with respect to the primary one. From now on, the secondary energy converter will be of the electric kind. This means that energy converters and energy storage systems will be electric motors and electric batteries respectively.

1.2.1   Classification Based on the Topology

Based on the connection between the ICE and the electric machine, the HEVs can be classified as follows ([8] - [12]):

- Series hybrid. This configuration is basically an electric vehicle in which the battery is charged by means of an electric generator, connected in series with an ICE. The ICE can work around its maximum efficiency points to drive the generator which charges the battery. The electrical power is transfered to the traction motor to drive the vehicle;

- Parallel hybrid. The power delivered to the wheels can be the summation of thermal and electrical power because the ICE and electric motor are rigidly connected by means of a gear set, a belt or a chain;

- Power split. The ICE and two electric machines are connected together to a planetary gear set (power split device), thus combining series and parallel operations through a mechanical or electrical power path;

- Series/parallel. This configuration uses clutches that can engage or disengage the connections between the two power sources, thus realizing several operations as a function of the working conditions.

Apart from the configurations that allow both series and parallel operations, the series configuration owns the advantage of letting the ICE working around its maximum efficiency working points, but has the drawback of introducing additional losses due to the two electric motors and, above others, to require major powertrain modifications with respect to the normal production vehicle. The parallel configuration allows the summation of the power (from the two sources) to be sent to the wheels and, therefore, the possibility to switch off the ICE in particular working conditions. The drawback is related to the optimal torque split between the two sources or regarding the electric motor, constrained to be connected with the ICE and thus requiring a focused design. Power split or series/parallel

configurations are much more flexible because they can exploit the advantages of both series and parallel architectures, based on the working conditions. In some cases, the use of a mechanical connection can lead to interesting advantages where powertrain modifications to be introduced are concerned.

1.2.2 Classification Based on the Size of the Electric Powertrain.

Based on the increased size of the additional components of the electric powertrain installed on board, an HEV can be classified as follows [13]:

- Micro Hybrids. Owning the possibility of implement Start&Stop systems, these configurations allow one to switch off the engine during idling, avoiding fuel consumption in these phases. Although it is one of the main characteristics of HEVs, it can be found also in non - HEVs;

- Mild Hybrids. These configurations of HEVs can be used to drive the vehicle in pure electric mode but their power is not sufficient to maintain the motion without the support of the traditional ICE. Regenerative braking and Start&Stop systems can be implemented.

- Full Hybrids. The main characteristics of mild hybrids are here summed to the possibility of such architectures to be ICE independent during limited driving ranges. Of course, larger battery capacities are needed together with the presence of accurate energy management strategies, to fully exploit the potential benefits of the vehicle hybridization.

- Plug - in Hybrids. In this configuration the electric battery can be interfaced with the grid, allowing its full recharge when the driving cycle is finished. PHEVs share the characteristics of both full hybrid electric vehicles, having electric motor and an ICE, and of all-electric vehicles, having a plug to connect to the electrical grid.

- Electric Vehicles. Whenever the ICE is removed, the vehicle remains propelled by the electric motors only, with the battery rechargeable from the grid.

From this classification it is clear how mild and full hybrid architectures are intermediate architectures that potentially allow one to obtain consistent fuel consumption and emission reductions by means of relatively small modifications of the overall chassis system. This thesis is therefore dealing with these kind of architectures.
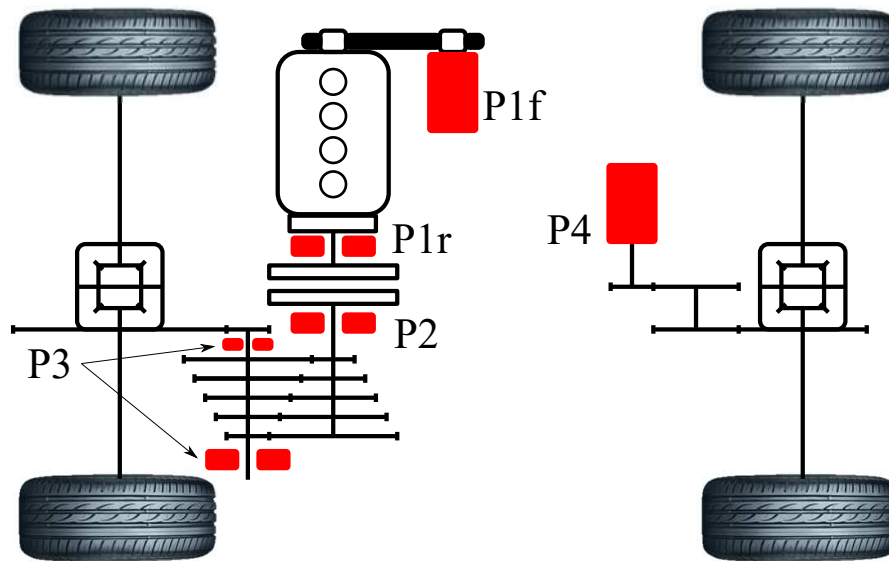
Fig. 1.2 Classification of hybrid architectures based on the position of the secondary energy converter.

1.2.3 Classification Based on the Position of the Secondary Energy Converter

Where mild and full hybrid architectures are concerned, the position of the electric motor is fundamental to undersand both the capabilities that the electric powertrain can offer, and the amount of modifications to be implemented for the installation. The choice of which hybrid configuration to consider is, as usual, a matter of compromises.

Based on the position of the electric motor with respect to the ICE, the classification is the following (Fig. 1.2):

- P1f. In this configuration the standard electric generator mounted on the front end accessory drive (FEAD) is substituted with a more powerful electric motor. Such an architecture is also called belt starter alternator (BSA) or belt starter generator (BSG). Regenerative braking can be performed but its efficiency is low due to the large amount of dissipated energy along the transmission, the engine and the belt. The connection between the electric motor and the ICE through the belt forces the former to be designed for high speeds (15 - 18 krpm), while the limited allowed space for the installation limits torque and power. However, the sensible advantages of this architecture provide cost effectiveness.

- P1r. Oppositely with respect to the previous configuration, the P1r electric motor is positioned on the output engine crankshaft. A more efficient regenerative braking can

be performed in this case and the motor can perform engine assistance together with being integrated inside the mechanical flywheel to improve the torque oscillation attenutation. However, due to its position, it should have a high torque density and meet axial requirements.

- P2. The previous configurations were ICE - dependent, in the sense that the coupling between the thermal and the electric machine could not be avoided. If the electric motor is mounted downstream of the mechanical clutch, disengaging it allows the ICE to be completely uncoupled with the motor, with the advantages of driving the vehicle in pure electric mode without dragging the engine with its pumping losses and inertia. In this case the motor speed should be linked with the maximum vehicle speed. Axial requirements are still important.

- P3. Moving downstream in the overall driveline, the electric motor can be placed at the input or output of the secondary transmission shaft. It has the same characteristics of the P2 configuration but regenerative braking is in this case maximized because of the presence of the differential only between the front wheels and the electric motor. Having to be integrated inside the transmission, its volume is still constrained.

- P4. With the P4 configuration the attention is moved on the opposite axle with respect to the one in which the ICE is positioned. The electric motor is connected to the wheels by means of a differential (of whatever kind) and although a re - thinking of the electric axle should take place, this configuration offers the possibility of maximizing the recovery of the energy together with giving full potential to the electric driving.

1.3   Thesis outline

The basic idea of this thesis work is to provide different methodologies to analyze a certain hybrid electric vehicle architecture both from a system level and from a component level point of view. The analyses that will be presented in next sections are not only focusing on the potential reductions in terms of fuel consumption and emissions that can be achieved by switching from conventional to HEV architectures, but also refer to additional issues that should be addressed when dealing with these kinds of systems.

Focusing on mild/full HEVs, based on the position of the secondary energy converter, the main goal can be the maximization of the energy recovery. Chapter 2 deals with the comparison between the P1f and P4 architectures, regarding regenerative braking potential.

Going more in - depth where the traction motor is concerned, Chapter 3 presents a method to establish the main mechanical characteristics of the electric motor of a certain family (e.g. given the typology, the kind of isotropy or anisotropy, the materials, the geometrical ratios between the different dimensions, ...). Electromechanical and thermal analyses are carried out, defining the motor volume, the current absorbtions for each working point and the cooling circuit characteristics.

Once the electric motor mechanical, thermal and electrical charactersitics are known, the presence of the battery pack in the model is also included. A map - based modeling for the electric battery is also considered in this case and Chapter 4 deals with it. A simple energy management strategy is introduced at this point to split the mechanical required torque to follow a prescribed driving cycle between the thermal and electric machines, taking into account all the limitations given by the electric powertrain. Based on this, a methodology for the electric battery sizing constituted by different and always more complete stages is presented and discussed.

The electric motor usage during conditions that are different with respect to the ones related to the previous chapter (e.g. cornering conditions) are analyzed in Chapter 5. Open loop braking during cornering manoeuvres are considered first, showing the oversteering tendency of the vehicle whenever the regenerative braking takes place. A simplified model for understanding the amount of introduced yaw moment due to a certain braking torque is developed, and takes into account the tires capabilities. From these considerations it is clear that the implementation of a hybrid electric architecture should not only be focused on the integration of the energy management strategy in the already existing vehicle/engine powertrain control unit. The attention is addressed also to the integration of the former in the network of the vehicle dynamics control systems.

Finally, the attention is focused on the system dynamics related to the driveline. A conventional powertrain is studied making use of classical system dynamics theories and a method for understanding the influence of each subcomponent on the filtering behavior of the transmission is presented. The perspectives of use of an additional actuator (the rear axle electric motor) to control the longitudinal dynamics are introduced and studied from the modeling point of view only.

Concluding remarks are given in Chaper 7.

Chapter 2

Mild Hybrid Electric Vehicles: Modeling and Potentialities

2.1 Introduction

Mild hybrid electric vehicles are vehicles with a low level of hybridization in which the electric machine has to assist the prime mover, the internal combustion engine. The power of such an electric machine is limited and smaller with respect to that produced by the thermal machine; therefore, its position and use should be properly decided to reduce power losses at minimum.

The role of the electric motor in such small hybrid vehicles is to perform a limited number of functionalities to reduce the utilization of the internal combustion engine. *Full electric start* is one of these working modes. The electric machine is driven until a certain vehicle speed in case of small amounts of longitudinal accelerations. Another interesting mode is the *regenerative braking*, in which the electric machine is driven as an electric generator to generate current and therefore electric power. The amount of energy stored can be re - used for several other purposes. From applied thermodynamics of internal combustion engines, it is well known that only between 35 and 38% of the energy contained in the fuel can be converted into mechanical energy. However, mechanical losses are also present. The main contribution is given by the rolling resistance, which plays for about 30 - 32% of the available mechanical energy, followed then by the engine friction and the accessories, which contribute for additional 25 - 29% of losses. During braking phases the lost mechanical energy is about 13 - 15% of the total, which is a relatively consistent percentage that can effectively be reduced or in some cases even elimitated.

The aforementioned functionalities can be realized with any of the various mild hybrid configurations provided that the electric powertrain available power is sufficient. The selection of one configuration rather than another should mainly be based on how efficiently the power flows from the electric machine to the wheels and vice versa, in addition to the required chassis installation modifications.

This chapter deals with the study of the influence of the electric machine position in the powertrain on the regenerative braking performance of the hybrid vehicle. Two configurations are analyzed: *P1f* and *P4* architectures.

Both the architectures have advantages in terms of simplicity and ease of control, but present different drawbacks. In the P1f configuration, for example, the presence of the internal combustion engine between the electric machine and the wheels reduces the effectiveness of the energy regeneration while requiring a higher amount of power for the traction. Oppositely, the P4 configuration does not have these kinds of drawbacks because of the (almost) direct connection between the electric motor and the wheels, but braking the rear axle of the vehicle can have implications from the vehicle handling and stability point of view. The general structure of the hybrid architecture under analysis is presented in Fig. 2.1.
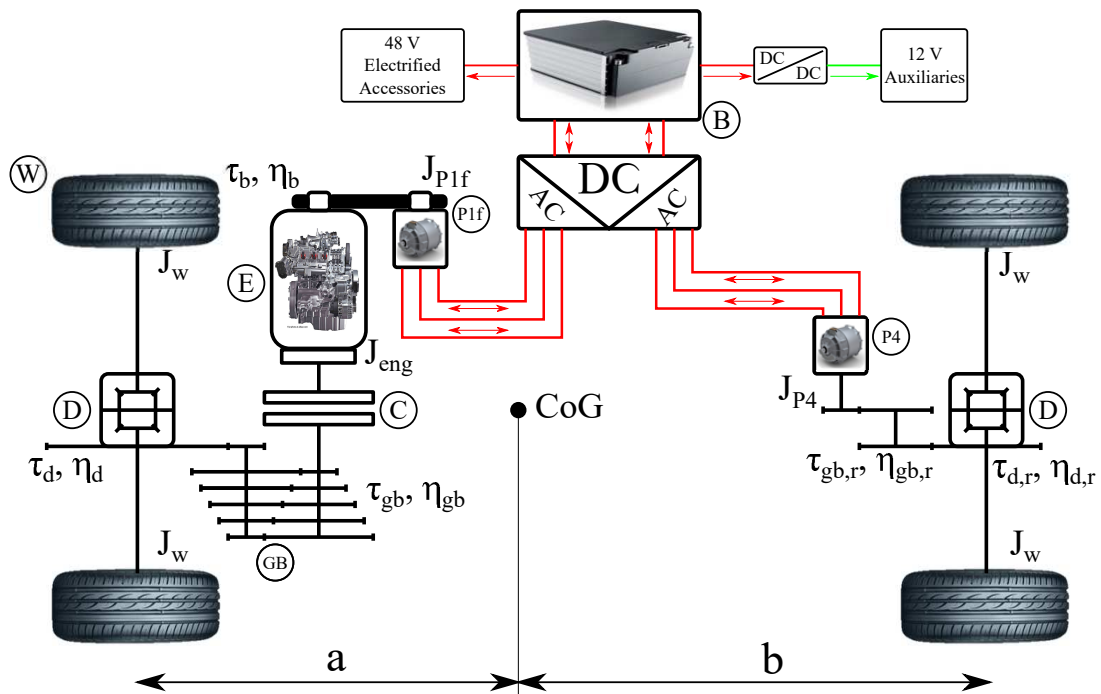
Fig. 2.1 Hybrid electric vehicle architecture under analysis. B = Battery, E = Engine, C = Clutch, GB = Gearbox, D = Differential, W = Wheels.

As mentioned, the P1f motor is connected to the engine by the belt transmission present on its front end, while the P4 motor drives the wheels of the rear axle, to which is connected by a single stage of reduction and a differential. A unique 48 V battery and a double stage inverter which converts DC to AC voltage supplies the two machines, with possibility of regeneration of energy. To reduce the resisting torque applied on the engine shaft due to the conventional accessories (water, oil and power steering pump, air conditioning compressor) generally mounted on the front end accessory drive, the same battery can supply power to (if present) an electrified version of such accessories. The 12 V network can be either supplied by an additional Lead - Acid battery (as in conventional vehicles) or by absorbing power from the 48 V battery through a step down DC/DC converter.

In the first part of this chapter the vehicle model will be described in all of its subcomponents, while in the second part the energy analysis will be performed. This analysis has the goal of understanding the amount of energy that during the regeneration phases dissipates in the different powertrain components before having reached the electric machine. It should be underlined that no attention is devoted to include the efficiency of the power electronics, the battery, or the electric motors, which are assumed to be 100%. This is done as a first trade off analysis, to observe the contributions to energy dissipation of the different powertrain subcomponents.

To assess the basic regenerative braking potential of the two architectures, the vehicle under consideration is a low segment vehicle. Data are omitted for confidentiality reasons.

2.2   Hybrid Vehicle Model

This section will present the modeling of the vehicle, of the powertrain, of the internal combustion engine and of the driver. For now, the electrical components are not considered (neither electric motors, nor the battery).

A number of simulation programs for design and optimization of electric and hybrid powertrains can be found in the literature. One of the most known is the Vehicle Simulation Program (VSP) [14] which is based on the creation of a series of pre - defined Matlab/Simulink components that can be assembled and modified by the user. Battery and electric motor empirical models are based on experimental data, and the vehicle performance, energy consumption and exhaust pollution can be computed. An evolution of this simulation tool has been lately realized [15] with a more flexible software and pre - defined models of the components based on look - up tables, steady - state or dynamic equations. Different vehicle configurations and driving cycles can be considered, comparing the

performance of the different solutions. Another Matlab/Simulink simulation program dedicated to hybrid vehicles is ADVISOR [16]. The efficiency of the electric motors and all the other powertrain components can be included by means of empirical look - up tables as a function of the motor speed and torque, including maximum torque and power limitations.

Despite the various simulation tools available, in this work a model of hybrid vehicle has been implemented in Matlab/Simulink environment due to its high level of flexibility offered in building different topologies of powertrain.

The overall implementation structure of the model is highlighted in Fig. 2.2, in which the different sub - blocks are shown. In the following, an accurate description of the sub - component modeling is provided. For the sake of simplicity, not all the power variables are shown. A more accurate scheme will be presented in Chapter 4. The reference speed
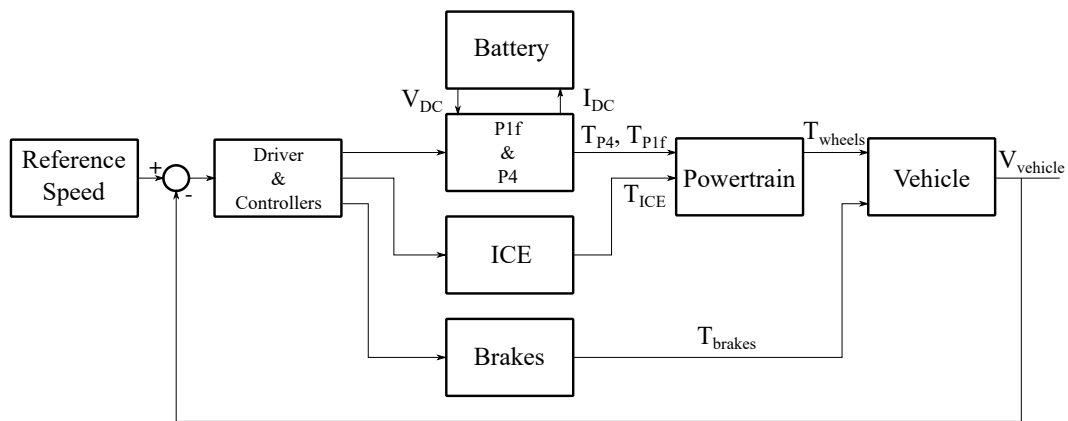
Fig. 2.2 Model structure of the hybrid architecture.

generator block contains all the driving cycle velocity profiles considered and it is compared with the actual vehicle velocity. The error between the two enters in the controller block which, based on traction or braking phases, on the status of the powertrain components and on the implemented torque split strategy, generates the reference torque points for the different actuators. The different torques are then sent to the powertrain block, which generates torques at the wheels level, translated into forces in the vehicle block.

2.2.1 Driver & Controllers

The driver block is constitued by a PI controller, responsible for the computation of the required throttle (α_t) or braking (β_p) position, to be then translated into the internal combustion engine required torque, to the electric motor required torque or to the passive

brakes required torque in the controllers block, in order to let the vehicle follow a desired longitudinal reference speed. In addition, a gear change duration of 0.2 s [96] is implemented and a maximum (2500 rpm) and minimum (1000 rpm) engine rotational speed is taken into account for gear up - shift and down - shift respectively. Clutch opening and closure is also controlled here. The gear change duration has been considered as constant regardless the engine speed due to the low dissipated energy in these transients compared to the available kinetic energy of the vehicle.

Controllers (responsible for the traction/braking distribution computation) are also implemented, but their description will be presented in Chapt. 4.

2.2.2   ICE

The Internal Combustion Engine is modeled as a torque generator, as a function of its rotational speed and of the throttle aperture α_{ice} defined by the controller. The engine torque - speed map is experimentally measured, together with the specific fuel consumption $q \, [g/\mathrm{HPh}]$.

At each simulation time step, the specific fuel consumption is known. The fuel flow rate can therefore be computed as:

$$\dot{m}_{\mathrm{fuel}}(t) = P_{\mathrm{mech}}(\omega, T, t) \, q(\omega, T, t) \tag{2.1}$$

where P_{mech} is the mechanical power. The amount of mass of fuel is computed integrating the fuel flow rate over the simulation time t_{f}:

$$\int_{t_0}^{t_{\mathrm{f}}} \dot{m}_{\mathrm{fuel}}(t) dt \tag{2.2}$$

If the mechanical power is zero (idling conditions), the fuel flow rate computation is substituted, considering directly a constant amount.

Finally, the engine resistance torque in over - running mode is also included, expecting its key role in the evaluation of the potential of the different mild hybrid architectures from fuel consumption, dissipated and recoverable energy points of view.

2.2.3 Powertrain & Vehicle

As already mentioned, performance and feasibility analysis of mild hybrid configurations are some of the goals of this and the following chapters. In addition, the vehicle will be driven on standard homologation cycles, characterized by relatively low longitudinal accelerations. Therefore, from this point of view, considering that for now the longitudinal driving comfort is neglected, the vehicle, wheels, and crankshaft inertias are taken into account, but they are rigidly connected to each other.

In the following, the model will be described as a function of the different sources of traction.

Front Wheel Drive Vehicle, ICE Traction

The net torque in output from the ICE is:

$$T_{\text{out,ICE}} = T_{\text{in,ICE}} - J_{\text{eng}}\dot{\omega}_{\text{eng}} \tag{2.3}$$

where $T_{\text{in,ICE}}$ is the torque computed from the engine map, J_{eng} is the crankshaft and flywheel inertia and $\dot{\omega}_{\text{eng}}$ is the crankshaft rotational acceleration.

The gearbox and final drive are modeled as a simple transmission ratio with an efficiency (τ_{gb}, τ_{d} and η_{gb}, η_{d} respectively). Gearbox efficiency is computed as a function of:

- Temperature

- Input torque

- Rotational speed of the input shaft

- Engaged gear

by means of experimental look up tables. The output torque from the gearbox is therefore:

$$T_{\text{out,gb}} = \eta_{\text{gb}}\eta_{\text{d}}T_{\text{out,ICE}}\tau_{\text{gb}}\tau_{\text{d}} \tag{2.4}$$

With infinitely stiff halfshafts and tire rims, the wheel torque is:

$$T_{\text{out,wheels,f}} = T_{\text{out,gb}} - J_{\text{w}}\dot{\omega}_{\text{w}} \tag{2.5}$$

where J_w is the tire moment of inertia and $\dot{\omega}_w$ is the tire rotational acceleration.

If R_r is the tire rolling radius, the front longitudinal tire force is:

$$F_{xf} = \frac{T_{out,wheels,f}}{R_r} \tag{2.6}$$

that during the simulations is always kept under the maximum permissible longitudinal force exploitable by the front tires:

$$F_{xf} < F_{xf,max} = \mu F_{zf} = \mu \frac{Mg}{l}\left(b - \frac{a_x h}{g}\right) \tag{2.7}$$

where μ is the friction coefficient of the tire - road contact and F_{zf} is the front vertical load, b is the distance between vehicle center of gravity and rear axle and h is the center of gravity height.

Finally, the equation of motion of the vehicle mass is:

$$Ma_x = F_{xf} - F_{res} \tag{2.8}$$

where M is the vehicle mass, a_x is the vehicle longitudinal acceleration and the resistant force F_{res} is computed by means of the coast down coefficients:

$$F_{res} = f_0 + f_1 V + f_2 V^2 \tag{2.9}$$

in which the vehicle speed is computed integrating the longitudinal acceleration over the simulation time T:

$$V = \int_0^T a_x dt + V_0 \tag{2.10}$$

Rear Wheel Drive Vehicle, P4 Traction

In this case, the torque is generated by the electric motor positioned on the rear axle. The net torque is:

$$T_{out,EMP4} = T_{in,EMP4} - J_{P4}\dot{\omega}_{em} \tag{2.11}$$

where $T_{in,EMP4}$ is the torque computed from the electric motor map, J_{P4} is the electric motor inertia and $\dot{\omega}_{em}$ is the electric motor rotational acceleration.

Between the electric motor and the wheels only a fixed transmission ratio ($\tau_{\mathrm{gb,r}}$) and a final drive ($\tau_{\mathrm{d,r}}$) is present. Therefore the torque to the wheels is:

$$T_{\mathrm{out,wheels,r}} = \eta_{\mathrm{gb,r}}\eta_{\mathrm{d,r}}T_{\mathrm{out,EMP4}}\tau_{\mathrm{gb,r}}\tau_{\mathrm{d,r}} - J_{\mathrm{w}}\dot{\omega}_{\mathrm{w}} \tag{2.12}$$

considering the transmission efficiencies $\eta_{\mathrm{gb,r}}$ and $\eta_{\mathrm{d,r}}$. Similarly to the front axle, the vehicle dynamic equation is:

$$Ma_{\mathrm{x}} = \frac{T_{\mathrm{out,wheels,r}}}{R_{\mathrm{r}}} - F_{\mathrm{res}} = F_{\mathrm{xr}} - F_{\mathrm{res}} \tag{2.13}$$

in which the rear axle longitudinal force is limited to the maximum permissible longitudinal force exploitable by the rear tires:

$$F_{\mathrm{xr}} < F_{\mathrm{xr,max}} = \mu F_{\mathrm{zr}} = \mu \frac{Mg}{l}\left(a + \frac{a_{\mathrm{x}}h}{g}\right) \tag{2.14}$$

All Wheel Drive Vehicle, ICE + P4 Traction

In case of parallel split between thermal and electric machine, the total traction force is the sum of that produced by the two machines. The computation of the torques to the wheels follows exactly the same expressions shown in the two previous subsections. Therefore the vehicle dynamic equation becomes:

$$Ma_{\mathrm{x}} = F_{\mathrm{xf}} + F_{\mathrm{xr}} - F_{\mathrm{res}} \tag{2.15}$$

Front Wheel Drive Vehicle, ICE + P1f Traction

Another torque split configuration can be the one in which the P1f helps the internal combustion engine providing a certain amount of the total required torque. In this case a mechanical coupling is interposed between the ice and the electric motor: the belt transmission is such a system. As a matter of fact, the standard alternator is positioned on the front end accessories drive (FEAD) together with tensioners, the A/C compressor and other accessories pulleys.

The P1f electric motor can provide both positive (traction) and negative (braking, battery charging) torque. The torque should therefore pass from the belt drive system, the engine, the gearbox and the differential before reaching the wheels. The opposite path is related to braking conditions.

To describe the efficiency of the belt drive system with a simple constant efficiency would lead to an oversimplification of the power available at the crankshaft (in case of traction) or at the level of the electric motor (in case of braking).

A model for belt drive system is therefore considered, which takes into account the slip losses. Such a model is described in [17] and implemented in the overall model. An efficiency variable as a function of the working conditions can therefore be obtained, feeding the model with the pretension of the belt or the amount of accessories connected to the belt, as examples. In the case of combined ICE and P1f traction the torque in output from the ICE will be:

$$T_{\text{out,ICE}} = \left(T_{\text{in,ICE}} + T_{\text{out,P1f}}\eta_{\text{b}}\tau_{\text{b}}\right) - J_{\text{eng}}\dot{\omega}_{\text{eng}} \qquad (2.16)$$

where $T_{\text{out,P1f}}$ is:

$$T_{\text{out,P1f}} = T_{\text{in,P1f}} - J_{\text{bds}}\dot{\omega}_{\text{em}} \qquad (2.17)$$

with J_{bds} being the inertia of the belt drive system and $T_{\text{in,P1f}}$ the P1f electric motor torque.

2.2.4 Brakes

To compute the braking torque at the vehicle level applied by the passive brakes, the braking pressure β_{p} is simply multiplied by the torque - pressure gain K_{p}. To split this torque between front and rear axle, a constant split ratio K_{sr} is considered as a first approximation model of the real brake system.

2.3 Energy Analysis

In this section, the regenerative braking potential for several braking maneuvers will be obtained and analyzed. It will be demonstrated where in the power chain the highest amount of vehicle kinetic energy is dissipated or, similarly, which mild hybrid architecture is able to more efficiently convert the energy from kinetic to electric.

Different ramps of speed (with negative slopes, in deceleration) have been given as the reference. The aim is to understand the amount of energy that, starting from the vehicle, is able to reach the electric motor and therefore to be converted into electric energy. A clear dependence on the vehicle speed is explained because of the kinetic energy, but a key factor that could affect the energy recuperation is expected to be the amount of deceleration. The former is varied from very low (20 km/h) to high speeds (100 km/h) while the latter

depends on the configuration under analysis. As an example, in case of P1f configuration the deceleration spans from very low values because the goal is that of illustrating the different dissipative actions under low deceleration levels.

Passive brakes are avoided and all the kinetic energy at the beginning of the simulation is dissipated in different powertrain components before reaching the electric motor.

2.3.1 Pure P1f

The belt drive system model is able to take into account the resistive loads (for instance the A/C compressor applies a resistant torque to the belt) and for the presence of automatic tensioners. In case of pure P1f braking, in order to separate the pure belt dissipations with other kind of dissipations, all the additional loads on the belt are considered null and the tensioner load has been set to a high value (high pretension). In this way, only inertia losses due to the pulleys and slip losses of the belt are taken into account. The kinetic energy of the vehicle at the beginning of the braking maneuver is:

$$E_{\mathrm{v}} = \frac{1}{2} M V_{\mathrm{x}}^2 = \int_{t_0}^{t_{\mathrm{f}}} [F_{\mathrm{xf}}(t) - F_{\mathrm{res}}(t)] V_{\mathrm{x}}(t)\, dt \qquad (F_{\mathrm{xf}}(t) < 0) \qquad (2.18)$$

The energy at the level of the wheels is:

$$E_{\mathrm{wheels,front}} = \int_{t_0}^{t_{\mathrm{f}}} F_{\mathrm{xf}}(t) V_{\mathrm{x}}(t)\, dt \qquad (F_{\mathrm{xf}}(t) < 0) \qquad (2.19)$$

The energy in output from the clutch (ICE side) is:

$$E_{\mathrm{clutch,out}} = \int_{t_0}^{t_{\mathrm{f}}} T_{\mathrm{clutch,out}}(t)\, \omega_{\mathrm{primary}}(t)\, dt \qquad \left(T_{\mathrm{clutch,out}}(t) < 0\right) \qquad (2.20)$$

where $T_{\mathrm{clutch,out}}$ is the engine torque multiplied by a value between 0 and 1 to model the absence of torque sent to the powertrain when the clutch is opened and $\omega_{\mathrm{primary}}$ is the rotational speed of the primary shaft. The energy output from the ICE (FEAD side) is:

$$E_{\mathrm{fead}} = \int_{t_0}^{t_{\mathrm{f}}} T_{\mathrm{fead,out}}(t)\, \omega_{\mathrm{ice}}(t)\, dt = \int_{t_0}^{t_{\mathrm{f}}} \frac{1}{\eta_{\mathrm{b}}(T_{\mathrm{em}}, \omega_{\mathrm{em}})} T_{\mathrm{em}}(t)\, \omega_{\mathrm{em}}(t)\, dt \qquad (T_{\mathrm{em}}(t) < 0)$$

$$(2.21)$$

And finally, the energy at the level of the FEAD electric motor is:

$$E_{\mathrm{em,P_{1f}}} = \int_{t_0}^{t_{\mathrm{f}}} T_{\mathrm{in,P_{1f}}}(t)\, \omega_{\mathrm{em}}(t)\, dt \qquad \left(T_{\mathrm{in,P_{1f}}}(t) < 0\right) \qquad (2.22)$$

Figure 2.3 presents the energy computed on different powertrain components at the end of each braking maneuver as a function of the initial vehicle speed for different amounts of deceleration. In particular, vehicle's kinetic energy, wheels' energy, clutch output energy, ICE output energy and electric motor energy are plotted.

As the vehicle speed increases, the difference between available energy at the wheels (dashed dotted lines) and vehicle's kinetic energy (dotted lines) is increasing with a not negligible influence of the deceleration, that leads this difference to increase when its amount is small. This is of strong interest for the potentialities of the aforementioned hybrid architecture: it is demonstrated that for low decelerations, typical of urban cycles for example, a very high quantity of kinetic energy is dissipated in aerodynamic and rolling resistances.

Energy in output of the clutch (red marked lines) is a function of the gearbox efficiency and is always smaller (in absolute value) than that at the wheels level, but the difference between the two is not correlated to the amount of deceleration.

The difference between ICE output (dashed lines) and clutch output energy is mainly due to the ICE resistant torque, and it is higher at lower decelerations. Finally, the difference between energy on FEAD side (crankshaft vs. electric motor), is basically not sensitive with the deceleration but and influence of the initial vehicle speed can be present.

Fig. 2.3 Plot of the energy vs. vehicle speed for different amount of deceleration. Top: -0.6 m/s^2, middle: -1 m/s^2, bottom: -1.2 m/s^2. Dotted lines: vehicle's kinetic energy, dashed dotted lines: energy at the wheels, red marked lines: energy in output from the clutch, dashed lines: energy at ICE out (FEAD side), continuous lines: energy available at the electric motor level.

Fig. 2.4 Plot of the energy vs. vehicle deceleration for different vehicle initial speeds. Top: 30 km/h, middle: 60 km/h, bottom: 100 km/h. Dotted lines: vehicle's kinetic energy, dashed dotted lines: energy at the wheels, red marked lines: energy in output from the clutch, dashed lines: energy at ICE out (FEAD side), continuous lines: energy available at the electric motor level.

Figure 2.4 presents the energy computed on the different powertrain components at the end of each braking maneuver as a function of the deceleration, for different initial vehicle speeds. As the deceleration increases, the general trend is that the amount of available energy at the electric motor level is closer to the vehicle's kinetic energy with respect to the same conditions in case of low decelerations. In addition, the amount of energy dissipated by the ICE due to its resistant torque seems to be more influential in case of low decelerations, reducing its influence whenever the initial speed is higher. The FEAD dissipated energy shows an increased influence in case of lower initial vehicle speed.

The aforementioned results can be clarified considering the amounts of dissipated energy in each subcomponent with respect to the total dissipated energy. The total dissipated energy in the powertrain, from the ground to the electric motor is:

$$E_{\text{diss,tot}} = |E_{\text{v}}| - \left|E_{\text{em,P}_{1\text{f}}}\right| \tag{2.23}$$

in which the dissipated energy due to resistance forces is:

$$E_{\text{diss,res}} = |E_{\text{v}}| - \left|E_{\text{wheels,front}}\right| \tag{2.24}$$

the dissipated energy in the powertrain is:

$$E_{\text{diss,pwt}} = \left|E_{\text{wheels,front}}\right| - \left|E_{\text{clutch,out}}\right| \tag{2.25}$$

the dissipated energy in the ICE is:

$$E_{\text{diss,ice}} = \left|E_{\text{clutch,out}}\right| - \left|E_{\text{fead}}\right| \tag{2.26}$$

and finally the dissipated energy in the BDS is:

$$E_{\text{diss,bds}} = \left|E_{\text{fead}}\right| - \left|E_{\text{em,P}_{1\text{f}}}\right| \tag{2.27}$$

The ratio between the dissipated energy in the ith component and the total dissipated energy for a braking maneuver (given an initial speeds and a deceleration) is plotted in Fig. 2.5.

As already described, the amount of ICE dissipated energy (blue bars) is more influential in case of small decelerations, both at low and high vehicle speeds. In particular, the lower the initial vehicle speed and the amount of deceleration, the higher the amount of energy dissipated in the ICE. This result is interesting because it demonstrates that the lack of possibility to open the clutch when braking with the electric machine penalizes the overall regeneration efficiency. Low average speeds and low decelerations (up to -0.5 m/s^2) are some of the main characteristics of homologation cycles (described in next chapter), so this effect is even more important and should be carefully considered when thinking about this hybrid architecture.

The BDS losses (red bars) follow the same trend where the initial speed is concerned, but present higher values when the deceleration is higher. Finally, dissipated energy due to aerodynamics and drag resistance is consistently high only at high decelerations when the initial speeds are low, but assumes the highest percentage of the total dissipated energy at high speeds regardless of the deceleration.
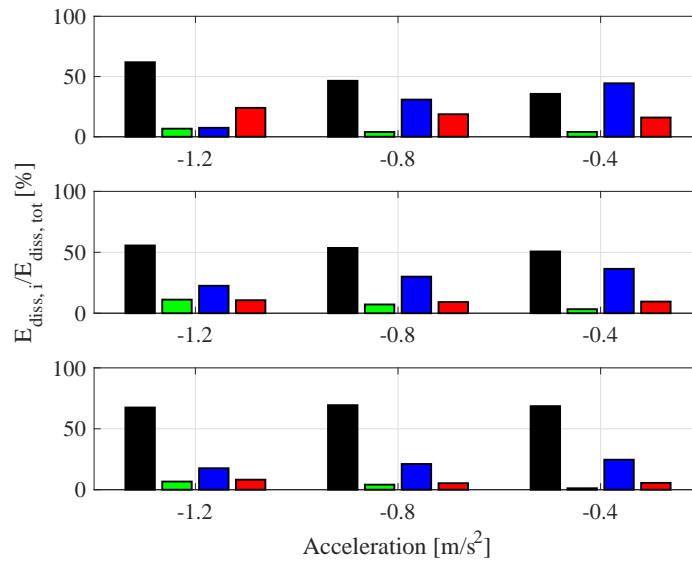
Fig. 2.5 Ratio between i^{th} and total dissipated energy vs. vehicle deceleration for different vehicle initial speeds. Top: 30 km/h, middle: 60 km/h, bottom: 100 km/h. Black bars: $E_{\text{diss,res}}$, green bars: $E_{\text{diss,pwt}}$, blue bars: $E_{\text{diss,ice}}$, red bars: $E_{\text{diss,bds}}$.

Summarizing, if the clutch opening is not allowed when braking the vehicle electrically, the most of the available kinetic energy is dissipated both in the ICE and in the BDS in the case of low speeds and low decelerations, while the aerodynamic and rolling resistances play a more important role in case of higher decelerations and higher speeds. The regeneration efficiency that the belt starter alternator can offer is therefore low due to the presence of a not negligible number of dissipative components between the road and the electric motor itself. Similar results can of course be obtained in the case of traction.

2.3.2 Pure P4

For the analysis of P4 energy regeneration during braking maneuvers, two configurations that reflect practical implementations are analyzed. The P4 electric motor can be extremely efficient during traction or braking phases because few dissipative components are present in the power chain. In this context, both the case in which the engine (with its resistance) is dragged by the transmission (closed clutch) and the case when the engine is uncoupled from the rest of the vehicle (open clutch) are analyzed in terms of regeneration efficiency.

Closed Clutch

The case of theclosed clutch is analyzed first since it takes into account energies that will then be considered as zero in the open clutch case.

The vehicle kinetic energy is:

$$E_v = \frac{1}{2}MV_x^2 = \int_{t_0}^{t_f} (F_{xr}(t) - F_{res}(t))V_x(t)\,dt \qquad (F_{xrw.}(t) < 0) \qquad (2.28)$$

The energy at the level of the rear wheels is:

$$E_{wheels,rear} = \int_{t_0}^{t_f} F_{xr}(t)V_x(t)\,dt \qquad (F_{xr}(t) < 0) \qquad (2.29)$$

The energy at the rear differential is:

$$E_{diff,rear} = \int_{t_0}^{t_f} T_{diff,rear}(t)\,\omega_{diff,rear}(t)\,dt = \int_{t_0}^{t_f} \frac{1}{\eta_{gb,rear}} T_{in,EMP4}(t)\,\omega_{em}(t)\,dt \qquad (T_{in,EMP4}(t) < 0)$$
$$(2.30)$$

And, finally, the energy at the P4 electric motor is:

$$E_{em,P4} = \int_{t_0}^{t_f} T_{in,EMP4}(t)\,\omega_{em}(t)\,dt \qquad (T_{in,EMP4}(t) < 0) \qquad (2.31)$$

Nevertheless, since the clutch is closed a portion of the total kinetic energy travels along the front powertrain reaching the engine and therefore the front wheels. The energy at the ICE level is:

$$E_{ICE} = \int_{t_0}^{t_f} T_{in,ICE}(t)\,\omega_{ice}(t)\,dt \qquad (T_{in,ICE}(t) < 0) \qquad (2.32)$$

which at the net of its inertia becomes:

$$E_{ICE,out} = \int_{t_0}^{t_f} \left[T_{in,ICE}(t) - J_{eng}\dot{\omega}_{eng}(t) \right] \omega_{eng}(t)\,dt \qquad (T_{in,ICE}(t) < 0) \qquad (2.33)$$

Finally, the energy at the front wheels is:

$$E_{wheels,front} = \int_{t_0}^{t_f} F_{xf}(t)V_x(t)\,dt \qquad (F_{xf}(t) < 0) \qquad (2.34)$$
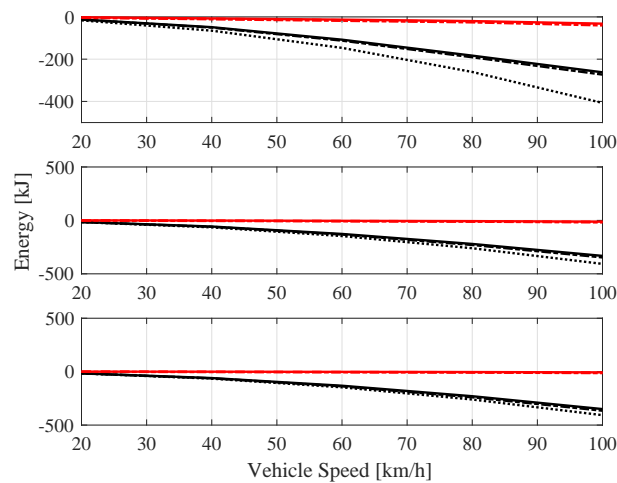
Fig. 2.6 Plot of the energy vs. vehicle speed for different amount of deceleration. Top:-1 m/s^2, middle: -2.1 m/s^2, bottom: -2.9 m/s^2. Black dotted lines: vehicle's kinetic energy, black dashed dotted lines: energy at the rear wheels, black continuous lines: energy at the electric motor P4, red dashed dotted lines: energy at ICE (FEAD side), red dashed lines: energy at ICE output (clutch side), red continuous lines: energy at the front wheels.
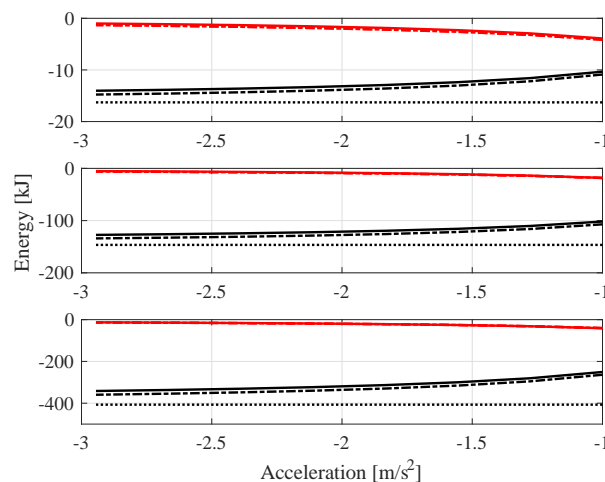
Fig. 2.7 Plot of the energy vs. vehicle deceleration for different vehicle initial speeds. Top: 20 km/h, middle: 60 km/h, bottom: 100 km/h. Black dotted lines: vehicle's kinetic energy, black dashed dotted lines: energy at the rear wheels, black continuous lines: energy at the electric motor P4, red dashed dotted lines: energy at ICE (FEAD side), red dashed lines: energy at ICE output (clutch side), red continuous lines: energy at the front wheels.

Figure 2.6 shows the amount of energy that reaches the different powertrain components as a function of initial vehicle speed for different decelerations. As already evidenced, the resistance forces due to aerodynamics and rolling resistances play an important role in the total energy dissipation, especially for low decelerations. With the clutch closed, a portion

of the available energy also dissipates inside the ICE and thus in the front powertrain. The portion of energy that dissipates in the front powertrain is however very small compared to that reaching the rear electric motor if the deceleration is high, while in case of low decelerations the clutch opening could provide a higher regeneration efficiency.

Figure 2.7 shows the amount of energy that reaches different powertrain components as a function of the amount of deceleration for different initial vehicle speeds. As the deceleration increases, the amount of energy that reaches the electric motor is always closer to the vehicle's kinetic energy as the dissipations in the system decrease. In addition, as already evidenced, the ICE dissipations play a more important role in the total dissipated energy when the vehicle speed and deceleration are both small.

In the context of P4 hybrid configuration, the computation of the dissipated energy in case of the closed clutch is slightly different with respect to the P1f configuration. The motivation is that two sources of energy dissipation (electric motor and ICE) are present, but they belong to axles coupled to each other only through the road. The computation of the dissipated energy should start from the ground and then proceed through the different components until reaching the two machines.

At the wheels level, the vehicle's kinetic energy is distributed between the resistant forces and the wheels forces of the two axles. Therefore, in terms of energy:

$$|E_\mathrm{v}| = \left(\left|E_\mathrm{wheels,front}\right| + \left|E_\mathrm{wheels,rear}\right|\right) + E_\mathrm{diss,res} \tag{2.35}$$

The energy at the level of the rear wheels is:

$$\left|E_\mathrm{wheels,rear}\right| = E_\mathrm{diss,pwt,r} + \left|E_\mathrm{em,P4}\right| \tag{2.36}$$

while at the front is:

$$\left|E_\mathrm{wheels,front}\right| = |E_\mathrm{ICE}| - E_\mathrm{diss,pwt,f} \tag{2.37}$$

Therefore, the energy conservation equation becomes:

$$|E_\mathrm{v}| = \left|E_\mathrm{em,P4}\right| + |E_\mathrm{ICE}| + E_\mathrm{diss,pwt,r} + E_\mathrm{diss,res} - E_\mathrm{diss,pwt,f} \tag{2.38}$$

that can be rearranged as:

$$E_\mathrm{diss,tot} = |E_\mathrm{v}| - \left|E_\mathrm{em,P4}\right| + E_\mathrm{diss,pwt,f} = |E_\mathrm{ICE}| + E_\mathrm{diss,pwt,r} + E_\mathrm{diss,res} \tag{2.39}$$

Notice that to the total dissipated energy ($|E_{\mathrm{v}}| - |E_{\mathrm{em,P4}}|$) includes the amount of dissipated energy at the front powertrain, for the sake of simplicity of the results. In this way the summation of the percentages of the different dissipated energies is 100%.
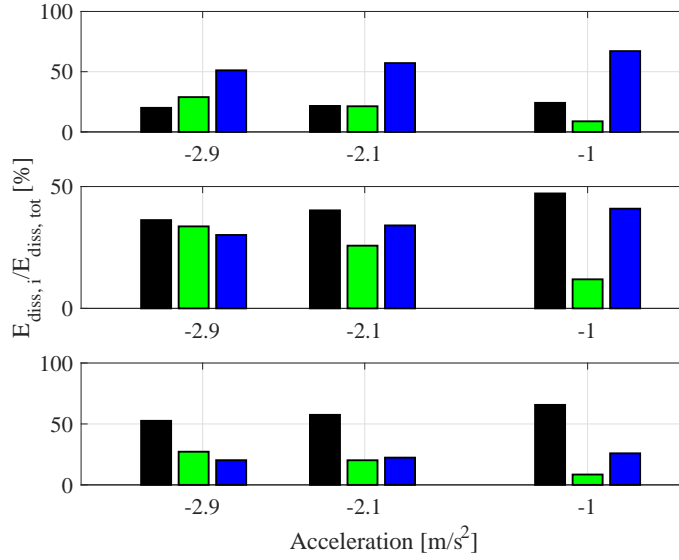
Fig. 2.8 Ratio between i^{th} and total dissipated energy vs. vehicle deceleration for different vehicle initial speeds. Top: 20 km/h, middle: 60 km/h, bottom: 100 km/h. Black bars: $E_{\mathrm{diss,res}}$, green bars: $E_{\mathrm{diss,pwt,r}}$, blue bars: E_{ICE}.

Figure 2.8 shows the ratio between the dissipated energy in the ith component with respect to the total dissipated energy expressed by Eq. 2.39 as a function of the deceleration for different initial vehicle speeds. The amount of dissipated energy related to the aerodynamic and rolling resistance increases as the deceleration decreases and as the initial vehicle speed increases. The dissipated energy related to the rear powertrain maintains almost the same percentage with changes in initial speed, but is less influential when dealing with lower decelerations. Finally, the energy that reaches the engine and therefore is dissipated is much more influent in the overall energy dissipation as the deceleration decreases and the initial vehicle speed is smaller.

Open Clutch

The open clutch configuration is a particular case of the closed clutch configuration in which the following considerations are taking place:

$$E_{\mathrm{ICE}} = E_{\mathrm{ICE,out}} = E_{\mathrm{wheels,front}} = 0 \tag{2.40}$$

therefore:

$$E_{\text{ICE}} = E_{\text{diss,pwt,f}} = 0 \tag{2.41}$$
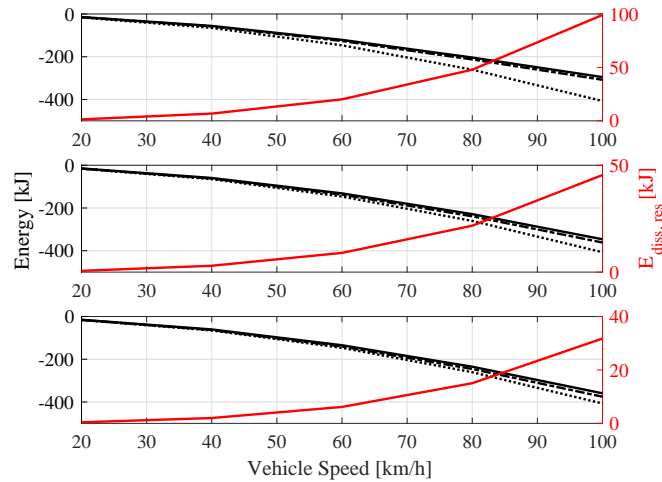
Fig. 2.9 Plot of the energy vs. vehicle speed for different amount of deceleration. Top:-1 m/s^2, middle: -2.1 m/s^2, bottom: -2.9 m/s^2. Dotted lines: vehicle's kinetic energy, dashed dotted lines: energy at the rear wheels, continuous lines: energy at the electric motor P4, red continuous lines: dissipated energy due to aerodynamics and rolling resistances.

For the open clutch configuration, it is therefore only needed to underline the importance of the energy dissipated due to the resistance forces. Figs. 2.9 and 2.10 present it on a separated y axis scale, showing its influence on the difference between kinetic and electric motor energy. The $E_{\text{diss,res}}$ increases when increasing the initial speed and its amplitude is smaller when dealing with high decelerations.
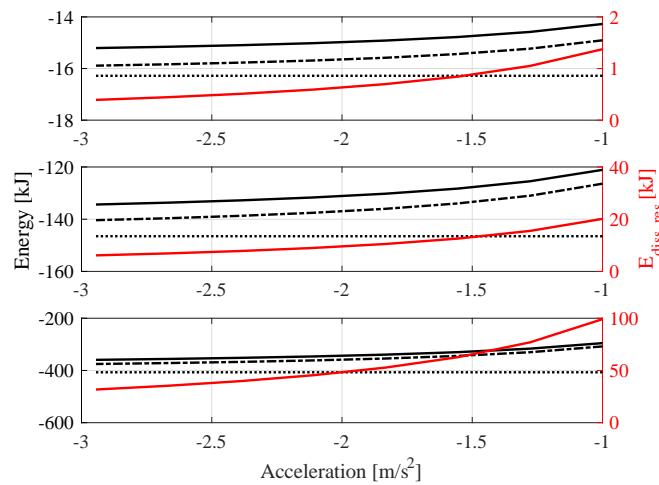
Fig. 2.10 Plot of the energy vs. vehicle deceleration for different vehicle initial speeds. Top: 20 km/h, middle: 60 km/h, bottom: 100 km/h. Black dotted lines: vehicle's kinetic energy, black dashed dotted lines: energy at the rear wheels, black continuous lines: energy at the electric motor P4, red continuous lines: dissipated energy due to aerodynamics and rolling resistances.

2.4   Chapter Summary

The two architectures of mild hybrid electric vehicle have been analyzed regarding their potential for total energy regeneration. The effects of all the dissipations in their components have been evaluated as a function of the vehicle speed when the braking starts and amount of deceleration.

Figures 2.11 and 2.12 summarize the main differences between vehicle's kinetic energy and energy that dissipates in the electric machines considering the analyzed configurations.

The P4 architecture with the open clutch configuration during braking seems to be very efficient from the energy regeneration point of view, due to the electric motor proximity to the road. As a matter of fact, the energy reaching the electric motor is close to the kinetic energy, whatever the initial speed or the deceleration. Thinking about this fact, only an in - wheel motor architecture could offer a higher amount of recoverable energy. The differences between kinetic and P4 energy are related mainly to the aerodynamics and rolling resistances and have been previously described in detail.

The P1f architecture has been restricted to realize small decelerations (to avoid slip problems of the belt based on the FEAD configuration under analysis). Nevertheless, in its range of working conditions, it can be a good compromise between chassis modifications and recoverable energy, especially when the initial braking speeds and the decelerations

are low. An appreciable behavior is shown, with results that in some cases are even better than to the ones obtained with P4 architecture with the closed clutch configuration.

However, there is no reason why, both in braking and therefore in traction phases, the clutch should maintain its closed conditions, forcing the electric machine to drag the engine and all the front powertrain. The effects of keeping the clutch closed are so severe that a configuration with such large potential and power installed on board reduces to behave like an architecture which offers a lower degree of hybridization.

Therefore, this chapter concludes with the remark that the P4 architecture is powerful and efficient, provided that during the use of the electric machine, a control strategy that governs the clutch opening and closure is introduced.

The benefits of the installation of such an electric machine on the overall fuel consumption of the vehicle are described in Chapter 4, while in the next chapter the attention is devoted to the electromagnetic and thermal design of a P4 electric motor for rear axle application.
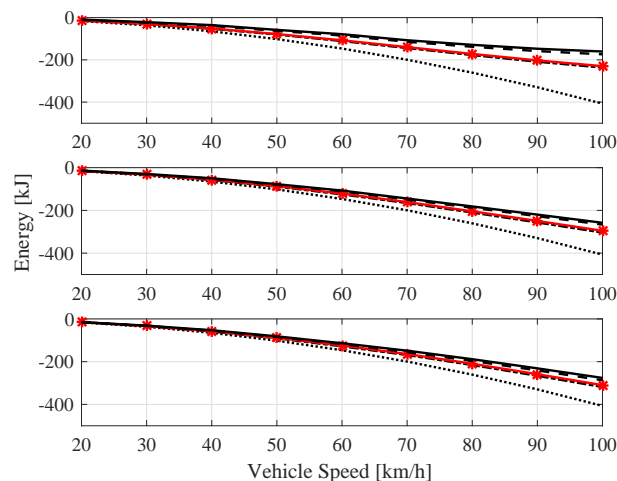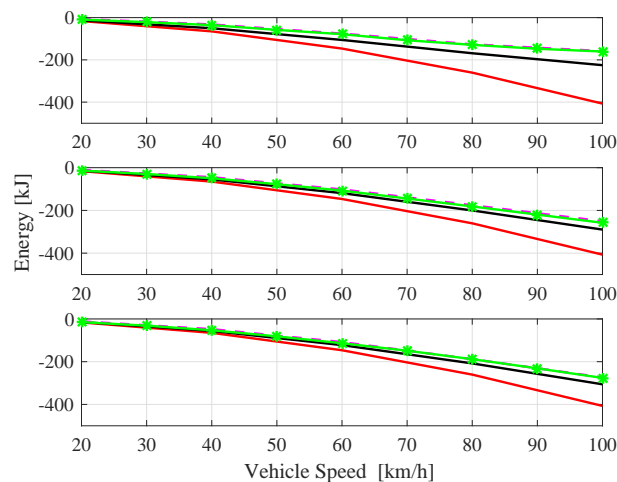

Fig. 2.11 Plot of the energy vs. vehicle speed for different amount of deceleration. Top:-0.6 m/s^2, middle: -1 m/s^2, bottom: -1.2 m/s^2. Red continuous lines: vehicle's kinetic energy, black continuous line: energy at P4 motor with open clutch, purple dashed lines: energy at P4 motor with closed clutch, green marked lines: energy at P1f motor.
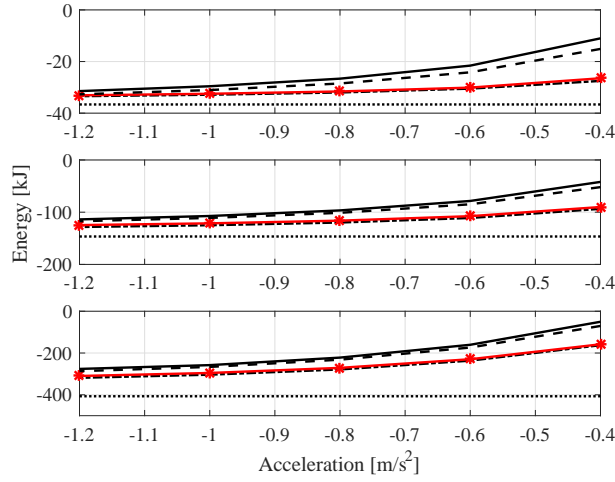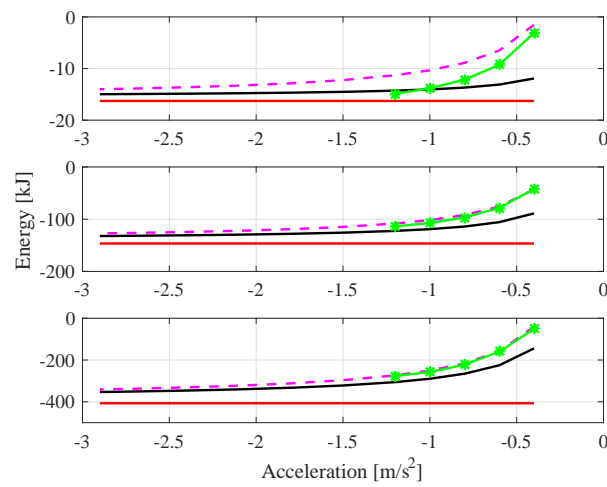
Fig. 2.12 Plot of the energy vs. vehicle deceleration for different vehicle initial speeds. Top: 20 km/h, middle: 60 km/h, bottom: 100 km/h. Red continuous lines: vehicle's kinetic energy, black continuous line: energy at P4 motor with open clutch, purple dashed lines: energy at P4 motor with closed clutch, green marked lines: energy at P1f motor.

Chapter 3

Design Selections and P4 Electric Motor Design

3.1 Introduction

The previous chapter analyzed two different mild hybrid architectures, showing that the proximity of the electric machine to the wheels of the vehicle allows an increase in the overall efficiency of the power transmission, both in the case of traction and braking conditions.

From this point of view, the P4 configuration presents the highest number of advantages. However, it would be interesting to more accurately test its potential, understanding the real advantages that it can introduce. In order to do so, more information (torque vs. speed map, efficiency, thermal characteristics) is required.

When selecting an electric motor, manufacturers only provide a limited amount of information, such as the torque speed map (in continuous and peak operations), rated current and efficiency map (rarely) together with some thermal characteristics. Precise data on these quantities regarding each admissible working point of the electric motor are, in general, not available.

The aim of this chapter is to design an electric machine for a rear axle hybrid vehicle. The goal is not only to apply the conventional electromagnetic design procedures and design control strategies to obtain all of those data and information that are commonly not available in catalogs. A framework for the design of a traction motor for mild hybrid vehicles is built to support preliminary component and system level analysis, and the mechanical characteristics of the electric motor are optimized for given motor families

(given the tipology, the materials, the number of phases, slots and pole pairs, etc.) based on the application under analysis.

Crucial relevance is given to the parameters that will feed the complete vehicle model, letting the performance and fuel consumption analysis to be performed taking into account for the losses in all the powertrain components.

The selection of the electric motor continuous and peak performance is based on its working conditions. More specifically, the required torque and power is obtained considering different specifications given both from its main operation (drive and brake the vehicle during driving cycles) and from secondary objectives (e.g. drive the vehicle in full electric on a ramp).

Once the performance criteria are defined, the design procedure for the electric machine will be presented. Such a procedure includes both the design for the constant torque zone of the motor and for the constant power zone. Particular importance is therefore given to the control strategies for field weakening. Phase and DC current maps are also obtained.

The chapter concludes with a thermal analysis on the designed motor.

3.2   Design Selections

In this section, particular importance is now given to the definition of the mechanical characteristics of the electric machine, such as peak/continuous torque and power rather than maximum speed. It is underlined that the vehicle considered (until the end of the work) is a C class sport utility vehicle. The introduction of P4 architecture can be cost effective from this range of segments on.

The procedure to obtain these characteristics is similar to the one that is generally followed when dealing with the design of the electric powertrain for full electric vehicles:

- Compute the required power;

- Select a proper transmission ratio to optimize the behavior of the installed electric machine on the vehicle in terms of efficiency and acceleration performance;

- Design the motor based on the mechanical characteristics;

- Design the energy storage system based on required power and energy requirements.

In this case the main difference is related to the behavior that such an electric machine is expected to exhibit during a driving cycle. Fig. 3.1 presents the four main widespread

driving cycles considered during fuel consumption and emission analyses. Tab. 3.1 shows the main characteristics of the aforementioned cycles.
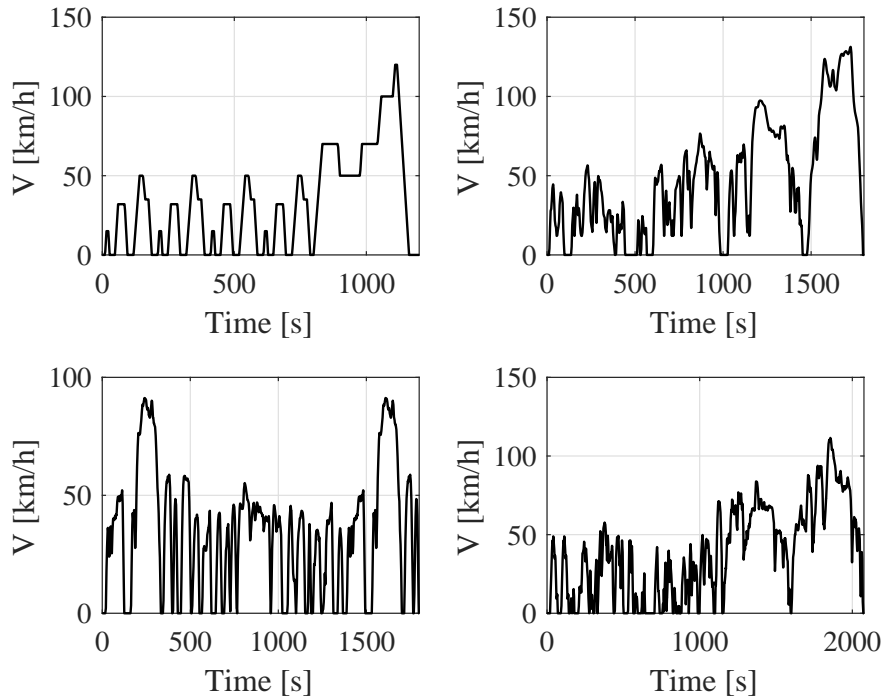
Fig. 3.1 The four main driving cycles considered. Top left: NEDC (New European Driving Cycle) cycle, top right: WLTP (Worldwide Harmonized Lightweight Vehicles Test Procedure) cycle, bottom left: FTP - 75 (Federal Test Procedure) cycle, bottom right: Artemis cycle.

	NEDC	WLTP	FTP - 75	Artemis
Duration, [s]	1200	1800	1874	2076
Distance, [km]	10.69	23.26	17.77	22.14
Average Speed, [km/h]	32.1	46.5	34.13	38.4
Maximum Speed, [km/h]	120	131.3	91.24	111.5
Minimum Acceleration, [m/s^2]	-0.84	-1.5	-1.47	-4.08
Maximum Acceleration, [m/s^2]	0.77	1.75	1.47	2.86

Table 3.1 Main characteristics of the four driving cycles considered.

Within the hybrid architectures under consideration, the full electric drive is performed up to predefined vehicle speeds, in most cases quite low (20 - 50 km/h). Therefore, the

need of high torque and power in this context is not justified. With a high potential for retrofit, the hybrid architecture under analysis should not be subjected to a massive adding of on - board power, with the penalty of the loss of benefits introduced by the electric powertrain. Finally, the thermal behavior of the machine should be analyzed, to fully understand the thermal loads the motor experiences during, for example, overloading conditions.

It is therefore clear how the design of the electric motor should be multidisciplinary. Since many physics are accounted for (mechanical, electromagnetic, thermal), it is worth-while to create a framework in which the different phenomena are modeled and for which a design methodology is established.

The literature on the subject is mainly oriented to the optimization of the electric motor electrical parameters for electric vehicle applications (e.g. [18] - [24]). A less specific methodology, but more comprehensive in all the different physical aspects is developed in this work considering established electric motor topological characteristics, with the main focus being the expected use of the electric machine during its different working conditions.

Given the mechanical characterstics of the electric motor (e.g. continuous and peak torque and power, base speed, maximum speed) its optimization could regard:

- Typology (permanent magnet, induction, switched reluctance, dc machines etc.);

- Materials (hard or soft magnetic materials, steel chemical composition, permanent magnets chemical composition etc.);

- Geometrical constraints (lenght to diameter ratio, rotor to stator diameter ratio, shoes to teeth width etc.)

- Topology (number of phases, number of slots, number of pole pairs etc.)

If, instead, all of these parameters are addressed to a particular class of machines and are selected based on consistent criteria, the optimization could regard the mechanical characteristics of the electric motor in order to avoid its over or under dimensioning. To this end, the aim is not to propose an innovative and optimized design methodology for electric motors, but to adapt and optimize their mechanical characteristics based on the vehicle and the application under analysis, considering a fixed class of motors.

Therefore, the mechanical characteristics of the electric machine are strictly dependent on the potential of the overall hybrid architecture and on the performance that is set to be realized. In the following, such aspects will be analyzed in detail.

3.2.1 Computation of the Electric Motor Mechanical Characteristics

Recalling Eq. 2.13, related to the case of pure rear traction:

$$F_{xr} = Ma_x + F_{res} \qquad (3.1)$$

it is possible to distinguish between three kind of forces:

- $F_{kinetic} = Ma_x$;

- $F_{resistances} = F_{res}$;

- $F_{traction} = F_{xr}$.

which, knowing the speed profile to be followed, allow one to compute different powers:

- $P_{kinetic} = Ma_x V$;

- $P_{resistances} = F_{res} V$;

- $P_{traction} = F_{xr} V$.

Considering the vehicle running the driving cycle in pure electric mode (which, as explained previously, is true up to predefined vehicle speeds), the electric motor required power can be computed taking into account a mechanical efficiency of the transmission interposed between the electric motor itself and the ground (η_t). Similarly, the electric motor torque can be computed for each point of the cycle if a transmission ratio between the electric motor and the wheels is considered (τ_{em}, which is $\tau_{gb,r} \cdot \tau_{d,r}$ in the previous chapter). In the case of traction:

$$\begin{cases} P_{em} = P_{traction}/\eta_t \\ T_{em} = F_{traction}R_r/(\eta_t\tau_{em}) \end{cases} \qquad (3.2)$$

while in the case of braking:

$$\begin{cases} P_{em} = \eta_t P_{traction} \\ T_{em} = \eta_t F_{traction}R_r/\tau_{em} \end{cases} \qquad (3.3)$$

The specifications of the electric motor design are the following:

- Peak power: based on the required power to reproduce a WLTP cycle, considering a maximum vehicle speed for pure electric traction $V_{\text{v,max,PE}}$ (WLTP cycle is here considered due to its imminent widespread use in homologation test procedures);

- Peak torque: based on the maximum torque to reproduce a WLTP cycle. To be verified according to other presented constraints, e.g. the effect of motor/wheels transmission ratio;

- Base speed: based on $V_{\text{v,max,PE}}$;

- Maximum speed: based on electric motor/wheels transmission ratio and maximum vehicle speed (along driving cycles).
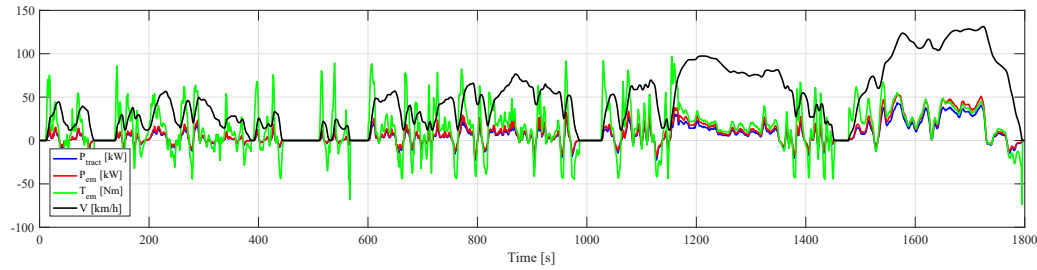
Fig. 3.2 Required power for traction, electric motor power and torque and vehicle speed during a WLTP driving cycle.

Figure 3.2 presents the time history of required traction power, electric motor power and torque and vehicle speed of a WLTP driving cycle, considering a fixed transmission ratio between the electric motor and the rear wheels.
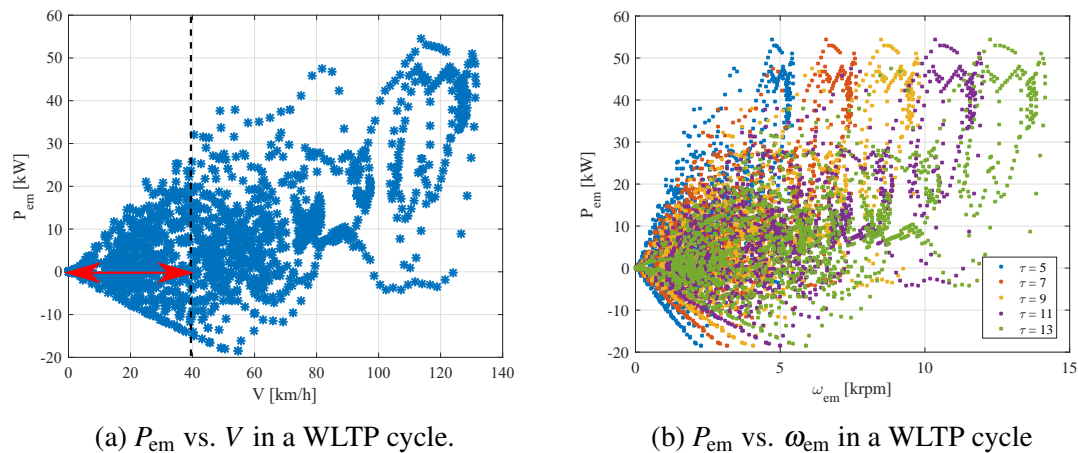
(a) P_{em} vs. V in a WLTP cycle.

(b) P_{em} vs. ω_{em} in a WLTP cycle

Fig. 3.3 Electric motor power during a WLTP cycle as a function of the vehicle and electric motor speed.

Peak and Nominal Power

Figure 3.3a shows the electric motor power plotted in terms of actual working points as a function of the vehicle speed and of its rotational speed. A maximum vehicle speed for pure electric traction ($V_{v,max,PE}$) has been set to 40 km/h, therefore finding the peak power of the motor (about 30 kW). No influence of the transmission ratio is present. As will be presented more clearly in next sections, this speed is of fundamental importance for managing the available stored energy on - board. In particular, it is used as a control parameter for the working conditions of the electric motor. The value of 40 km/h has been chosen because it is the average speed of the WLTP cycle in the low and medium driving conditions (city driving). The nominal power of the motor has been selected to be one third of the peak power (10 kW).

Peak Torque

The peak torque specification is given by the value of torque required for letting the vehicle follow the driving cycle. This value is strictly dependent from the transmission ratio, as presented in Fig. 3.4; the lower the transmission ratio, the higher the peak torque and the lower the maximum electric motor speed. Oppositely, a higher transmission ratio allows a reduction of the required peak torque, but increases the working range of the motor in terms of speed.

As will be presented in further sections, the electric motor torque is directly proportional to its rotor volume and therefore to its mass, while the maximum electric motor speed is instead a function of the electromagnetic design and of the applied control strategy. To drive the design to a high torque/low speed motor or vice versa, means then to put more effort on the electromagnetic design rather than on mass reduction.

Maximum Speed - 1

Another specification that can be set for the electric motor design parameter selections is the maximum electric motor speed. Generally speaking, for this kind of application, the connection between the motor and the wheels can be permanent or releasable. If it is permanent the motor's shaft always rotates together with the vehicle's wheels, while if releasable this connection can be opened by means of clutches. In the first case, the motor should be designed based on the maximum vehicle speed while, in the second one, an additional component should be introduced to decouple the motor from the rest of the vehicle.
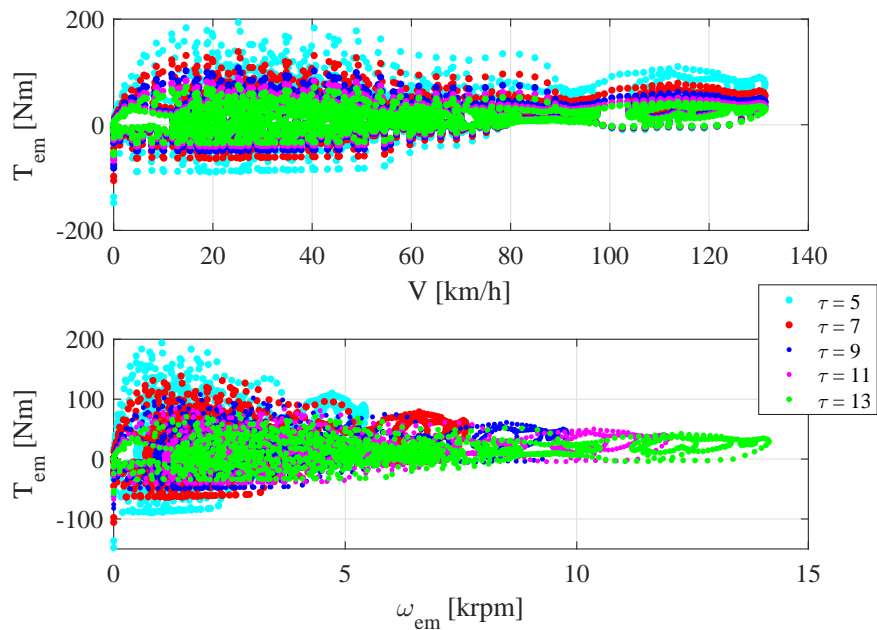
Fig. 3.4 Electric motor torque as a function of its speed (down) and of the vehicle speed (up) during a WLTP cycle.

For this application, the first type of connection has been selected, and the maximum electric motor speed should be in agreement with the maximum vehicle speed along WLTP cycle (130 km/h).

$\tau_{em}\,[-]$	10	11	12	13
$\omega_{em,max}\,[rpm]$	11026	12129	13232	14334

Table 3.2 Selectable electric motor maximum speeds depending on motor/wheels transmission ratio based on WLTP maximum vehicle speed.

Table 3.2 presents the values of the maximum electric motor speed as a function of the rear transmission ratio. Based on the maximum vehicle speed, reasonable values for $\omega_{em,max}$ can stand between 12 and 15 krpm, leading to transmission ratios between 11 and 13. Making reference to Fig. 3.4, the aforementioned transmission ratios lead to required peak torque between 80 and 90 Nm. The final transmission ratio is obtained after considering additional constraints later described.

Base Speed

The electric motor base speed is the one at which the maximum power is reached. Coherently, it can be chosen as the speed relative to $V_{v,max,PE}$. The effect of the transmission ratio is then the following:

$$\omega_{em,base} = V_{v,max,PE}/R_r \tau_{em} \tag{3.4}$$

Table 3.3 presents the values of the selectable base speeds depending on different transmission ratios values.

$\tau_{em} [-]$	10	11	12	13
$\omega_{em,base} [\text{rpm}]$	3537	3890	4244	4598

Table 3.3 Selectable electric motor base speeds depending on motor/wheels transmission ratio.

The definition of the electric motor specifications based on the driving cycles allows one to obtain its main characteristics, which will be the input for the design phase. These specifications are a function of the overall vehicle architecture, in which the electric motor is used to maximize the regeneration of energy and to support the ICE during the traction phases. Pure electric vehicle mode is however an important working mode. Therefore, additional functional requirements are considered apart from the main ones related to the driving cycle. These are:

- Hill start: maximum ground slope that the vehicle must be able to overcome in transient conditions. The ground slope is set to 15% and the acceleration to 1 km/h/s.

- Torque @ max speed: the vehicle must be able to travel in pure electric mode at a speed that can be considered the maximum WLTP speed.

- Maximum acceleration: the acceleration time 0 - 50 km/h must be less than 10 s.

Before considering the aforementioned requirements as verification for the specifications drawn until now, a more refined model for the computation of the required torque and power at the electric motor level is considered.

Recalling Newton's second law, the difference between the available and the required power for motion (P_a and P_n respectively) generates a variation of the vehicle's kinetic

energy in time:

$$P_a - P_n = \frac{dT}{dt} \tag{3.5}$$

The vehicle's kinetic energy takes into account for the different inertias that should be accelerated. In particular the inertia of the electric motor, of the wheels and of the vehicle mass itself are taken into account:

$$T = \frac{1}{2}J_{em}\omega_{em}^2 + \frac{1}{2}J_w\omega_w^2 + \frac{1}{2}MV^2 \tag{3.6}$$

which reporting all the contributions at the level of the vehicle becomes:

$$T = \frac{1}{2}J_{em}\left(\frac{V}{R_r}\tau_{em}\right)^2 + \frac{1}{2}J_w\left(\frac{V}{R_r}\right)^2 + \frac{1}{2}MV^2 = \frac{1}{2}\left(M + \frac{J_w}{R_r^2} + \frac{J_{em}\tau_{em}^2}{R_r^2}\right)V^2 \tag{3.7}$$

that is modified taking into account for the transmission efficiency as:

$$T = \frac{1}{2}\left(M + \frac{J_w}{R_r^2} + \frac{J_{em}\eta_t\tau_{em}^2}{R_r^2}\right)V^2 \tag{3.8}$$

The available mechanical power is simply:

$$P_a = \eta_t T_{em}\omega_{em} \tag{3.9}$$

while, neglecting the terms dependent to the square of the speed (which are negligible at low speeds), the required power for motion is:

$$P_n = Mg\left(f_0\cos\alpha + \sin\alpha\right)V = AV \tag{3.10}$$

Finally, the electric motor torque as a function of the required acceleration and of the transmission ratio is therefore:

$$T_{em} = \left(\frac{J_{em}\eta_t\tau^2}{R_r^2} + \frac{J_w}{R_r^2} + M\right)\frac{R_r}{\tau\eta_t}a_x + \frac{AR_r}{\tau\eta_t} \tag{3.11}$$

Hill Start

The hill start electric motor required torque is plotted against the transmission ratio and presented in Fig. 3.5 in case of road slope of 15 % for different accelerations. To keep the torque below the thresholds previously defined (90 Nm max), the transmission ratio should

be increased at least to a value of 12, to be also compliant with different acceleration slopes.
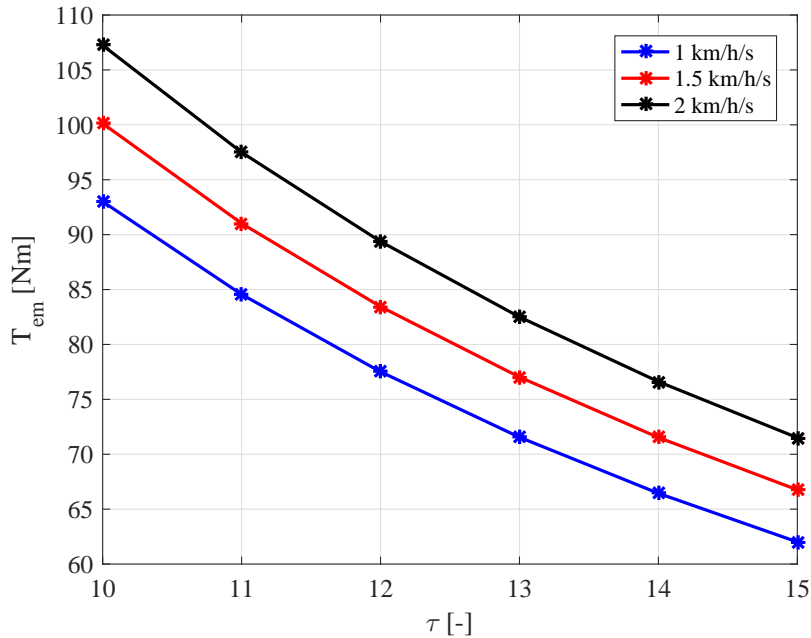
Fig. 3.5 Required torque for traction versus transmission ratio for different accelerations in case of grade driving.

Torque @ max speed

The required torque to drive the vehicle at constant speed of 130 km/h can be obtained modifying Eq. 3.11, neglecting the inertial terms and including in this case the aerodynamics resistances:

$$T_{em} = \left[Mg\left(f_0 + KV^2\right) + \frac{1}{2}\rho C_x A V^2 \right] \frac{R_r}{\tau} = 30 \text{Nm} \tag{3.12}$$

which is the minimum torque that the motor should provide at its maximum speed, leading to another constraint.

Maximum Acceleration

Finally, considering the set transmission ratio (12) and the maximum torque in the low speed region of the motor (90 Nm), neglecting the effect of the road grade and of the

aerodynamics contibutions, the maximum realizable acceleration is:

$$a_{\text{x,max}} = \left[\frac{T_{\text{em}} - Mgf_0 \frac{R_{\text{r}}}{\tau \eta_{\text{t}}}}{\left(\frac{J_{\text{em}} \eta_{\text{t}} \tau^2}{R_{\text{r}}^2} + \frac{J_{\text{w}}}{R_{\text{r}}^2} + M \right)} \right] \frac{\tau \eta_{\text{t}}}{R_{\text{r}}} = 7.3\text{km/h/s} > 5\text{km/h/s} \qquad (3.13)$$

satisfying the acceleration constraint too.

Summarizing, the required characteristics of the motor are drawn in Tab.3.4

Parameter	Value
Peak Power	30 kW
τ_{em}	12
Peak Torque	90 Nm
Nominal Power	10 kW
Nominal Torque	30 Nm
Base Speed	4244 rpm
Max Speed	13930 rpm
Torque @ Max Speed	30 Nm
Max Road Slope	15 %

Table 3.4 Required electric motor characteristics.

3.3 Basic Concepts of Electric Motor Design

In this section the design of the P4 electric motor for the hybrid electric vehicle will be presented. The considered typology, architecture and methodology will be selected and motivated.

Electric motor for EV (or HEV) applications presents the following requirements:

- high torque and power density;

- high efficiency;

- high speed range;

- high torque at low speeds, high power for cruise speed;

- overload capabilities.

The literature on the subject mainly focuses on the comparison between interior and surface mounted permanent magnet motors (e. g. [25] - [28]), induction, permanent magnet and switched reluctance motor drives (e. g. [29] - [32]), indicating that surface mounted and interior permanent magnets present basically the same performance, with the latter having higher overload capabilities. Induction machines present characteristics similar to those of interior PM machines but suffer more losses both at low and high speeds, while switched reluctance motors have the benefit of the absence of permanent magnets with the drawback of lower torque density than that of the other classes of machines.

In this work the attention is addressed to surface mounted Permanent Magnet Synchronous Machines (PMSMs). They can be classified as Brushless DC Drives (BLDC) and Brushless AC Drives (BLAC) based on the back electromotive force (emf), trapezoidal or sinusoidal respectively.

In PMSM machines it is necessary that a stator magnetomotive force (mmf) and a rotor flux are present and are stationary with respect to each other having a nonzero phase shift. Stator currents generate the stator mmf while the permanent magnets generate the rotor flux. The rotor flux and stator mmf zero relative speed is the result of injecting a set of polyphase currents phase shifted from each other by the same phase shift between the phase windings. In the following, these basic concepts will be recalled.

Current Density. The wire current density decision is a crucial stage of the design of any electric motor. It is mainly determined by the type of cooling that will be available once the motor is installed. For this application, since the motor is expected to have high performance, the value of current density chosen is 20 A/mm^2, characteristic of a liquid cooled machine. Since both the torque and the power in nominal operations are one third of their peak values, the nominal current density is considered to be 6 A/mm^2.

Torque per Rotor Volume and Air Gap Shear Stress. The torque per unit rotor volume (TRV) is an useful parameter to evaluate the performance of a machine. It is defined as:

$$TRV = \frac{T_{em}}{V_r} = \frac{T_{em}}{\pi r^2 L} \tag{3.14}$$

where r is the rotor radius and L is the motor length. The torque can also be related to the average shear stress at the rotor surface σ. In this case the expression of the torque becomes:

$$T_{em} = \sigma 2\pi r^2 L \tag{3.15}$$

and the two parameters are linked by the following relation:

$$TRV = 2\sigma \tag{3.16}$$

The torque per rotor volume or the air gap shear stress are important quantities which should be selected at the beginning of the design. They make reference to particular classes of electric motors, identified by different operational characteristics (electric and magnetic). For the application under analysis a value of $\sigma = 30\text{kN/m}^2$ has been selected, suitable for high performance motors [33].

Length over Rotor Diameter Ratio. A high torque - inertia ratio is very important in the automotive field due to the intermittent operations that the motor should accomplish. A value for ratio L/D_ro is chosen between 2 and 3, guaranteeing the desired characteristics [33].

MMF Force. If a current I flows inside a coil wrapped around a piece of magnetic material, this system can be considered as a magnetic field source. If the wire is wrapped N times, the application of Ampere's law allows to find the magnetic field produced by it. The results is therefore:

$$F = NI \tag{3.17}$$

that means that the coil can be considered as a mmf source of values F.

Coil MMF. Considering now a stator with one turn of a coil, an air gap and a rotor, assuming that the rotor and the stator iron have zero reluctance, the mmf produced by the coil is completely used to overcome the reluctance of the two air gaps in the path of the flux. When plotting the mmf as a function of the rotor angle, a rectangular distribution of peak to peak amplitude NI (in case of N turns) is produced. This rectangular distribution has a dominant fundamental component but is rich in harmonics that do not contribute in torque production and therefore should be minimized.

Sinusoidal MMF. Considering one phase only, a sinusoidal mmf waveform can be obtained both with concentric and with distributed windings. The first presents advantages in terms of ease of manufacturing but drawbacks of the relatively high amount of copper and therefore resistive losses, the second has the advantage of better slot use but presents the disadvantage of longer end turns.

Induced EMF. If the winding is made of N turns, a flux linkage is generated, and changes as a function of the rotor angle. Therefore, an induced electromotive force (emf) is produced. The waveform of the emf is dependent on the flux linkage waveform λ, function of the air gap flux ϕ, the rotor magnet flux density, and the stator configuration.

If the air gap flux is sinusoidal, with an electrical rotational frequency of the machine ω_e and amplitude ϕ_m, the emf is:

$$e = -\frac{d\lambda}{dt} = -N\phi_m\omega_e\cos(\omega_e t) = -2\pi N\phi_m f_e\cos(\omega_e t) \tag{3.18}$$

which means basically that the emf is mainly a function of the electrical frequency of the machine. Therefore, the excitation frequency of the voltage directly controls the speed of the machine.

Rotating Magnetic Field. As said before, a rotating magnetic field is produced by only injecting a set of balanced currents in the phases (zero total sum and phased by the same amount of spatial displacement between them). If their amplitude is I_p and they rotate with a frequency ω_e:

$$
\begin{aligned}
I_a &= I_p\sin(\omega_e t) \\
I_b &= I_p\sin\left(\omega_e t - \frac{2\pi}{3}\right) \\
I_c &= I_p\sin\left(\omega_e t + \frac{2\pi}{3}\right)
\end{aligned}
\tag{3.19}
$$

If P is the number of poles, the individual phase mmfs per pole are:

$$
\begin{aligned}
F_a &= \frac{NI_p}{P}\sin(\theta)\sin(\omega_e t) \\
F_b &= \frac{NI_p}{P}\sin\left(\theta - \frac{2\pi}{3}\right)\sin\left(\omega_e t - \frac{2\pi}{3}\right) \\
F_c &= \frac{NI_p}{P}\sin\left(\theta + \frac{2\pi}{3}\right)\sin\left(\omega_e t + \frac{2\pi}{3}\right)
\end{aligned}
\tag{3.20}
$$

Now, manipulating the previous expressions with trigonometric properties ($\sin\alpha\sin\beta = -\frac{1}{2}[\cos(\alpha-\beta) - \cos(\alpha+\beta)]$), considering the summation of the three mmfs gives:

$$F_{abc} = \frac{3}{2}\frac{NI_p}{P}\cos(\theta - \omega_e t) \tag{3.21}$$

which demonstrates that the resultant stator mmf has a constant amplitude but varies sinusoidally, presenting a maximum when the stator position and the angular position of the current phasor coincides. This means that the speed of the resultant magnetic field is equal to the angular speed of the stator currents, and if the rotor is revolving at the same

speed of stator excitation, the relative speed between stator mmf and rotor flux is therefore zero.

Permanent Magnets. Permanents magnets are hard magnetic materials. The available types include alnico, ferrite, rare - earth samarium - cobalt and neodymium - iron - boron. NdFeB magnets are the most popular due to their higher performance and lower cost with respect to the samarium cobalt ones.

Once they are magnetized they present a very wide hysteresis cycle. Considering the magnetization in the first quadrant (recoil), once the external exciting circuit allows $H = 0$, the flux density leaving the magnet is equal to the remanence and is denoted by B_r. On the other hand, if the permeability surrounding the magnet is zero, no flux flows out of the magnet ($B = 0$) and the magnetic field is the coercivity H_c. The equation of the magnet flux density is therefore:

$$B_m = B_r + \mu_0 \mu_m H \tag{3.22}$$

where μ_0 and μ_m are the magnetic permeability of air and magnet respectively.

For values of external permeance between zero and infinity, the working point lies on the aforementioned straight line. The permeance coefficient (PC) is the slope of the load line connecting the operating point and the origin. Temperature tends to shrink the demagnetization curve towards the origin, reducing the magnet performance.

Synchronous Machine Relationships. Without entering too much into the details, some basic relationships between torque, current, air gap flux and magnetomotive force will now be given.

If B_m is the flux density of a magnet and 2β its magnet arc, constant positive and negative flux density can be found when plotting it as a function of the rotor angle. By Fourier analysis, the fundamental harmonics will be:

$$B_{m1} = \frac{4}{\pi} B_m \sin \beta \tag{3.23}$$

When considering Eq. 3.18, the machine flux is present instead of the magnet flux density. It is demonstrated in [34] that when assuming a sinusoidal magnet flux density distribution, integrating along an electrical pole gives as a result a sinusoidal flux linkage with amplitude:

$$\phi_m = \frac{B_{m1} DL}{P/2} \tag{3.24}$$

where D is the stator bore lamination diameter, L is the motor length and P is the number of poles. The peak induced emf therefore becomes:

$$E = \frac{4}{\pi} NDLB_\mathrm{m} \frac{\omega_\mathrm{e}}{P/2} \sin\beta \tag{3.25}$$

The torque is derived from the computation of the electromagnetic power. Considering N_ts as the number of turns per phase instead of the expression $\frac{4}{\pi}N$, the expression of the torque is:

$$T = \frac{3}{2} \left(B_\mathrm{m} \sin\beta\right) DLN_\mathrm{ts}I_\mathrm{m} \sin\delta \tag{3.26}$$

where δ is the torque angle.

A 3 phase Permanent Magnet Synchronous Machine Brushless AC Motor has been chosen for the aforementioned application due to its smoother output torque with respect to a BLDC. Concentrated windings rather than distributed ones are considered due to the higher fill factor value and short end turns length (small end turns resistance).

After this short review on the basic concepts of permanent magnet synchronous machines, this chapter will give more details regarding the design of the P4 electric motor.

As shown in Sect. 3.2, a rear axle electric motor has to accomplish a limited number of tasks such as full electric start and regenerative braking. Nevertheless, where its functionalities are concerned, the design is based on its maximum torque and power requirements. This decision has been taken based on the fact that the application under analysis in not conventional, and frequent transitions from point to point are expected.

In this case, the electric motor has to provide a peak power of 30 kW and a peak torque of 90 Nm, and it will be designed based on these peak values considering high wire current density. Considering then a maximum electric motor speed of 14000 rpm and a low voltage application (48 V), flux weakening control strategies are required to keep the output power constant reducing the electric motor torque as a function of the speed. In addition, windings (number of turns of conductors for each slot) are designed based on considerations related to the base speed (speed at which the supply voltage reaches its maximum value and that theoretically the motor cannot overcome).

Finally, considering that the motor is frequently subjected to overloads during its operation (a full electric start is basically a very high power request), the motor is therefore subjected to a thermal analysis to understand the influence of high current peaks on winding, teeth and magnet temperatures.

Section 3.4 will present the design procedure to define the motor dimensions starting from a value of required torque and a fixed wire current density. The procedure does not take into account the possibility of the motor to run over to its base speed but provides a conservative way to compute the motor sizes starting from some basic dimensions.

Section 3.5 describes the dynamic model of the PMSM, presents the windings design of the electric motor and makes considerations relative to the field weakening control strategy.

It should be underlined that in this work the field weakening it is studied and implemented only from the functional point of view. Since the aim will be to obtain accurate static maps to be implemented in more complex vehicle dynamic models, based on the proper analytical field weakening strategy implementations, for each point of the torque - speed map of the motor the correct d and q axis current split is therefore computed.

Section 3.6 presents the results of a thermal analysis on the electric machine under different operating conditions such as continuous and peak working points.

3.4   Constant Torque Region

This section is devoted to compute the size of the motor starting from some main motor dimensions and basic assumptions related to its constructive characteristics.

The procedure is present in [35] and is based on the solution of the magnetic circuit that models the presence of stator and rotor back irons, magnets and air gap.

3.4.1   Design Theory

Despite all the differences in PM brushless motors in terms of architectures, configurations and characteristics, their operation is always a child of the same equation. PM motors produce a torque based on Lorentz force equation:

$$T = R(qv \times B) \tag{3.27}$$

where R is the rotor radius, q is the amplitude of the charge, v is the speed of the charge and B is amplitude of the magnetic flux density. Because of the cross product, to obtain the maximum torque, the two vectors should stand at 90 degrees. In that case the speed vector should travel in axial direction and the magnetic flux in radial direction to produce a

torque oriented in circumferential direction. The equation can also be rewritten as:

$$T = Rq\frac{dl}{dt}B = RB\int idt\frac{dl}{dt} = RB\int idl = RBiL \tag{3.28}$$

Therefore, of fundamental importance is the computation of the magnetic flux density traveling from the magnets, passing through the air gap, intercepting the charges flowing into the wires, closing into the stator back iron (which has the task of providing a magnet flux return path) and coming back to the rotor.

The scheme for the analysis considers a linear translational motor that owns a structure that repeats indefinitely in both directions. Spacers between the magnets are of nonmagnetic materials, attached to ferromagnetic back iron. The stator is composed of ferromagnetic back iron with slots containing the windings of one phase. Slots are oriented in order to have one slot per pole per phase. In addition, flux from one magnet splits equally and couples to the two magnets adjacent to it. Finally, the magnetic field due to the current in the slots is not considered since it does not contribute to the force and back emf generated.

The equivalent magnetic circuit is shown in Fig. 3.6. It presents two currents generators with $\phi_r/2$ being the flux source of one half of the magnet and magnet reluctances $2R_m$ in parallel to the current generators. R_r and R_{ml} are the rotor back iron and the magnet to magnet reluctances respectively, R_s is the stator back iron reluctance and finally $2R_g$ is the reluctance of one half of the air gap.
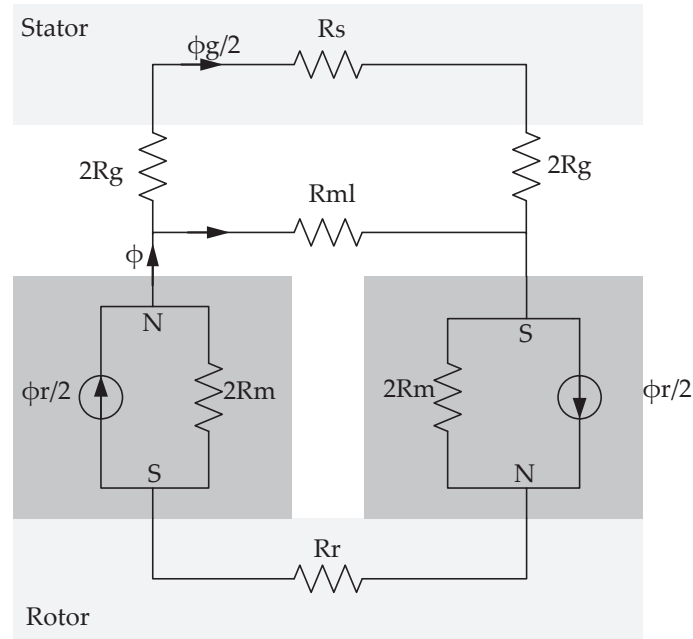
Fig. 3.6 Magnetic circuit equivalent model.

By making some simplifications regarding the fact that some reluctances are negligible with respect to others (R_s and R_r are neglected), the air gap flux related to the magnet flux can be expressed as:

$$\phi_g = \frac{1}{1 + \tilde{P}_m/P_g} \phi_r \tag{3.29}$$

where $\tilde{P}_m$ is a permeance due to magnets and P_g is due to the air gap. $\tilde{P}_m$ is:

$$\tilde{P}_m = P_m k_{ml} = \frac{\mu_r \mu_0 \alpha_m \tau_p L}{l_m} k_{ml} \tag{3.30}$$

where $\alpha_m = \tau_m/\tau_p$ is the magnet fraction, τ_p is the magnet pole (Inner stator radius $\cdot$ 2π/number of magnets), L is the motor length, l_m is the magnet length in the radial direction and k_{ml} is the magnet leakage factor:

$$k_{ml} = 1 + \frac{4l_m}{\pi \mu_r \alpha_m \tau_p} \ln \left[1 + \pi \frac{g}{(1 - \alpha_m)\tau_p} \right] \tag{3.31}$$

a coefficient that describes the flux path shape out of the magnet and along the air gap g.

The air gap permeance describes the net permeance seen by the magnet flux that enters the stator. Air gap area is:

$$A_g = \frac{\tau_p L(1 + \alpha_m)}{2} \tag{3.32}$$

while its permeance is:

$$P_g = \mu_0 \frac{\tau_p L(1 + \alpha_m)}{2gk_c} \tag{3.33}$$

in which k_c is the Carter coefficient, a value that corrects the actual air gap length because of the extra flux path distance over the slot.

Finally, the air gap flux can be written as a function of the permeance coefficient $P_c = l_m / (gC_\phi)$ and $C_\phi = 2\alpha_m / (1 + \alpha_m)$:

$$\phi_g = \frac{1}{1 + \mu_r k_c k_{ml}/P_c} \phi_r \tag{3.34}$$

or similarly in terms of flux densities:

$$B_g = \frac{C_\phi}{1 + \mu_r k_c k_{ml}/P_c} B_r \tag{3.35}$$

The computation of the air gap flux is of fundamental importance for the computation of, among other parameters, the width of stator and rotor back iron.

3.4.2 Design Implementation

Fixed Parameters. Many unknown parameters are involved in the design of PMSM brushless motors while some other should be fixed. Generally, what is done is to fix the known parameters (such as the total motor volume) or other topological constraints (number of phases, poles and slots). Conductor packing factor, lamination stacking factor, magnet remanence, maximum steel flux density and coil flux density are other parameters to impose. In general, the parameters are subdivided according to the following criteria:

- Parameters chosen to maximize the performance;

- Parameters chosen according to experience and literature values;

- Parameters that can be varied to find optimal design.

Table 3.5 presents these parameters.

Name	Description	Decision Criteria	Obtained From
J_{max}	Max slot current density	Sizing parameters	Cooling capabilities
N_{ph}	Number of phases	Topological	Topology
g	Air gap length		Mechanical tolerance
B_r	Magnet remanence		Type of magnet
μ_r	Magnet recoil permeability	Maximize	Type of magnet
B_{max}	Max steel flux density	Performance	Type of iron
ρ_s	Iron Density		Type of iron
k_{st}	Lamination stacking factor		
k_{cp}	Conductor packing factor		
α_m	Magnet fraction	Experience	
w_s	Slot opening	or	
α_{sd}	Shoe depth fraction	Literature	
l_m	Magnet length		Permeance coefficient
R_{so}	Stator outside radius		Ratio R_{so}/R_{ro}
L	Motor length		Ratio L/D_{ro}
N_m	Number of magnets	Varied	
N_s	Number of slots	for	
R_{ro}	Rotor outside radius	Optimal Design	

Table 3.5 Decision criteria for fixed parameters values.

Parameters chosen to maximize performance.

Air gap. Has a direct influence on the reluctance of the magnetic circuit. The smaller the air gap, the smaller the reluctance and the better the motor works. The minimum air gap possible is nevertheless limited by mechanical tolerance and construction. This value is set to $g = 0.5$mm according to manufacturing capabilities.

Type of magnet. Has a direct influence on the performance of the machine. Usually, for this type of application a rare earth magnet type is the choice due to their remanence and straight demagnetization curves where the motor operates. This gives the motor much more capability for overload and good performance. In this design a sintered NdFeB magnet is used; its characteristics are shown in Tab. 3.6.

Material	Remanence $B_r [T]$	Permeability μ_r
NdFeB	1.25	1.05

Table 3.6 NdFeB Magnet characteristics.

One important fact to consider in the magnet is the operation point. Depending on the load and the temperature the magnet can be demagnetized and reduce the performance of all the design. This consideration will be explained further in the selection of the magnet length l_m and also in the chapter of thermal analysis.

Type of iron. To determine the machine efficiency, the two basic properties of interest are the B - H curve and the iron losses of the steel. The B - H curve set the possible flux levels and the degree of saturation while the type of steel determines the iron losses. The losses are usually a function of the degree of Silicon in the steel. Increasing the amount of Silicon (up to a maximum of 3 percent) can reduce the losses in the steel. On the other hand, the loss calculation is an estimation and is worthwhile only if the data are accurate (often they are not). Based on the aforementioned considerations, steel *M400-50A* with non oriented grains has been selected due to its high percentage of Silicon (2 %).

Parameters chosen according to experience and literature values.

Stacking factor, filling factor, magnet fraction, shoe depth fraction and slot opening. Some values are difficult to calculate and at the end are obtained just by experience. For all these parameters standard and conservative values are considered.

Magnet length. Once the air gap length has been chosen, of crucial importance is the magnet length value decision. These two values have a direct influence on the magnet operation point and the possibility of demagnetization under overloading conditions.
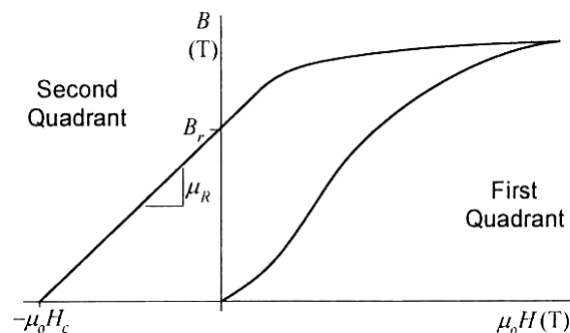
Fig. 3.7 The B-H loop of a permanent magnet.

When the magnet is faced to a magnet circuit, which has infinite permeance, the operating point of the magnet lies on the y axis at the point B_r. On the other hand, when the magnet is placed in a magnetic environment with zero permeance, the operation point of the magnet lies in the x axis, second quadrant in the point known as *coercivity point*. For permeance values between zero and infinity, the operation point lies somewhere in the second quadrant. The magnitude of the slope of a line drawn from the operation point to the origin is known as the *permeance coefficient, PC*, and is computed as:

$$PC = \frac{l_m}{gC_\phi} \tag{3.36}$$

where $C_\phi = A_m/A_g$ is the concentration factor.

From Fig. 3.8, it can be seen that the closer the PC value is to infinity, the closer is the operating point to the remanence. Nevertheless, using such a high value would imply an infinite magnet length l_m, which is unfeasible. On the other hand, it can be seen that with increasing temperature the curve moves down and with particularly high temperatures a "knee" can arise in the curve. Usually a magnet operating in the linear zone returns to its initial value even if high temperatures are reached. In case that the "knee" is reached, the magnet could return through a different path and demagnetization could occur. This is why the PC coefficient must be bigger than certain value to ensure high performance and avoid demagnetization problems. Usually the values chosen for the design are $4 < PC < 6$. For this specific work a value of $PC = 5$ is chosen, and assuming $C_\phi = 1$, from Eq. 3.36 the magnet length can be computed:

$$l_m = 5g = 2.5\text{mm} \tag{3.37}$$
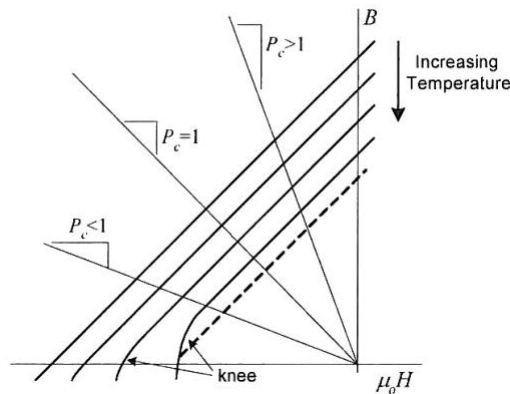
Fig. 3.8 Influence of temperature in the demagnetization curve.

Stator outer radius. The stator outer radius can not be varied freely because there are optimal values for the ratio $R_{\mathrm{ro}}/R_{\mathrm{so}}$ that allow the motor to be optimally designed and not to saturating. In this case, this value is taken from [35] and is $R_{\mathrm{ro}}/R_{\mathrm{so}} = 0.5$, which leads to $R_{\mathrm{so}} = 2R_{\mathrm{ro}}$.

Motor axial length. As explained previously, for inertia and stability the optimal ratio between length and rotor diameter is $2 < L/D_{\mathrm{ro}} < 3$. This implies that the best value for the length in terms of rotor radius is $4R_{\mathrm{ro}} < L < 6R_{\mathrm{ro}}$.

Parameters that can be varied to find the optimal design.

Finally, there are parameters that can be varied to find the optimal design. The best design is driven starting from these parameters and their different combinations.

Number of magnets and slots. Even though these are parameters can be varied, they have to be varied together according to valid combinations.

Increasing the number of magnets leads to higher torque with the same current density (according to the torque equation), but could lead to high iron and transistor losses (the electric frequency of the current must be pf with $p = N_{\mathrm{m}}/2$ and f the mechanical rotation frequency of the machine). As in this specific application a high speed is required (14000 rpm) a small number of magnets is chosen: $N_{\mathrm{m}} = 4$.

With this number of magnets, the number of slots is chosen to have *concentrated windings*, which leads to facility of construction. To have concentrated windings the number of slots must be: $N_{\mathrm{s}} = 6$.

Rotor outer radius. The rotor radius is varied freely in the next subsection to find the optimal geometrical dimensions for this application.

These were the fixed parameters considered for the design. The procedure continues with the computation of geometric, magnetic and electric parameters.

Geometric Parameters. From Fig. 3.9 the various radii are associated by:

$$
\begin{aligned}
R_{\mathrm{sb}} &= R_{\mathrm{so}} - w_{\mathrm{bi}} \\
R_{\mathrm{si}} &= R_{\mathrm{sb}} - d_{\mathrm{s}} = R_{\mathrm{so}} + g \\
R_{\mathrm{ri}} &= R_{\mathrm{ro}} - l_{\mathrm{m}} - w_{\mathrm{bi}}
\end{aligned}
\tag{3.38}
$$

The angular pole and slot pitch (in radians and meters) are:

$$\theta_p = \frac{2\pi}{N_m}, \tau_p = R_{si}\theta_p$$
$$\theta_s = \frac{2\pi}{N_s}, \tau_s = R_{si}\theta_p \tag{3.39}$$

Tooth width at the stator surface is:

$$w_t = R_{si}\theta_s - w_s \tag{3.40}$$

The width of the slot bottom is:

$$w_{sb} = R_{sb}\theta_s - w_{tb} \tag{3.41}$$

Shoe height is:

$$d_1 = d_2, d_1 + d_2 = \alpha_{sd}w_{tb} \tag{3.42}$$

Slot depth is:

$$d_3 = d_s - \alpha_{sd}w_{tb} \tag{3.43}$$

Therefore the slot area is:

$$A_s = d_3\left[\theta_s\left(R_{sb} - \frac{d_3}{2}\right) - w_{tb}\right] \tag{3.44}$$

Another geometric parameter that should be accounted for is the number of slots per pole per phase, defined as $N_{spp} = N_s/N_m/N_{ph}$.

Magnetic Parameters. As discussed before, the flux from each magnet splits equally in both the stator and rotor back irons and is coupled to adjacent magnets. The back iron flux is therefore:

$$\phi_{bi} = \frac{\phi_g}{2} \tag{3.45}$$

The back iron width is a function of the maximum steel flux density B_{max} and of the stack lamination factor k_{st}:

$$w_{bi} = \frac{\phi_g}{2B_{max}k_{st}L} \tag{3.46}$$
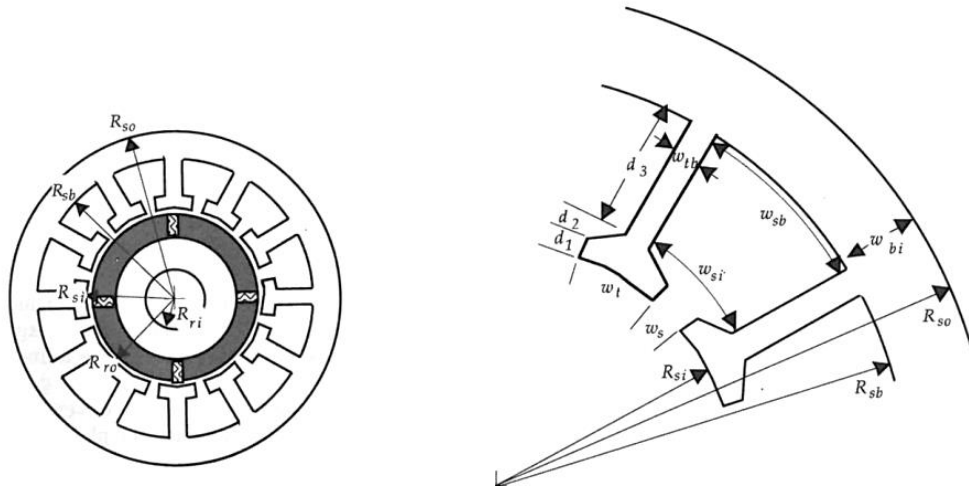
(a) Radial flux motor topology showing geometri-(b) Slot geometry for the radial flux motor topol-
cal definitions.   ogy.

Fig. 3.9 Radial flux motor topology and slot geometry.

Finally, each tooth must carry $1/N_{sm}$ of the air gap flux. Therefore:

$$w_{tb} = \frac{\phi_g}{N_{sm}B_{max}k_{st}L} = \frac{2}{N_{sm}}w_{bi} \tag{3.47}$$

where $N_{sm} = N_{spp}N_{ph}$ is the number of slots per magnet pole.

Electromechanical Parameters. The current in one slot is distributed among n_s conductors occupying the slot cross-sectional area A_s. Part of this area is occupied by conductor insulation, inevitable gaps between slot conductors and additional insulation around the slot periphery, called slot liners. As a result, only a fraction of the total cross sectional area is occupied by the slot conductor themselves. This fraction is taken into account by specifying a **conductor packing factor** as:

$$k_{cp} = \frac{\text{area\quad occupied\quad by\quad conductors}}{\text{total\quad area}} \tag{3.48}$$

Typically k_{cp} is less than 50 percent, but it can be higher under special circumstances. Therefore, given the rms slot current density, the rms slot current is:

$$I_s = J_{max}k_{cp}A_s \tag{3.49}$$

while the peak value is:

$$I_s = \sqrt{2}J_{max}k_{cp}A_s \tag{3.50}$$

Parameter	Obtained from	Value
J_{max}	Cooling capabilities	20 A/mm^2
N_{ph}	Topology	3
g	Mech. tolerance	0.5 mm
B_r	NdFeB magnet	1.25 T
μ_r	NdFeB magnet	1.05
B_{max}	M400-50A steel	1.6 T
ρ_s	M400-50A steel	7650 kg/m^3
k_{st}		0.95
k_{cp}		0.4
α_m		0.9
w_s		2 mm
α_{sd}		
l_m	Permeance coefficient PC	2.5 mm
R_{so}	Ratio R_{so}/R_{ro}	$2R_{ro}$
L	Ratio L/D_{ro}	$4R_{ro} < L < 6R_{ro}$
N_m	Concentrated winding	4
N_s	Concentrated winding	6
R_{ro}		Free

Table 3.7 Fixed parameters values

In this way the computation of the number of conductors inside each slot can be neglected (it will be the core of next section). Torque can instead be computed considering the three phases and the slot current:

$$T = \frac{3}{2} N_m k_d k_p B_g L N_{spp} I_s R_{ro} \tag{3.51}$$

which becomes:

$$T = \frac{3}{2} N_m k_d k_p B_g L N_{spp} \sqrt{2} J_{max} k_{cp} A_s R_{ro} \tag{3.52}$$

where k_d and k_p are the distribution and the pitch factor, expressed as:

$$k_d = \frac{\sin\left(N_{spp}\pi/2N_{sm}\right)}{N_{spp}\sin\left(\pi/2N_{sm}\right)} \quad k_p = \mathrm{int}\left(N_{spp}\right)/N_{spp} \tag{3.53}$$

A summary of the values for each parameter are presented in Tab. 3.7.
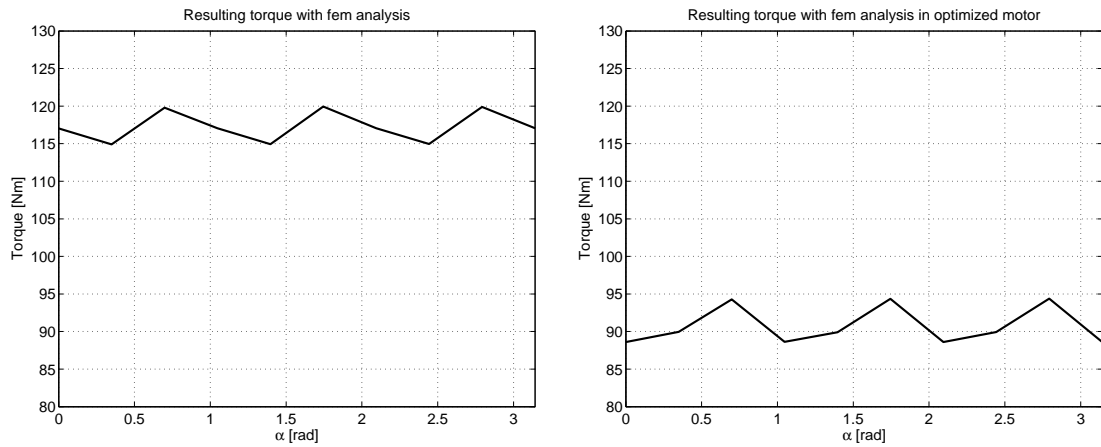
(a) FEM Torque as a function of the rotor angle in case of preliminary motor parameters.

(b) FEM Torque as a function of the rotor angle in case of optimized motor parameters.

Fig. 3.10 Torque produced by the motor before and after the optimization.

3.4.3 Analytical and Numerical Results

The presented procedure has been implemented inside a MATLAB code. An arbitrary value of the rotor outer radius has been chosen with all the other parameters fixed. By means of the torque equation it has been possible to evaluate it. The procedure is of course iterative and stopped until the value reached the target torque of 90 Nm. Table 3.8 shows the preliminary results. To verify them, a finite element model of the electric motor has been created through the use of the commercial software COMSOL Multiphysics.

COMSOL uses Maxwell's equations for the computation of the flux density, the magnetic vector potential and scalar potential. The main inputs to the model are the geometry (obtained from analytical results), the magnet properties and the slot current density (same as the ones in Tab. 3.7). The rotor angle has been varied to realize a complete electrical revolution.

Parameter	Value
Torque	90 Nm
Stator diameter	164 mm
Rotor diameter	82 mm
Length	200 mm

Table 3.8 Resulting main motor parameters from Hanselman procedure.

Fig. 3.10 shows that the Hanselman procedure is conservative with respect to the numerical one. This is reasonable because the model considered in [35] is linear in terms of materials characteristics. The numerical model, instead, considers the complete B - H curve of the steel, leading to a more precise solution. With these considerations, the dimensions of the motor have been again iteratively varied until the target torque value is accomplished. The final motor dimensions are presented in Tab. 3.9. Winding design is presented in next section because related to the constant power region of the motor characteristic.

Parameter	Value
Torque (average)	90 Nm
Stator diameter	148 mm
Rotor diameter	74 mm
Length	200 mm

Table 3.9 Motor resulting from finite element optimization.

3.5   Constant Power Region

PMSM windings are properly designed to accomplish characteristics such as small phase resistance, sinusoidal back emf and low contributions of higher order flux harmonics. Another important design issue is related to the achievement of the base speed when the DC voltage reaches the maximum allowed by the battery. It is well known that under this speed the induced emf due to the magnets is not overcoming the maximum DC voltage, allowing therefore the current to flow in the machine phases. Conversely, above this speed the induced emf is constrained to be lower than the dc link by weakening the air gap flux linkages. This section is devoted to the dynamic modeling of the PMSM and to the design and analysis for high speed operation. The goal is, again, not to establish a novel design procedure but that of easily obtain the performance parameters (e.g. absorbed currents, mechanical power) in each motor operational point.

The dynamic model of a PMSM is based on the transformation from the three phases system to its equivalent two phases system in direct and quadrature axis. the rotor has no windings while the magnets are modeled as flux linkage sources. The flux linkages of the stator d and q axes are obtained from the machine magnetic equations. The model is derived considering the equivalent two phases system written in the rotor reference

frame. This choice is performed to obtain constant (and not a function of the rotor angle) inductances for the windings. The equivalence between the three phases system with the two phases system is performed through trigonometric transformations that preserve the power invariance.

3.5.1 Dynamic Modeling of the PMSM

Starting from the three phase system, the machine electric equations are:

$$
\begin{cases}
v_a = R_s i_a + \frac{d}{dt} \lambda_a \\
v_b = R_s i_b + \frac{d}{dt} \lambda_b \\
v_c = R_s i_c + \frac{d}{dt} \lambda_c
\end{cases}
\tag{3.54}
$$

where R_s is the phase resistance, considered equal for all the three phases; v_{abc} are the voltages across the phases, i_{abc} are the phase currents. The magnetic equations are instead:

$$
\begin{cases}
\lambda_a = L_{aa} i_a + M_{ab} i_b + M_{ac} i_c + \lambda_{ma} \\
\lambda_b = M_{ab} i_a + L_{bb} i_b + M_{bc} i_c + \lambda_{mb} \\
\lambda_c = M_{ac} i_a + M_{bc} i_b + L_{cc} i_c + \lambda_{mc}
\end{cases}
\tag{3.55}
$$

where:

$$
L_{aa} = L_i + L_a \cos(2\theta)
$$

$$
L_{bb} = L_i + L_a \cos\left(2\theta - \frac{4\pi}{3}\right)
$$

$$
L_{cc} = L_i + L_a \cos\left(2\theta - \frac{2\pi}{3}\right)
$$

$$
M_{ab} = -\frac{1}{2}L_i + L_a \cos\left(2\theta - \frac{2\pi}{3}\right)
$$

$$
M_{bc} = -\frac{1}{2}L_i + L_a \cos(2\theta)
$$

$$
M_{ac} = -\frac{1}{2}L_i + L_a \cos\left(2\theta - \frac{4\pi}{3}\right)
$$

$$
\lambda_{ma} = \lambda_m \cos(\theta)
$$

$$
\lambda_{mb} = \lambda_m \cos\left(\theta - \frac{2\pi}{3}\right)
$$

$$\lambda_{mc} = \lambda_m \cos\left(\theta - \frac{4\pi}{3}\right)$$

are the machine auto (L_{aa}, L_{bb} and L_{cc}) and mutual (M_{ab}, M_{bc} and M_{ac}) inductances, θ is the rotor electrical angle, λ_m is the permanent magnet flux and L_i and L_a are the isotropic and anisotropic inductances respectively expressed as:

$$L_i = \frac{L_d + L_q}{2} \tag{3.56}$$

and

$$L_a = \frac{L_d - L_q}{2} \tag{3.57}$$

with L_d and L_q the inductances in direct and quadrature machine axis.

The auto and mutual inductances therefore become:

$$L_{aa} = L_i + L_a \cos(2\theta) = \frac{L_d + L_q}{2} + \frac{L_d - L_q}{2} \cos(2\theta)$$

$$L_{bb} = L_i + L_a \cos(2\theta - 240) = \frac{L_d + L_q}{2} + \frac{L_d - L_q}{2} \cos\left(2\theta - \frac{4\pi}{3}\right)$$

$$L_{cc} = L_i + L_a \cos\left(2\theta - \frac{2\pi}{3}\right) = \frac{L_d + L_q}{2} + \frac{L_d - L_q}{2} \cos\left(2\theta - \frac{2\pi}{3}\right)$$

$$M_{ab} = -\frac{1}{2}L_i + L_a \cos\left(2\theta - \frac{2\pi}{3}\right) = -\frac{1}{2}\frac{L_d + L_q}{2} + \frac{L_d - L_q}{2} \cos\left(2\theta - \frac{2\pi}{3}\right)$$

$$M_{bc} = -\frac{1}{2}L_i + L_a \cos(2\theta) = -\frac{1}{2}\frac{L_d + L_q}{2} + \frac{L_d - L_q}{2} \cos(2\theta)$$

$$M_{ac} = -\frac{1}{2}L_i + L_a \cos\left(2\theta - \frac{4\pi}{3}\right) = -\frac{1}{2}\frac{L_d + L_q}{2} + \frac{L_d - L_q}{2} \cos\left(2\theta - \frac{4\pi}{3}\right)$$

$$\lambda_{ma} = \lambda_m \cos(\theta)$$

$$\lambda_{mb} = \lambda_m \cos\left(\theta - \frac{2\pi}{3}\right)$$

$$\lambda_{mc} = \lambda_m \cos\left(\theta - \frac{4\pi}{3}\right)$$

Making use of the matrix notation, the electric and magnetic equations can be rewritten as follows:

$$\begin{Bmatrix} v_a \\ v_b \\ v_c \end{Bmatrix} = \begin{bmatrix} R_s & 0 & 0 \\ 0 & R_s & 0 \\ 0 & 0 & R_s \end{bmatrix} \begin{Bmatrix} i_a \\ i_b \\ i_c \end{Bmatrix} + \frac{d}{dt} \begin{Bmatrix} \lambda_a \\ \lambda_b \\ \lambda_c \end{Bmatrix} \tag{3.58}$$

$$
\begin{Bmatrix} \lambda_a \\ \lambda_b \\ \lambda_c \end{Bmatrix} = \frac{L_d + L_q}{2} \begin{bmatrix} 1 & -\frac{1}{2} & -\frac{1}{2} \\ -\frac{1}{2} & 1 & -\frac{1}{2} \\ -\frac{1}{2} & -\frac{1}{2} & 1 \end{bmatrix} \begin{Bmatrix} i_a \\ i_b \\ i_c \end{Bmatrix} +
$$

$$
+ \frac{L_d - L_q}{2} \begin{bmatrix} \cos(2\theta) & \cos\left(2\theta - \frac{2\pi}{3}\right) & \cos\left(2\theta - \frac{4\pi}{3}\right) \\ \cos\left(2\theta - \frac{2\pi}{3}\right) & \cos\left(2\theta - \frac{4\pi}{3}\right) & \cos(2\theta) \\ \cos\left(2\theta - \frac{4\pi}{3}\right) & \cos(2\theta) & \cos\left(2\theta - \frac{2\pi}{3}\right) \end{bmatrix} \begin{Bmatrix} i_a \\ i_b \\ i_c \end{Bmatrix} +
$$

$$
+ \lambda_m \begin{Bmatrix} \cos(\theta) \\ \cos\left(\theta - \frac{2\pi}{3}\right) \\ \cos\left(\theta - \frac{4\pi}{3}\right) \end{Bmatrix}
$$

$$(3.59)$$

that become:

$$
\{v_{abc}\} = [R_s]\{i_{abc}\} + \frac{d}{dt}\{\lambda_{abc}\} \tag{3.60}
$$

$$
\{\lambda_{abc}\} = [L_i]\{i_{abc}\} + [L_a]\{i_{abc}\} + \{\lambda_{m,abc}\} \tag{3.61}
$$

Equations written in the stator frame of reference are extremely useful to understand the physical concepts related to the three phases systems and the parameters behind the electrical circuits of PMSM. The drawback of this approach can be immediately shown by means of Eq. 3.61, in which matrix $[L_a]$ is dependent on the rotor electrical angle. In this way the model parameters are a function of an independent variable as the rotor angle, and the model itself is therefore non linear in terms of its parameters. To overcome this problem, a transformation from a stator three phases system to a rotor two phases system allows one to obtain a model constituted by linear differential equations with constant parameters. Such a transformation can be found in literature and therefore will not be presented.

The electrical equations come out to be:

$$
\begin{cases} v_d = R_s i_d + \frac{d}{dt}\lambda_d - p\omega_m \lambda_q \\ v_q = R_s i_q + \frac{d}{dt}\lambda_q + p\omega_m \lambda_d \end{cases} \tag{3.62}
$$

where ω_m is the mechanical rotational speed and p is the number of pole pairs. The magnetic equations are instead:

$$\begin{cases} \lambda_d = \frac{3}{2}\frac{L_d+L_q}{2}i_d + \frac{3}{2}\frac{L_d-L_q}{2}i_d + \sqrt{\frac{3}{2}}\lambda_m \\ \lambda_q = \frac{3}{2}\frac{L_d+L_q}{2}i_q + \frac{3}{2}\frac{L_d-L_q}{2}i_q \end{cases} \tag{3.63}$$

which simplify as follows:

$$\begin{cases} \lambda_d = \frac{3}{2}\frac{L_d+L_q}{2}i_d + \frac{3}{2}\frac{L_d-L_q}{2}i_d + \sqrt{\frac{3}{2}}\lambda_m = \frac{3}{2}L_d i_d + \sqrt{\frac{3}{2}}\lambda_m \\ \lambda_q = \frac{3}{2}\frac{L_d+L_q}{2}i_q + \frac{3}{2}\frac{L_d-L_q}{2}i_q = \frac{3}{2}L_q i_q \end{cases} \tag{3.64}$$

Since in this frame of reference transformation the power is preserved, it can be simply expressed as:

$$P = \left(v_d i_d + v_q i_q\right) \tag{3.65}$$

Substituting the expressions of d and q voltages into Eq. 3.65, three contributions of power are taking place:

- Joule losses: $P_j = R_s\left(i_d^2 + i_q^2\right)$;

- Magnetic energy variation: $P_{magn} = i_d \frac{d}{dt}\lambda_d + i_q \frac{d}{dt}\lambda_q$

- Mechanical: $P_{mech} = p\omega_m\left(\lambda_d i_q - \lambda_q i_d\right)$

The expression of the steady state mechanical torque is therefore:

$$T_{em} = p\left[\sqrt{\frac{3}{2}}\lambda_m i_q + \frac{3}{2}\left(L_d - L_q\right)i_q i_d\right] \tag{3.66}$$

which is constituted by one term depending on the permanent magnet properties and quadrature axis current in addition to another term depending on the anisotropy of the machine. The production of mechanical torque is therefore function of the amount of current injected in quadrature and direct axis. Thus, the rotational speed that the motor can reach is of course a function of the voltage across the windings but also of their magnetic properties, such as the inductances.

3.5.2   Field Weakening

PMSM are machines able to deliver constant torque until a specific speed named *base speed*. This is the speed at which the back electromotive force produced by the magnets equals the supply DC bus voltage from the battery. Given a certain amount of torque required by the user, below the base speed the amount of absorbed current is constant and proportional to the torque. To increase the speed from zero to the base one, the inverter has to increase the supply voltage, increasing therefore the electric motor power. To increase the speed above the base one, particular control strategies should take place in order to reduce the field produced by the magnets, keeping the power as much constant as possible and allowing the electric motor then to run until speeds much higher than the base speed (even 3 or 4 times higher). Such techniques are called *field weakening* techniques and their implementation in the inverter control logics is well established. In the following, the theory behind the field weakening will be presented.

Circles Diagram

To analyze the field weakening capabilities it is necessary to consider a proper tool. The *cirlces method* is an useful method to understand mainly the limitations (in terms of speed and torque) of a given electric motor, but is also a tool to study the possible control strategies to optimize its performance. The description is presented for the generic anisotropic motor. However, the considerations for an isotropic motor are straightforward.

Substituting the flux linkages equations (3.64) into the electrical equations (3.62) neglecting the time derivatives of the flux linkages, the latter become:

$$\begin{cases} v_d = R_s i_d - p\omega_m \frac{3}{2} L_q i_q \\ v_q = R_s i_q + p\omega_m \left(\frac{3}{2} L_d i_d + \sqrt{\frac{3}{2}} \lambda_m \right) \end{cases} \tag{3.67}$$

In a complex plane having the x - axis as the direct axis and y - axis the quadrature one, the summation of the voltages becomes:

$$\left(v_d + j v_q \right) = \left[R_s i_d - p\omega_m \frac{3}{2} L_q i_q \right] + j \left[R_s i_q + p\omega_m \left(\frac{3}{2} L_d i_d + \sqrt{\frac{3}{2}} \lambda_m \right) \right] \tag{3.68}$$

The vector summation of the voltages in the direct and quadrature axis is equal to the DC voltage originating into the battery. Generally speaking, a DC/AC converter (named

inverter) has the goal of converting a constant DC voltage into an AC sinusoidal one. In doing so, the generated sinusoidal signal has ideally a peak to peak amplitude equal to the DC value. The amplitude of the sinusoidal signal is therefore:

$$V_s = \frac{V_{DC}}{2} \tag{3.69}$$

thus:

$$v_d^2 + v_q^2 = V_s^2 \tag{3.70}$$

Similarly, for the right hand side of Eq. 3.68:

$$V_s^2 = \left(R_s i_d - p\omega_m \frac{3}{2} L_q i_q \right)^2 + \left[R_s i_q + p\omega_m \left(\frac{3}{2} L_d i_d + \sqrt{\frac{3}{2}} \lambda_m \right) \right]^2 \tag{3.71}$$

that, with the assumption of neglected phase resistances becomes:

$$V_s^2 = \left(-p\omega_m \frac{3}{2} L_q i_q \right)^2 + \left[p\omega_m \left(\frac{3}{2} L_d i_d + \sqrt{\frac{3}{2}} \lambda_m \right) \right]^2 \tag{3.72}$$

and therefore:

$$\frac{2}{3} \frac{V_s^2}{(p\omega_m)^2} = \left[\frac{3}{2} \left(L_q i_q \right)^2 + \left(\sqrt{\frac{3}{2}} L_d i_d + \lambda_m \right)^2 \right] \tag{3.73}$$

Equation 3.73 thus relates the maximum voltage available at the level of the DC bus, the mechanical rotational speed of the motor, the flux linkage of the permanent magnets and the inductances of the machine with the currents flowing in direct and quadrature axis. Such equation is extremely important to understand the potential and limits of an electric motor, but should be presented in parallel to another equation, or better, inequality. As a matter of fact, the algebraic summation of the *dq* currents should not overcome the maximum permissible current i_{max}:

$$i_q^2 + i_d^2 < i_{max}^2 \tag{3.74}$$

therefore, the set of two equations should be satisfied together, leading to the following system:

$$\begin{cases} \frac{2}{3} \frac{V_s^2}{(p\omega_m)^2} = \left[\frac{3}{2} \left(L_q i_q \right)^2 + \left(\sqrt{\frac{3}{2}} L_d i_d + \lambda_m \right)^2 \right] \\ i_q^2 + i_d^2 = i_{max}^2 \end{cases} \tag{3.75}$$

The parametric form of the two equations is:

$$\begin{cases} i_{d,1} = -\sqrt{\frac{2}{3}}\frac{\lambda_m}{L_d} + \frac{2}{3}\frac{V_s}{p\omega_m L_d}\cos(\theta) \\ i_{q,1} = \frac{2}{3}\frac{V_s}{p\omega_m L_q}\sin(\theta) \end{cases} \tag{3.76}$$

and:

$$\begin{cases} i_{d,2} = i_{max}\cos(\theta) \\ i_{q,2} = i_{max}\sin(\theta) \end{cases} \tag{3.77}$$

Equation 3.73 written in parametric form shows an elliptic behavior only if the two inductances are different (anisotropic machine) while the current limitation is described by a circle. Figure 3.11 shows a representation of the current circle and of the speed circle as a function of an increasing rotational speed. It is clear from Eq. 3.76 that the increase of the speed generates always smaller circles, centered in the point with coordinates $C = \left[-\sqrt{\frac{2}{3}}\frac{\lambda_m}{L_d}; 0\right]$.
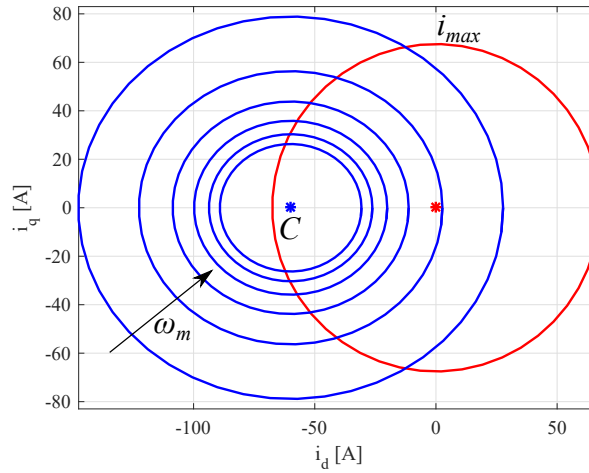
Fig. 3.11 Circle diagram of an anisotropic motor. The effect of the increasing speed on the voltage circle is presented.

The last important quantity that should be introduced in the same diagram is the torque. Considering the expression of the mechanical torque (Eq. 3.66), it can be rewritten as follows:

$$i_q = \frac{T/p}{\left[\frac{3}{2}L_q + \sqrt{\frac{3}{2}}\left(L_d - L_q\right)i_d\right]} \tag{3.78}$$

that is the equation of an hyperbola. Therefore, given a constant amount of torque, an infinite number of combinations between direct and quadrature currents satisfy the equation. However, such combinations should satisfy the voltage (Eq. 3.73) and current (Eq. 3.74) limitations. Figure 3.12 shows the torque curves in case of anisotropic and isotropic motor. The effect of the motor isotropy is that of having torque curves independent from the d axis current.
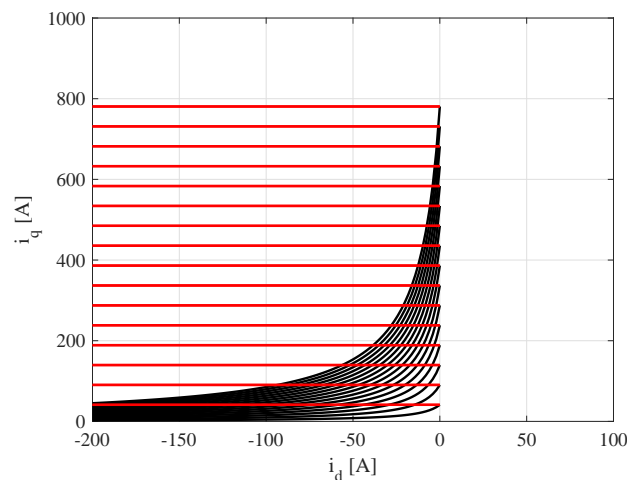
Fig. 3.12 Constant torque curves for anisotropic (black lines) and isotropic (red lines) motor.

Control Strategy

The circles diagram, as said, is very useful to understand the different operational modes of a PMSM. At this point they should be properly described. A strategy with the aim of maximizing the produced torque in each working point is considered in this case, from zero speed to maximum speed, ω_{max}. The method is implemented conceptually and has three steps: mode I, II and III.

Mode I. This mode works in the region from zero speed to the base speed ω_b. In this region the main constraint is the one related to the maximum current, which limits the motor capabilities. Thus, the maximum torque limited by the current occurs in the tangent point to the torque level curves. Voltage and speed can be increased linearly and proportionally to allow the motor operate continuously in this tangent point of maximum torque.

This mode gives constant torque as output and is feasible until the voltage reaches the maximum value allowed by the DC link. Above it, field weakening comes into play and mode II of the strategy starts.

The point of operation for an anisotropic IPM motor is presented in Fig. 3.13. For an SPM motor instead (as the one designed in this work), the point of operation lies in the q-axis as the torque level curves are horizontal lines and not hyperbolas. Current in the d - axis is thus zero.
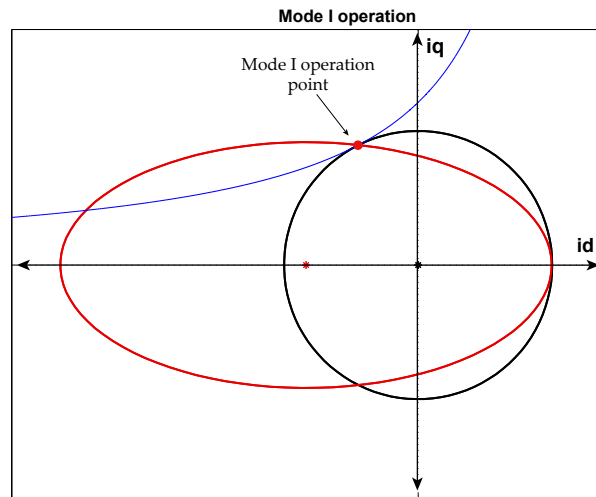
Fig. 3.13 Mode I operation in flux weakening.

With voltage at the maximum value, in order to reach higher velocities it is necessary to reduce the field excitation exactly as done in separately excited DC machines. In permanent magnet motors the field of excitation is fixed (due to magnets), therefore the only way to overcome this limitation is to "weaken" it (from here the name "field weakening").

As the flux produced by the magnets is directed in the positive sense of the d-axis, a negative d-current must be injected in the phases in order to obtain a flux weakening. The strategies to select the values of d and q current to obtain the maximum torque possible are described in mode II and III.

Mode II. This mode works in a region where both current and voltage are limited, but the first restriction is more important than the second one. The points of maximum torque for the voltage limits are known as *maximum torque per voltage (MTPV)* trajectory and are presented in Fig. 3.14.

MTPV trayectory

Maximum torque per
voltage trajectory

iq

id
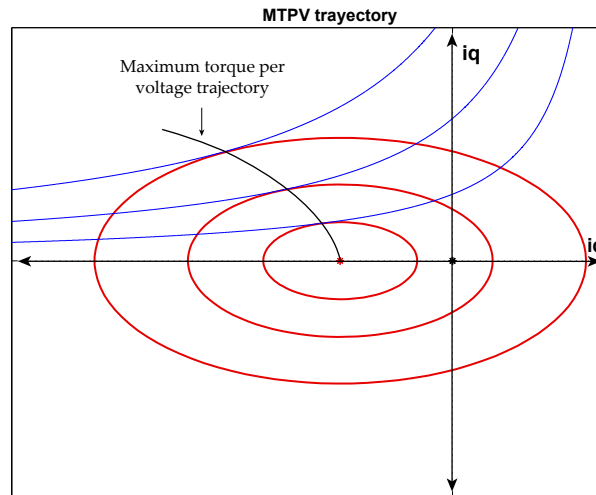
Fig. 3.14 Maximum torque per voltage trajectory for an IPM.

However, these points are not reachable due to current constraints, thus, the best point for selection is the intersection between the voltage and current limits as shown in Fig. 3.15.

Mode II

iq

Mode II operation point
at ω

MPTV point

id

Voltage limit ellipse
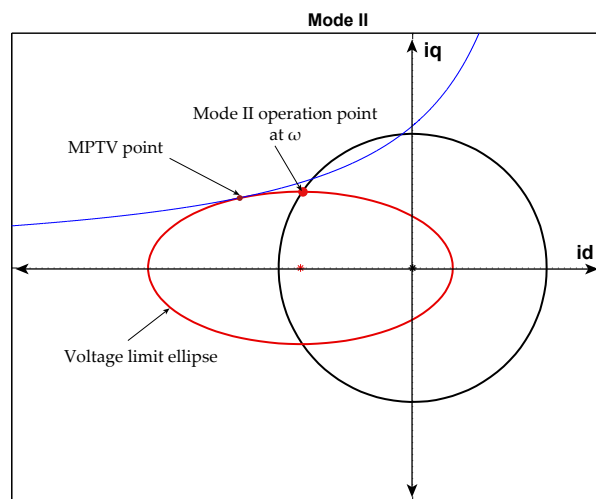
Fig. 3.15 Mode II operation in flux weakening.

Mode III. Mode III is not always reachable. It is considered only in the case when the point of infinite speed C is inside the maximum current circle. At a certain speed, the MTPV point will be inside the current constraint and therefore the best option for

maximum torque is to select this point instead of the intersection between voltage and current limits as shown in Fig. 3.16.
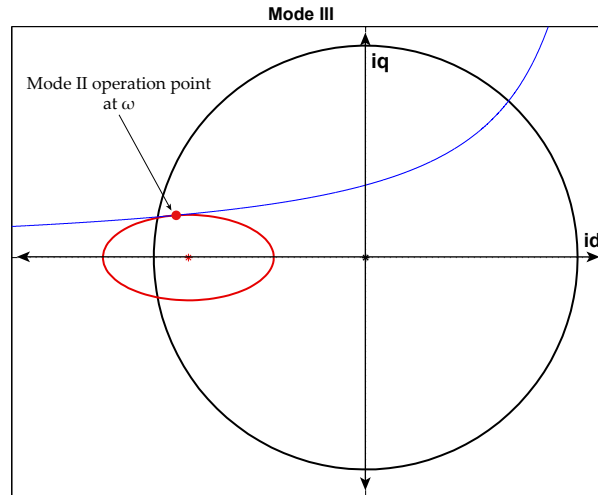
Fig. 3.16 Mode III operation in flux weakening.

The overall control control strategies both for anisotropic and isotropic motors are presented in Fig. 3.17, remembering that mode III for the second type of motors is a straight line in the d-q plane due to horizontal level curves for torque.
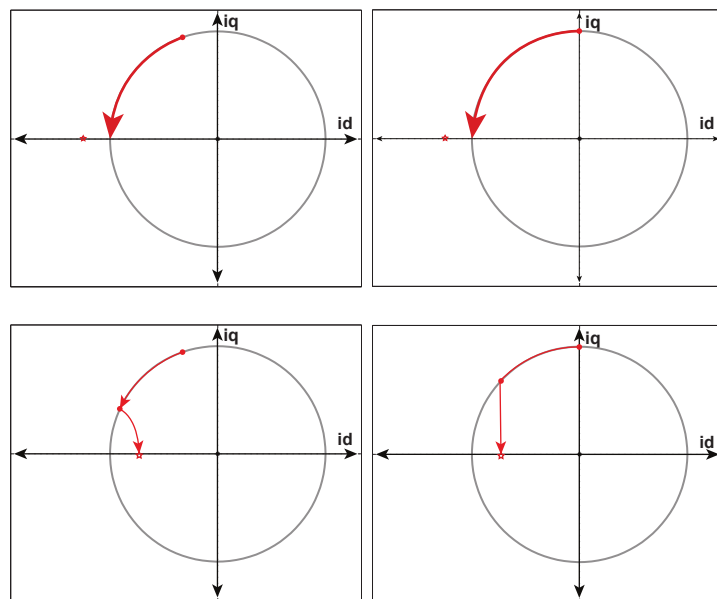
Fig. 3.17 IPM (left) and SPM (right) field weakening strategies for finite speed (top) and infinite speed (bottom) motors.

3.5.3 Design Implementation

The implementation of the presented field weakening techniques requires information related to particular electrical quantities of the motor, that should be properly computed or designed.

Recalling the system of equations 3.75, the only known variable is V_s, which is coming from the fixed design parameters, while ω_m is made vary to analyze the behavior of the motor at different speeds. The inductances L_d and L_q, together with the magnet flux λ_m, should be computed. In addition, the maximum current i_{max} is a function of the maximum slot current and of the slot area, but because of issues that will be explained in the following, is not known a priori.

The computation of the inductance of a coil can be defined as the ratio between the flux linkage of the coil (λ) and the current in the coil (i):

$$L = \frac{\lambda}{i} = \frac{\phi N}{i} \tag{3.79}$$

where ϕ is the magnetic flux and N is the number of windings of the coil. It is a fundamental design quantity that should be defined as a function of the required performance of the motor. However, the most critical point is that both the inductances and the maximum current, are related to N.

Magnetic Fluxes Computation

The computation of the magnetic fluxes is based on numerical analysis since it is the only way to obtain accurate results. The flux density can be expressed as:

$$\mathbf{B} = \nabla \times \mathbf{A} \tag{3.80}$$

where $\mathbf{A}$ is the magnetic vector potential, and the flux can be calculated using the Stoke's theorem:

$$\phi = \int_{\partial S^+} \mathbf{B} \cdot d\mathbf{s} = \int_{\partial S^+} (\nabla \times \mathbf{A}) \cdot d\mathbf{s} = \int_{\partial K^+} \mathbf{A} \cdot d\mathbf{l} \tag{3.81}$$

In Fig 3.18 the verse of the current is also considered.
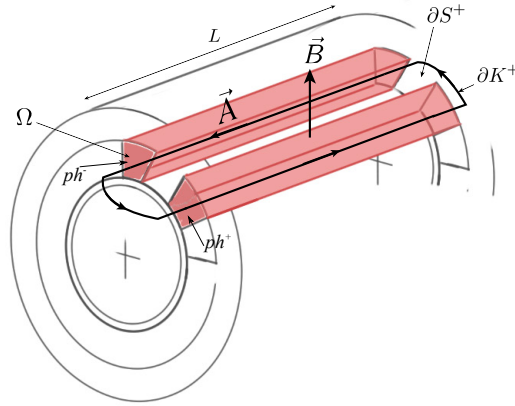
Fig. 3.18 Area used to calculate the flux in the slot.

Therefore the last part of Eq. 3.81 can be rewritten as:

$$\oint_{\partial K^+} \mathbf{A} \cdot d\mathbf{l} = A_{(avg,ph^+)}L - A_{(avg,ph^-)}L \tag{3.82}$$

where $A_{\mathrm{avg,ph^+}}$ and $A_{\mathrm{avg,ph^-}}$ are the average values of $\mathbf{A}$, expressed by integral terms as:

$$
\begin{aligned}
A_{\mathrm{avg,ph^+}} &= \frac{\int A_{\mathrm{ph^+}} dA}{\mathrm{Area_{ph^+}}} = \frac{\int A_{\mathrm{ph^+}} dA}{\Omega} \\
A_{\mathrm{avg,ph^-}} &= \frac{\int A_{\mathrm{ph^-}} dA}{\mathrm{Area_{ph^-}}} = \frac{\int A_{\mathrm{ph^-}} dA}{\Omega}
\end{aligned}
\tag{3.83}
$$

The equation for the flux is finally:

$$\phi = \frac{L}{\Omega} \left[\int A_{\mathrm{ph^+}} dA - \int A_{\mathrm{ph^-}} dA \right] \tag{3.84}$$

which considering that N coils are connected for one phase becomes:

$$\phi = N \frac{L}{\Omega} \left[\int A_{\mathrm{ph^+}} dA - \int A_{\mathrm{ph^-}} dA \right] \tag{3.85}$$

The computation of d and q inductances, requires the respective fluxes to be found out. To this end, through the use of the software COMSOL Multiphysics, using the model built for the constant torque region analysis, an easy procedure is carried out:

- Disable the magnets;

- Apply d and q currents;

- Compute the magnetic vector potential;

- Compute the flux.

In the software, the phases are supplied by means of current densities (not directly by currents). Therefore, to obtain a balanced set they are expressed as:

$$J_A = J_{\max} \cos\left(\frac{N_m}{2}\theta_m + \beta\right)$$
$$J_B = J_{\max} \cos\left(\frac{N_m}{2}\theta_m + \frac{2\pi}{3} + \beta\right) \qquad (3.86)$$
$$J_C = J_{\max} \cos\left(\frac{N_m}{2}\theta_m - \frac{2\pi}{3} + \beta\right)$$

where θ_m is the parametric rotation imposed on the rotor and β is a parameter that can be fixed to obtain currents exclusively in the d-axis or q-axis. A $\beta = 0$ gives currents in the direct axis while, as an example, for this configuration a value of $\beta = \pi/2$ gives a current completely in the quadrature axis.

Applying the aforementioned current densities, the magnetic vector potential is computed by the software as a function of the rotor mechanical angle. Post processing is therefore needed to compute the flux. The magnet flux computation is at this point straightforward, disabling the phases and enabling the magnets. Finally, the inductances follow the expressions presented in Eq. 3.79 with the remark that the current i should be:

$$i = \sqrt{\frac{3}{2}} \frac{\sqrt{2}J_{\max}k_{cp}A_{slot}}{2N} \qquad (3.87)$$

where the factor $\sqrt{2}$ brings the rms value to its maximum while the factor $\sqrt{\frac{3}{2}}$ is the conversion factor bewteen a stationary three phase system and a rotation equivalent two phase system.

Winding Design and Motor Torque and Power Speed Characteristics

In the expressions of the inductances, the magnet flux linkage and the maximum current, the number of windings in each motor slot, N, is always present. For this application, N is chosen such that the voltage circle computed considering the predefined base speed intersects the current circle exactly in the point of coordinates $[0; i_{\max}]$. In this way the performance of the motor is ensured, meeting design issues and functionalities. Figure 3.19 shows the influence of the number of windings on the construction of the circle diagram.
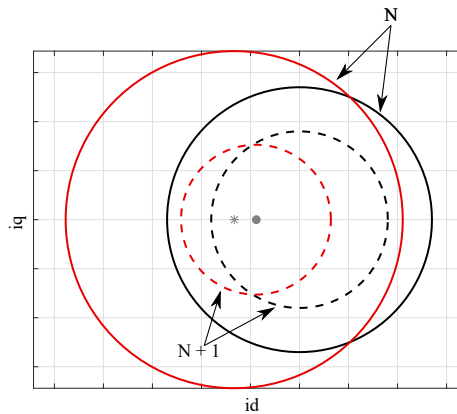
Fig. 3.19 Influence of number of windings N in the construction of the circle diagrams.

After some iterations, the number of windings and therefore the inductances and the magnet flux linkage are found. The resulting circle diagram is shown in Fig. 3.20
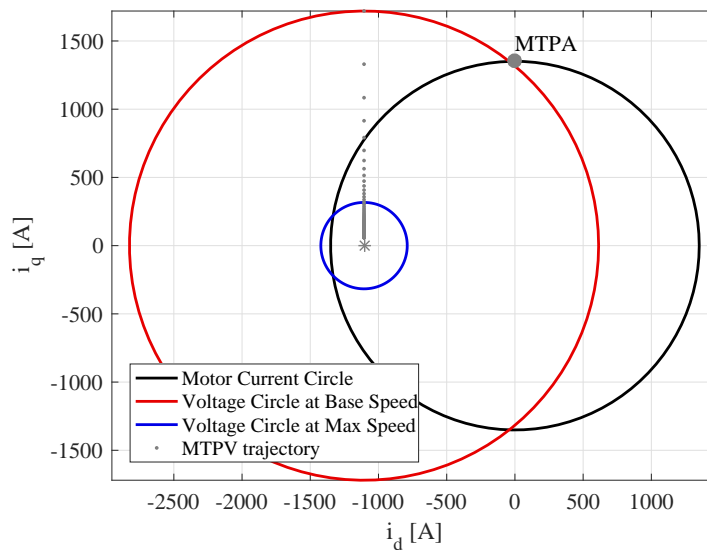
Fig. 3.20 Circle diagram of the not optimized motor

At this point, according to the control strategy presented in Sect. 3.5.2, the speed of the motor is varied from base to its maximum value. For any speed, the point of operation (the couple of dq currents) is obtained and the torque can be computed. Finally, to carry out the torque speed characteristic for the whole region of operation, different values of the current density (and therefore maximum current) are selected.

The design of the traction motor still needs one last step forward. The results presented should in practice be subjected to a last optimization.

As shown in [36], it is possible to plot the saliency ratio (a quantity depending on how much the machine is anisotropic) with respect to the normalized magnet flux linkage, whether the motor is an SPM or an IPM. In this plot the different working areas of the motor can be found, and they are related to its possibility to be driven at infinite or limited speed.

Making reference to the circle diagram of Fig. 3.11, it is clear that if the center of the voltage circle stands inside the current circle, the motor has potentially infinite speed (neglecting the internal friction). The more the speed increases, the more the voltage circle reduces, but there will always be a current circle (even very small) which intersects the former. Similarly, if the center of the voltage circle stands outside the current circle related to the maximum current, it is intuitive to realize that above a certain speed the intersection between the two does not hold anymore.

Again with reference to [36], it is demonstrated that if the center of the voltage circle is moved exactly in the boundary between finite and infinite speed property, for an isotropic motor the optimum performance are reached. This means that the abscissa of the center of the voltage circle should be:

$$C_x = -\sqrt{\frac{2}{3}}\frac{\lambda_m}{L_d} = i_{max} \tag{3.88}$$

To obtain this result, the magnet flux linkage should therefore be increased, or the d axis inductance should be reduced, or both. An easy way to perform this modification is to increase the magnet length l_m. This would increase the magnet flux (and therefore λ_m) together with increasing the air gap reluctance of the magnetic circuit, reducing the d axis inductance. The modification of the motor geometry is presented in Fig. 3.21 while the values of magnet flux and inductances are reported in Tab. 3.10.

Parameter	Value
N	2
L_d	0.017 mH
L_q	0.017 mH
λ_m	0.0281 Wb

Table 3.10 Optimized motor parameters
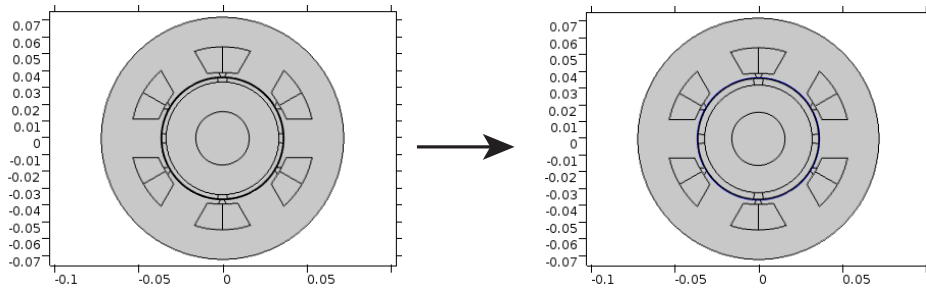
Fig. 3.21 Motor before and after optimization.

The motor optimization produces therefore the circle diagrams of Fig. 3.22 and the torque speed characteristics of Fig. 3.23.
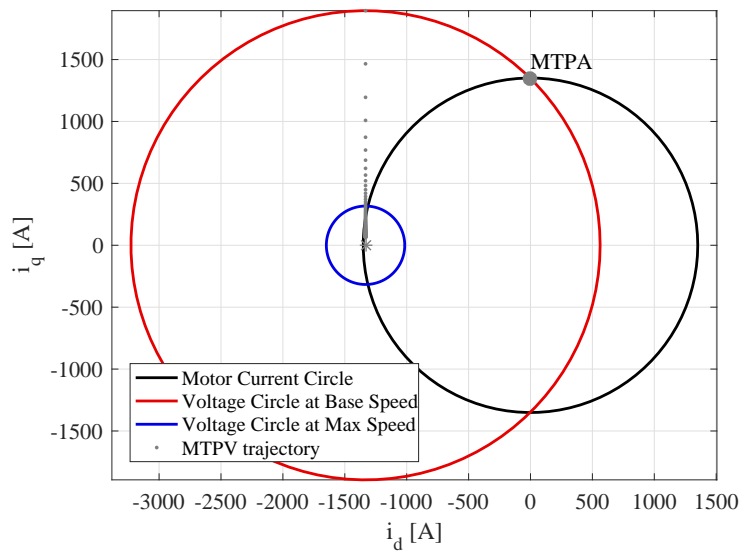
Fig. 3.22 Circle diagram for the optimized motor.
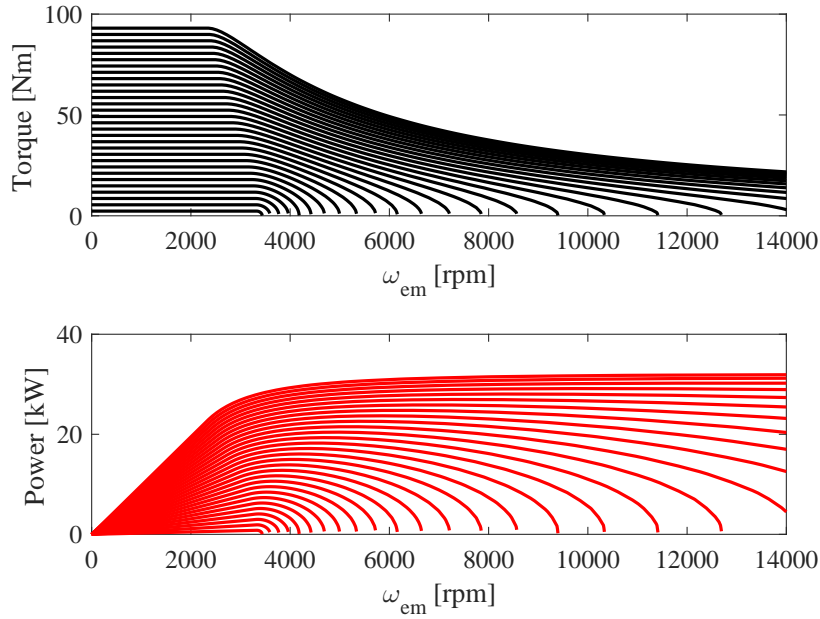
Fig. 3.23 Torque and speed characteristic for the optimized motor as a function of different current densities (from 0.5 to 20 Arms).

3.5.4 Electric Motor Maps

Based on the specifications presented in previous sections, an optimized version of the motor has been obtained. Therefore, the maps of current density, phase current and DC current as a function of each working point of the motor can be obtained.

Considering the field weakening issues highlighted in Sect. 3.5.2 and according to the strategy presented in Fig. 3.17, for each current density and for each electric motor speed, the direct and quadrature axis are computed.

The phase current is computed as:

$$i_{\text{phase,rms}}\left(T,\omega\right) = \sqrt{\frac{2}{3}} i_{\text{max,dq}}\left(T,\omega\right) \frac{1}{\sqrt{2}} = \sqrt{\frac{2}{3}} \sqrt{i_{\text{q}}^2\left(T,\omega\right) + i_{\text{d}}^2\left(T,\omega\right)} \frac{1}{\sqrt{2}} \qquad (3.89)$$

while the DC current is computed considering the power conservation of the three to two phase transformation, neglecting the magnetic energy variation in time:

$$V_{\text{DC}} i_{\text{DC}} = R_{\text{phase}}\left(i_{\text{q}}^2 + i_{\text{d}}^2\right) + p\omega_{\text{m}}\left(\frac{3}{2} L_{\text{d}} i_{\text{d}} i_{\text{q}} + \sqrt{\frac{3}{2}} \lambda_{\text{m}} i_{\text{q}}\right) - p\omega_{\text{m}} \frac{3}{2} L_{\text{q}} i_{\text{d}} i_{\text{q}} \qquad (3.90)$$

having neglected the parenthesis (T, ω). The current is therefore:

$$i_{\text{DC}} = \frac{1}{V_{\text{DC}}} \left[R_{\text{phase}} \left(i_q^2 + i_d^2 \right) + p \omega_m \left(\frac{3}{2} L_d i_d i_q + \sqrt{\frac{3}{2}} \lambda_m i_q \right) - p \omega_m \frac{3}{2} L_q i_d i_q \right] \qquad (3.91)$$

Figures 3.24 - 3.26 present contour plots for current density, phase current and DC currents. The high phase currents were expected and are justified by the very low battery voltage. Additional considerations will be carried out at the end of this chapter.
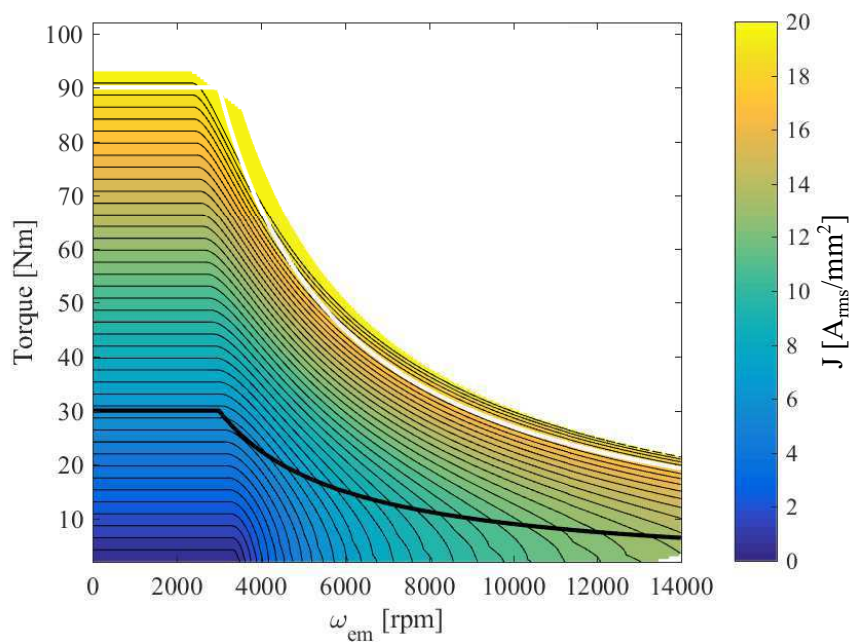
Fig. 3.24 Contour plot of current density $\left[\text{Arms}/\text{mm}^2\right]$ as a function of the electric motor torque and speed together with peak torque - speed curve (white) and continuous one (black).
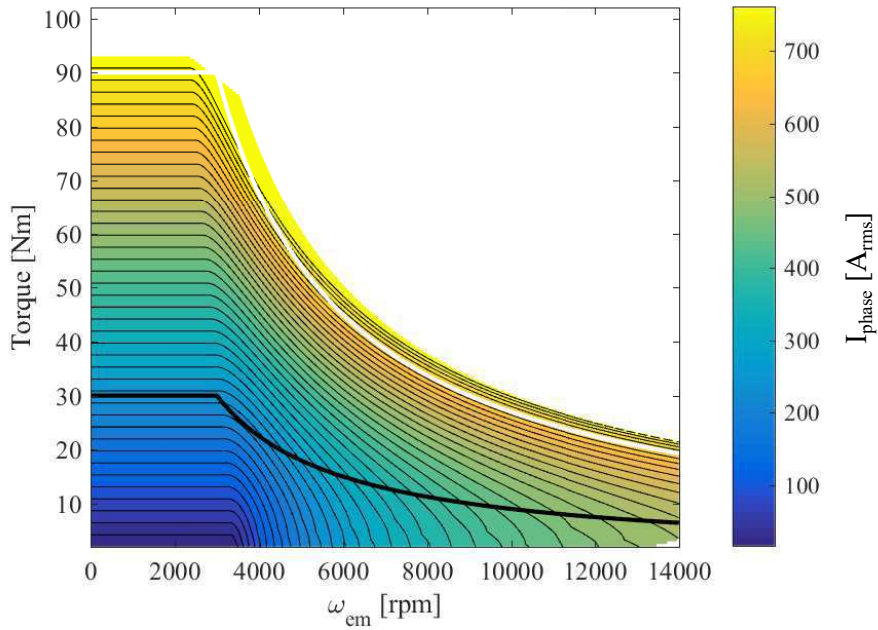
Fig. 3.25 Contour plot of phase current [Arms] as a function of the electric motor torque and speed together with peak torque - speed curve (white) and continuous one (black).
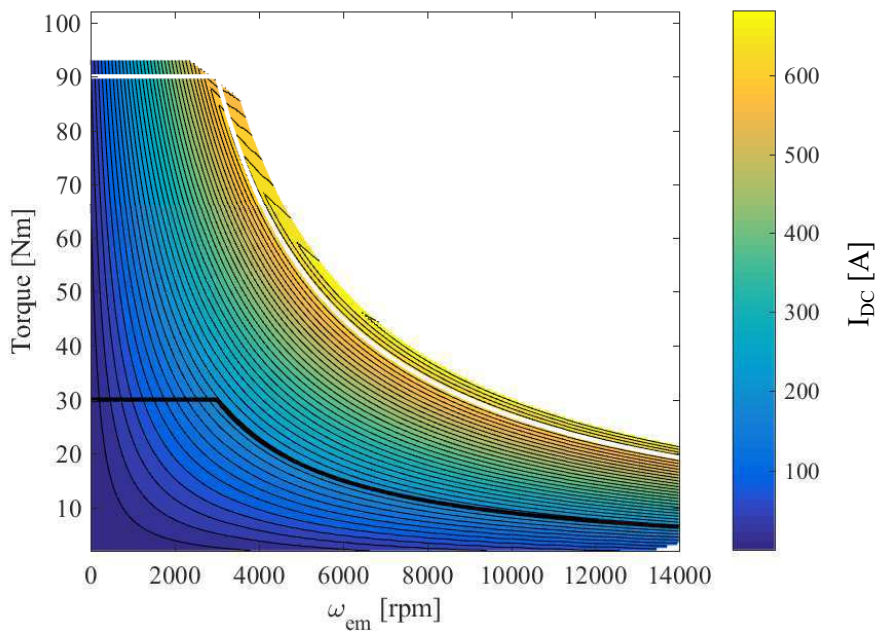
Fig. 3.26 Contour plot of DC current [A] as a function of the electric motor torque and speed together with peak torque - speed curve (white) and continuous one (black).

3.6 Thermal Analysis on PMSM

Thermal design and analysis of the electric machine is of capital importance because performance and sizing of a motor is ultimately dependent upon its thermal rating.

This importance is reflected by the fact that designing a motor starts and finishes with thermal considerations. At the beginning of the design, a value of J is selected taking into account the desired cooling system. At the end of the design, the cooling system is effectively designed and the machine is tested to obtain its thermal capabilities in continuous and transient mode. The present chapter is precisely dedicated to the last part.

3.6.1 Cooling and Thermal issues

The motor components that are limited in temperature are bearings (because of their life), plastic cover (low melting point), wire or slot liner and magnets (demagnetization). The last two are the most important [38].

For the wires, the temperature limit is fixed by the type of insulation chosen. Heat transferred by joule losses make the insulation melt and short-circuit the machine. For the magnets, instead, the main problem is demagnetization. As already underlined in Fig. 3.8, the demagnetization curves decrease with the increase of temperature. This is not a problem as long as the operation point of the motor does not reach the "knee" in the curves as shown in Fig. 3.27, where the magnet passes from point A (no load at 20 °C), to B (full load at 20 °C), to C (full load at 100 °C), to D (no load at 100 °C) and finally returns to A.
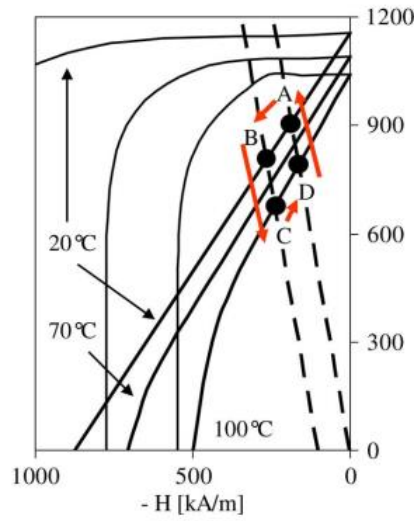
Fig. 3.27 Magnet operation points without demagnetization.

In case the knee is encountered, the magnet is demagnetized as shown in Fig. 3.28, in which it passes from A (no load at 20 °C), to B (full load at 20 °C), to C (full load at 100 °C), to D (no load at 100 °C) through another path and finally it does not return to the initial point A.
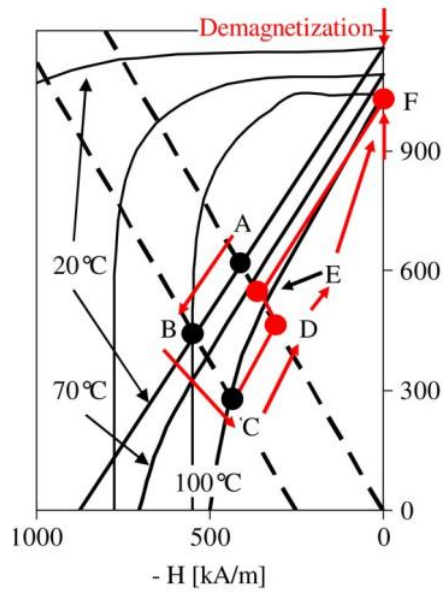
Fig. 3.28 Magnet operation points with demagnetization.

To avoid such problems, it is important to choose a point far away from the knee by selecting a PC value bigger than 4. Therefore, it is important to design an appropriate cooling system that allows the magnet to remain under 100 °C.

3.6.2 Losses

The losses in the electric machine are of two types:

- Joule losses: are computed as $3R_{ph}I_{ph,rms}^2$. Details of the computation are presented subsequently.

- Iron losses: correspond to the eddy current losses, anomalous currents and hysteresis. The equations used for their computation are taken from [37] and correspond to:

$$
\begin{aligned}
P_e &= K_e \hat{B}^2 f^2 \\
P_a &= K_a \hat{B}^{1.5} f^{1.5} \\
P_h &= K_h \hat{B}^\alpha f
\end{aligned}
\tag{3.92}
$$

where the values of K and α are constants obtained by experiments and interpolations, $\hat{B}$ correspond to the peak value of flux density current in $[T]$ and f the frequency of the current source. These equations are accurate only if the material loss data are accurate.

3.6.3 Implementation

For thermal design implementation, three software tools have been used: Matlab, Comsol and Motor-CAD. The first one for the computation of Joule losses, the second for the computation of iron losses and, through last one, a lumped parameters circuit analysis model has been built and used for thermal time domain simulations.

In modern thermal design there are two options: finite element analysis (FEA) or lumped parameters model analysis. While FEA gives in general more accurate solutions for particular examples, it can be time consuming. Lumped - circuit analysis is more useful for faster and more interactive design procedures. Therefore, the second option is chosen here and a typical lumped - circuit model from Motor-CAD is presented in Fig. 3.29
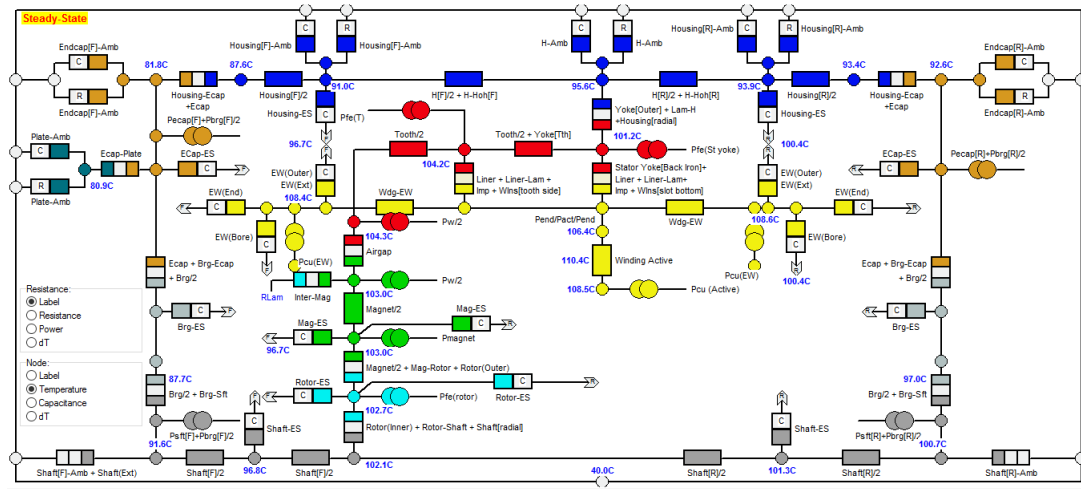
Fig. 3.29 Lumped-circuit model in Motor-CAD.

Joule Losses Computation

For the application of the Joule losses equation it is necessary to know the phase resistance R_{ph} and the phase current in rms $I_{ph,rms}$. This two values are computed in the following.

Phase resistance. In order to compute the phase resistance, the well known equation for the wire resistance is considered:

$$R_{ph} = \rho_{cu} \frac{L}{A} \tag{3.93}$$

while to obtain the values of L and A it is helpful to recall Fig. 3.30.
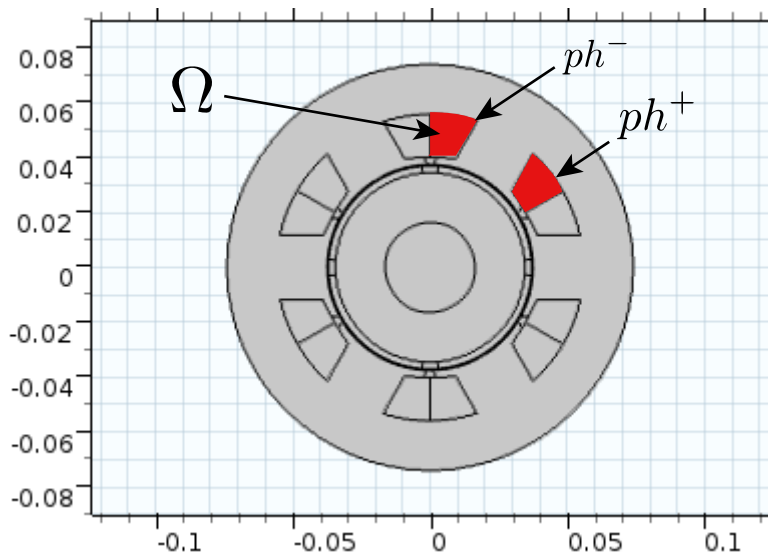
Fig. 3.30 One concentrated coil in the motor

A coil enters in ph^+ and travels through the motor axial length L. Then, it makes a circular path (known as end turn) from ph^+ to ph^-, with a length L_{et}. The last term can be computed considering geometric parameters and simple trigonometry.

All the path it is traveled twice, hence the total length to be considered in the resistance equation is $2(L+L_{et})$.

The area considered must be the corresponding to *one wire*. From Fig. 3.30, one-half slot area is Ω and therefore with N turns entering this area with a conductor packing factor of k_{cp}, the area of one wire becomes $A_{1\text{wire}} = (\Omega k_{cp})/N$.

Finally, considering that this path for one wire is repeated N times in one slot and that there are $N_{sp} = N_s/N_{ph}$ slot occupied by one phase, the final equation for the phase resistance is:

$$R_{ph} = \rho_{cu}(N \cdot N_{sp})\frac{2(L+L_{et})}{\frac{k_{cp}\Omega}{N}} = 2N^2 N_{sp}\rho_{cu}\frac{L+L_{et}}{k_{cp}\Omega} \tag{3.94}$$

Phase current. The values of phase current are taken simply from the current maps presented in Fig. 3.25.

Iron Losses Computation

The constant values K_e, K_a, K_h and α are obtained from [37]. In this paper a proper calculation for the M400-50A steel constants is performed. Regarding the peak flux density $\hat{B}$, COMSOL is used to simulate and obtain the proper value. It should be underlined that this computation must be done for every point in the working region of the motor as the flux density in the iron changes for different speeds (based on the flux weakening and on different current densities).

Finally, the frequency is obtained from the known relation $f_{el} = pf_{mec}$ where p is the number of pole pairs; the stator mass is obtained directly from Motor-CAD as the equations are expressed in $[\text{W/kg}]$.

3.6.4 Cooling design

For the cooling design, the motor geometrical dimensions are transferred to Motor-CAD as presented in the next figures.
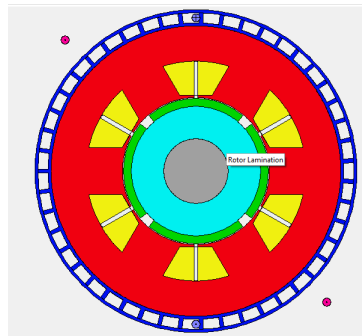
Fig. 3.31 Designed motor in Motor-CAD, front view.
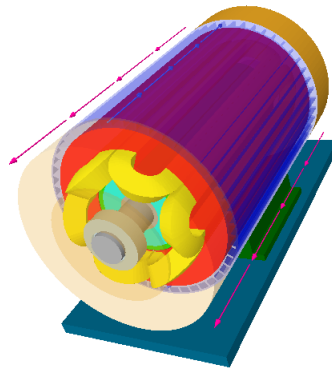
Fig. 3.32 Designed motor in Moor-CAD, 3D view.

Recalling the rule of thumb presented Sect. 3.3, for current densities between 20 and 30 A/mm^2 liquid cooling is necessary.

In this case, the cooling system considers a water jacket and forced air (simulating the movement of the car) as shown in Fig. 3.31. The different parameters for the cooling are presented in Tab. 3.11.

Type of cooling	Values
Water inlet Temp.	50 °C
Water flow rate	30 l/min
Forced air Temp.	50 °C

Table 3.11 Cooling parameters

The values of water flow are reasonable considering a normal cooling system for automotive applications; the forced air temperature is consistent with the motor position (rear axle).

Temperature limits

As mentioned before, the most important thermal limits are the Copper insulation (for short-circuit) and the magnet (for demagnetization). Considering that wiring is done with type - H insulation and the magnet chosen is NdFeB, the temperature limits are presented in Tab. 3.12.

Parameter	Temperature limit
Type-H Copper insulation	180 °C
NdFeB magnet	100 °C

Table 3.12 Temperature limits

Thermal characterization

Thermal characterization of the motor has been done considering a first order model characterized by two parameters: thermal resistance (K) and time constant (τ). The temperature evolution in time is:

$$T = KP_{diss}\left(1 - e^{t/\tau}\right) \tag{3.95}$$

In order to obtain K and τ, the simulations have been performed for the points shown in Fig. 3.33, and the results are interpolated for all the rest of the motor map.
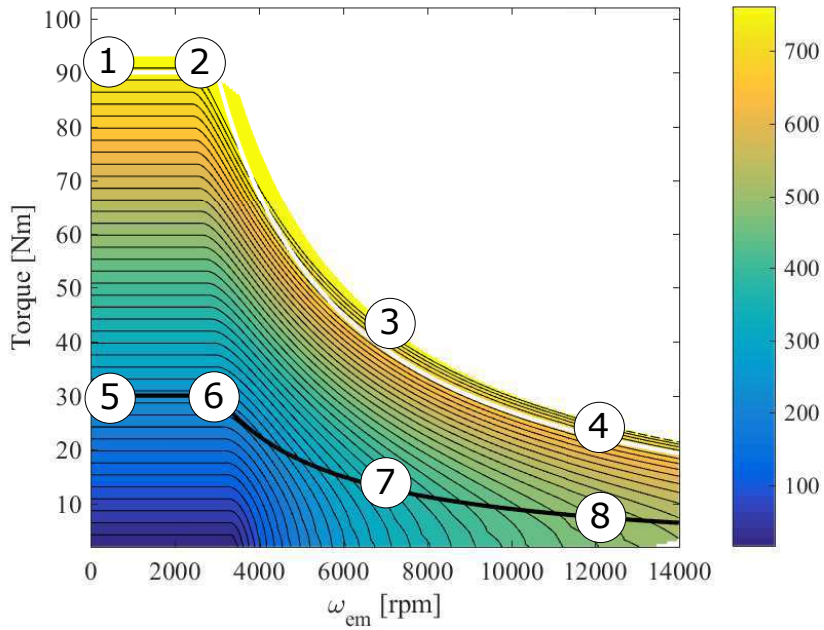
Fig. 3.33 Study points for thermal characterization

Results: K and τ maps

Figure 3.34 presents the simulation results for one of the most important and stressed points, thermally speaking, due to its high value of phase current and requirement to be a continuous operating point.
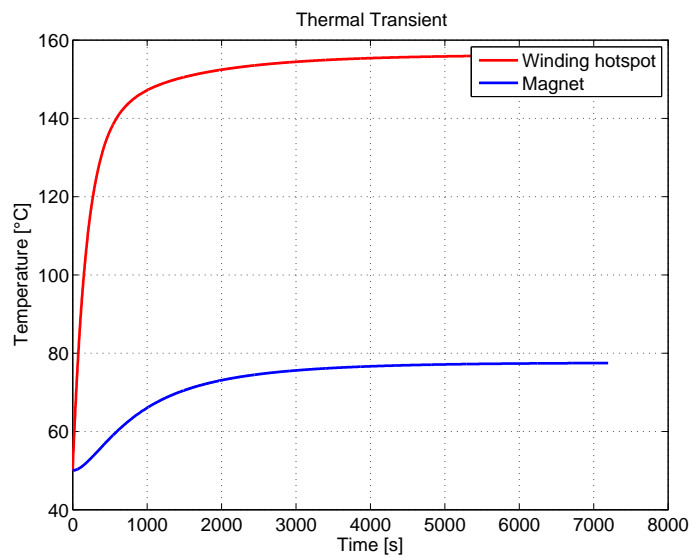
Fig. 3.34 Temperature simulation results for point 8.

The value of thermal resistance K and can be calculated by

$$K = \frac{T_{ss}}{P_{diss}} \qquad (3.96)$$

where T_{ss} is the steady state temperature of the subsystem under consideration and P_{diss} is the power dissipated in such subsystem. The value of τ is obtained as the time when the temperature reaches 63 % of its steady state value.

From Fig. 3.34 is important to notice that the values of thermal resistance and time constant are different for the magnet and the winding hot - spot. This happens because the magnets are isolated from the main heat sources and so they are protected from severe transient overloads. However, it is underlined that for this severe thermal point, both the winding and the magnet do not exceed the limit temperatures.

Repeating the same process for the other points results in different values of K and τ. It is clear, therefore, that the machine can not be characterized by a single value of K and τ and the thermal analysis need to be performed for all the working region. For this purpose the simulations are done for the points presented in Fig. 3.33 and the results are interpolated.
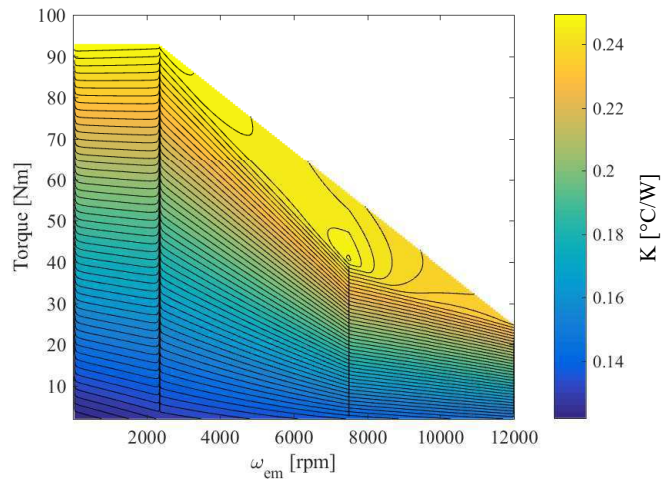
(a) Winding thermal resistance.
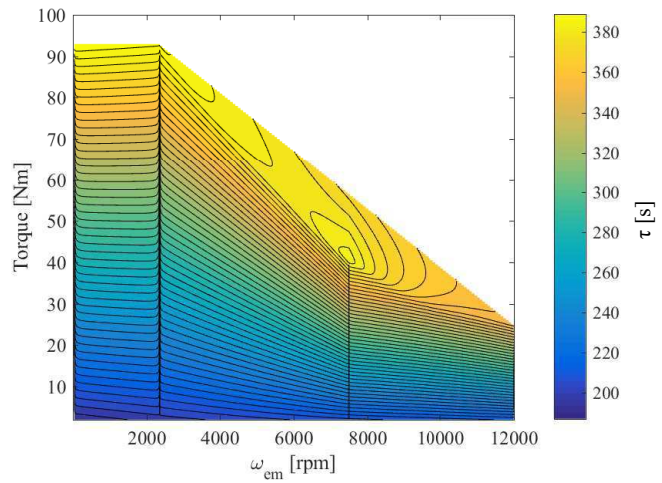
(b) Winding thermal time constant.

Fig. 3.35 Thermal resistance and time constant for the winding as a function of the torque and the speed of the electric motor.

By means of the maps presented in Fig. 3.35 it is possible to consider the model described by Eq. 3.95 for any working point of the electric motor. In this case only the winding thermal resistance and time constant are presented.

Finally, Tab. 3.13 summarizes the expected (from Tab. 3.4) and the actual outcomes of the electric motor design while Tab. 3.14 presents other specific output parameters.

	Operation mode	**E. V.**	**A. V.**	**Unit**
Max. Power	continuous	10	10	kW
Max. Power	transient	28.2	31	kW
Max. Torque	continuous	10	10	Nm
Max. Torque	transient	90	93	Nm
Base speed	continuous	4200	3000	rpm
Base speed	transient	4200	2350	rpm
Max speed	continuous	13900	14000	rpm
Max speed	transient	13900	14000	rpm
Air gap shear stress	continuous	30	18	kN/m^2
Torque @ Max. Speed	transient	30	21	Nm

Table 3.13 Expected (E. V.) and actual (A. V.) outcome of the motor design.

The motor obtained is a high performance machine that accomplishs almost all of the initial requirements, with a value of air gap shear stress σ of 18 kN/m^2. Higher values of σ could be accomplished considering higher current densities and therefore better cooling performance.

The low voltage application limits the motor base speed, slightly lower than the expected in continuous mode, close to half of the expected value in transient conditions. This is clearly one of the limitations occurring when dealing with low voltage applications. Similar considerations are carried out where the torque at maximum speed is concerned.

Other specific values are presented below:

	Value	Unit
Batteries Voltage V_{DC}	48	V
Number of phases N_{ph}	3	-
Pole pairs $p = N_m/2$	2	-
Stator slots N_s	6	-
Number of turns N	2	-
Stator outer diameter D_{so}	144	mm
Rotor outer diameter D_{ro}	72	mm
Stack length L	200	mm
Air gap g	0.5	mm
Base speed at continuous mode	3000	rpm
Max. speed at continuous mode	14000	rpm
Max. torque at continuous mode	30	Nm
Current at continuous mode (phase rms)	251	A
Base speed at transient mode	2350	rpm
Max. speed at transient mode	14000	rpm
Max. torque at transient mode	93	Nm
Current at transient mode (phase rms)	779	A
Phase rated voltage $Vs = V_{DC}/2$	24	V
Phase resistance R_{ph}	0.00087	Ω
Maximum steady state temperature (winding)	160	°C
Maximum steady state temperature (magnet)	72	°C
Mass (obtained with Motor-CAD)	26	kg

Table 3.14 Motor specifications

3.7   Chapter Summary and Future Works

In this chapter the design framework of an electric machine for mild hybrid electric vehicle applications has been established. After selecting a particular class of motors characterized by, for example, typology, geometrical constraints, topology and materials, the optimization is performed regarding the mechanical characteristics of the motor (maximum torque, maximum power, maximum speed) with the goal to obtain a machine adapted both on the vehicle and on the application under analysis.

The procedure follows with the application of conventional techniques for the design of PMSM motors. Where the constant torque region of the motor is concerned, both analytical and numerical techniques have been adopted, showing how the analytical methods provided an underestimation of the actual torque value as well as an overestimation of the motor mass. The constant power region design is characterized by the study of the field weakening techniques and the consequent characterization of the motor in each of its working points in terms of phase and DC currents. It has been shown how the winding inductances and the magnets geometry can be tuned to obtain the highest torque and power given a maximum current density.

A small consideration needs to be done regarding the current absorbtions obtained for this motor, high in terms of maximum values (around 700 A for peak values of phase currents), but expected given such high demanding requirements and low voltage capabilities. It is clear that, just by changing the number of turns in the coil, a motor with the same dimensions can be powered with a higher voltage source, giving the same performance and leading to lower current absorbtions. This happens since the optimal performance of an electric machine is not determined by voltage or currents, but is based on current densities and therefore cooling capabilities.

Finally, a thermal analysis on the designed motor has been carried out by means of a finite element model of the motor itself. Different working points on the torque speed map have been selected based on their values of current while being simulated from the transient and steady state thermal dynamics point of view. The power losses which generate temperature increase consider both the Joule losses in the copper windings and the iron losses due to hysteresis. Considering a first order model for the description of the temperature time response in different physical points of the motor, the different thermal resistances and time constants have been identified through numerical simulations, evidencing how an electric motor can not be identified by a single value of the two aforementioned parameters valid for the overall working range of the machine. A general map of these variables for any electric motor working point has been created, with the goal of using it during electric powertrain assessment analyses.

Further steps involve the introduction of additional design parameters (PMSM, IPM - number of slots, number of poles - isotropy, anisotropy) into the optimization loop in order to extend the framework to different motor classes, considering the same goal of fitting the electric machine with the vehicle and the application.

Chapter 4

Powertrain Design and Control Strategies for Efficiency Enhancements of P4 Architecture

4.1 Introduction

Chapter 2 presented the vehicle architecture under analysis and the modeling of the conventional powertrain components such as the engine, gearbox and wheels. A deep analysis regarding the impact of different hybrid architectures on the maximum recoverable energy during braking conditions has been conducted, showing the influence of each vehicle and powertrain dissipation on the total dissipated energy (from kinetic to electric energy). The P4 architecture therefore underlined how the proximity of the electric machine to the ground can improve the regeneration efficiency as well as for traction, but no attention was given to the electric powertrain modeling, design and control for energy efficiency enhancements. This chapter is devoted to fill this lack. First of all, the modeling of the electric powertrain components will be presented and discussed. An energy analysis regarding the electric battery will be performed and a design optimization of this main component is therefore carried out. It will be demonstrated how the battery for such hybrid architectures plays a central role because of its main limitations. Finally, the advantages in terms of fuel consumption reduction and overall energy efficiency enhancements with the on - board installation of the electric powertrain are presented and analyzed, considering the presence of the Energy Management System (EMS).

4.2 Electric Powertrain Modeling

When dealing with energy and fuel consumption analysis on hybrid electric vehicles, the modeling of the electric components and the variables related to them is of particular importance. A simple example can be the battery state of charge. The overall management of the energy on - board, of the power split between the two prime movers and thus the potential improvements where the fuel consumption is concerned are strictly dependent on its accurate computation/estimation. Another example can be the current incoming or outgoing from the battery, a function of the mechanical load (negative or positive) that the electric machine has to deal with, or the electric motor temperature, which can lead to its possible unuse during part of the driving cycle.

4.2.1 Electric Motor and Rear Gearbox

Chapter 3 was devoted to design an electric machine for a rear axle hybrid vehicle based on the established tasks that it should accomplish while travelling on driving cycles (i. e. regenerative braking, electric start). Static maps of torque, DC current, and phase current are therefore obtained and can be introduced into the model.

Since the computation of the DC current (Eq. 3.91) already takes into account the resistive losses, based on a certain rotational speed and required torque, the computed DC current from the map of Fig. 3.26 accounts therefore for the motor efficiency (even though only due to resistive losses).

The rear Gearbox is modeled with a transmission ratio and a constant efficiency as presented in Sect. 2.2.3.

Finally, the electric motor thermal behavior has been modeled as presented in Sect. 3.6.

4.2.2 Battery

As previously introduced, the battery is the key component for hybrid electric vehicles, especially for those of the mild kind, intermediate architectures between engine assistant hybrid and full hybrid. Considering a certain hybrid powertrain architecture, all the applicable power split strategies are a function of the battery characteristics and limitations.

The maximum admissible current, state of charge and temperature are some of the main variables involved that characterize the battery working conditions and influence the reciprocal operations between it and the other electric powertrain components.

The State Of Charge (SoC) is for sure the principal of these variables. Generally speaking, the battery SoC is the fundamental state at the base of any system that manages the energy on board; this is explained by considering the functionalities of an hybrid vehicle for mild architectures. Supposing to know the path to be followed in terms of speed, the (for now called) "controller" should be able to provide the *optimal* split between the two power sources. Based on this fact, considerations regarding the hybrid architecture under analysis should take place. *Charge Sustaining* mode is a control working mode that avoids the complete discharge of the battery and has the goal of maintaining it around an average value for all the driving cycle, providing also an energetic balancing. *Charge Depleting* mode, oppositely, allows the complete discharge of the battery. If the latter control mode is very suitable for plug in hybrids because of the possibility to recharge the batteries after the cycle is followed, the former does not have this feature, leading therefore to a more accurate energy management.

The presented examples had the goal to underline and put in evidence the central role owned by the battery SoC. For this reason its accurate and reliable evaluation is of fundamental importance. The battery SoC is defined as the amount of electrical charge stored in the battery with respect to the total charge capacity:

$$SoC = \frac{Q(t)}{Q_{\text{nom}}} \tag{4.1}$$

where Q_{nom} is the nominal charge capacity. The SoC dynamics is instead:

$$\dot{SoC}(t) = \begin{cases} -\frac{1}{\eta_c} \frac{i(t)}{Q_{\text{nom}}} & i(t) > 0 \\ -\eta_c \frac{i(t)}{Q_{\text{nom}}} & i(t) < 0 \end{cases} \tag{4.2}$$

where η_c is the charge efficiency, which accounts for different kind of losses such as current intensity and temperature. The integration of Eq. 4.2 is straightforward only if the battery capacity is considered as a constant.

To correlate battery current and voltage to the actual battery SoC, an electric circuit model can be used. Actually, different models of the battery electric circuit have been analyzed in the literature considering different orders of approximation ([39] - [43]). Of course, the more the model is complex, the more it is potentially able to represent the relevant variables. However, the drawback stands in the potentially high number of parameters to be known or estimated.

One simpler model that can be considered is the so called zero order model, which does not take into account for the voltage dynamics but assumes the battery to be constituted by

a voltage source in series with an internal resistance [7]. The battery power is therefore defined as:

$$P_{\text{batt}}(t) = V_{\text{load}} i(t) = V_{\text{oc}} i(t) - R_0 i(t)^2 \tag{4.3}$$

where V_{load} is the voltage load, V_{oc} is the open circuit voltage and R_0 is the internal resistance. Solving for the current leads to:

$$i(t) = \frac{V_{\text{oc}}}{2R_0} - \sqrt{\left(\frac{V_{\text{oc}}}{2R_0}\right)^2 - \frac{P_{\text{batt}}}{R_0}} \tag{4.4}$$

This model does not need a high number of parameters and is sufficiently reliable to represent the quantities of interest, but has the drawback of not including the SoC as a function of the open circuit voltage. In addition, it cannot account for the temperature dependence of its parameters as well as the battery degradation in time and the state of health.

To this end, the experimental curve of the open circuit voltage as a function of the battery SoC is considered. Together with the open circuit voltage, the experimental variation of the internal resistance of the battery and of the maximum admissible DC current as a function of the SoC are considered.

By using experimental curves of the battery parameters of interest, their dynamic behavior is therefore neglected. However, the knowledge of V_{oc}, R_0 and $i_{\text{DC,max}}$ as a function of the battery SoC is already very important for the following analysis and for the general aim of this work.
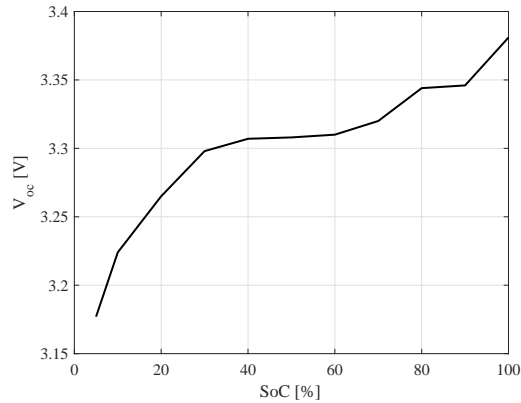
(a) Cell V_{oc} vs. SoC
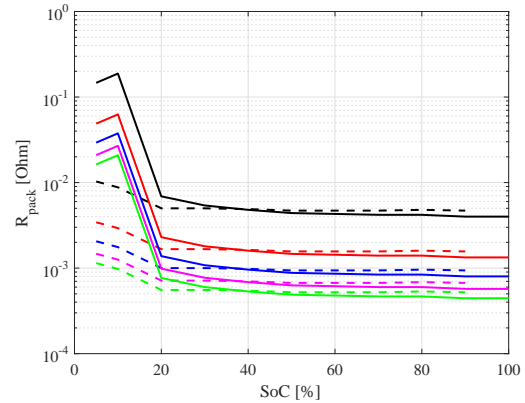
(b) R_{pack} vs. SoC. Continuous lines: discharge characteristics, dashed lines: charge characteristics.
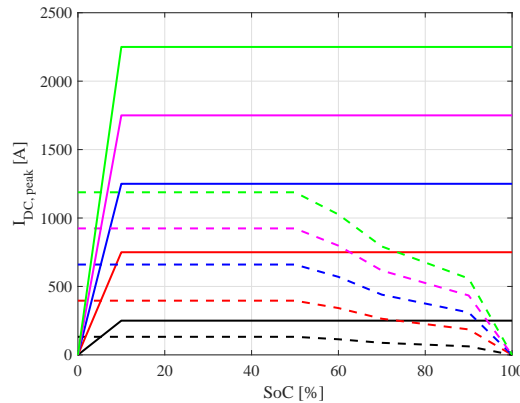
(c) $I_{DC,peak}$ vs. SoC. Continuous lines: discharge characteristics, dashed lines: charge characteristics.

Fig. 4.1 Characteristics of the Li - Ion battery under consideration. (a) Cell open circuit voltage vs. SoC, (b) R_{pack} vs. SoC, (c) $I_{DC,peak}$ vs. SoC. Black lines: $Q_{nom} = 4.4$Ah, red lines: $Q_{nom} = 13.2$Ah, blue lines: $Q_{nom} = 22$Ah, magenta lines: $Q_{nom} = 30.8$Ah, green lines: $Q_{nom} = 39.6$Ah. Data provided by the industrial partner of the project.

Figure 4.1 presents the open circuit voltage of the battery cell (a) in addition to the battery pack resistance (b) and maximum current limits (c) as a function of the battery SoC for a Li - Ion Battery considering different values of capacity (from 4.4 to 39.6 Ah) both in charge and discharge conditions. These experimental characteristics have been provided by the industrial partner of the project.

The battery model is further improved by considering its thermal behavior. The internal electric resistance is considered to compute the amount of dissipated power, while the time

evolution of the temperature is obtained by means of the same model presented for the electric motor, of course considering a different thermal resistance and time constant.

4.2.3   Auxiliary Loads

Several auxiliary loads are present in a vehicle system. Some of them are served by the ICE, connected to its shaft by means of a belt transmission, some others receive the required power directly from the battery installed on board. Generally, the air conditioning compressor, the power steering pump and the alternator are the main accessories connected to the belt drive system and taking part of the FEAD. These auxiliaries are mainly responsible for the additional torque that the ICE should provide, leading to an increase of fuel consumption. Other electrical loads are of a different nature. The main ones can be categorized for example in multimedia, light and body electrical loads.

The accurate modeling of such components can be quite difficult on one side, but also useless if the analysis is performed at a system level. To overcome this issue, the usual approach is to consider the maps of such accessories, analytical or tabulated expressions of their absorbed power and required torque as a function of their rotational speed if, for example, they are connected with the ICE. Similarly, if uncoupled from the ICE, they can be modeled as constant (or variable) power absorptions which discharge the battery.

4.3   Energy Management System

Managing the on - board energy in HEVs means to decide the amount of power that the two (or more) sources of energy have to deliver to the wheels in order to follow a certain driving path.

Generally speaking, the control of HEVs is constituted by two main controllers. A low level controller is responsible for the different energy sources to provide the exact amount of requested power, established by the high level controller. For each time instant, this computes the optimal power split between the sources of energy on - board.

The Energy Management System (EMS) is nothing else than the high level controller. The EMS is basically interposed between the driver and the components' controllers: it receives the required power from the driver to follow a speed profile, and sends to the different actuator controllers the amount of torque that the components should develop.

Different categories of EMS have been proposed in the literature, but the general trend is to distinguish them in two main families:

- Rule - Based Strategies: the power split between the different prime movers is based on rules, which generate at each time instant the control to be realized. Such rules are based mainly on heuristic approaches or on deep knowledge of the process.

- Model - Based Strategies: the actuator set points are obtained through the minimization of a cost function over a fixed and known path.

The optimization of the energy flow on a HEV is not an easy task if potentially high benefits want to be achieved. Model based strategies offer the largest benefits due to their ability to find a solution of the optimization problem for each time instant. Techniques to obtain the solution vary from analytical (Pontryagin's minimum principle [44] - [49], equivalent consumption minimization strategy [50] - [54]) to numerical ones (like dynamic programming [55] - [56] or genetic algorithms [57]). However, they require the exact knowledge of the path to be followed.

Rule based strategies do not involve mathematical procedures to find the solution of the allocation problem, but are mainly based either on the knowledge of the system characteristics, or on heuristic considerations ([58] - [61]). In addition, their application does not require knowledge of the driving cycle. In this work, since the aim is to establish a preliminary framework for the study of the P4 architecture, this kind of technique is considered due to its simplicity and intuitiveness.

Figure 4.2 shows a canonical scheme for HEV control. The EMS, as said, is responsible for the selection of the split between the power sources (ICE and one or more electric motors). In doing this, it receives as inputs different physical variables coming from the electric powertrain (e - PWT), such as the SoC, battery temperature, EM temperatures, maximum admissible battery charge and discharge currents. It is worth underlining that all of these variables can be easily measured or selected apart from the SoC. The battery management system (BMS) has the goal of estimating the state of charge of the battery, based on measurable variables (like the voltages across the cells). The subject of SoC estimation has been widely touched in years in the literature, both regarding vehicle's batteries and mobile phones or electronic components' batteries. However, in this work the battery state of charge is assumed to be known, either via the BMS or via numerical estimations.
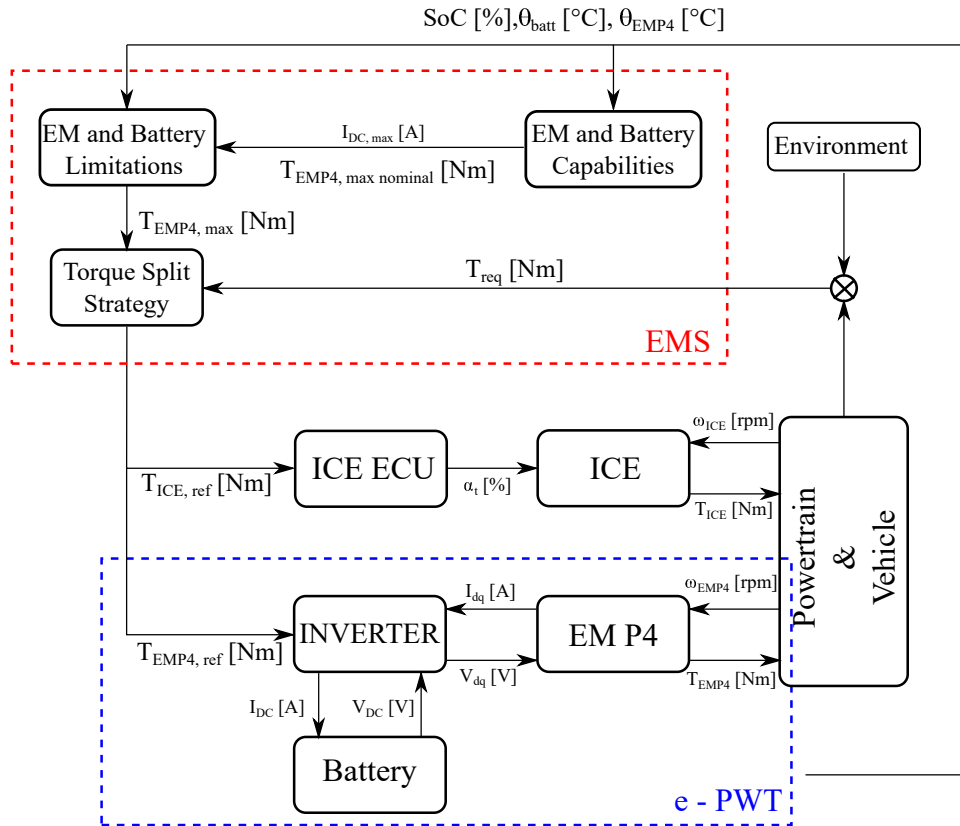
Fig. 4.2 Adopted control scheme for hybrid electric vehicle including higher level controller (EMS) and lower level controller (e - PWT). EM = Electric Motor, ECU = Engine Control Unit.

In the following, the different sub - blocks related to the EMS will be described.

4.3.1 EMs and Battery Limitations and Capabilities

The potential savings related to the installation of an hybrid architecture have been depicted in Chapt. 2 in addition to the amount of energy that can be recovered and therefore used for traction. Those analyses have been conducted in the absence of any kind of limitations related to the electric powertrain, simply considering that all the energy at the electric motor level would be recovered, completely and with unitary efficiency.

It is clear that these assumptions do not suit real components within real world applications. Electric devices always suffer from thermal problems, and in these kinds of applications, in which the continuous operation is almost never realized, the issue is even more serious. In addition, the electric machines present limitations related to their design such as maximum torque, maximum speed and constant power region. Furthermore, the effective operational region of the battery SoC stands between 20/30 and 80/85 %. All of

these limitations have the impact of limiting the maximum available electric traction or braking torques.

The variables entering into the EMS subsystem are:

- SoC [%] - State of Charge

- θ_{EMP4} [°C] - P4 electric motor temperature

- $\theta_{battery}$ [°C] - Battery temperature

- T_{req} [Nm] - Required torque

Based on the actual SoC, the block *EM and Battery Capabilities* computes the maximum admissible DC current I_{DCmax} that can be handled both by the battery and by the electric motor. Maps like those presented in Fig. 4.1c are considered for the battery ($I_{DCmax,b}$) as a function of the selected nominal capacity, while where the electric motor is concerned, the maximum value of absorbed current ($I_{DCmax,EM}$, Fig. 3.26) is considered for each electric motor speed. The comparison is performed based on this criterion:

$$I_{DCmax} = \min \left[I_{DCmax,b} \left(SoC, Q_{nom} \right) ; I_{DCmax,EM} \left(\omega_{em} \right) \right] \tag{4.5}$$

Fig. 3.26 has then been reversed to consider as inputs the electric motor speed and the DC current. In this way, ω_{em} and I_{DCmax} are used to compute the maximum amount of torque that the electric motor can provide given a certain speed and a maximum amount of DC current. This variable is depicted as $T_{EMP4max,nominal}$ and is the main input of the following *EM and Battery Limitations* block.

By means of rules imposed on the aforementioned variables, the limitations related to the electric traction or braking torques are introduced. Such rules are implemented in the control strategy using simple membership functions, which range between 0 and 1. If any of the limitations do not occur, the functions are all equal to 1, allowing the electric motor to produce the required maximum traction or braking torque depending on the operational mode under consideration. If only one limitation is going to take place, the maximum electric motor torque $T_{EMP4max,nominal}$ (positive or negative) is then reduced proportionally to the value computed with the membership function, generating a new variable called $T_{EMP4max}$ (positive or negative). This variable will then enter in the block *Torque Split Strategy*.

Having more than one limitation means limiting the product of the different membership functions output. The membership functions are set up in order to make the electric powertrain work whithin the following ranges:

- SoC: between 30% and 80%. The SoC membership function realizes the statement that the electric battery cannot be used outside its overall working range. To avoid the total discharge, when the SoC is less than 30% the membership function starts to limit the electric motor traction torque, while if equal to 20% the admissible traction torque becomes zero. Similarly, to avoid total charge, from a SoC equal to 80% the membership function starts to limit the electric motor braking torque, but when the SoC reaches 90% avoids the regenerative braking.

- Electric motor temperature: less than 130°C. Based on the electric motor thermal analysis (Sect. 3.6), the thermal parameters have been implemented in the first order thermal model. The electric motor temperature (in particular, the electric motor windings temperature) is checked at each time step and when it reaches 110°C the relative membership function start to limit the electric motor usage, both in traction and in braking conditions. Once the value of 130°C is reached the electric motor cannot be used anymore.

- Battery temperature: less than 60°C. Starting from 50°C the battery temperature membership function limits the electric motor usage until the maximum value of 60°C takes place, meaning of no more electric motor usage.
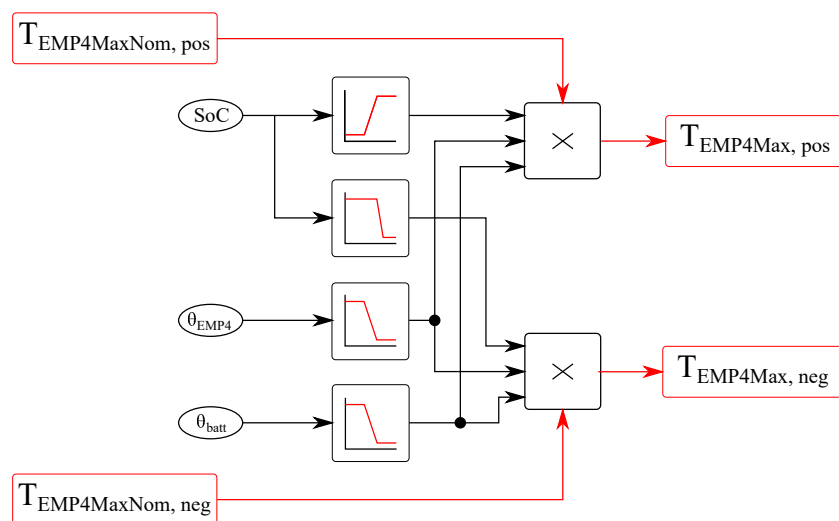
Fig. 4.3 Electric motor and battery limitations scheme.

Figure 4.3 shows the implementation of the limitations related to the electric powertrain usage. Further limitations can be easily added and implemented. As a result, torques $T_{\text{EMP4Max,pos}}$ and $T_{\text{EMP4Max,neg}}$ are obtained.

4.3.2 Torque Split Strategy

The torque split strategy controller is responsible of establishing the correct amount of torque that the different prime movers have to develop in order to let the vehicle follow the prescribed driving cycle.

The P4 hybrid architecture is a non conventional parallel hybrid architecture, in which the connection between the ICE and the electric machine is realized not by mechanical couplers but through the road. This means that both in traction and in braking phases, the electric motor can exploit its optimal position with respect to the road.

Connecting, as an example, the electric motor with the rest of the front powertrain during braking conditions, results in a clear and consistent reduction of the recoverable energy as presented in previous chapters. In addition, since the implementation of the P4 architecture implies small variations to the chassis system, it is therefore worth considering a strategy able to handle these constraints.

The *Simple Hybrid* strategy includes the minimal functionalities of a mild hybrid vehicle: Regenerative braking, full electric start, start and stop.

Regenerative braking is the main functionality of this strategy. It allows storage in the battery of a non negligible amount of energy otherwise wasted during braking phases.

The energy regenerated during braking phases can be stored and used during traction phases or, alternatively, can supply electrified accessories. From this point of view, one idea could be to uncouple the conventional accessories from the FEAD, electrifying them. This would lead both to a reduction of the ICE load and to a higher level of control of the accessories with the goal of reducing useless actuations. Limiting the use of the regenerated energy to allow electric traction only, can lead to interesting advantages related to fuel consumption and emission reductions or to added features as electric urban driving.

In full electric start the electric motor is used to drive the vehicle until a certain speed, to be imposed based on several factors (driving cycle, battery SoC, electric power installed on - board, electric motor capabilities).

Start and stop is an additional feature easily implementable which can lead to the elimination of the idle fuel consumption (in this application, for a 1.4 l SI turbocharged

engine the industrial partner of the project provides 0.64 l/h). Actually, it is not strictly related with the architecture under analysis because the re - start of the engine is not performed with the P4 electric motor. Efficient starters or the presence of the P1f electric motor can allow this feature. It is anyway worth to introduce it as an active part of the Simple Hybrid strategy to evaluate its impact on the consumptions and emission reductions.

The torque split strategy block is constituted of three main steps:

- Definition of the traction and braking required torque. In Sect. 2.2.1 the computation of α_t and β_p has been explained. Both of them are values varying between 0 and 100 (or - 100 in case of braking). The required traction torque at the ground level T_{req} is computed considering the maximum capabilities of the powertrain (conventional and electric) as:

$$T_{req} = \left[T_{ice,max}\left(\omega\right) \tau_{gb} \tau_d + T_{em,max}\left(\omega\right) \tau_{gb,r} \tau_{d,r} \right] \alpha_t \qquad (4.6)$$

where $T_{ice,max}$ and $T_{em,max}$ are the maximum engine and electric motor torques, computed through their torque - speed maps. The throttle position has the goal of partializing the maximum available torque at the ground level.

The required braking torque at the ground level is similarly computed considering the maximum capabilities of the passive brake system and of the electric powertrain:

$$T_{brake,req} = - \left[T_{passive,max} + T_{em,min}\left(\omega\right) \tau_{gb,r} \tau_{d,r} \right] \beta_p \qquad (4.7)$$

where the $-$ sign is introduced to have a requested braking torque as a positive number, $T_{passive,max}$ is the maximum brake torque realizable by the passive brake system and β_p has the goal of partializing the maximum brake torque at the ground level.

- Receiving the traction and braking admissible torque at the electric motor level $T_{EMP4max,pos}$ and $T_{EMP4max,neg}$.

- Torque split computation. The basic idea behind the torque split computation is to give the priority to the electric traction and braking, maximizing its performance. Therefore, whenever any electric mode is active, the front powertrain clutch opens, uncoupling the ICE with the rest of the vehicle.

Based on whether the phase is of traction or braking, the strategy is slightly different:

  - In case of $T_{brake,req} > 0$ (braking phase), the priority is given to the regenerative braking. Given $\tau_{gb,r}$ and $\tau_{d,r}$ the transmission ratios of the rear powertrain as

described in Sect. 2.2.3, the strategy can be summarized as follows. **If**:

$$T_{\text{EMP4max,neg}}\,\tau_{\text{gb,r}}\,\tau_{\text{d,r}} \geq T_{\text{brake,req}} \qquad (4.8)$$

then:

$$\begin{cases} T_{\text{ICE}} = 0 \\ T_{\text{EMP4}} = -T_{\text{brake,req}}/\tau_{\text{gb,r}}\,\tau_{\text{d,r}} \\ T_{\text{b,passive}} = 0 \\ \text{ClutchStatus} = 0 \end{cases} \qquad (4.9)$$

else:

$$\begin{cases} T_{\text{ICE}} = 0 \\ T_{\text{EMP4}} = -T_{\text{EMP4max,neg}} \\ T_{\text{b,passive}} = T_{\text{brake,req}} - T_{\text{EMP4max,neg}}\,\tau_{\text{gb,r}}\,\tau_{\text{d,r}} \\ \text{ClutchStatus} = 0 \end{cases} \qquad (4.10)$$

– In case of $T_{\text{req}} > 0$ (traction phase), the priority is given to the electric traction. **If**:

$$T_{\text{EMmax,pos}}\,\tau_{\text{gb,r}}\,\tau_{\text{d,r}} \geq T_{\text{req}} \qquad (4.11)$$

then:

$$\begin{cases} T_{\text{ICE}} = 0 \\ T_{\text{EMP4}} = T_{\text{req}}/\tau_{\text{gb,r}}\,\tau_{\text{d,r}} \\ T_{\text{b,passive}} = 0 \\ \text{ClutchStatus} = 0 \end{cases} \qquad (4.12)$$

else:

$$\begin{cases} T_{\text{ICE}} = T_{\text{req}}/\left(\tau_{\text{gb}}\,\tau_{\text{d}}\right) \\ T_{\text{EMP4}} = 0 \\ T_{\text{b,passive}} = 0 \\ \text{ClutchStatus} = 1 \end{cases} \qquad (4.13)$$

The last condition is related to the case in which the electric motor maximum torque (positive) is not sufficient to drive the vehicle in pure electric mode. In this case, the hybrid mode (thermal + electric) is not taken into account. This is done with the aim of evaluating the effective performance of this kind of hybrid architecture, without mixing the different working modes. The motivation will also be more clear in next sections (4.4.2, 4.4.3), in which the design of the energy storage system will be analyzed. In case no limitations

regarding the battery SoC, its temperature or the electric motor temperature take place, whether the electric motor can provide the torque to drive the vehicle along the driving cycle, the mode is pure electric. Oppositely, if for any reasons the electric motor cannot provide the required torque to the wheels, it is switched off and the traction is demanded from the thermal engine. In addition to this control scheme, Sect. 4.4.3 will introduce an additional constraint related to the pure electric mode regarding the vehicle speed below which the electric motor could effectively provide torque. The motivations are further explained.

Finally, it should be noticed that in almost all the working modes the clutch status is supposed to be zero, meaning disengaged clutch. This is in line with the idea of giving the priority to the electric traction or braking, maximizing its performance. Of course, a manual transmission is not suitable for this kind of architecture, in which, instead, an automatic transmission (AT), a dual clutch transmission (DCT), or an automated manual transmission (AMT) should be used.

4.4   Design Optimization of the Electric Battery

The energy storage system (ESS) is the main subsystem installed on a hybrid electric vehicle. Depending on the typology of the architecture, it allows the realization of particular working modes as well as the storage of the energy for future driving. The design of the ESS is of fundamental importance when dealing with hybrid vehicles, especially because of its main parameters: power and capacity. The former is mainly dependent on the path that the vehicle should follow in electric or hybrid mode, the latter, that basically is the integral of the battery current over a certain cycle time, is strictly dependent on the autonomy that the vehicle can offer both in pure electric and in hybrid mode.

The design of the battery pack for the hybrid architecture under analysis is fundamental because it represents an intermediate configuration between a micro hybrid (engine assistant mode only) and a full hybrid (pure electric mode for the most of the cycle time). As said, the main functionality or, more clearly, the main goal of this architecture of hybrid vehicle is regenerating the maximum amount of energy. The need of understanding which battery size would be optimal to 1) recover most of the available energy, 2) reach the lowest fuel consumption and 3) introducing the smallest amount of mass is therefore of fundamental importance.

A summary of battery sizing methodologies available in literature can be subdivided as a function of the hybrid architectures they are applied to:

- Hybrid electric vehicles. Hofman et al. [62] analyzed different hybrid vehicle architectures to find the optimal configuration and size of the energy storage system. The main design variables involve vehicle mass, volume, cost and efficiency, varied as a function of the configurations by means of scaling coefficients and summed to form an objective function to be minimized. In [63], a dynamic programming technique is applied to overcome the influence of the control strategy. Scaling factors are applied to the ICE, electric motor and battery power to analyze different rates of hybridization. Several full and torque split hybrid powertrains are considered. An optimal sizing methodology for torque split mild hybrid powertrain components is studied in [64], in which dynamic programming is compared to a simple rule based strategy. The results of optimal hybridization ratios obtained through the two techniques are very similar.

- Plug - in hybrid electric vehicles. Tara et al. [65] studied the possibility to extend a hybrid electric vehicle to a plug - in hybrid by adding an external battery to an existing one. Based on different rules and assumptions implemented in the energy management strategy of the vehicle, an optimal size of the additional battery is obtained. NiMH technology is found to be the best compromise between vehicle performance and battery cost and volume. In [66] and [67] the electric battery sizing law is based on the full electric driving range while in [68], convex optimization is applied to minimize objective functions composed by operational and component costs.

- Fuel cell vehicles. In [69] and [70] dynamic programming is used to minimize cost functions. The influence of regenerative braking energy on the battery size is studied considering different constant conversion efficiencies during braking phases. The analysis shows the influence of driving cycles and control strategy on the battery sizing.

In this section the electric battery sizing for a mild hybrid electric vehicle will be carried out considering different methodologies that do not involve numerical optimizations. First, the maximum amount of recoverable energy over different driving cycles will be analytically computed to establish a reference value, obtainable in the absence of any kind of powertrain losses. This value would give a first input to the battery sizing in case of complete and perfect regeneration. A second analysis is then carried out as a sensitivity of the battery capacity on the fuel consumption. Considering the simple torque split strategy presented in Sect. 4.3.2, the vehicle runs in pure electric mode until a certain vehicle speed, allowed by the e - powertrain limitations. Provided to guarantee the equilibrium between

recovered and used energy, the fuel consumption is compared for the different battery sizes. A more refined design methodology is finally presented, including the effects of maximum electric traction speed, initial battery state of charge and capacity.

4.4.1   Battery Sizing: Maximum Recoverable Energy over a Cycle

To compute the maximum recoverable energy over a cycle, recall the equation of motion of a point mass subjected to inertia and resistant forces in which F_{tract} is the traction force:

$$F_{\text{tract}} = F_{\text{pwt}} - F_{\text{brake}} = F_{\text{kin}} + F_{\text{aero}} + F_{\text{roll}} + F_{\text{grade}} \tag{4.14}$$

where F_{kin} is the inertia force due to acceleration and mass of the vehicle, F_{aero} is the aerodynamic resistance, F_{roll} is the rolling resistance and F_{grade} is the resistance to the motion due to the road grade. Resistance forces can be merged in a unique term, F_{res}, without differentiating between its contributions. By multiplying left and right terms by the velocity and integrating them over the cycle duration, the energy balance is obtained:

$$E_{\text{tract}} = E_{\text{kin}} + E_{\text{aero}} + E_{\text{roll}} + E_{\text{grade}} = E_{\text{kin}} + E_{\text{res}} \tag{4.15}$$

At this point, it is convenient to separate the energy computation in acceleration and deceleration phases. With the superscript $+$ the energies in acceleration phases are represented, while those in deceleration are identified with the superscript $-$. It is worthwhile to underline the presence of coasting decelerations and their implications: while the deceleration is very low, it could actually be realized only considering the resistances to motion, thus eliminating the possibilities to recover the energy.

Provided that the kinetic energy net variation over the cycle is zero (i. e. $E_{\text{kin}}^{-} = \text{-}E_{\text{kin}}^{+}$), and that in case of acceleration phases the amount of energy delivered by the powertrain is:

$$E_{\text{pwt}}^{+} = E_{\text{kin}}^{+} + E_{\text{res}}^{+} \tag{4.16}$$

during deceleration phases the vehicle needs to dissipate the entire amount of kinetic energy accumulated during the tractive phases (E_{kin}^{+}). To this end, resistant forces can contribute, therefore reducing the potential amount of energy regeneration. The amount of potential energy regeneration during braking phases is the total vehicle kinetic energy accumulated during the traction phases, less the overall resistance to motion during braking:

$$E_{\text{reg,pot}} = E_{\text{kin}}^{+} - E_{\text{res}}^{-} \tag{4.17}$$

In addition, it is possible to compute the influence that each energy contribution has on the total required energy to move the vehicle:

$$E_{\text{kin}\%} = \frac{E_{\text{kin}}^+}{E_{\text{pwt}}^+}; E_{\text{res}\%} = \frac{E_{\text{res}}^+}{E_{\text{pwt}}^+} \tag{4.18}$$

and the percentage of recoverable energy computed with respect to the kinetic energy accumulated during acceleration phases:

$$E_{\text{reg}\%} = \frac{E_{\text{reg,pot}}}{E_{\text{kin}}^+}; \tag{4.19}$$
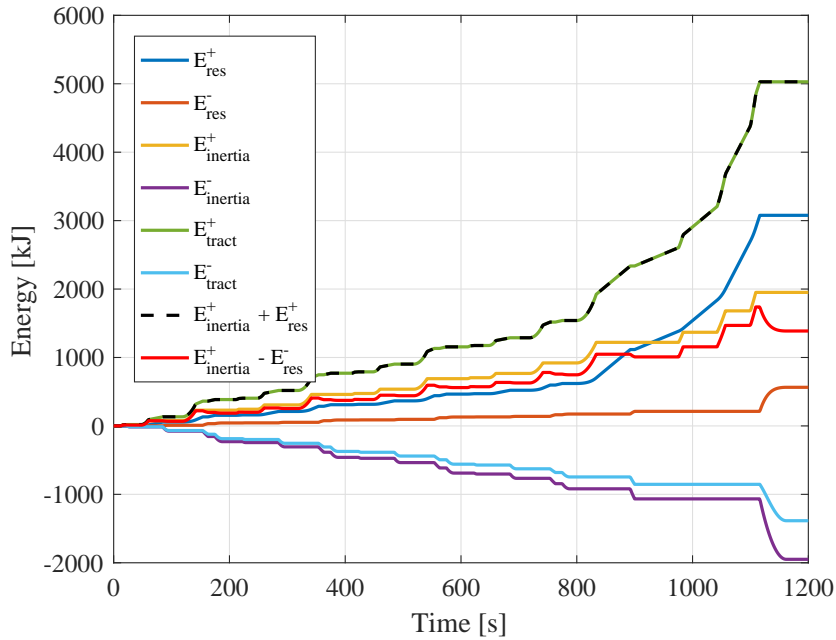
Fig. 4.4 Different energies over a NEDC cycle.

Figure 4.4 shows the time history of the different energies over a pure ICE NEDC driving cycle. Where the sizing of the electric battery is concerned, of particular interest would be the amount of energy that potentially can be recovered and, therefore, stored. It is true that Eq. 4.17 gives the amount of potential energy recovered and does not take into account that this energy would be somehow re - used for the traction phases or cannot be stored in the case of a too high state of charge. However, in this section the regenerative braking potential of the main driving cycles will be highlighted together with their implications on battery sizing. Therefore, the sizing is performed based on the assumption that all the available recoverable energy can be stored.

Based on the potential recoverable energy over the different driving cycles analyzed, the battery capacity can be computed:

$$Q = \frac{E_{\text{reg,pot}}}{3.6 V_{\text{DC}}} \tag{4.20}$$

where the energy is expressed in kJ and V_{DC} is the nominal battery voltage.
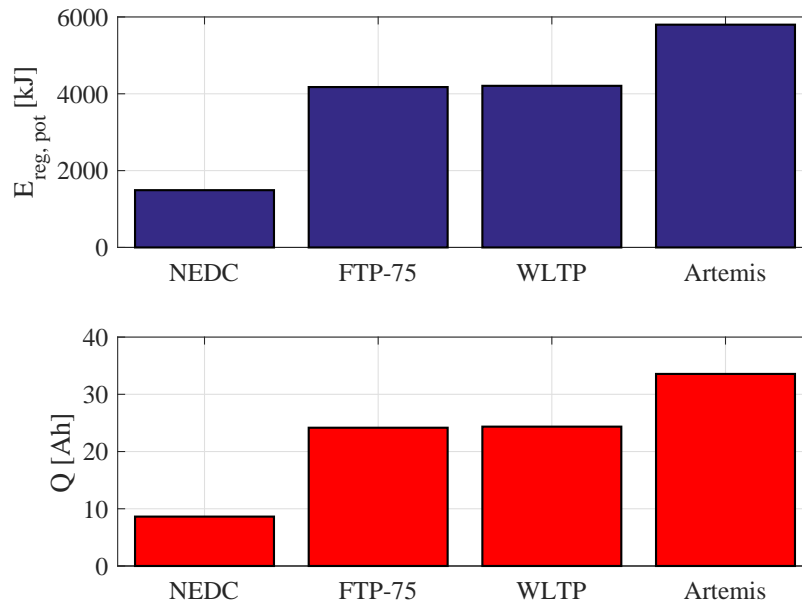
Fig. 4.5 Influence of the different driving cycles on the potential recoverable energy and on the battery sizing.

Figure 4.5 shows the influence of the different homologation cycles on the potential recoverable energy and on the theoretical dimensions of the electric battery. NEDC presents the lowest amount of recoverable energy due to low average speed and decelerations. Thus, designing the electric battery based on this cycle theoretically means considering a very small battery capacity (lower than 10 Ah). Moving to more realistic driving cycles, the FTP and WLTP cycles present higher potential recoverable energy, therefore increasing the required battery capacity to store all the available energy. Finally, the Artemis cycle is the strongest one considered for the analysis, comprehensive of its urban and extra urban part. The potential recoverable energy is very high due to the large amount of kinetic energy stored in traction phases. In this case the theoretical battery capacity exceeds 30 Ah.

It is again worthwhile to underline that these values of battery capacity are only indicative. They consider a situation in which the vehicle runs over the cycle starting

with a fully discharged battery, and reaches the end with a fully charged one, without re - using the stored energy. In addition, the first approximation sizing here presented does not take into account for any losses present in the powertrain. Transmission efficiencies and electric motor conversion efficiency do actually play a significant role in the overall energy recuperation. With these assumptions it is clear that the described design methodology would lead to a consistent oversizing of the energy storage system, with direct implications on the added mass.

4.4.2 Battery Sizing: Effect of e - PWT Limitations and Battery Capabilities

A more refined analysis regarding the battery sizing is now described. In this case the analysis is performed based on the vehicle model described in Sect. 2.2, on the torque split strategy proposed in Sect. 4.3.2, accounting for all the electric powertrain limitations and considering the electric motor designed in Chapt. 3. In such way, it is possible to show the influence of the battery capacity on the actual recoverable energy, comparable to the theoretical one computed in the previous section.

For the sake of consistency with the analysis presented in Sect. 4.4.1, the hybrid architecture is allowed to exploit the maximum amount of recoverable energy from the cycle. This is realized in practice by leaving the vehicle to run in pure electric mode until any of the electric powertrain limitations take place. The maximum electric traction speed is therefore not constant and varies along the cycle, but the regeneration is always allowed.

The four driving cycles previously analyzed will still be considered. To guarantee the battery state of charge equilibrium, three cycles (one after the other) are simulated. The results in terms of energy are obtained as a difference between the energies (recovered and consumed) at the end of the last cycle and the same energies at the end of the previous one.
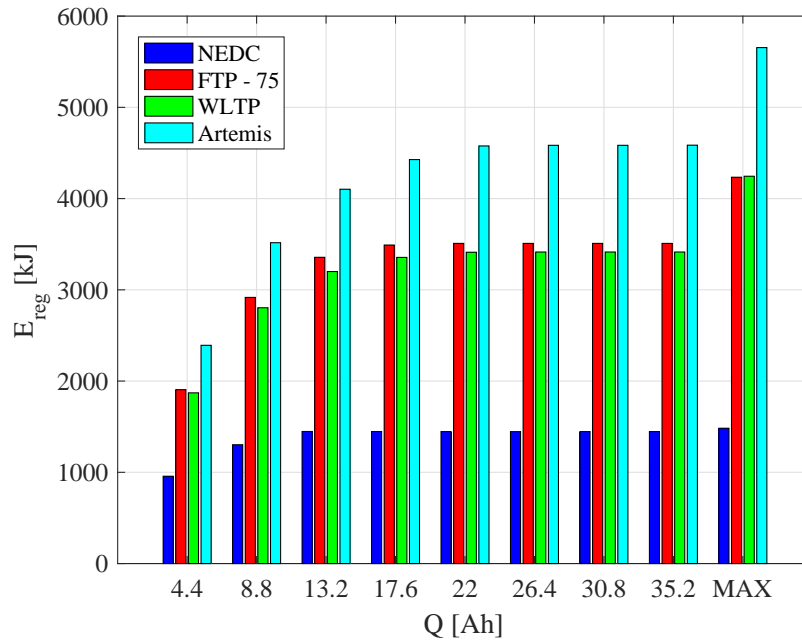
Fig. 4.6 Effect of the battery capacity on the actual recovered energy along different driving cycles. The bars labeled with MAX are relative to the recovered energies computed through the method presented in Sect. 4.4.1.

Figure 4.6 shows the actual recovered energy E_{reg} compared with the maximum exploitable by the driving cycle (MAX, Sect. 4.4.1) as a function of the battery size for the same driving cycles previously analyzed. The increase of the battery capacity allows a higher energy storage, which anyway presents a saturation. Even though a large battery size is considered (as in the case of 35 Ah) the energy that the electric powertrain is able to recover is inevitably constrained by its own limitations (e. g. efficiencies, temperatures, maximum currents). This gap is only dependent on the characteristics of the physical components. By converse, the reduction of the battery capacity leads to a reduction of the actual recoverable energy due to, instead, the reduced capabilities of the battery itself to recover energy.

An interesting consideration comes from the considered driving cycle. It is shown that if the NEDC cycle is taken into account, even a low battery size is able to recover almost all the available energy from the cycle itself. The same battery can be instead completely undersized if stronger and more critical (rather than realistic) driving cycles such as the WLTP are under analysis. Therefore, the choice of the cycle is strictly important for the correct electric powertrain design, and analyzing "light" test procedures could lead to strong underdesign of the energy storage system.
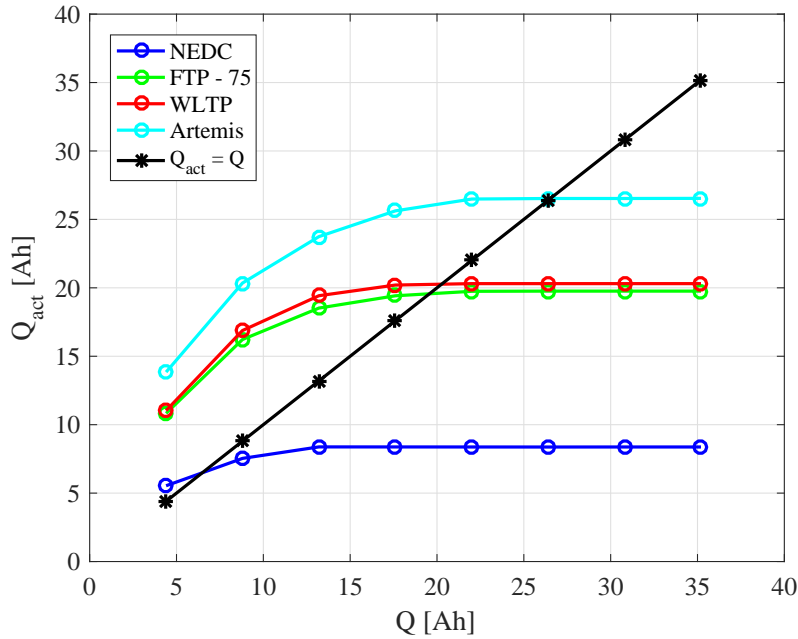
Fig. 4.7 Recovered energy along the cycle (expressed in Ah) as a function of the different capacities considered.

The amount of recovered energy for each cycle and for each battery size under analysis can be translated into an energy expressed in terms of [Ah], having the meaning of actual exploited capacities Q_{act}. They are plotted in Fig. 4.7 as a function of the nominal capacities considered. As an example, if a point with $Q = 4.4$ Ah and $Q_{act} \approx 10$ Ah for the WLTP cycle is considered, even though the nominal battery capacity is 4.4 Ah the recovered energy over the cycle is more than twice this value. This means basically that during the cycle the battery was charging and discharging more than two times.

If the line $Q_{act} = Q$ is plotted also, it is clear that the points of actual capacities standing above such line ($Q_{act} > Q$) are relative to conditions in which the battery charges and discharges more than one time per cycle. By converse, the points standing on the line are relative to conditions in which the battery charges a quantity of energy that is the exact amount of the considered battery size ($Q_{act} = Q$). From Fig. 4.7 it is shown that after the equality point the energy actually recovered does not increase anymore. It can be stated that such point is the minimum required battery size which allows to recover the maximum amount of energy from the cycle.

Finally, it is worthwhile to underline that charging or discharging phases are compliant with the battery characteristics and limitations as presented in Sect. 4.3.1.
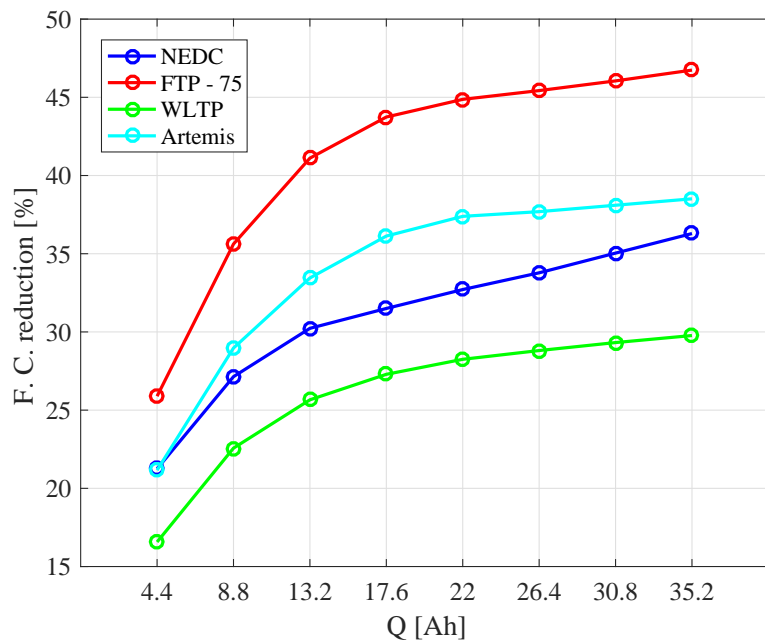
Fig. 4.8 Fuel consumption reductions with respect to normal production ICE powered vehicle (data not reported for confidentiality reasons).

Figure 4.8 presents the fuel consumption percentage reductions with respect to the normal production ICE powered vehicle consumptions (not presented for confidentiality reasons) as a function of the different battery nominal capacities. The percentage reductions follow the same trend relative to the recovered energy, i.e. a saturation when the increase in capacity takes place.

Although the presented methodology for battery sizing displays the potential fuel consumption reductions and the influence of the capacity on the total recovered energy, underlining the importance of considering realistic mission profiles for real driving conditions, it shows unrealistic working modes for the electric battery. As a matter of fact, if any limit to the maximum electric traction speed is considered, it is clear that along the cycle the battery state of charge is always decreasing until it reaches (and maintains) its minimum value.

Figure 4.9 presents this kind of unrealistic working condition for the case of the WLTP cycle and a battery size of 22 Ah. The cycle is in equilibrium (initial SoC equals final SoC, energy recovered equals the energy consumed) but due to the unconstrained electric traction usage, the battery SoC stabilizes around its minimum. Such a strong and uncontrolled condition of work could lead to reductions of the battery life.
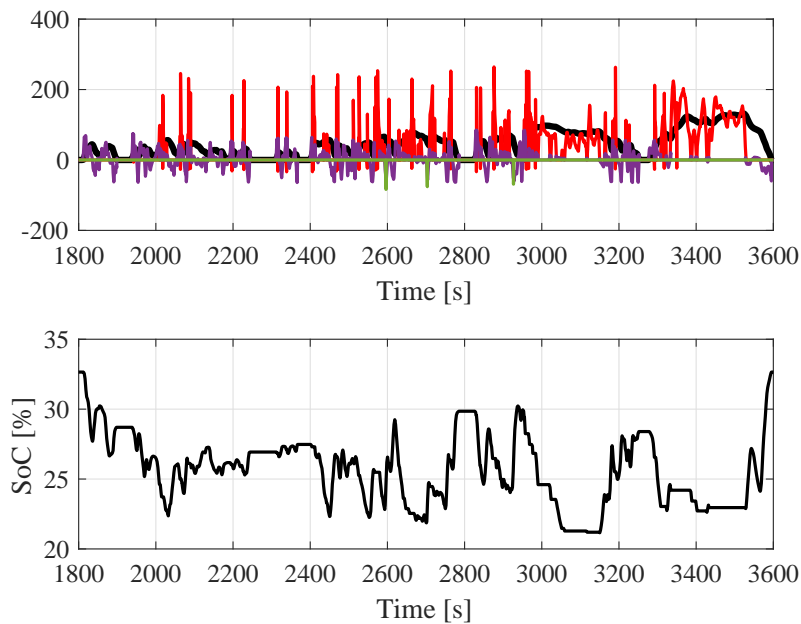
Fig. 4.9 Top: time history of velocity (black), ICE torque (red), EMP4 torque (magenta), passive brakes (green) during a WLTP cycle. Bottom: time history of the battery SoC during the same cycle.

To this end, a third methodology is considered and takes into account both the energy recovery phases in addition to those of traction.

4.4.3 Battery Sizing: Effect of Electric Traction Maximum Speed

Based on the results presented in the previous section, the battery size affects the maximum recoverable energy over a cycle due to its effective capabilities (i.e. charge and discharge velocity, admissible currents) and it is possible to find a size compliant with the need of recovered energy maximization and minimization of the added mass.

However, if the electric traction maximum speed is not controlled, the electric motor will always provide power to the wheels during the starting phases of the vehicle until any of the limitations considered in Sect. 4.3.1 take place, which bring the electric motor available torque to be smaller than the required one. When this happens, recalling Sect. 4.3.2, the electric motor is switched off and the traction is provided by the ICE.

It is clear that this kind of strategy always brings the battery to function about its minimum allowed working conditions with clear implications on its life. This section

investigates the influence that a controlled usage of the electric motor during traction phases has on the recoverable energy and on battery sizing.

Different vehicle speed limits have been considered in the analysis. It is of high importance to underline that during the simulations, whenever such speeds are reached, the electric motor torque is set to zero and the required torque to let the vehicle follow the speed profile is provided only by the ICE. In addition, considering a triplet constituted by a driving cycle, a selected maximum electric traction vehicle speed $V_{\mathrm{max,PE}}$ and a battery capacity, in case that the selected vehicle speed is so high that the battery SoC reaches the minimum (Sect. 4.3.1), the simulation is stopped and the value of recovered energy for this triplet is not considered. This is done to avoid misunderstandings in the interpretation of the data because a too low SoC would lead to a not guaranteed selected vehicle speed.
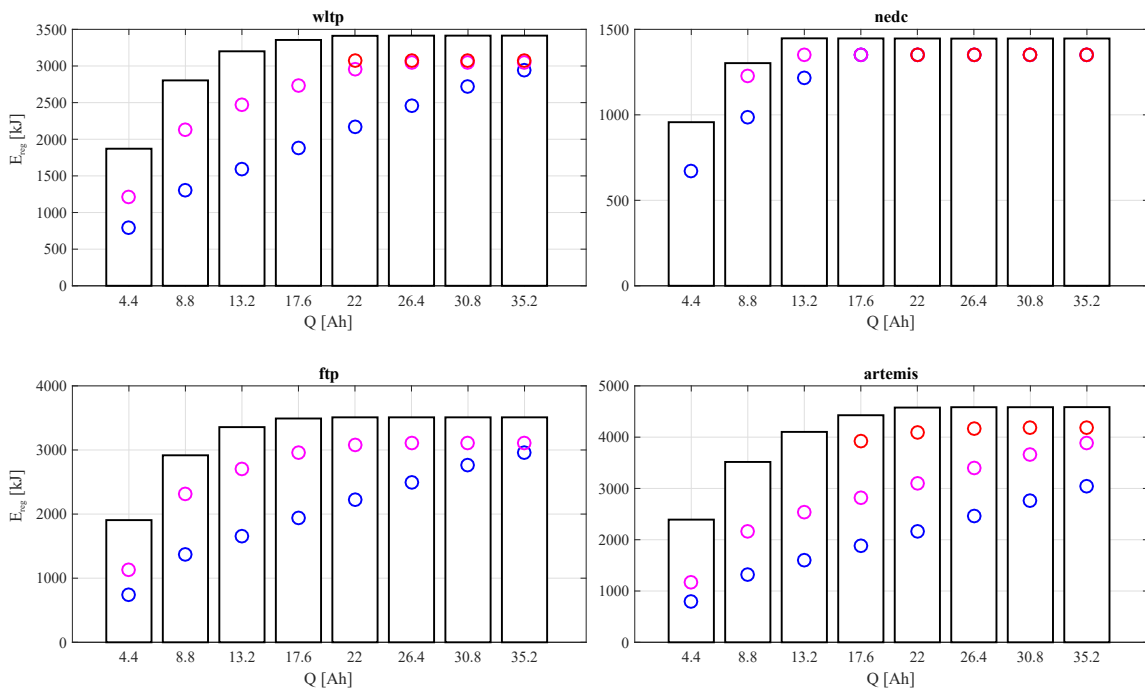
Fig. 4.10 Effect of the maximum electric traction speed on the recovered energy vs. battery capacity over different driving cycles. Bars: Energies computed from Sect. 4.4.2, blue circles: $V_{\mathrm{max,PE}} = 20$ km/h, magenta circles: $V_{\mathrm{max,PE}} = 30$ km/h, red circles: $V_{\mathrm{max,PE}} = 40$ km/h. $SoC_0 = 50$ %.

Figure 4.10 presents the sensitivity analysis of the maximum electric traction vehicle speed on the recovered energy as a function of the selected battery capacity for the four driving cycles previously considered. The white bars refer to the actual recovered energies in the absence of speed limits (Sect. 4.4.2). If too low, the vehicle speed has the main influence of reducing the recovered energy. This fact is clear because if any speed limitations are imposed during braking phases, a continuous charging of the battery pack

with a small amount of discharge phases takes place. The recovered energy is low in the case of a low battery size, but tends to a saturation point, as evidenced in case of NEDC cycle for example.

Oppositely, in case of higher electric traction speed, the battery charges but consistently discharges too, leading to failure to achieve completely charged pack. Similarly, some points are not included in the plots because of the achievement of the minimum battery SoC during the cycle.

The recovered energy seems to depend on the battery capacity only if the electric traction speed is relatively small, leading to a linear like dependency. Whenever the consumed energy is consistently lower than the recovered one, the battery always results to be saturated, forced to work above its own maximum limitations. When increasing the traction speed, the consumed energy directly increases, with the consequence of a gradual increase in the recovered energy, even when considering the same battery size. This is explained by the fact that if the electric traction speed becomes higher, there are less possibilities for the battery to reach its full charge.

Beyond a certain speed, the minimum SoC can be reached by the battery. In case this happens, the working point under analysis is not considered due to the impossibility to guarantee the same maximum electric traction speed for all the cycle. However, with an increase in battery size, the recovered energy seems to reach the maximum admissible, as shown by the red circles, clearly due also to a consistent consumed energy during the cycle.

The presented analysis had the goal of underlining the influence of the battery characteristics on the regenerative braking potential and how the electric traction capabilities are affected by the two aforementioned parameters. It is clear that the presented results are valid if and only if the initial state of charge (SoC_0) is the one considered during the simulations (50 %). Values differing from the mentioned one cause different results and different trends of the energies.
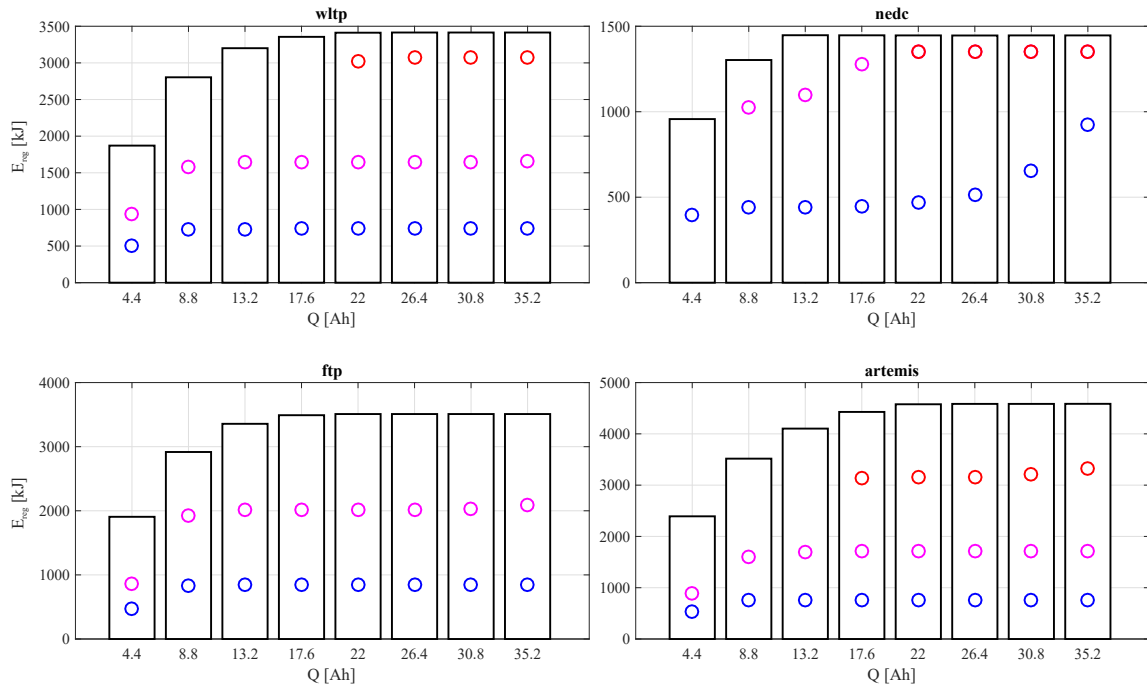
Fig. 4.11 Effect of the maximum electric traction speed on the recovered energy vs. battery capacity over different driving cycles. Bars: Energies computed from Sect. 4.4.2, blue circles: $V_{\text{max,PE}} = 20$ km/h, magenta circles: $V_{\text{max,PE}} = 30$ km/h, red circles: $V_{\text{max,PE}} = 40$ km/h. $SoC_0 = 70$ %.

As an example, Fig. 4.11 presents the values of the recovered energies considering a different (and higher) SoC_0. The results are somehow close to those of Fig. 4.10 only in the case of a high speed of electric traction (as in WLTP and NEDC). For lower speeds of transition between electric and ICE traction, the effect of starting the cycle with a higher SoC_0 is that of having reduced the recovered energy.

The SoC_0 is a fundamental parameter that affects the regenerative/traction performance of the system and therefore the potential fuel consumption reduction. Just thinking to start the driving cycle with the battery pack fully charged or fully discharged leads to two completely different situations. Despite its importance, unfortunately the SoC_0 is not aprioristically known. Due to the clearly different utilization of the vehicle in real life with respect to the standard driving cycles, it is therefore not possible to know a priori which will be the initial state of charge of the battery whenever the vehicle is switched on, also because the vehicle under analysis is not a PHEV. Therefore, since both the design optimization of the energy storage system and the control strategy itself cannot be strictly dependent on this parameter, the easiest way to handle this issue is to study the sensitivity of the initial state of charge on the energy recovered or consumed.

As already mentioned, the state of charge is universally recognized as the state to check the status of the battery in terms of amount of energy storable or usable. Almost all the control strategies for hybrid vehicles are mainly based on the state of charge knowledge and, being not directly measurable, much effort has been spent regarding its estimation.

Focusing on battery design issues, it should be more convenient to translate the initial state of charge into an initial energy contained in the pack (E_0). Speaking about an initial state of charge of 50 % avoiding any specification regarding the capacity is like saying that the tank of a vehicle is 50 % full of fuel without actually knowing how much fuel is contained inside and, therefore, without knowing the distance that could actually be travelled. From now on the variable of interest for the design procedure will be anyway the initial state of charge, but it should always be kept in mind that in declaring the initial state of the battery, its actual capacity should also be mentioned.

Figures 4.10 and 4.11 suggest the need of a different analysis that takes into account both the recovery and the use of the energy for traction. Following the analysis performed in Sect. 4.4.2, the idea can be that of finding an optimal battery size that allows to make the system work in an equilibrium condition (recovered energy equals the consumed one) but knowing the maximum electric traction speed that realizes it.

(a) $SoC_0 = 50$ %. (b) $SoC_0 = 70$ %.
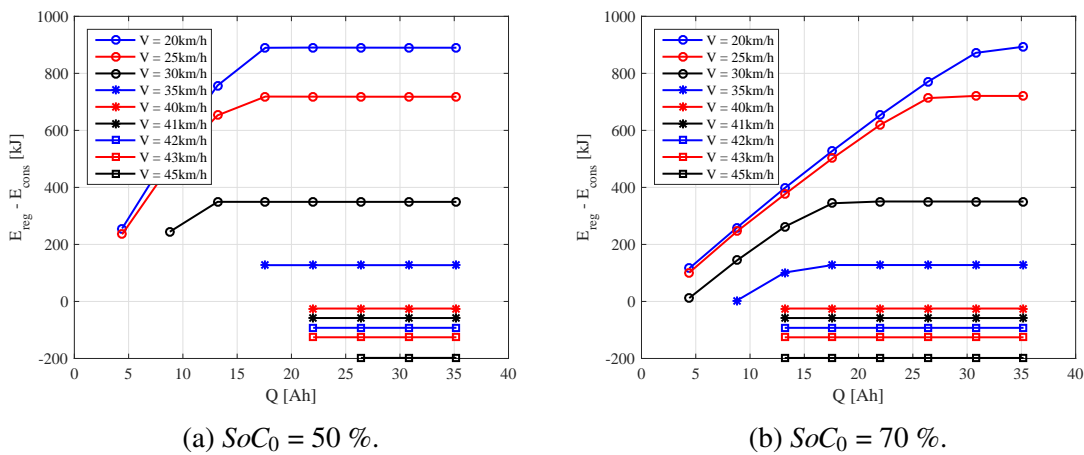
Fig. 4.12 Difference between recovered and consumed energy over an NEDC cycle as a function of the battery capacity for different maximum electric traction speeds considering $SoC_0 = 50$ % (a) and $SoC_0 = 70$ % (b).

Figure 4.12 presents the difference between recovered and consumed energy (from now on called ΔE) over a NEDC cycle as a function of the battery capacity for different maximum electric traction speeds in the case of different values of SoC_0. For the sake

of clarity, the motivation why only particular values of capacity have been considered is related to the characteristics of the single cell (see Sect. 4.2.2).

With reference to the lines related to a low electric traction speed (e. g. 20 km/h, blue circle marked), it is shown that ΔE increases with the battery capacity. Since the consumed energy over these lines is the same, the increment is only due to the rise of the effective storable energy. Above a certain size, ΔE remains almost constant because the battery is in the fully charged condition. In addition, the influence of the initial state of charge is clearly visible. The lower the SoC_0, the smaller the battery size that allows the charge saturation, while a higher SoC_0 delays the battery charge saturation to higher sizes. The driving cycle, in these conditions, is started with an already charged battery and so the potential of energy recovery is strictly reduced.

Whenever the speed of electric traction is increased, ΔE reduces due to the increase of the consumed energy. Considering as an example the lines corresponding to a speed of 35 km/h (blue asterisk marked), the influence of the initial state of charge is the achievement of the energetic equilibrium with a smaller battery size when the SoC_0 is high (b). This happens since, again, the battery is already quite fully charged and the energy that can be recovered is exactly equal that spent, considering the imposed electric traction speed.

Finally, when considering the lines related to a speed of 40 km/h (red asterisk marked), ΔE points have values slightly lower than zero. Supposing that these points are energy balance points, a higher initial state of charge allows them to extend to lower battery sizes. The motivation is again related to the initial amount of charge contained in the battery. It is clear that for equal consumed energy, a battery with lower capacity discharges faster than a battery with higher capacity. If the battery is more charged at the beginning of the driving cycle, even considering a lower capacity, the vehicle is able to follow the prescribed cycle, avoiding the limitation of the minimum SoC.

Considering a driving cycle, each of the points present in Fig. 4.12 is named p and is characterized by a capacity, an initial state of charge, a maximum electric traction speed and difference between recovered and consumed energy:

$$p = (Q, SoC_0, V_{\mathrm{max,PE}}, \Delta E) \tag{4.21}$$

The points of equilibrium are points in which the recovered energy equals the consumed energy and are characterized by a value of $\Delta E = 0$. Therefore, assigning the superscript * to such values, it is found that:

$$p^* = \left(Q^*, SoC_0^*, V_{\mathrm{max,PE}}^*\right) \tag{4.22}$$

which means that each equilibrium point is characterized by a certain value capacity, initial state of charge and maximum electric traction speed. Thus, focusing on equilibrium points only, it is possible to understand the interactions occuring between the battery size, the initial state of charge and, as a consequence how the maximum electric traction speed varies or interacts between the two.

Several simulations have been performed considering a dense range of maximum electric traction speeds, selecting an interval of possible SoC_0 variable between 40 and 70 %. The same previous values for the battery capacities have been considered, spanning between 4.4 and 44 Ah.

Given a certain driving cycle, if the focus is on equilibrium points only, this allows one to study the influence of the battery initial state of charge on the battery size that allows said equilibrium. As a consequence, the values of the maximum electric traction speed to achieve the equilibrium are also obtainable. In this way, many possible initial working conditions of the battery pack are analyzed and the optimal size that satisfies the equilibrium conditions can be found, comparing different driving cycles too.
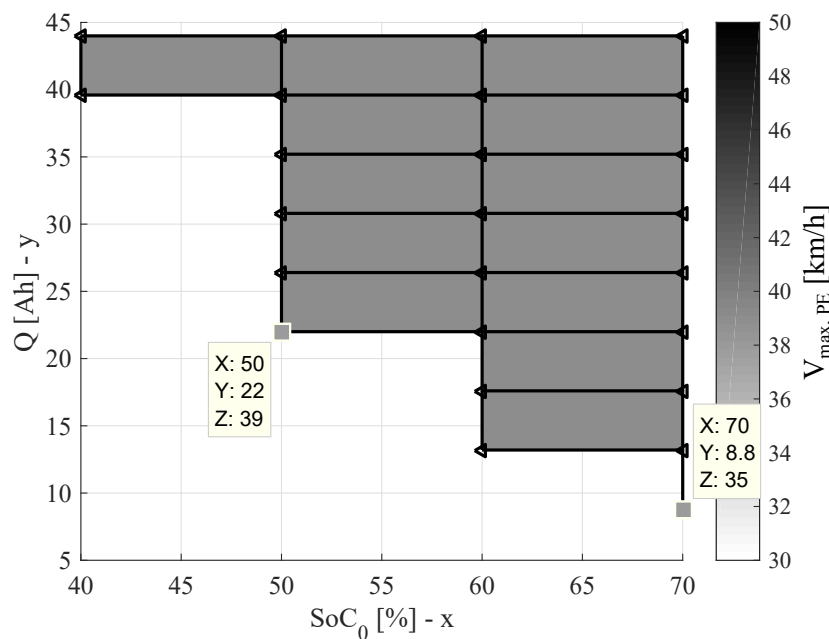
Fig. 4.13 Sensitivity analysis regarding the influence of the battery capacity and the initial state of charge on the maximum electric traction vehicle speed that guarantees the energy balance. NEDC cycle.

Figure 4.13 presents a sensitivity analysis regarding the use of the electric energy (control parameter: $V_{\text{max,PE}}$) on the achievement of the energetic equilibrium (ΔE) as

a function of the characteristics of the electric powertrain (parameter: Q) for different working conditions in which the vehicle can start to work (parameter: SoC_0). The actual initial state of the battery charge plays a fundamental role in the definition of the battery size. Statistical analysis can be experimentally performed, trying to estimate an average value of the SoC_0 for many different cycles, based on which the battery should be designed. This issue is, however, out of the scope of this work, but the intention is that of giving some design hints, regardless the real world data.

The initial battery state of charge reduces the required capacity to obtain an equilibrium state whenever it is high, which means anyway lower than its maximum allowable (based on the technology). The higher the SoC_0, the lower the battery size can be to allow this equilibrium state. Provided that the energy consumed for the electric traction is maintained as constant, this is demonstrated by the fact that if, at the beginning of the cycle, the battery is consistently charged, it has basically a larger working range before reaching its minimum state of charge. Therefore, to achieve the equilibrium, in these conditions its size could even be smaller than that of a battery that is low charged when the cycle starts.
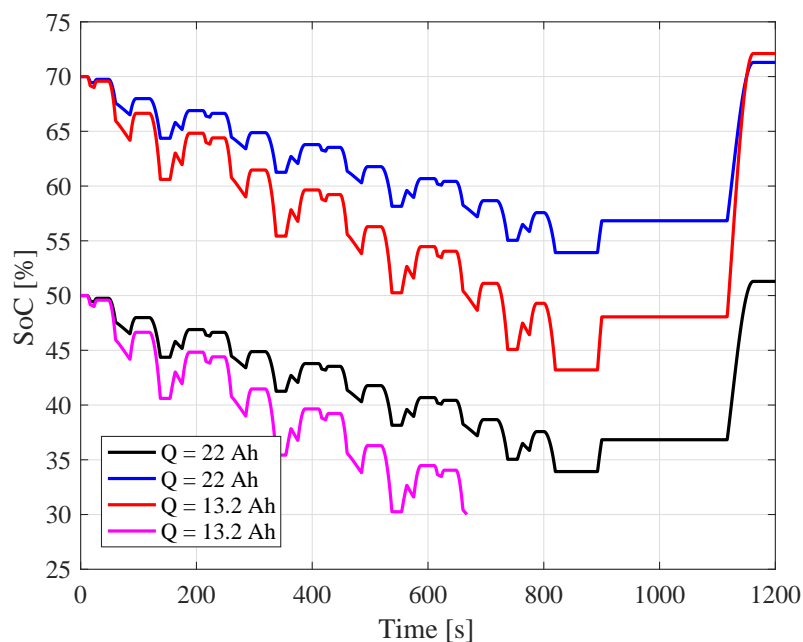
Fig. 4.14 Battery capacity influence on the battery state of charge along a NEDC cycle considering the same consumed energy for all the simulatons ($V_{\text{max,PE}} = 39$ km/h).

Figure 4.14 explains more clearly the aforementioned statements. All the simulations have been conducted considering a maximum electric traction speed of 39 km/h to have a constant consumed electric power and energy. The energetic equilibrium (when it can be

realized) is satisfied apart from the very small difference between initial and final SoC (on the order of 1%). Considering a capacity of 22 Ah, the equilibrium is found regardless the SoC_0. When switching to a lower capacity, the battery does not reach its minimum charge only in the case of $SoC_0 = 70\%$. This explains the results in Fig. 4.13, and what has been previously mentioned.

Clearly speaking, in case that the average initial state of charge is very low a large capacity is then required to always guarantee a condition of energy balance.

Proceeding with the other three driving cycles previously considered, the same analysis can be carried out. In this way the battery size able to satisfy the energy balance for all the cycles can be therefore found.
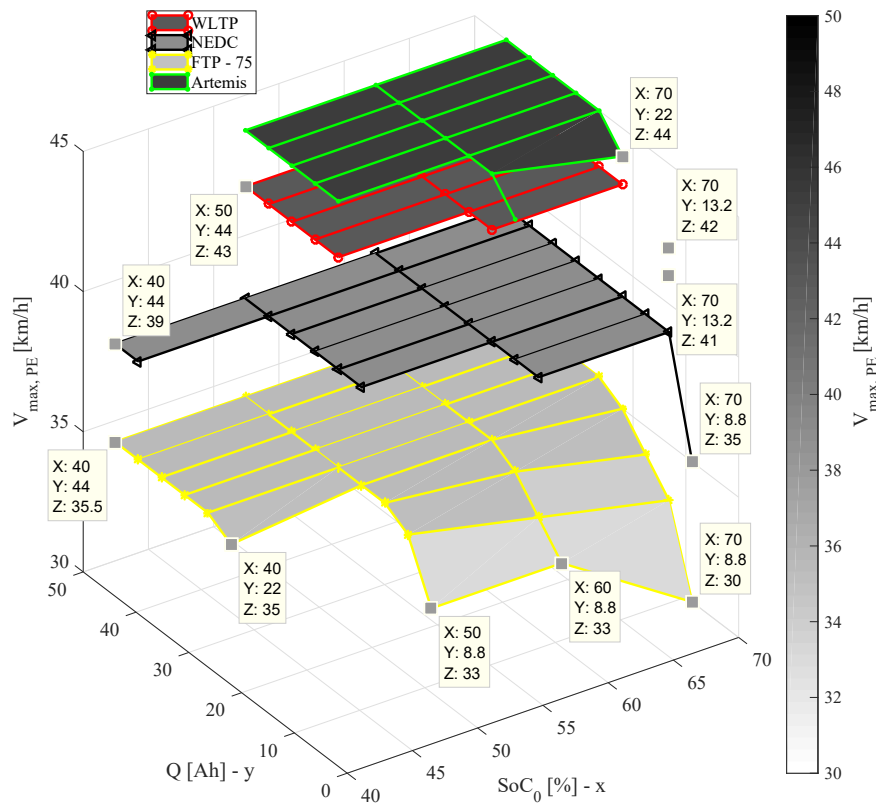
Fig. 4.15 Sensitivity analysis regarding the influence of the battery capacity and the initial state of charge on the maximum electric traction vehicle speed that guarantees the energy balance. Different driving cycles.

Figure 4.15 presents the sensitivity analysis regarding the influence of the battery capacity and the initial state of charge on the maximum electric traction vehicle speed for energy equilibrium in the four driving cycles considered. As already shown, if the initial state of charge is high, the battery capacity that guarantees the energy balance could be small (between 8 and 20 Ah) while, oppositely, if the average initial state of charge is low (between 40 and 50 %), the capacity must increase. Regarding the maximum electric traction vehicle speed, it clearly depends on the considered driving cycle, but tends to decrease in the case of high initial state of charge, due to the reduction of the required capacity.

Finally, the analysis suggests the need of evaluate a limited range of initial battery state of charges (based on statistical analysis of experimental data) in addition to the most representative driving cycles in which the hybrid vehicle is going to function. By performing the presented procedure, overlapping in the same plot the different sensitivity analysis, it is possible to find out the minimum battery capacity that allows the energy balance to be satisfied for the different driving cycles considered.

After the size of the battery is selected, since each driving cycle will be characterized by a maximum electric traction vehicle speed that guarantees the energy balance, a set of such speeds is obtained. The question would be which one to choose: one speed would be compliant with one cycle but not with another one. The message here is that of having considered several working conditions (driving cycles) for the hybrid vehicle architecture, and the energy storage system is sized based exactly to take them into account. The optimal maximum electric traction speed would be the result of an additional optimization process.

A simple example is now presented. Assuming that the average initial state of charge is SoC_0^*, capacity Q^* is the one selected because compliant with all the driving cycles analyzed. For each of them, a maximum electric traction speed is obtained. If each cycle is called as C_1, C_2, ..., C_n, then:

$$
\begin{aligned}
C_1 &\to V_{\text{max,PE},1} \\
C_2 &\to V_{\text{max,PE},2} \\
&\cdots \\
C_n &\to V_{\text{max,PE}n}
\end{aligned}
\tag{4.23}
$$

Of particular interest would be to create a ΔSoC correlation matrix between the different cycles and the different maximum electric traction speeds to understand, having fixed the battery size, what is the influence of considering a certain $V_{\text{max,PE}}$ out from the cycle that

has designated it. A correlation matrix could be helpful in the comprehension of which speed has less influence on the overall energy balance, regardless of the driving cycle.

4.5 Chapter Summary and Future Works

In this chapter, the modeling of the electric powertrain, the design of a control strategy for the torque split between the thermal and electric powertrain and a new methodology regarding the battery pack sizing has been discussed, analyzed and presented. The electric motor model consists of its DC and phase current map as a function of each working point, defined by a torque and a rotational speed. Its efficiency takes into account for the Joule effect Copper losses. Through the use of manufacturer tables, the considered battery model takes into account the variation of the open circuit voltage and the resistance as a function of the actual battery state of charge, together with the maximum allowed charge and discharge currents. The model, by the way, considers only the battery resistance in series with the open circuit voltage. Different and more accurate models could actually be considered, but for the purposes of this work this one has been considered suitable.

The control strategy involves the use of rules based on all the electric powertrain limitations (battery and motor temperature, state of charge) that partialize the use of the electric machine at each time instant. This strategy for the torque split is simple and based on the system knowledge, and is practical for implementation in real time applications. The ease of use and implementation of this control strategy is furthermore appreciated because on this basis, the energy storage system sizing is performed.

Four design methodologies, from the simplest to the most complex and complete, have been presented and discussed. The first one is the more intuitive and is based on the energy recovery potential of the driving cycle itself: the battery is designed to recover all the energy available. The second one considers both the energy recovered and the energy consumed for electric traction. A sensitivity analysis regarding the dimension of the battery pack on the recovered energy over different cycles showed a consistent saturation of the recoverable energy potential, allowing to find an optimal size for storing all the available energy with the minimum additional mass. Nevertheless, the uncontrolled electric traction forces the battery to always operate around its minimum charge condition. The third methodology overcomes the drawback of the previous one relative to the minimum charge of the battery due to the uncontrolled electric traction speed. Considering different electric traction vehicle speeds, it has been evidenced how the lower is the vehicle speed, the larger is the battery capacity that allows to recover all the available energy. Instead, based on a

fixed low electric traction vehicle speed, if the initial battery state of charge increases, it reduces the recoverable energy. A fourth and last methodology introduced a sensitivity analysis regarding the influence of the battery capacity and of its initial state of charge on the presence of the energy balance points and on the electric traction speed to achieve them. It is shown how a higher initial state of charge is able to extend the balance points to lower battery capacities.

Such kind of progressive method having the aim to determine the potential and limits of the energy storage system for a mild hybrid electric vehicle, regarding its use on different driving cycles, has not been deeply investigated in the literature and is therefore considered the main contribution of this chapter.

Further works involve the battery sizing for mild hybrid electric vehicle architectures accounting for the presence of different kinds of electrified accessories (such as electrified water pump, air conditioning compressor, electrified power steering pump) and their relative energy management control.

Chapter 5

Vehicle Dynamics Implications During P4 Electric Motor Use

Previous chapters analyzed the potential of installations of hybrid architectures on normal production vehicles, together with the design of a traction motor for the rear axle and the sizing of a suitable battery pack for the specific application. The different component characteristics have been implemented in the model specifically developed and the results in terms of fuel consumption reduction, stored energy and regeneration efficiency have been produced.

The working mode of the P4 electric motor until now consists of its activation during traction or braking phases based on the necessary torque to allow the vehicle to follow the established driving path. In addition, it is well known that such driving profiles are not subjected to strong accelerations or decelerations, holding to the almost complete avoidance of full wheel slip due to high wheel torques.

The vehicle dynamics considered until now is of course the longitudinal one, and the electric traction or braking performance therefore do not affect it negatively. This chapter makes a step forward from this point of view and analyzes the influence of the regenerative braking performed with the rear axle P4 electric motor on the vehicle lateral stability. The application of a braking torque during, as an example, a cornering maneuver can lead to the possibility of reduced tire lateral capabilities, with direct consequences of reducing the vehicle maneuverability.

5.1   Introduction

As presented in previous chapters, the P4 architecture can lead to a consistent regeneration of energy when travelling on standard driving cycles. The position of the electric powertrain with respect to the ground and the optimization of the traction motor design are in this context important tasks to be achieved.

Although the connection of the electric powertrain to the vehicle's rear axle can lead to advantages related to the lack of substantial dissipative compontents between the electric motor and the wheels, its usage, if not properly controlled, is similar to that of old handbrakes. It is therefore clear that if the adhesion conditions are poor (wet or icy road) or the amount of required braking torque is sufficiently high, due to the longitudinal load transfer from the rear to front axle, the wheels could lose partial or total adhesion, with the consequence of possible locking. If the driving is straight and the conditions are not so poor the driver could be able to avoid instability, maybe transfering again vertical load to the rear axle and, in case, countersteering. The situation is different when the aforementioned case study occurs during a cornering maneuver. The effect of the lateral load transfer deteriorates the total vehicle adhesion even more.

Vehicle stability control has been widely investigated in the last 20 years where passenger vehicles are concerned. Direct yaw moment control (DYC) is the widespread methodology for improving vehicle stability, mainly realized through the use of differential braking [71]. The different control of solenoid modulators in the hydraulic brake system allows different brake pressures to be obtained on the wheels of the same/different axle. In this way, an external yaw moment that is helpful to stabilize the vehicle in case of critical situations is generated. As an example, the electronic stability program (ESP or ESC) widely installed on many passenger vehicles works exactly in this way [72]. The drawbacks of its implementation regard the need for accurate measurement or estimation of the main vehicle dynamics variables (e.g. yaw rate and sideslip angle) in addition to the fact that differential braking, if used in acceleration, reduces it and may not provide the correct longitudinal response to the driver.

The development and the market introduction of HEVs and EVs opened to manufacturers the possibility to implement similar control methodologies for enhancing vehicle stability by making use of faster and more controllable actuators: the electric motors. Several works have been carried considering 2WD or 4WD hybrid or electric vehicles in which electric motors provide traction or braking torques to the wheels independently of each other.

The general control structure includes the presence of a high level controller (responsible for the generation of the corrective yaw moment to be introduced at the vehicle level, tipically based on a reference vehicle model), a control allocation stage (responsible to translate the yaw moment into a wheel braking/traction torque references) and a low level controller (responsible for the actual realization of the reference torques considering actuator limitations). PID, Optimal control, fuzzy logic and sliding mode controller (SMC) are the main candidates for the high level controllers ([73] - [80]). Control allocation strategies are mainly considered when dealing with over actuated systems (e.g. four wheels independently driven). Analyzed low level controllers can be of the classical PID or SMC kind.

In the context of this work, the P4 configuration has an axle motor at the rear axle, connected to the wheels by an open differential. Not many studies involve the influence of an axle braking/traction torque on the vehicle stability as well as the analysis of the interaction between axle motor torque and wheel passive braking torques. In [81] an open loop braking in a turn maneuver in which the braking torque is provided by the rear axle motor is presented. It is shown how for high friction surfaces the vehicle tends to oversteer (driver needs to countersteer) while in low friction surfaces the same maneuver leads to completely unstable operation. It is claimed that one of the possible solutions to overcome this problem can be to control the rear wheel slips, to be limited to certain thresholds. In [82] a model predictive controller is used to blend rear axle motor braking and friction brake torques with the constraints of: 1) maximizing the energy recovered while applying the required braking force, considering the limitations of the electric powertrain and 2) limiting the yaw rate tracking error. It is shown by simulation results that an oversteering tendency is inevitably introduced and should be compensated by the introduction of friction braking torques. Bayar et al. [83] considered a high level controller to compute the total longitudinal force and yaw moment required to track a desired vehicle speed and yaw rate. A control allocation is responsible for the computation of the optimal longitudinal slips to be achieved by each wheel through the slip tracking controller, which computes the amount of torque to be applied on each wheel and at the electric motor level. In this way, a controller blending regenerative and friction braking is designed to guarantee the vehicle stability. In [84] a fuzzy logic controller is designed to enhance the vehicle stability during critical maneuvers. The errors of sideslip angle and yaw rate are used to compute a corrective yaw moment to stabilize the vehicle while, based on oversteer or understeer detection, the rear axle electric motor as well as the friction brakes are used to generate such yaw moment. Alcantar et al. [85] designed a robust controller for rear axle hybrid electric vehicles. The regenerative braking is maximized considering electric motor braking torque up to the torque limits of the electric powertrain. To guarantee stability,

the control actuator is a center coupling device, that connects the front with the rear axle. When the coupling is used, the required braking torque is distributed on the front axle too, enhancing the stability. A linearized version of the nonlinear vehicle model is considered and the transfer function between center coupling torque and vehicle yaw rate is obtained and used for control purposes. Different approaches have been followed in [86] and [87], in which analyses regarding the powerslide motion (drift) of automobiles are performed. The basic idea behind these works is to obtain the longitudinal tire slips which allow the vehicle to maintain its steady state motion based on optimal control theory and then translate such required slips into front and rear axle torques. The linearization of the nonlinear vehicle model allows a three degrees of freedom bicycle model including longitudinal, lateral and yaw motion to be obtained.

In the context of hybrid architecture equipped with axle motors, particular interest should be given to:

- The comprehension of the introduced yaw moment due to the application of an axle braking torque in case of different driving conditions;

- The comprehension of the criteria to switch between regenerative and friction braking, maximizing the energy regeneration performance while guaranteeing stability.

As a matter of fact, in case of direct yaw moment control through differential braking, the introduced yaw moment computation is straightforward (algebraic sum of the axle longitudinal forces multiplied by half of the track). In case that the longitudinal braking forces are provided by the electric motor through an open differential, the aforementioned algebraic summation is zero due to equality of the braking forces on the same axle. What is changing in this case is the lateral capability of the tires, affected by the load transfer (longitudinal and lateral) and by the application of longitudinal forces. In addition, based on the tire characteristics and their interaction with the road, based on different driving and braking conditions (e.g. lateral acceleration and required braking torque) it should be possible to understand how to detect a loss of stability by means of the main quantities measured on board the vehicle.

5.2   Vehicle Modeling

The transmission of power between the ICE and the front wheels and between the P4 electric motor and the rear wheels has already been presented in Chapt. 2 and 4. In this context, the front and rear powertrain are modeled with fixed transmission ratios
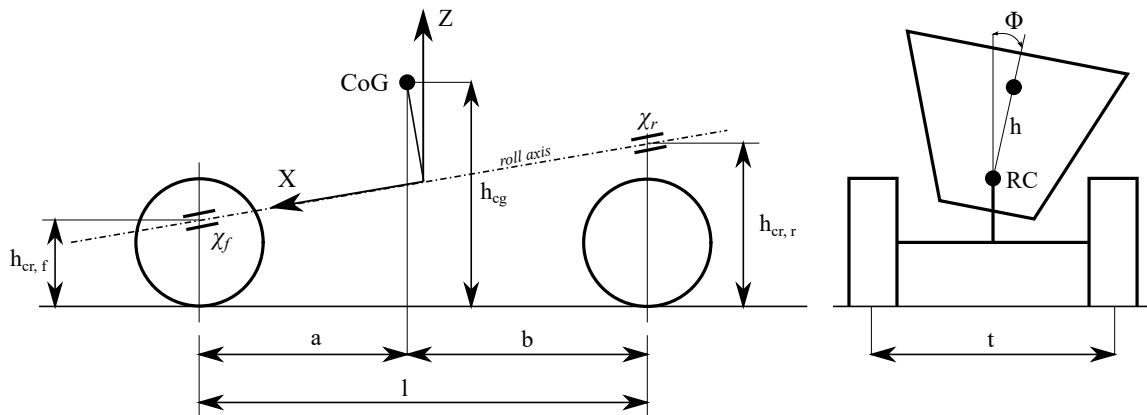
Fig. 5.1 Lateral and front view of the vehicle model. RC = Roll Center, CoG = Center of Gravity.
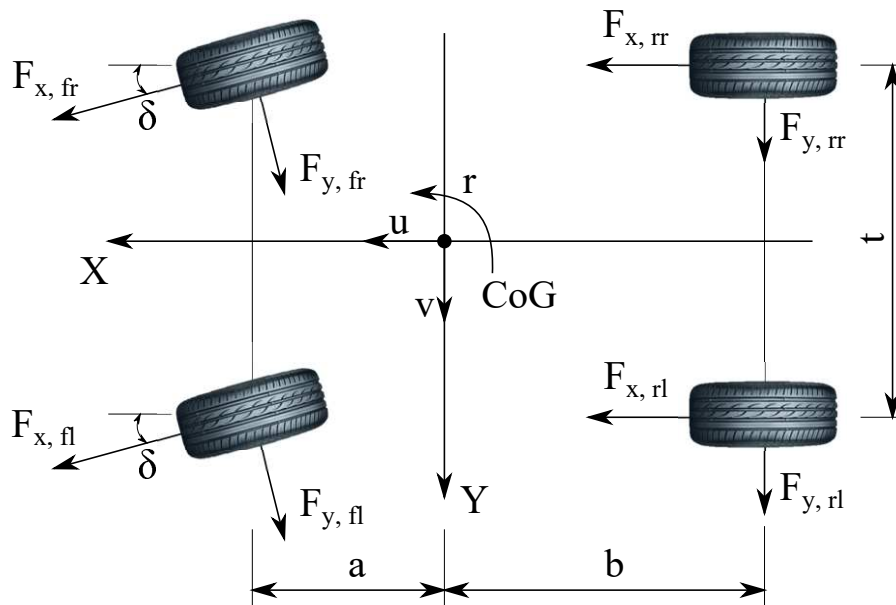
Fig. 5.2 Upper view of the vehicle model including the forces exchanged by the tires with the road.

and efficiencies. The halfshafts, together with transmission shafts of the gearboxes, are considered rigid. The ICE and P4 machines are still modeled with their torque - speed - efficiency maps. What should be included in the model is the presence of the vehicle dynamics in the yaw plane (XZ plane). To this end, the steering system is considered without any compliance as well, and a transmission ratio R_f models the different rotation angle between the driver steering wheel and wheel king - pin axis.

With reference to Figs. 5.1 and 5.2, the vehicle model is comprehensive of the degrees of freedom of interest for the analysis that will be performed. In fact, the eight degrees of freedom model includes the rigid body degrees of freedom of longitudinal, lateral and yaw motion, the roll degree of freedom, and the rotational degrees of freedom of the four

wheels. The body fixed frame of reference (XYZ) has origin in the vertical projection of the center of gravity along the roll axis.

The vehicle has a total mass M, sprung mass m_s, moment of inertia J_z and J_x with respect to Z and X axes and coupled moment of inertia J_{xz}. In the YZ plane, h is the distance between the vehicle center of gravity and the roll axis, and the roll angle is denoted as ϕ. The longitudinal, lateral and yaw velocities of the roll center in the body fixed reference frame are u, v and r. Finally, the wheel king - pin axis rotation is denoted as δ.

The equation of motion along the longitudinal axis x is:

$$M\left(\dot{u} - rv\right) = \left(F_{x,fl} + F_{x,fr}\right)\cos\delta - \left(F_{y,fl} + F_{y,fr}\right)\sin\delta + F_{x,rl} + F_{x,rr} - 0.5\rho C_x A u^2 \quad (5.1)$$

The equation of motion along the lateral axis y is:

$$M\left(\dot{v} + ru\right) + m_s h\ddot{\phi} = \left(F_{y,fl} + F_{y,fr}\right)\cos\delta + \left(F_{x,fl} + F_{x,fr}\right)\sin\delta + F_{y,rl} + F_{y,rr} \quad (5.2)$$

The equilibrium of moments about z axis is:

$$J_z\dot{r} - J_{xz}\ddot{\phi} + \dot{u}m_s h\phi = \left(F_{y,fl} + F_{y,fr}\right)a\cos\delta + \left(F_{y,fl} - F_{y,fr}\right)\frac{t}{2}\sin\delta - \left(F_{y,rl} + F_{y,rr}\right)b +$$
$$+ \left(F_{x,fl} + F_{x,fr}\right)a\sin\delta + \left(-F_{x,fl} + F_{x,fr}\right)\frac{t}{2}\cos\delta + \left(-F_{x,rl} + F_{x,rr}\right)\frac{t}{2}$$
$$(5.3)$$

And finally, the equation of motion about the roll axis is:

$$J_x\ddot{\phi} - J_{xz}\dot{r} - \left(\dot{v} + ru\right)m_s h + \left(\chi_f + \chi_r\right)\phi + \left(\Gamma_f + \Gamma_r\right)\dot{\phi} = m_s gh\phi \quad (5.4)$$

Forces $F_{x,fl}$, $F_{x,fr}$, $F_{x,rl}$ and $F_{x,rr}$ are the longitudinal tire ground forces of front left, front right, rear left and rear right wheels computed in the frame of reference of the wheels themselves, while $F_{y,fl}$, $F_{y,fr}$, $F_{y,rl}$ and $F_{y,rr}$ are the lateral ones. The front and rear wheelbases are a and b, t is the track while χ_f, χ_r, Γ_f, Γ_r are the front and rear suspension equivalent roll stiffnesses and dampings.

The remaining four degrees of freedom are related to the four wheels rotational dynamics. The equation of motion of the generic rotational degree of freedom of the wheel is:

$$J_w\dot{\omega}_{jk} = T_{t,jk} - T_{b,jk} - F_{x,jk}R_0 \quad (5.5)$$

where the subscripts j and k stand for front or rear and left or right respectively. The term J_w refers to the moment of inertia of the wheel along its rotational axis and R_0 is the rolling radius. The traction and braking torques at the jkth wheel are $T_{t,jk}$ and $T_{b,jk}$ respectively

The purpose of the following analysis is to study the influence of the regenerative braking on the vehicle stability during cornering meneuvers. In this case the traction is given by the ICE while the braking torques are coming both from the P4 electric motor and, if necessary, from the passive brakes. In addition, the only powertrain inertia taken into account is that of the wheels, considered fundamental because of its clear implications with the tire - ground force generation. The ICE and EM inertias are neglected because their effect is negligible. Therefore, considering the presence of an open differential both on the front and on the rear axle, for a wheel belonging to the front axle the traction torque is:

$$T_{t,fk} = \frac{1}{2} T_{ICE} \tau_{gb} \tau_d \tag{5.6}$$

where τ_{gb} and τ_d are the transmission ratio of the gearbox and of the front differential. The braking torque on the front axle is provided by the passive brakes while that on the rear can be either provided by the P4 electric motor, or by the passive brakes, or by both. In the case of electric braking:

$$T_{b,rk} = \frac{1}{2} T_{EMP4} \tau_{gb,r} \tau_{d,r} \tag{5.7}$$

where $\tau_{gb,r}$ is the rear transmission ratio between the electric motor and the differential while $\tau_{d,r}$ is the rear differential transmission ratio. In the case of passive braking, starting from the braking pedal position β_p, considering the brake pressure gain K_p and a split ratio between front and rear axle K_{sr}, the front and rear passive braking torques are:

$$T_{b,fk} = \frac{1}{2} \beta_p K_p K_{sr}; T_{b,rk} = \frac{1}{2} \beta_p K_p \left(1 - K_{sr}\right) \tag{5.8}$$

In this case, the braking torque split between passive and electric braking is described in Sect. 5.4.

The lateral and longitudinal tire - ground forces are computed by means of the nonlinear Magic Formula tire model in case of combined slip [95]:

$$
\begin{aligned}
F_{x,jk} &= F_{x,jk} \left(\sigma_{jk}, \alpha_{jk}, F_{z,jk} \right) \\
F_{y,jk} &= F_{y,jk} \left(\sigma_{jk}, \alpha_{jk}, F_{z,jk} \right)
\end{aligned}
\tag{5.9}
$$

where σ_{jk} and α_{jk} are the longitudinal and lateral slips of the tires while $F_{z,jk}$ are the normal forces at each corner.

The vertical forces are computed taking into account the static load, the longitudinal and the lateral load transfers:

$$
\begin{aligned}
F_{z,fk} &= \frac{Mgb}{2l} - \frac{Ma_x h_{cg}}{2l} \pm \frac{Ma_y}{t} \left(\frac{b}{l} h_{cr,f} + \frac{\chi_f}{\chi_{tot}} h \right) \\
F_{z,rk} &= \frac{Mga}{2l} + \frac{Ma_x h_{cg}}{2l} \pm \frac{Ma_y}{t} \left(\frac{a}{l} h_{cr,f} + \frac{\chi_r}{\chi_{tot}} h \right)
\end{aligned}
\tag{5.10}
$$

where h_{cg} is the height of the center of gravity from the ground, $h_{cr,f}$ and $h_{cr,r}$ are the roll center height from the ground of front and rear axle and χ_{tot} is the summation of the equivalent roll stiffness on both axles. The $-$ sign stands for the inner wheel while the $+$ for the outer one.

The longitudinal slip for each tire is:

$$
\sigma_{jk} = 1 - \frac{V_{jk}}{\omega_{jk} R_0}
\tag{5.11}
$$

in the case of traction and:

$$
\sigma_{jk} = \frac{\omega_{jk} R_0}{V_{jk}} + 1
\tag{5.12}
$$

in the case of braking. V_{jk} is the longitudinal velocity of the wheel center, expressed as:

$$
V_{jk} = \sqrt{u_{jk}^2 + v_{jk}^2} \cos \alpha_{jk}
\tag{5.13}
$$

where u and v are the longitudinal and lateral components of the jkth wheel center speed and α_{jk} is the sideslip angle of the tire:

$$
\begin{aligned}
\alpha_{fk} &= \arctan \left(\frac{v + ra}{u \pm rt/2} \right) - \delta \\
\alpha_{rk} &= \arctan \left(\frac{v - rb}{u \pm rt/2} \right)
\end{aligned}
\tag{5.14}
$$

where the sign $+$ is related to the right wheel while $-$ for the left one. Suspension steering effects (roll steer, jounce steer) as well as tire force sensitivity due to wheel camber angle are neglected because they are considered higher order effects.

5.3 Open Loop Maneuvers

The use of the rear axle electric motor for energy regeneration during straight line braking can be consistently effective especially in case of not medium to high initial vehicle speeds and decelerations.

During cornering, the energy regeneration seems not to be an issue. Problems related to lateral stability, passenger safety and vehicle maneuverability are so important that the introduction of an additional degree of freedom that could actually affect the overall system behavior seems to be avoidable. However, cutting off additional recoverable energy (apart from that recovered during straight line braking) that could be used for following traction phases, seems instead to be wasteful. The regenerative braking system could also be affected by possible misuses and, therefore, it is necessary to understand how to handle with such kind of faults. Finally, if the rear axle regenerative braking during cornering maneuvers is able to affect the vehicle lateral maneuverability, it could be used in a proper and controlled way to change its behavior (e.g. giving more sportiness introducing slight oversteering moments). As always happens, a compromise can be the solution.

The main chassis system parameters responsible for the overall vehicle characteristics and, in case, stability, are the tires "status". In general, the loss of vehicle maneuverability can be attributed to a temporary or definitive lack of ability by one or more tires to generate lateral forces. This can be caused by several reasons, but the most frequent are related to low vertical forces or to a decreased availability of lateral forces due to an increase of the longitudinal one. In extreme cases, the two aforementioned conditions can occur together, leading to an almost completely unstable behavior of the vehicle with a consequent total lack of possibility of driver interventions. Therefore, it is extremely important to avoid tire saturation, especially on low friction surfaces.

Focusing on the architecture considered within this thesis, it is easy to understand that the energy recovery performed with the rear axle electric motor could actually create problems. During steady state cornering meneuvers, lateral load transfers cause unloading and loading of the inner and outer wheels respectively. In this situation the outer wheels are therefore able to develop higher lateral forces with respect to the inner ones, which instead are limited by lower vertical forces. Recalling the well known interaction between longitudinal and lateral forces of a pneumatic tire, it is clear that the application of (as an example) a braking force on the less loaded wheel of an axle can easily create tire saturation with consequent total slip. Therefore, applying a braking torque with the rear axle electric motor and splitting it equally between left and right wheels can effectively create risks regarding the lateral stability. To avoid them, it is necessary first of all to understand the

impact of this braking torque application on the vehicle stability and maneuverability. To make a step ahead, once the plant is identified, proper control systems are designed to allow energy regeneration without affecting the vehicle lateral dynamics.

The focus is therefore on understanding what are the effects of the application of a rear axle braking torque on the vehicle handling and stability.

5.3.1 Physical Comprehension of the Phenomena

For a better understanding of the different phenomena occuring during braking in a turn events, such a maneuver is analyzed in different conditions.

Although the required braking torque at the ground level can be low for a C class vehicle (e.g. 1000 Nm, vehicle mass between 1400 and 1600 kg), if the torque provided by the electric motor (considering the transmission ratio between the motor and the wheels) is not enough, the passive brakes should intervene to fill the gap. From now on, it is assumed that the electric motor capabilities in terms of available torque at its shaft are much larger than the required braking torque at the wheels to slow down the vehicle. In this way, the braking maneuver is dictated only by the electric motor without influence of the passive brakes.

Figure 5.3 presents all the variables of interest concerning a braking in a turn maneuver. The yaw rate, the vehicle sideslip angle, the wheel sideslip angles, the longitudinal slips of the wheels and the applied braking torques are plotted in time together with the steering angle evolution. The required braking torque at the level of the wheels is 600 Nm, the initial vehicle speed is 70 km/h and the reference speed is 20 km/h. Up to 2 seconds of the simulation the vehicle runs in steady state cornering, presenting a β lower than zero and front sideslip angles larger (in magnitude) than those at the rear axle. Longitudinal slips are coherently close to zero, meaning the vehicle is experience nearly pure lateral dynamics. From 2 seconds on, the braking torque starts to be different from zero. In particular, as previously mentioned, the overall braking torque required from the driver is provided by the electric motor, and this torque is then split equally between left and right half shafts. Whereas the torque increases in magnitude, the longitudinal slips perceive variations: the slip of the rear inner wheel (RL) decreases consistently up to threshold values around 10 - 15 %. Similarly, the rear sideslip angles decrease and become even larger (in magnitude) than those of the rear axle.

It is noticeable that in this time frame, from 2 to 5 seconds, the reduction of the vehicle speed due to the applied braking torques is not yet taking place in a consistent way. This

can be verified also looking at the yaw rate and the vehicle sideslip angle. When the braking torque reaches its maximum, there is a span of time in which the yaw rate increases by a small amount before decreasing due to the vehicle speed reduction. A similar behavior happens with the sideslip angle: it decreases before increasing its value at lower speeds. In this time frame the lateral - longitudinal interaction of the tires is taking place.

Figure 5.4 presents the same previous maneuver but performed starting from a vehicle speed of 50 km/h and applying a braking torque of 1000 Nm. A similar behavior with respect to the previous maneuver is therefore present even if less accentuated concerning the yaw rate and sideslip angle of the vehicle. However, the same lateral - longitudinal interaction is observed.
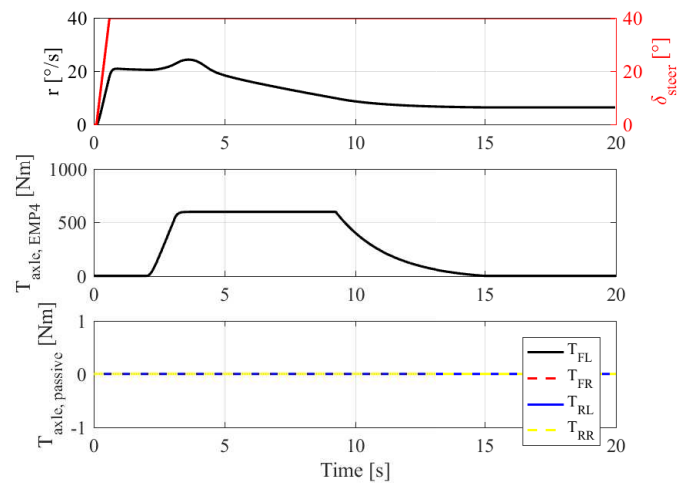
(a) Steering angle, yaw rate, P4 axle braking torque and passive brakes braking torques.
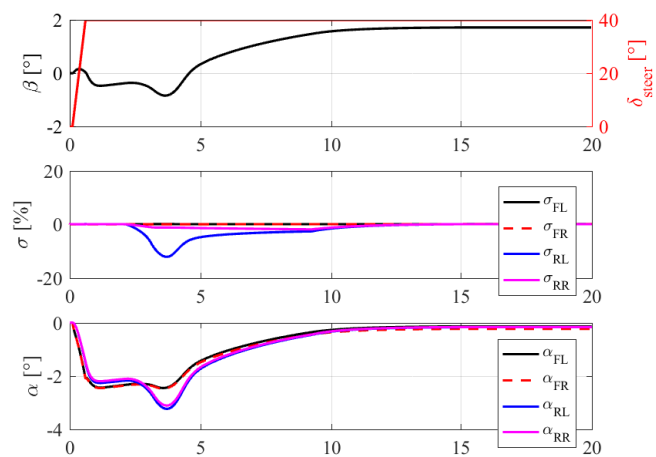
(b) Vehicle sideslip angle, longitudinal slips and tire sideslip angles.

Fig. 5.3 Time evolution of yaw rate, vehicle sideslip angle, tire longitudinal slips, tire sideslip angles and applied P4 axle braking torque during a braking in a turn event starting from a vehicle speed of 70 km/h.
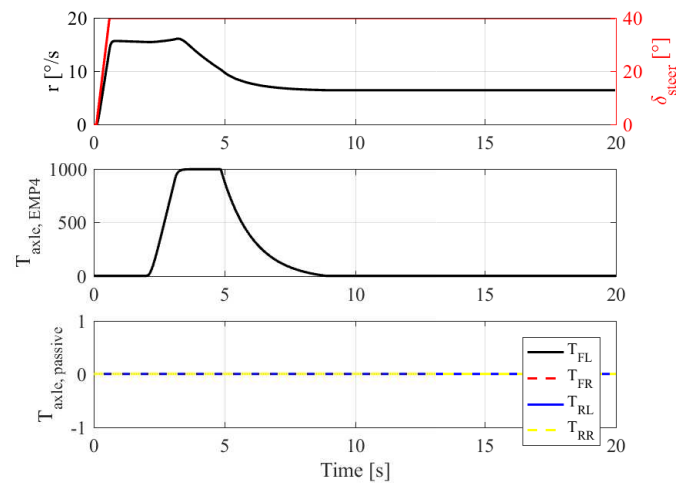
(a) Steering angle, yaw rate, P4 axle braking torque and passive brakes braking torques.
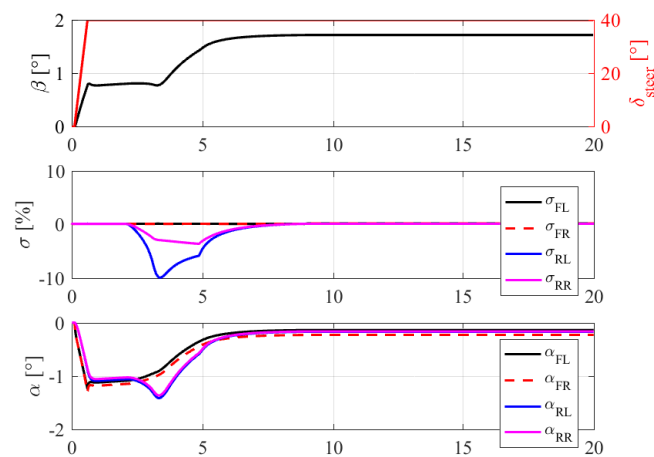
(b) Vehicle sideslip angle, longitudinal slips and tire sideslip angles.

Fig. 5.4 Time evolution of yaw rate, vehicle sideslip angle, tires longitudinal slips, tire sideslip angles and applied P4 axle braking torque during a braking in a turn event starting from a vehicle speed of 50 km/h.

When looking to the time evolutions of yaw rate and sideslip angle of the vehicle, a common behavior can be drawn. The application of a braking torque on the rear wheels leads to increase the longitudinal slips of those wheels, therefore reducing their exploitable lateral forces. For the small time frame in which the speed is not decreasing due to the applied braking torques, to guarantee the same lateral acceleration the rear wheels must develop larger sideslip angles. Due to the presence of a consistent amount longitudinal slip, one or more tires can undergo saturation, reducing therefore the capability of the vehicle to

counteract the centrifugal force. In the most extreme cases, the driver can lose the control of the vehicle.

Focusing on the time frame related to the lateral - longitudinal interaction, when looking to the yaw rate a noticeable increase is evidenced, clearly caused by the presence of a body yaw acceleration. Such acceleration can be created only by the presence of an additional yaw moment applied in the counterclockwise direction (positive) with respect to the vehicle axis of reference. Due to the presence of an open differential that distributes the torque equally between the left and right wheels, no differential braking is generated. Therefore, the additional applied yaw moment is not generated by the introduction of the external braking forces on the rear axle but is due to the loss of lateral adherence by one or more tires on the axles in which the braking torque is applied. Similarly, when looking to the vehicle sideslip angle, a reduction is observed, meaning of a tendency of the vehicle to nose in.
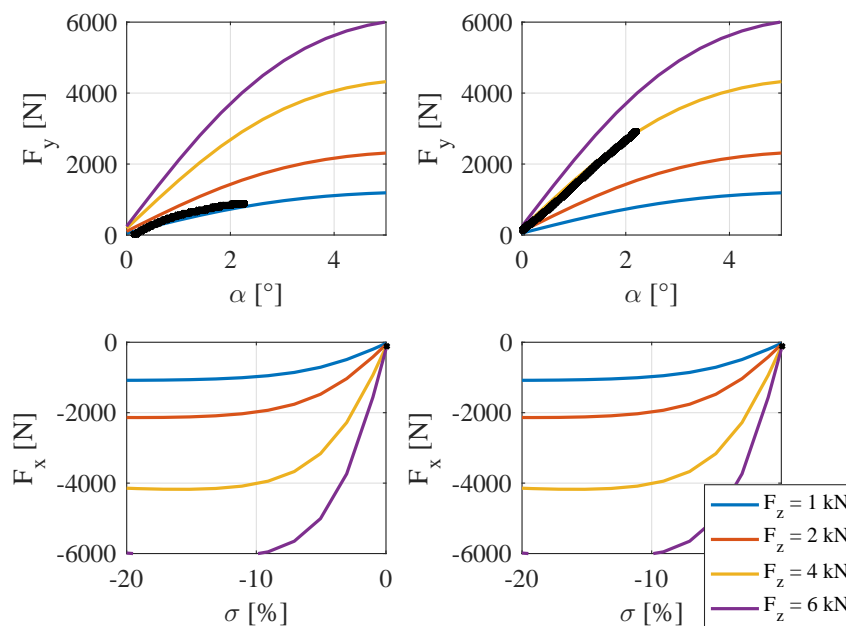
Fig. 5.5 Actual lateral and longitudinal forces of rear left (left) and rear right (right) tires (black points) plotted versus their lateral and longitudinal slips in absence of braking torque, 70 km/h vehicle speed. The force vs. slip plots coming from the Pacejka's Magic Formula are additionally plotted considering different vertical loads.

Figure 5.5 presents the actual lateral and longitudinal forces plotted versus their lateral and longitudinal slips during the first part of the braking in a turn maneuver previosly presented, for the rear left and rear right tires. In addition, the $F_y - \alpha$ and the $F_x - \sigma$ plots are also presented for different vertical loads. In this figure the longitudinal forces are

not yet applied and the condition is of pure cornering. The sideslip angles of rear left (RL) and rear right (RR) wheels are almost the same but the vertical loads acting on each wheel is clearly different due to the lateral load transfer. Therefore, the RL wheel (inner with respect to the cornering) develops a lower lateral force. At this stage the longitudinal forces are still null and the longitudinal slips are close to zero.
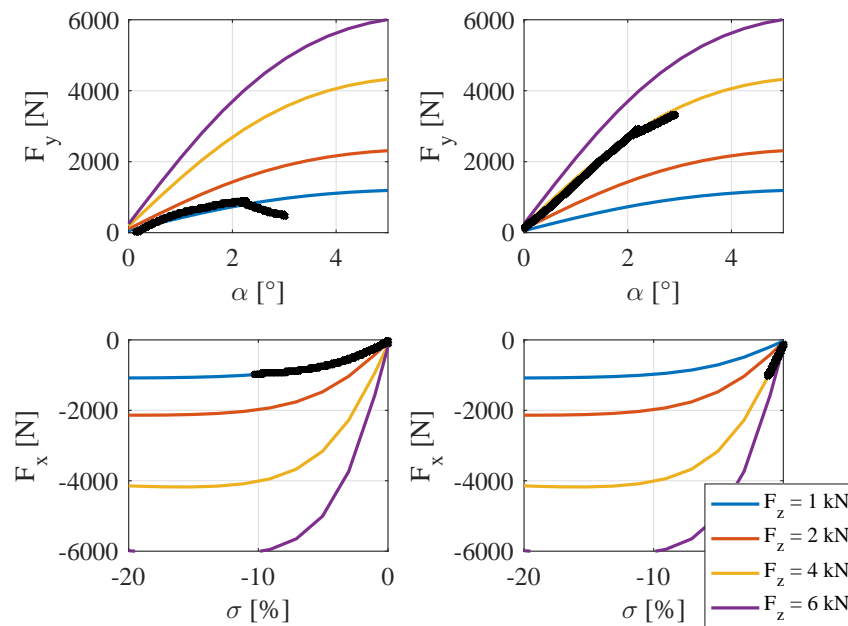
Fig. 5.6 Actual lateral and longitudinal forces of rear left (left) and rear right (right) tires (black points) plotted versus their lateral and longitudinal slips during a braking in a curve maneuver, 70 km/h initial vehicle speed, 600 Nm applied axle braking torque. The force vs. slip plots coming from the Pacejka's Magic Formula are additionally plotted considering different vertical loads.

The introduction of braking forces (equal for RL and RR wheels, Fig. 5.6) has the effect of increasing the sideslip angles of the wheels. Since the RR wheel is more loaded than the RL, despite the presence of a not null longitudinal force and of a longitudinal load transfer due to the deceleration, it is still capable of developing a sufficiently high lateral force. In addition, the longitudinal slip assumes a relatively small value, which allows the tire to work still in its linear region. The application of an equal braking force on the RL wheel instead produces a much larger longitudinal slip (out of linearity of the tire) and this, together with the loss of vertical load due to the deceleration, makes the lateral force inevitabily drop, causing loss of lateral adhesion. The result of such a large interaction between the vertical, longitudinal and thus lateral forces is perceived by the vehicle as an external yaw moment that pushes the vehicle inside the curve. In the case of

constant trajectory manuever, the driver is forced to countersteer in order to maintain the same trajectory.

Different from the wide variety of techniques to control the performance and the stability of a vehicle by introducing an external yaw moment through the use of different traction/braking forces on the same axle (torque vectoring/differential braking techniques), in this case the introduced yaw moment is internal and indirect.

If the aim is therefore to maximize the regeneration of energy while maintaining the vehicle in a stable field of operation, it is clear that all the aforementioned interactions between longitudinal vehicle speed, applied braking torque, tire lateral/longitudinal capabilities and introduced yaw moment should be clarified.

5.3.2 Braking Torque to Yaw Moment Gain

If the interactions between yaw and roll motion are neglected, Eq. 5.3 can be rewritten as follows:

$$
\begin{aligned}
J_z \dot{r} = {} & \left(F_{y,fl} + F_{y,fr}\right) a \cos\delta + \left(F_{y,fl} - F_{y,fr}\right) \frac{t}{2} \sin\delta - \left(F_{y,rl} + F_{y,rr}\right) b + \\
& + \left(F_{x,fl} + F_{x,fr}\right) a \sin\delta + \left(-F_{x,fl} + F_{x,fr}\right) \frac{t}{2} \cos\delta + \left(-F_{x,rl} + F_{x,rr}\right) \frac{t}{2}
\end{aligned}
\tag{5.15}
$$

The yaw equation of motion presents on the left hand side the inertia term and on the right hand side the external moments. These moments are both a function of longitudinal and lateral forces and therefore can be rearranged as:

$$
J_z \dot{r} = y_1 a \cos\delta + y_2 \frac{t}{2} \sin\delta - y_3 b + x_4 a \sin\delta + x_5 \frac{t}{2} \cos\delta + x_6 \frac{t}{2}
\tag{5.16}
$$

If now the subdivision regards front and rear axle, the equation becomes:

$$
J_z \dot{r} = M_{zyf} - M_{zyr} + M_{zx}
\tag{5.17}
$$

which expresses that the total yaw moment due to the tire forces is the algebraic summation of a contribution related to longitudinal forces, one related to front lateral forces and another related to rear lateral forces.

During steady state cornering, the application of a braking torque on the rear axle affects in a first phase the rear wheels decreasing their lateral capabilities, and in a second phase the overall vehicle speed, reducing the lateral acceleration and therefore the lateral forces to overcome it. In this first phase the vehicle exhibits an oversteering tendency,

which can be translated into a fictitious introduction of an external yaw moment applied on the vehicle. This yaw moment is therefore a function of the lateral - longitudinal interaction of the tires. Therefore, it is interesting to focus the attention on the reduction of the component M_{zyr}, mainly responsible for the increase of the total yaw moment.

A simplified expression of the yaw equation of motion is now considered. Eq. 5.16 is linearized and the terms y_2, x_4, x_5 and x_6 are neglected:

$$J_z \dot{r} = M_z = \left(F_{y,fl} + F_{y,fr} \right) a - \left(F_{y,rl} + F_{y,rr} \right) b \tag{5.18}$$

The lateral - longitudinal interaction of the tire forces can be expressed through the elliptic approximation:

$$F_{y,jk} = F_{y,jk}^0 \sqrt{1 - \left(\frac{F_{x,jk}}{\mu F_{z,jk}} \right)^2} \tag{5.19}$$

which, considering the Taylor expansion of the square root, becomes:

$$F_{y,jk} = F_{y,jk}^0 \sqrt{1 - \left(\frac{F_{x,jk}}{\mu F_{z,jk}} \right)^2} \approx F_{y,jk}^0 \left[1 - \frac{1}{2} \left(\frac{F_{x,jk}}{\mu F_{z,jk}} \right)^2 \right] \tag{5.20}$$

with the term $F_{y,jk}^0$ having the meaning of lateral force in absence of longitudinal actions.

Applying a braking torque on the rear axle, two longitudinal braking forces arise on the rear wheels. A brand new yaw moment can be therefore computed considering Eq. 5.20:

$$
\begin{aligned}
M_z^* = \left(F_{y,fl} + F_{y,fr} \right) a &- F_{y,rl}^0 \left[1 - \frac{1}{2} \left(\frac{F_{x,rl}}{\mu F_{z,rl}} \right)^2 \right] b - F_{y,rr}^0 \left[1 - \frac{1}{2} \left(\frac{F_{x,rr}}{\mu F_{z,rr}} \right)^2 \right] b+ \\
&+ \left(F_{x,rl} - F_{x,rr} \right) \frac{t}{2}
\end{aligned}
\tag{5.21}
$$

that is:

$$
\begin{aligned}
M_z^* = \left(F_{y,fl} + F_{y,fr} \right) a &- \left(F_{y,rl}^0 + F_{y,rr}^0 \right) b + \frac{1}{2} F_{y,rl}^0 \left(\frac{F_{x,rl}}{\mu F_{z,rl}} \right)^2 b+ \\
&+ \frac{1}{2} F_{y,rr}^0 \left(\frac{F_{x,rr}}{\mu F_{z,rr}} \right)^2 b + \left(F_{x,rl} - F_{x,rr} \right) \frac{t}{2}
\end{aligned}
\tag{5.22}
$$

A brief consideration is now drawn up. If the lateral - longitudinal forces interaction is neglected (third and fourth terms of Eq. 5.22), the computation of the introduced yaw moment due to the applied longitudinal forces can be simply obtained by subtracting Eq. 5.18 from Eq. 5.22, noticing that the first two terms of the two equations are the same

since they express the lateral forces in absence of longitudinal interactions. Therefore:

$$\Delta M_z = M_z^* - M_z = \left(F_{x,rl} - F_{x,rr}\right) \frac{t}{2} \tag{5.23}$$

which is the equation at the base of any yaw moment control acted through differential braking.

Since the lateral - longitudinal tires interaction cannot be neglected in this application, the computation of ΔM_z becomes less trivial. Recalling the use on an open differential between the electric motor and the half shafts, in steady state conditions the braking forces on left and right rear wheels are:

$$F_{x,rl} = F_{x,rr} = \frac{T_{b,axle}}{2R_0} \tag{5.24}$$

leading the moment M_z^* to be:

$$M_z^* = \left(F_{y,fl} + F_{y,fr}\right) a - \left(F_{y,rl}^0 + F_{y,rr}^0\right) b + \frac{b}{2} \left(\frac{T_{b,axle}}{2\mu R_0}\right)^2 \left(\frac{F_{y,rl}^0}{F_{z,rl}^2} + \frac{F_{y,rr}^0}{F_{z,rr}^2}\right) \tag{5.25}$$

where $T_{b,axle}$ is the braking torque at the rear axle. Finally, ΔM_z is:

$$\Delta M_z = \frac{b}{2} \left(\frac{T_{b,axle}}{2\mu R_0}\right)^2 \left(\frac{F_{y,rl}^0}{F_{z,rl}^2} + \frac{F_{y,rr}^0}{F_{z,rr}^2}\right) \tag{5.26}$$

In steady state cornering, the tire is assumed to work in its linear region. Therefore:

$$F_{y,rk} = -C_{rk}\alpha_{rk} \tag{5.27}$$

which leads to:

$$\Delta M_z = -\frac{b}{2} \left(\frac{T_{b,axle}}{2\mu R_0}\right)^2 \left(\frac{C_{rl}}{F_{z,rl}^2} + \frac{C_{rr}}{F_{z,rr}^2}\right) \alpha_r \tag{5.28}$$

having assumed the same sideslip angle for left and right rear wheels.

Equation 5.28 therefore expresses the amount of introduced yaw moment as a function of an impulsive introduction of the rear axle braking torque. In the expression the friction coefficient appears at the denominator, as well as the vertical loads of the rear corners. The minus sign is compensated by the fact that in the adopted convention the tires sideslip angles are considered negative.

Since the wheels sideslip angles are not measurable variables it is worthwhile to translate them in more usable quantities. Recalling the conventional bicycle model, the sideslip angle of the rear wheels is:

$$\alpha_r = \beta - \frac{br}{V} \tag{5.29}$$

where β is the vehicle sideslip angle, r is the vehicle yaw rate and V is its velocity. Both β and r can be expressed as a function of the wheels steering angle δ through the sideslip and the yaw rate gains:

$$\beta = \frac{b}{l}\left(1 - \frac{MaV^2}{blC_r}\right)\frac{1}{1 + K_{us}\frac{V^2}{gl}}\delta \tag{5.30}$$

$$r = \frac{V}{l + K_{us}V^2}\delta \tag{5.31}$$

where K_{us} is the understeering gain expressed as:

$$K_{us} = \frac{M}{l}\left(\frac{b}{C_f} - \frac{a}{C_r}\right) \tag{5.32}$$

Since the main inputs to compute the sideslip angle of the rear wheels are the vehicle speed and the wheels steering angle, the yaw moment variation can be plotted as a function of the rear axle required braking torque and of another variable which can in any case express the same meaning of the sideslip angle, measurable and able to enclose both the information regarding vehicle speed and steering angle: the lateral acceleration. The result is presented in Fig. 5.7. It should be underlined that the variables such as lateral acceleration, vehicle speed, yaw rate and vehicle sideslip angle are computed in steady state motion and before the application of the braking torque. This means that the yaw moment variation lasts a very small amount of time before the vehicle speed starts to decrease.

Fig. 5.7 Yaw moment variation as a function of the application of a rear axle braking force for different driving conditions.

Equation 5.28 and its relative representation in a 3D surface plot can be computed offline and gives a first order idea of the amount of introduced yaw moment after the application of a rear axle braking torque based on different cornering conditions. The obtained ΔM_z is a function of all the introduced approximations:

- Steady state vehicle motion.

- Neglected yaw moment variation of front lateral ($y_2 = 0$) and longitudinal forces ($x_4 = x_5 = x_6 = 0$).

- Lateral - Longitudinal forces interaction through approximated elliptic behavior.

- Linearized tire lateral behavior.

Finally, the vertical loads appearing in Eq. 5.28 are computed based on Eqs. 5.10.

5.3.3   Longitudinal Adherence Limitations

The expression of ΔM_z takes into account the modification of the tires lateral capabilities when longitudinal forces are applied but is not representative of their longitudinal behavior.

Due to lateral and longitudinal load transfers, one or more wheels could substantially decrease its maximum longitudinal adherence and the application of a high braking or traction forces could lead the wheel (or the wheels) to fully slip.

A simplified analysis of the tire road interaction can actually limit the region of ΔM_z application to stable, not slipping, tire working conditions.

Recalling the well known relation between longitudinal and vertical tire forces through the longitudinal adherence coefficient μ_x:

$$F_{x,jk} = \mu_{x,jk} F_{z,jk} \tag{5.33}$$

which, whenever operating in the tire linear range, can be expressed as:

$$\mu_{x,jk} = K_\sigma \sigma_{jk} \tag{5.34}$$

being σ the tire longitudinal slip and K_σ the slope of the curve, it is possible to select different required braking torque and different vehicle speeds (or lateral accelerations), check the minimum of the four vertical loads (comprehensive of the lateral and longitudinal load transfers):

$$F_z^* = \min \left[F_{z,fl}\left(a_x, a_y\right), F_{z,fr}\left(a_x, a_y\right), F_{z,rl}\left(a_x, a_y\right), F_{z,rr}\left(a_x, a_y\right) \right] \tag{5.35}$$

and compute the actual longitudinal adherence of that corner as:

$$\mu_{x,act} = \frac{T_{b,axle}}{2R_0 F_z^*} \tag{5.36}$$

In this way the attention is focused directly on the less loaded corner, the one that can more easily reach complete slip conditions. Figure 5.8 presents the surface plot of the actual longitudinal adherence of the least loaded corner. Values higher than 1.5 are reached, meaning full slip conditions, and thus are not feasible.

The surface of the longitudinal adherence of the least loaded corner should actually be limited considering the maximum longitudinal adhesion exploitable by the tire. Considering the formulation present in [95], the peak longitudinal adhesion μ_p in the absence of any wheel camber is:

$$\mu_p = \mu \left(p_{dx1} + p_{dx2} dF_z\right) \lambda_\mu \tag{5.37}$$

where p_{dx1} and p_{dx2} are the longitudinal coefficient of the Magic Formula, λ_μ is a scaling factor, μ is the friction coefficient and dF_z is the normalized change in vertical load,
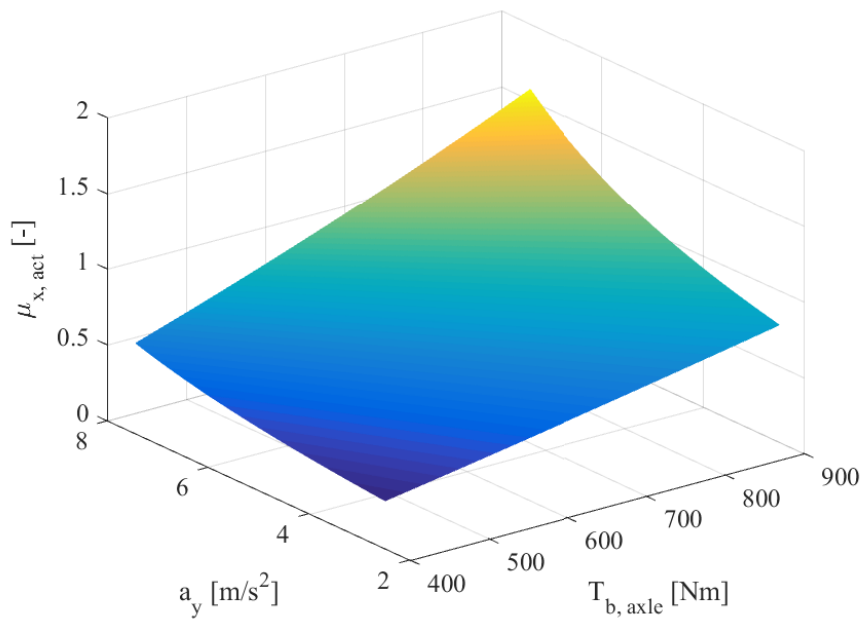
Fig. 5.8 Actual longitudinal adhesion of the least loaded wheel plotted as a function of the lateral acceleration and required rear axle braking torque.

expressing the variation of the vertical load compared to a nominal one. To be conservative, it could be convenient to assume a maximum longitudinal adherence of 80 % of μ_p. In this way, Fig. 5.8 modifies as presented in Fig. 5.9. It is noticeable how, due to the large lateral load transfers in case of high lateral accelerations, the amount of admissible rear axle required braking torque becomes very small.

Finally, the surface of ΔM_z should also be limited and the result is presented in Fig. 5.10.
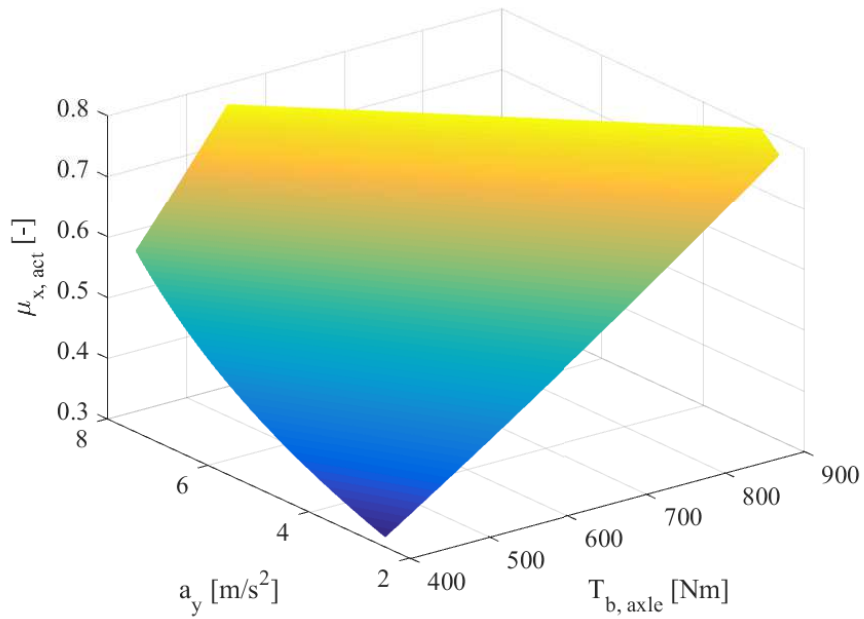
Fig. 5.9 Actual corrected longitudinal adhesion of the least loaded wheel plotted as a function of the lateral acceleration and required rear axle braking torque.
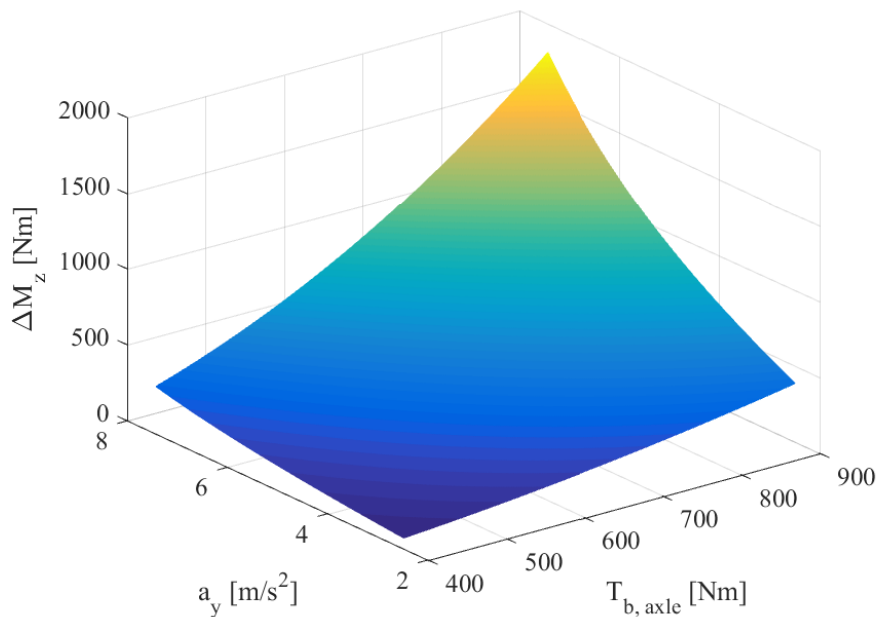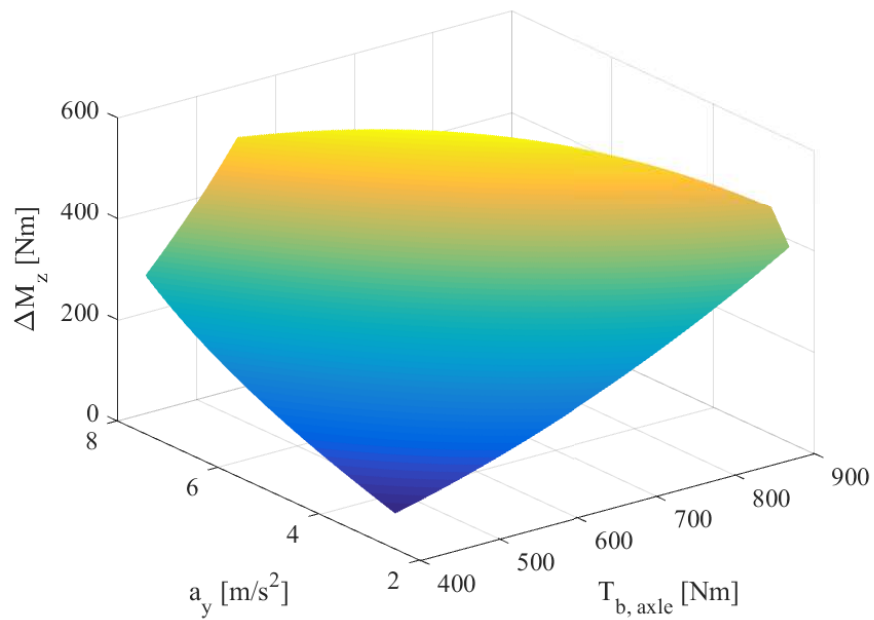

Fig. 5.10 Adherence limited yaw moment variation as a function of the application of a rear axle braking force for different driving conditions.

Therefore, an offline optimization of the electric motor usage in braking phases during cornering conditions can be performed based on the following steps:

- Select a range of vehicle speeds and lateral accelerations and compute the rear wheels sideslip angles based on the bicycle model.

- Compute the tire vertical loads based on each working condition.

- Compute the rear cornering stiffness of the tires considering the vertical loads previously computed.

- Compute ΔM_z based on Eq. 5.28.

- Compute the actual longitudinal adherence based on Eq. 5.36.

- Find the points overcoming the maximum imposed longitudinal adherence and translate these points to ΔM_z.

5.4   Braking Torque Split Strategies

Open loop maneuvers have been presented to explain the different phenomena taking place during braking in a turn events. However, closed loop controls should be implemented, expecially because of all the uncertainties around the system under analysis (tires, ground surface, external forcing functions).

Performing regenerative braking through the rear axle electric motor without any control system monitoring the main variables of interest could easily lead to instability of the vehicle even in the case of high friction surfaces.

Since the braking systems installed on - board are now two (passive braking system and rear axle electric motor), it is worthwhile to understand how to distribute the braking torque between them in order to maximize the regeneration of energy while preveserving stability.

Maximization of recovered energy translates into the major use of the rear axle electric motor which, at a certain point, should be stopped in order to limit the oversteering effect at the vehicle level. Oppositely, the conventional front/rear brake split ratio, for which the braking system is designed, guarantees vehicle stability but, in case of front engined front wheel drive vehicles, allows small amounts of rear axle braking forces.

Therefore, two baseline electric - passive braking split strategies are considered:

- *Limited EMP4 Braking*. To maximize the regeneration of energy the electric braking is activated first when the required braking torque applied by the driver is different from zero. The produced electric braking is maintained equal to the required braking torque until a lack of stability is detected. In this case, part of the required braking torque to stop the vehicle is transferred to the front passive brakes, but the amount of rear split that would be managed by the passive brakes is however produced by the electric machine.

- *EMP4 Braking with Conventional Split*. The amount of electric motor braking torque is equal to the amount of braking torque that would be applied on the rear axle in case of pure passive braking for all the whole braking maneuver.

(a) Evolution of the main quantities. (b) Energies.
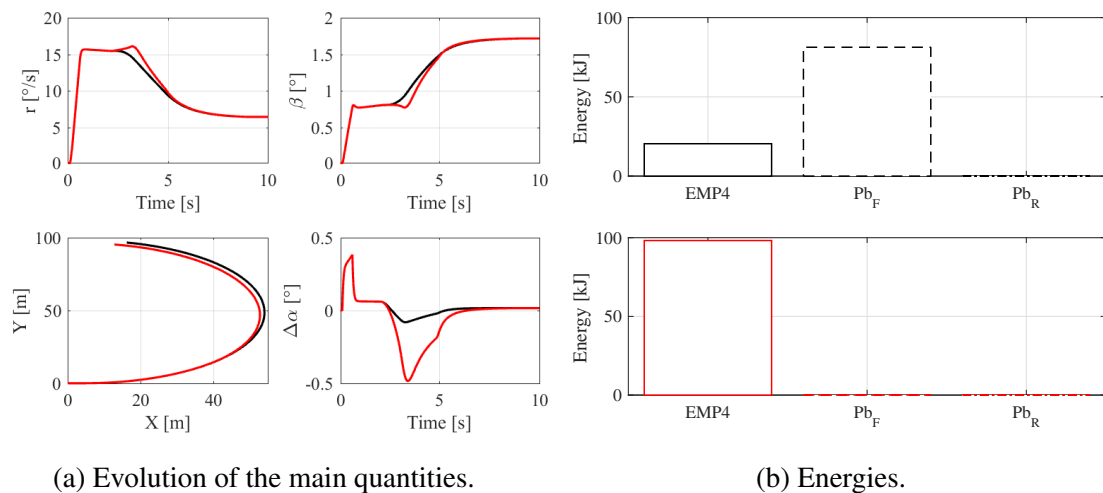
Fig. 5.11 Time evolution of yaw rate, vehicle sideslip angle, trajectory and tires sideslip angles difference between front and rear axle during a braking in a turn event starting from a vehicle speed of 50 km/h in case of required braking torque of 1000 Nm. Black curves: EMP4 Braking with Conventional Split, red curves: Limited EMP4 Braking.

Figure 5.11 shows the time evolution of yaw rate, vehicle sideslip angle, trajectory and tires sideslip angles difference between front and rear axle for a braking in a turn maneuver (initial speed 50 km/h, steering angle 40 degrees) with a required braking torque of 1000 Nm considering the two aforementioned braking split strategies. Since the maneuver does not provokes rear tires saturation, it is possible to brake the vehicle simply by applying the overall torque through the electric braking. This is demonstrated also by the energy, completely managed in case of Limited EMP4 Braking by the EMP4. However, this braking split strategy introduces a not negligible oversteering effect, demonstrated by the more closed trajectory, by the increase of the yaw rate after the application of the braking

torque (2 seconds) or by looking at the tires sideslip angles difference, negative after the application. As presented also in Fig. 5.4, the minimum longitudinal slip is realized on the RL wheel and has a magnitude close to 10 %. It is therefore expected that a slight increase of required braking torque would bring the vehicle to a complete unstable operation.

Oppositely, the EMP4 Braking with Conventional Split shows a more stable behavior with a lower oversteering tendency. This is realized simply by applying the conventional front/rear braking split considering the rear electric braking. To guarantee more stability, the regeneration of energy is much more limited as presented in Fig. 5.11b. In this case the rear longitudinal slips are clearly lower than the ones obtained with the previous braking split maneuver. This strategy is the same found in conventional vehicles, with the difference that the rear braking is electric and not passive. Passive brakes are in any case present due to the possible intervention of the ABS, which should however be considered.

In case of *Limited EMP4 Braking* strategy, it is clear that whether the lateral acceleration is high (high lateral load transfer) or the required braking torque is high (high longitudinal load transfer and applied braking force) or both, the rear longitudinal slips would be larger (in magnitude), causing a reduction of the lateral capabilities and a reduced maneuverability. In this case, a stability *detector* is required to move some braking torque from the rear to the front axle in order to avoid the complete loss of stability.

A case in which the vehicle loses its stability, due to an extended use of the rear axle braking torque is now presented. Figure 5.12 shows the time evolution of yaw rate, vehicle sideslip angle, rear longitudinal slips and tire sideslip angle difference between the front and rear axle for a braking in a turn maneuver (initial speed 50 km/h, steering angle 40 degrees) with a required braking torque of 2000 Nm, considering the two aforementioned braking split strategies. When the maneuver is performed considering the EMP4 Braking with Conventional Split, the time evolutions of the yaw rate or of the vehicle sideslip angle are regular, decreasing the former and increasing the latter without particular issues. The small oversteering tendency is verified by $\Delta\alpha$ ($\alpha_f - \alpha_r$), becoming negative after the application of the braking torque. Since a low braking torque is demanded to the rear axle, the longitudinal slips are small as well. When the same maneuver is performed with the Limited EMP4 Braking strategy in the absence of any stability detector, the vehicle loses maneuverability at about 3 seconds. the yaw rate and sideslip angle experience an increase/decrease in their amplitude before the vehicle actually starts to slow down, and this is motivated by the issues presented in Sect. 5.3.2. The RL tire longitudinal slip drastically decreases as well as the wheels' sideslip angle difference.
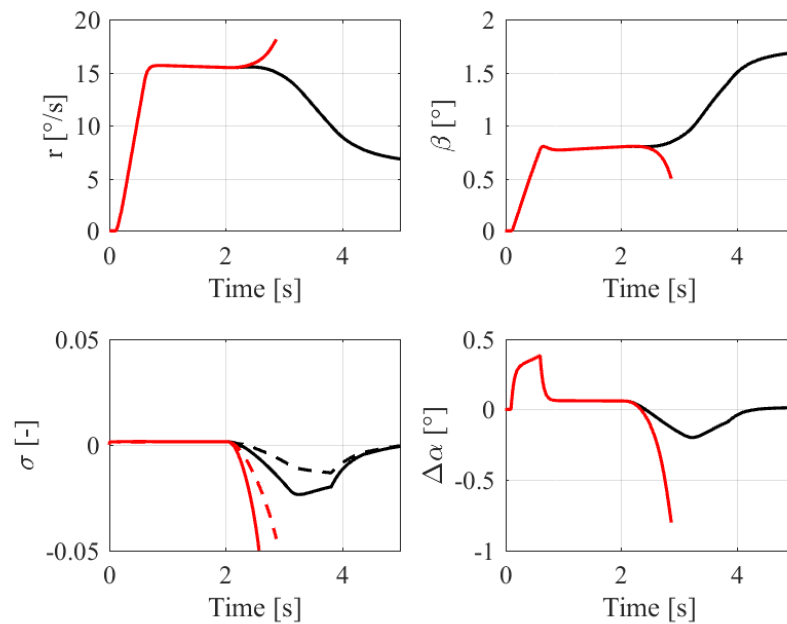
Fig. 5.12 Time evolution of yaw rate, vehicle sideslip angle, rear longitudinal slips (continuous: left tire, dashed: right tire) and tires sideslip angles difference between front and rear axle during a braking in a turn event starting from a vehicle speed of 50 km/h in case of required braking torque of 2000 Nm. Black curves: EMP4 Braking with Conventional Split, red curves: Limited EMP4 Braking.

As a matter of fact, Fig. 5.12 presents the main stability loss *detectors*, variables able to identify whether the vehicle, during these maneuvers, could encounter possible unstable conditions.

Yaw rate is the first candidate. Easily measurable due to the additional vehicle dynamics controls (VDC) installed on board, it is the main variable used by the ESP. In Fig. 5.12 it is shown how it would drastically increase during unstable conditions like the ones analyzed here. Therefore, setting particular thresholds, the use of the rear axle braking can be limited in favor of a distributed front/rear braking. However, the thresholds should be set based on empirical data or on a model that considers the adhesion variation of the tires (as the one presented in previous section).

Vehicle sideslip angle is another candidate. In particular, its time derivative is able to detect the velocity at which the vehicle tends to nose in the curve. Here again, thresholds should be established, but the main issue regarding the use of this possible detector is its availability. The vehicle sideslip angle is a variable measurable only using expensive sensors generally not installed on - board in normal production vehicles. Its estimation has

been the subject of several research studies in the last years. For these reasons it could be worthwhile to search for a different detector.

A more direct correlation between recovered energy and stability could be obtained if longitudinal slips were used as detectors for stability loss. As a matter of fact, the exploited rear slips have a direct correlation with the energy recovered since they represent the amount of adhesion at the tire - ground level. In addition, the thresholds are more easily settable since, based on the lateral - longitudinal tire behavior, a map of admissible longitudinal slips as a function of the lateral acceleration and of the required braking torque can be obtained and used for control purposes. However, the tire characteristics should be very well known. The longitudinal slip is again not directly measurable unless using expensive sensors generally not installed on - board in conventional vehicles. Nevertheless, the ABS system provides an accurate estimation for this variable which could be actually used.

The difference between front and rear tires sideslip angles $\Delta\alpha$ seems to present the best compromise between measurability and threshold setting. First of all, there is no need for estimations or particular sensors to compute it. Based on the single track bicycle model, the front and rear sideslip angles are:

$$\alpha_{\mathrm{f}} = \beta + \frac{ar}{V} - \delta \tag{5.38}$$

$$\alpha_{\mathrm{r}} = \beta - \frac{br}{V} \tag{5.39}$$

Therefore, $\Delta\alpha$ is:

$$\Delta\alpha = \frac{lr}{V} - \delta \tag{5.40}$$

thus requiring only the yaw rate, the vehicle speed and the wheels' steering angle to be measured, quantities generally present in the signal network of conventional vehicles.

Where the stability detection is concerned, as previously mentioned a rear axle braking torque introduces a fictitious yaw moment on the vehicle, causing it to present an oversteering tendency. It is well known that based on the sign of $\Delta\alpha$ the vehicle can be defined to have an understeering ($\Delta\alpha > 0$), neutral ($\Delta\alpha = 0$) and oversteering ($\Delta\alpha < 0$) tendency. The thresholds definition is therefore easily settable for any working condition (lateral acceleration or required braking torque).
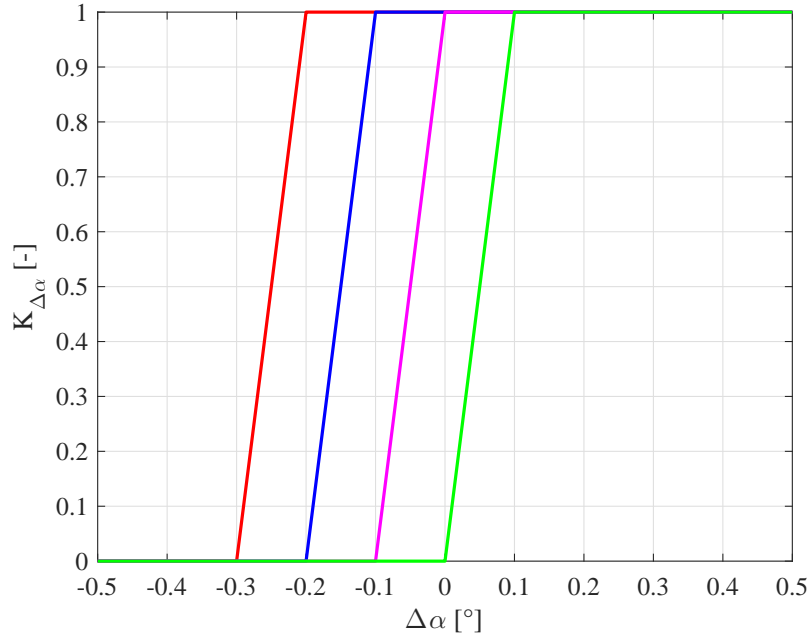
Fig. 5.13 Possible thresholds for $\Delta\alpha$. Red: 1, Blue: 2, Magenta: 3, Green: 4.

Therefore, $\Delta\alpha$ is chosen as the vehicle stability detector during a braking in a turn maneuvers. Its function is to move the braking torque from rear to front (and vice versa) based on reaching (or not) the set thresholds presented in Fig. 5.13.

Based on the selected threshold (1 - 4), the coefficient $K_{\Delta\alpha}$ is computed as a function of the actual $\Delta\alpha$. $K_{\Delta\alpha}$ is then multiplied by the required braking torque $T_{b,axle}$ to generate the variable $S_{Tb,\Delta\alpha}$:

$$S_{Tb,\Delta\alpha} = K_{\Delta\alpha}T_{b,axle} \tag{5.41}$$

This variable is compared to the required braking torque. An absence of stability issues is translated into not reaching the threshold, leading to a unitary value of $K_{\Delta\alpha}$. The variable $S_{Tb,\Delta\alpha}$ is therefore equal to the required braking torque and the braking phase can still be performed using the rear axle electric motor.

When $K_{\Delta\alpha}$ reduces under 1, the signal $S_{Tb,\Delta\alpha}$ is lower than the required braking torque. In this case, the portion of braking torque not coverable by the electric motor is transferred to the front axle. In particular, a fictitious variable expressing the amount of braking torque to be applied by the passive brakes is computed as:

$$T_{b,axle,passive} = T_{b,axle} - S_{Tb,\Delta\alpha} \tag{5.42}$$

Based on the split ratio K_{sr} of the passive brakes hydraulic plant, the front/rear axle passive braking torques are computed:

$$T_{b,f,passive}^0 = K_{sr} T_{b,axle,passive} \tag{5.43}$$

$$T_{b,r,passive}^0 = (1 - K_{sr}) T_{b,axle,passive} \tag{5.44}$$

At this point, the amount of rear axle passive braking torque can be managed by the electric motor, so that it would not be dissipated. Therefore, the rear axle electric braking torque would be:

$$T_{b,axle,EMP4} = S_{Tb,\Delta\alpha} + T_{b,r,passive}^0 \tag{5.45}$$

while the front passive one:

$$T_{b,f,passive} = T_{b,f,passive}^0 \tag{5.46}$$

In this way, the rear passive brakes will not be activated apart in the case that $T_{b,axle,EMP4}$ is higher than the maximum admissible torque provided by the electric motor (limitations in its torque - speed map). In that case the remaining rear axle braking torque can be provided by the rear passive brakes. This situation is realistic also whenever the battery state of charge is too high to avoid the recuperation of energy.

Figure 5.14 presents the time history of yaw rate, sideslip angle, longitudinal slips and $\Delta\alpha$ for *EMP4 Braking with Conventional Split* strategy (black lines) and *Limited EMP4 Braking* strategy considering the different thresholds presented in Fig. 5.13. Although the conventional split strategy is on, an oversteering behavior is however present (as observed from the negative $\Delta\alpha$, black curve). When the limited EMP4 braking strategy is on, the influence of the different selected thresholds is that of distributing more or less braking torque between the front and rear axle, based on the limit values of $\Delta\alpha$. For example, threshold 4 establishes that coefficient $K_{\Delta\alpha}$ falls to zero when $\Delta\alpha$ passes from 0.1 to 0 degrees. Based on the braking in a turn conditions under analysis (braking torque of 2000 Nm, vehicle speed of 50 km/h), $K_{\Delta\alpha}$ is always zero, meaning of rear axle braking distribution equals the conventional one. As a matter of fact, this threshold produces time responses similar to those related to the conventional split strategy. Oppositely, threshold 1 falls to zero when $\Delta\alpha$ switches from -0.2 to -0.3 degrees. In this case the rear axle braking torque is allowed until $\Delta\alpha$ reaches the value of -0.3 degrees, leading to a higher oversteering effect, as also seen from the yaw rate and the sideslip angle. Longitudinal slips are therefore automatically maintained at not dangerous values.

Figure 5.15 shows P4 and front passive brake energies for the different thresholds presented in Fig. 5.13. It is therefore verified how moving the thresholds to lower values (in negative sense) of $\Delta\alpha$ allows to increase the energy recovery however guaranteeing the vehicle stability as shown in Fig. 5.14.

(a) Yaw rate.

(b) Sideslip angle.

(c) Longitudinal slips (continuous lines: RL, dashed lines: RR).

(d) $\Delta\alpha$

Fig. 5.14 Time history of the main variables of interest for *EMP4 Braking with Conventional Split* strategy (black lines) and *Limited EMP4 Braking* strategy considering the different thresholds presented in Fig. 5.13. Braking in a turn maneuver (braking torque of 2000 Nm, vehicle speed of 50 km/h).

Fig. 5.15 P4 and front passive brakes energies for the different thresholds presented in Fig. 5.13. Braking in a turn maneuver (braking torque of 2000 Nm, vehicle speed of 50 km/h).

Figures 5.16 and 5.17 present the same $\Delta\alpha$ threshold sensitivity during a braking in a turn maneuver considering the same required braking torque (2000 Nm) starting the maneuver with an initial speed of 70 km/h. The effect of a higher initial speed reduces the lateral capabilities of the tires due to a larger lateral load transfer, therefore increasing the yaw rate and decreasing the sideslip angle even when considering the conventional split strategy. In this case the amount of oversteering tendency given just by the braking and cornering maneuver is much larger that the previous one, as demonstrated by the large peak of $\Delta\alpha$. When applying threshold 1 to 3, a peak in the yaw rate and sideslip angle appears, motivated by the larger contribution of the electric braking alone compared with the case of conventional split which, however, produces a large increase of the two variables around 3 seconds, as previously observed. This is also verified looking at the longitudinal slips. At the beginning of the braking maneuver (2 seconds) the RL slips increase until the considered $\Delta\alpha$ threshold is reached. At this point, additional braking torque is provided by the front axle but the RL slips still remain high. From 4 seconds on, depending on the considered threshold, a third peak of longitudinal slip appears since the braking torque is again provided by the electric braking only. However, since it is assumed that it is not possible to separately control the braking torques of the wheels of the same axle, the resulting oversteering effect is therefore unavoidable. Finally, the energies are directly correlated with the thresholds: the lower are the $\Delta\alpha$ thresholds, the higher is the energy recovered with the electric braking while, setting the thresholds close to zero, the

regeneration of energy is similar to the one obtainable in case of conventional braking split, provided that zero $\Delta\alpha$ is impossible to be obtained due to the just mentioned fact.

(a) Yaw rate.

(b) Sideslip angle.

(c) Longitudinal slips (continuous lines: RL, dashed lines: RR).

(d) $\Delta\alpha$
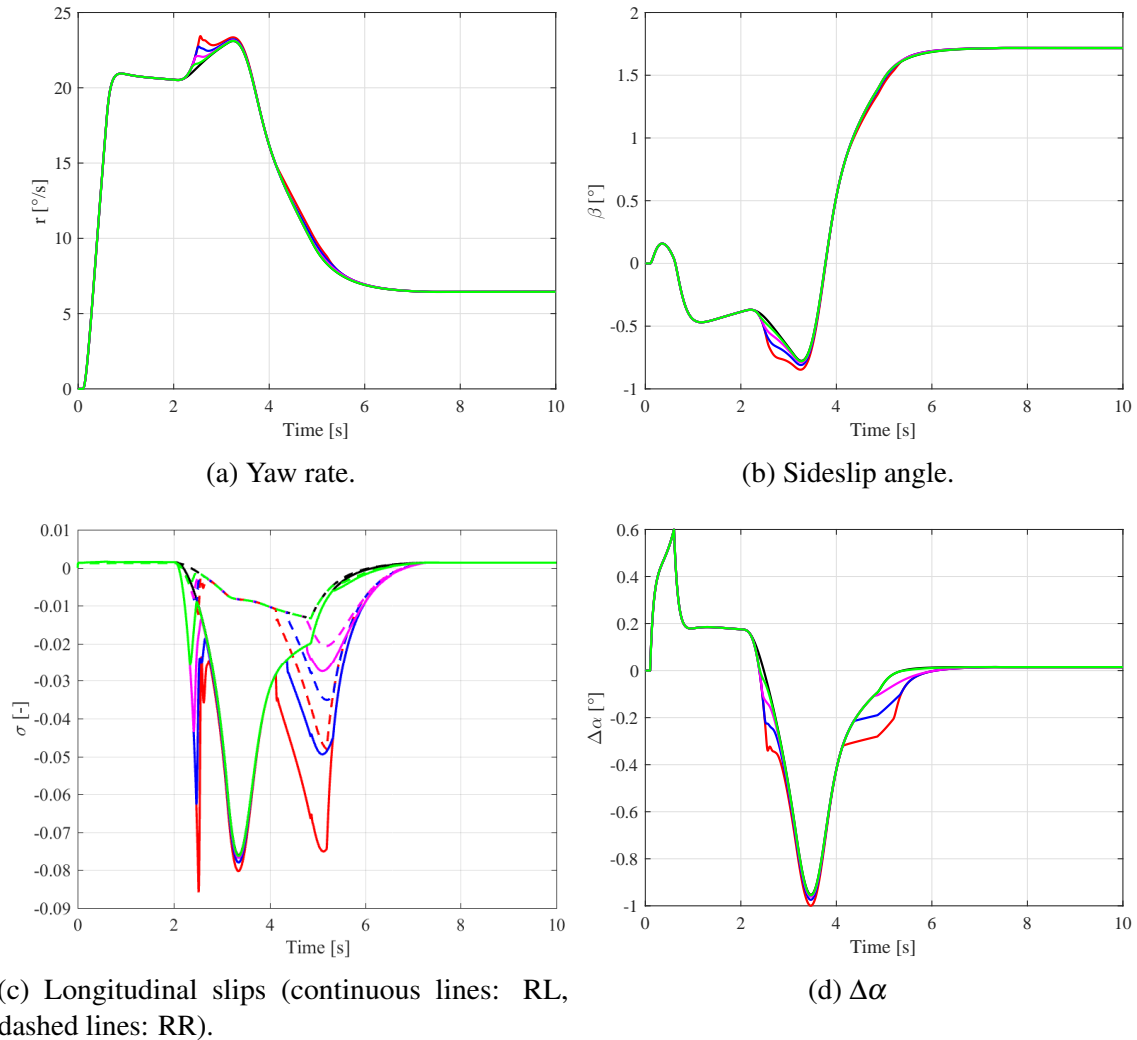
Fig. 5.16 Time history of the main variables of interest for *EMP4 Braking with Conventional Split* strategy (black lines) and *Limited EMP4 Braking* strategy considering the different thresholds presented in Fig. 5.13. Braking in a turn maneuver (braking torque of 2000 Nm, vehicle speed of 70 km/h).
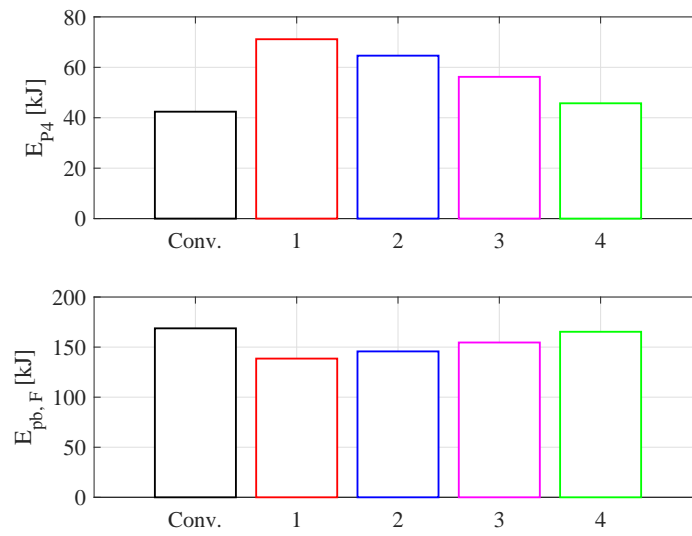
Fig. 5.17 P4 and front passive brakes energies for the different thresholds presented in Fig. 5.13. Braking in a turn maneuver (braking torque of 2000 Nm, vehicle speed of 70 km/h).

Another interesting sensitivity analysis is regarding the inclination of the thresholds presented in Fig. 5.13.
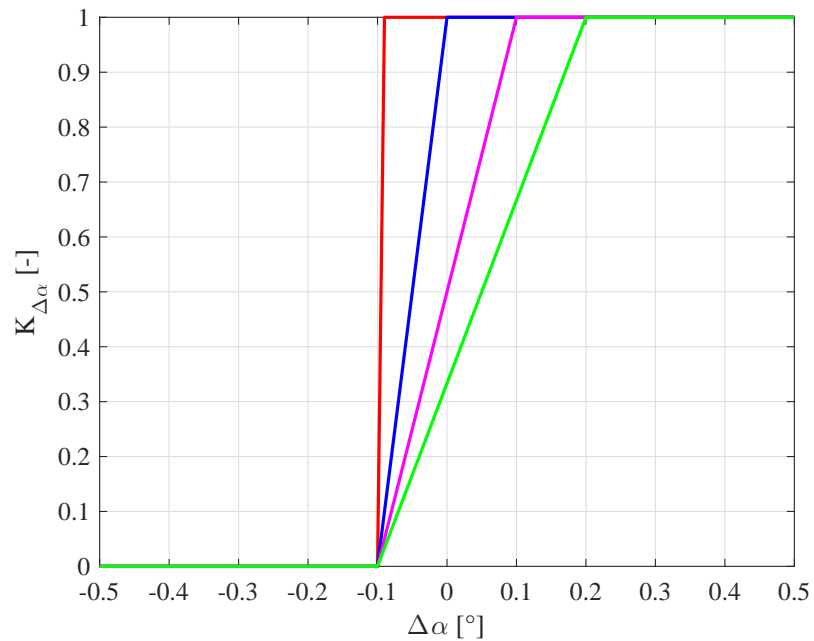
Fig. 5.18 Possible thresholds for $\Delta\alpha$. Red: 1, Blue: 2, Magenta: 3, Green: 4.

Figure 5.18 presents the coefficient $K_{\Delta\alpha}$ as a function of $\Delta\alpha$ for different slopes. The revious braking in a turn maneuver considering a required braking torque of 2000 Nm and an initial vehicle speed of 50 km/h is again under analysis.

(a) Yaw rate.

(b) Sideslip angle.

(c) Longitudinal slips (continuous lines: RL, dashed lines: RR).
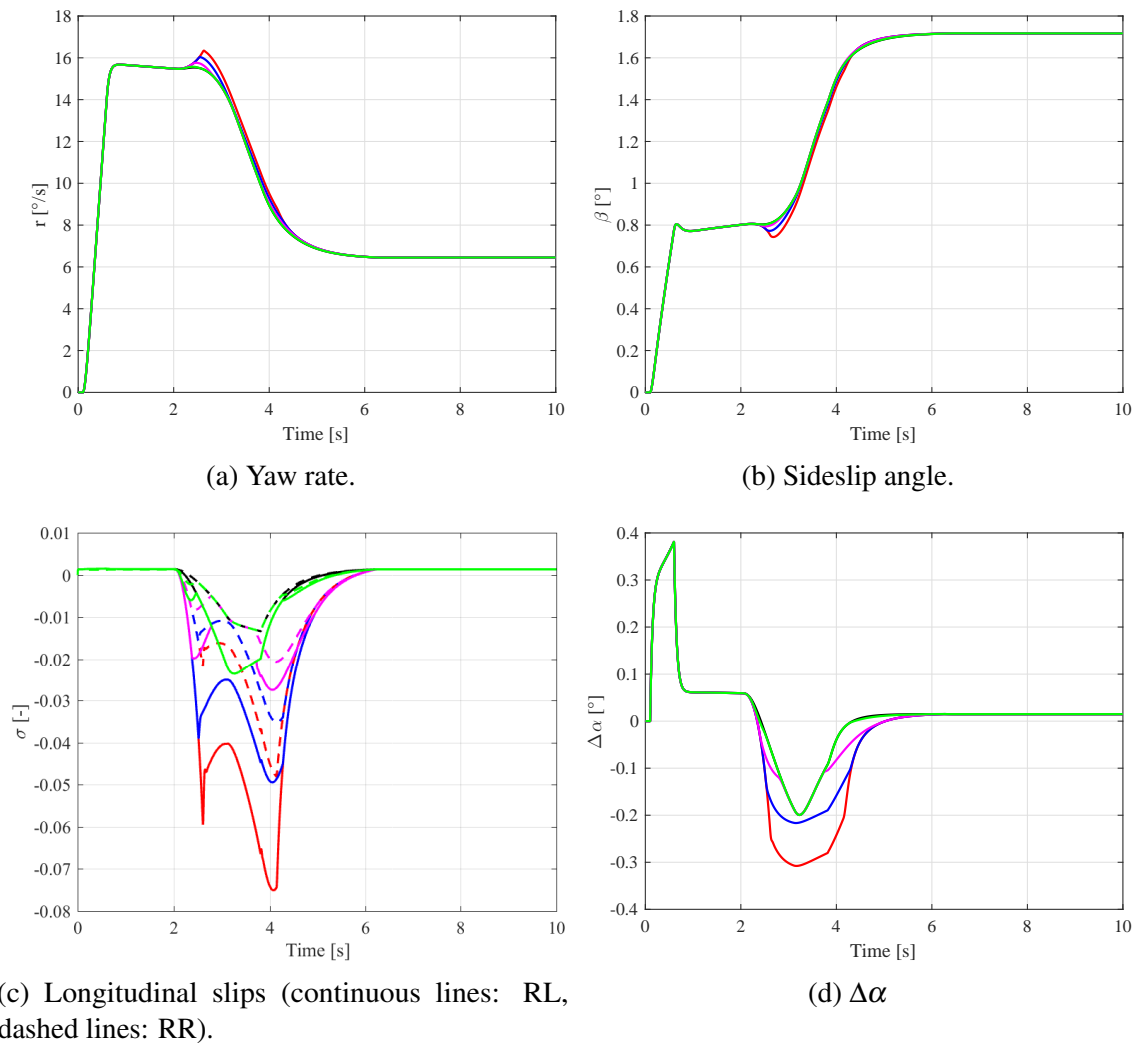
(d) $\Delta\alpha$
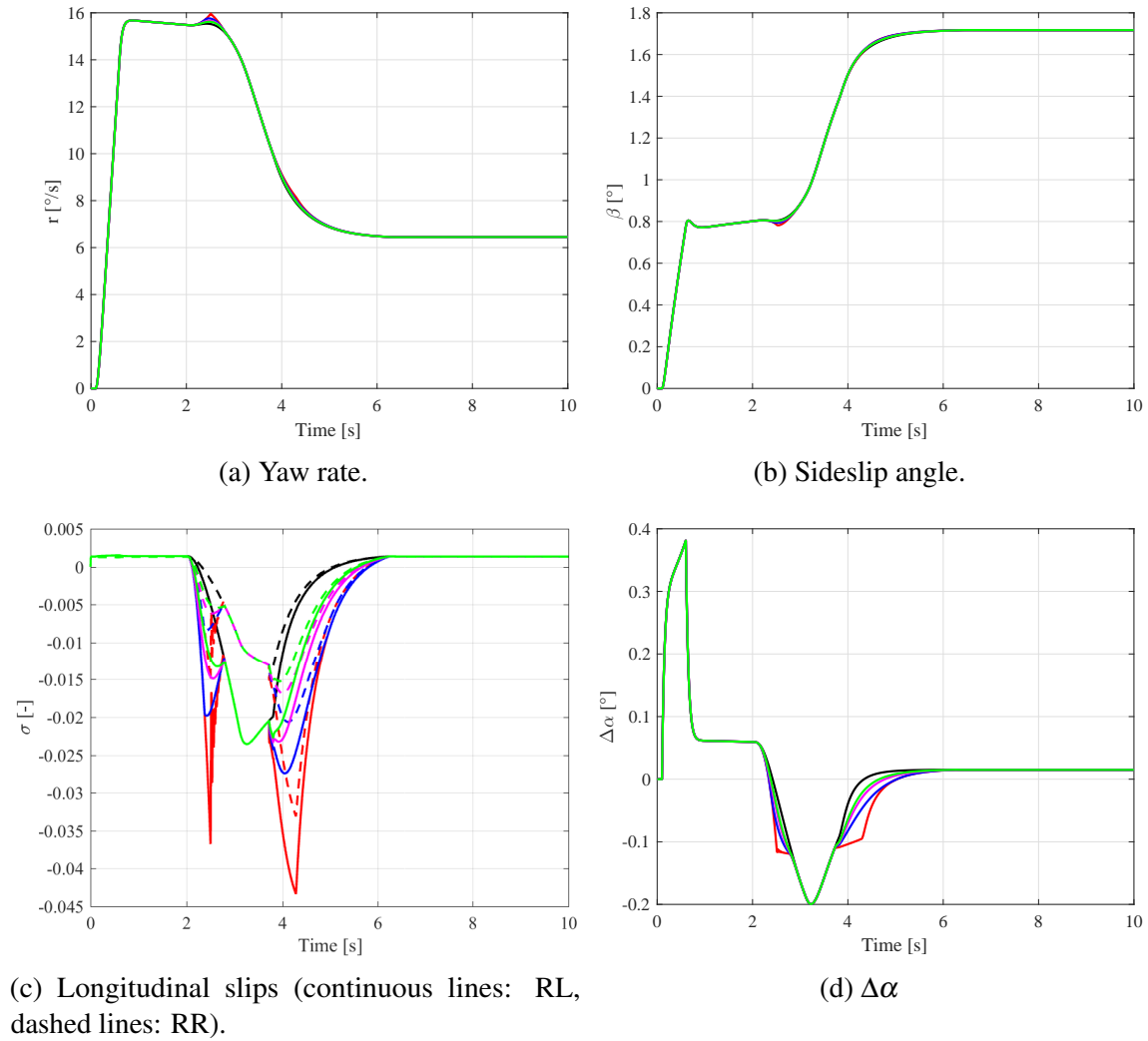
Fig. 5.19 Time history of the main variables of interest for *EMP4 Braking with Conventional Split* strategy (black lines) and *Limited EMP4 Braking* strategy considering the different thresholds presented in Fig. 5.18. Braking in a turn maneuver (braking torque of 2000 Nm, vehicle speed of 50 km/h).
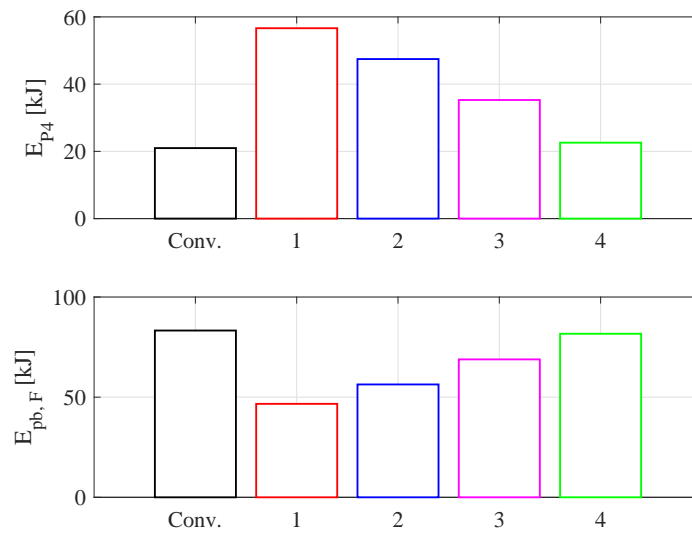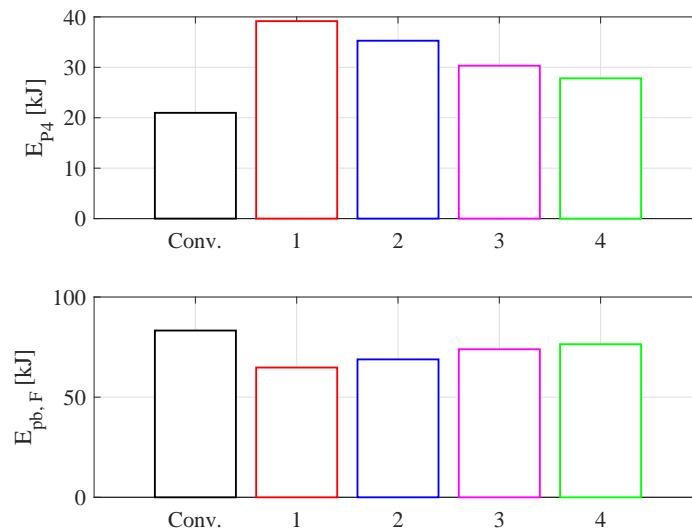
Fig. 5.20 P4 and front passive brakes energies for the different thresholds presented in Fig. 5.18. Braking in a turn maneuver (braking torque of 2000 Nm, vehicle speed of 50 km/h).

Figure 5.19 shows the time histories of the variables under analysis in case of the thresholds of Fig. 5.18. All of them force the coefficient $K_{\Delta\alpha}$ to be zero when $\Delta\alpha$ equals to -0.1 degrees. The difference between them is that the former can start to be lower than one close to -0.1 (threshold 1) or far from it (threshold 4). This means that in case 1, the electric braking alone is maintained for longer time than in case 4, which starts to be limited when $\Delta\alpha$ is still positive.

The results are in line with expectations and shows larger exploited longitudinal slips in case of threshold 1 with coherent increase/decrease of yaw rate and sideslip angle during the application of the electric braking alone. Passing from threshold 1 to 4, the time responses are much more similar with the ones obtained in case of conventional split.

The difference between front and rear tire sideslip angles has been selected as a stability detector to limit the electric braking during cornering maneuvers in order to guarantee a considerable amount of energy regeneration without losing vehicle stability and maneuverabiliy. It is actually the unique parameter that offers the possibility to impose objective stability limit thresholds without resorting to estimation techniques, which are not always reliable if different and various driving conditions are accounted for.

The sensitivity of the different $\Delta\alpha$ thresholds has been performed to show how they can affect the utilization of longitudinal adhesion of the tires without actually measuring or estimating any of the quantities related to it. However, a more in - depth analysis regarding which thresholds to apply based on any driving condition should be performed.

In order to maximize the regeneration of energy during cornering maneuvers, the braking torque split strategy could be designed to distribute the front and rear braking torques on the basis of the aforementioned detector, according to the vehicle lateral dynamics, but able to have impacts on the longitudinal braking behavior. The use of front/rear sideslip angle difference as a stability detector for braking in a turn maneuvers constitutes the main contribution of this chapter, but clearly requires experimental validations to prove its reliability.

In this section only the possibility to switch between pure electric rear axle braking and electric braking with conventional split has been considered. Since the individual control of the wheel torques is not possible, a certain amount of oversteering during the braking phase will always appear. In addition, it has been shown that the combined lateral and longitudinal driving conditions can affect the vehicle stability (and therefore introduce oversteer) even in the case of relatively low required braking torques.

As an example, the reference $\Delta\alpha$ could actually be imposed to be always equal to zero in order to avoid oversteering and guaranteeing the vehicle (in worst case) to behave as a neutral one. However, once the threshold $\Delta\alpha = 0$ is reached, the conventional braking distribution takes place and the oversteering tendency is therefore unavoidable. As previously presented, $\Delta\alpha$ is always negative during the braking phase.

The need for integration between hybrid vehicle torque split strategies and on - board normal production VDC systems can offer a higher number of degrees of freedom to be utilized with in order to improve the vehicle safety. Therefore, both the overall braking plant and its relative control systems should be re - designed and adapted for the integration of focused electric motor control strategies. In this way, a possible idea can be to exploit the capabilities of commercial electronic stability programs in parallel with the braking split strategies described in this section to overcome the unavoidable oversteering effect encountered when considering a conventional braking torque distribution. In addition, the presence of the ABS as the main active system should be considered in order to avoid that certain braking torques would cause one or more wheels to slip. In a control system schematic, it should let the required braking torque to be sent to the braking torque split strategy during all the cases in which it does not detect any wheel slip. Otherwise, it should intervene to properly control the wheels brake torques.

5.5   Conclusions and Future Works

In this chapter, an extension of the canonical working modes for hybrid electric vehicles has been analyzed and studied under different points of view. The possibility to recover energy during braking phases in the presence of lateral accelerations has high importance since, otherwise, the available kinetic energy would be dissipated by the passive brakes. However, several drawbacks concerning the vehicle stability emerge when extending the rear axle regenerative braking to these conditions.

An 8 DOF vehicle model including longitudinal, lateral, yaw and roll motion as well as the wheels' rotational dynamics has been built considering a combined slip tire model and accurate computation of lateral and longitudinal load transfer.

Open loop maneuvers have been first performed to give a more clear comprehension of the different phenomena influencing the vehicle dynamics. An increase of the vehicle yaw rate as well as a reduction of the sideslip angle is highlighted after the application of a rear axle braking torque. The vehicle perceives a yaw acceleration and tends to be pushed inwards the curve, clear exhibition of an oversteering tendency.

An important contribution of this chapter is therefore given by the computation of the braking torque to yaw moment gain. A simplified model for the vehicle yaw motion is considered, as well as the lateral - longitudinal tire forces interactions, implemented through the elliptic approximation. The difference between the yaw moment computed in case of rear axle braking and the one considering steady state cornering constitutes the introduced yaw moment which causes the vehicle to be pushed inwards the curve, and can be plotted as a function of the lateral acceleration of the vehicle in steady state cornering conditions and of the required braking torque. The knowledge of the amount of introduced yaw moment could be of interest when dealing with control strategies for enhanced vehicle dynamics. Furthermore, it represent an exhaustive representation since it takes into account the lateral - longitudinal tire interactions.

The final section of this chapter is devoted to understand how to control the rear axle regenerative braking in order to guarantee the vehicle stability trying to maximize the regeneration of energy. Two braking torque split strategies have been analyzed. In the first one, the amount of rear axle electric braking torque is equal to the amount of braking torque that would be applied in case of passive friction brakes, given a constant apportionment between front and rear braking contributions. In the second one, the electric braking torque is firstly activated until a possible lack of stability is detected, with a following partialization of the rear axle braking torque. The stability detector considered in the analysis is the difference between front and rear sideslip angles, a parameter easily

computable since requires few quantities already acquired on board. A sensitivity analysis regarding the thresholds to be imposed on this parameter for limiting the rear axle electric braking torque has been presented, evidencing the need of integration between hybrid braking split strategies with normal production VDC control systems in order to improve the vehicle safety and maneuverability without losing the possibility to recover consistent amount of energy.

Future works include the study of blending strategies for braking maneuvers between electric motor and passive brakes systems with the possibility to individually control the friction braking forces on the wheels in order to reduce oversteering effects while maximizing the energy recovery.

Chapter 6

Driveability Aspects and Perspectives

As the last subject of this thesis work, the analysis of the hybrid electric vehicle architecture is focused on issues related to the longitudinal driving comfort. Specifically speaking, the characteristics of a vehicle concerning its ability to fastly respond to the driver inputs without affecting his own vibrational comfort is known by the name of driveability.

In this chapter, the concept of driveability in passenger cars will be introduced, specifying the issues related to this subject. Then, driveability is analyzed through the use of a dynamic model specifically built for these purposes. It will be presented a formal methodology for the analysis of a conventional powertrain where its vibrational behavior is concerned, together with simplified techniques for the evaluation of the driveability. Additional analysis examines the sensitivity of passive powertrain components parameters (such as stiffness or damping elements) on the improvements of the vehicle driveability.

Finally, the usage of the rear axle electric machine as an active actuator to control the longitudinal dynamics is considered as a future perspective regarding driveability enhancements. The presence of the electric motor improves the fuel economy but could also be used to achieve a better driveability if a proper control strategy is implemented. The present chapter, however, is limited to modeling and system dynamics analyses; control issues are not dealt but are considered as future developments.

It is underlined that part of the work described in this chapter has been previously published in [89] and [90].

6.1 Introduction

Driveability describes the complex interactions between the driver and the vehicle where the transmission of vibrations from the latter to the former is concerned. In general, it expresses the ability of the vehicle (but more in general of the powertrain) to reduce as much as possible the transmissibility of vibrations which either itself or the internal combustion engine is producing.

The concept of driveability is directly linked to the driver comfort due to implications regarding the transmitted vibrations, but also to the vehicle performance because it is a measure of how fast the vehicle would respond to a certain driver input.

Today, driver comfort perception is a criterion that strongly affects the marketability and the competitiveness of passenger cars. Since, however, it is related to subjective perceptions, the trend is to translate particular measured metrics into objective evaluation criteria [88].

Generally speaking, driveability is a subject that mostly regards the powertrain system of a vehicle. A simple example is presented to clarify this statement. Suppose now to drive a vehicle at constant speed, with a fixed gear engaged. If, suddenly, the accelerator pedal is strongly pushed, immediately the request of an additional torque to be provided is sent to the electronic control unit (ECU), which receives this information and sets the specific actions to be realized (e. g. throttle valve opening). Due to the combustion process and the mechanical inertia of the engine, a lag of time is therefore observed between the driver request (accelerator pedal) and the effective mechanical torque production (presence of a non zero longitudinal acceleration). Thus, the longitudinal acceleration will increase in time with a certain slope until a steady state condition is reached. As a direct example, the slope of the acceleration is a measure of how fast the powertrain is able to transform the engine torque into an acceleration. It is clear that the stiffer is the powertrain, once the torque is available at the engine shaft, the sooner the vehicle would accelerate and reach a certain speed.

Oppositely, a stiffer powertrain will have a negative influence on the vibratory behavior of the vehicle itself. Considering a step of the engine input torque, a stiffer powertrain can lead to higher oscillations of longitudinal acceleration, affecting the driving comfort.

Another example can be related to the ability of the powertrain to attenuate the induced vibrations coming from the non smooth engine torque. Due to its internal construction, it is well known that the engine torque contains a consistent amount of harmonics. If not properly attenuated or even canceled, these can be transmitted to the driver, causing then a

misconfort. The proper introduction of passive filtering powertrain components can solve these issues.

These simple examples allow the understanding that driveability can be improved by acting on powertrain parameters (including engine injection strategies), and should include comfort and performance characteristics.

A passenger car's driveability is mainly evaluated and improved by means of a large amount of track tests, in which calibration processes of the ICE control algorithms or fine tunings of each driveline's element take place. Since the *time to market* is becoming extremely important where the introduction of a product in the market is concerned, the actual car makers' needs are related to the development of accurate mathematical models able to reproduce the more relevant driveability phenomena, in addition to the application of standard techniques helpful for the comprehension of which powertrain parameters could lead to a driveability improvement. The satisfaction of these needs could bring to a reduction in the number of tests on prototypes and of the development costs.

A literature review regarding the dynamic models developed for driveability analysis is presented in the following.

Couderc et al. [91] showed the need of having a nonlinear model especially for the study of the gear mesh, clearances and clutch friction effects. The lumped parameter model includes the torsional degrees of freedom of flywheel, clutch assembly, gearbox, differential, half shafts, wheels and vehicle inertia as well as the longitudinal degrees of freedom of vehicle chassis and engine block. The wheels are assumed to be connected to the ground, with negligible slip. Linearised equations allow a frequency domain analysis.

Capitani et al. [92] underlined that the main driveability information have to be searched for in a range of frequencies around 10 Hz. They emphasised the presence of different resonances in the longitudinal acceleration spectrum at around $4 - 5$ Hz (as a function of the engaged gear) and at about twice that value. A nine degrees of freedom dynamic model is proposed, while a simplified two degrees of freedom model including engine inertia and equivalent vehicle inertia connected by stiffness and damping can be used for control design purposes.

Sorniotti [93] analysed driveline models with different level of complexity. The simplest one includes just the compliance of the half shafts and a sensitivity analysis regarding the impact of their stiffness on the longitudinal acceleration response is presented. A more detailed model considers the chassis dynamics including the suspension and engine mounts. A deep sensitivity analysis has then been performed demonstrating that a signifi-

cant coupling occurs between sprung/unsprung mass and the engine/gearbox/differential group.

Galvagno et al. [94] considered a P4 HEV architecture, analyzed from the driveability point of view. A 16 degrees of freedom coupled torsional – longitudinal linear dynamic model is adopted to study the frequency response function between engine torque (input) and seat longitudinal acceleration (output), showing the presence of the first natural frequency of the transmission in the range of 1–10Hz, depending on the gear ratio.

Several models are therefore present in literature, each one presenting a certain peculiarity (i.e. the modeling of a certain component rather than another). Different analyses have also been performed, showing the influences of the variation of one or more powertrain parameters on the driveability characteristics of a passenger vehicle.

What seems to be missing is a comprehensive model capable of reproducing all the desired phenomena in the relevant frequency range for driveability analysis (up to 30 Hz) in addition to a unified methodology aimed at the comprehension of which powertrain parameters are able to improve it.

6.2   Vehicle Model and Validation

Figure 6.1 shows the general block diagram representation of the model. The main inputs to the model are the torque coming from the ICE (T_{ice}) after having removed the belt drive losses and the generalized external forces F_{ext}, that take aerodynamic, grade and rolling resistances into account. The model is split into a linear and a nonlinear block.
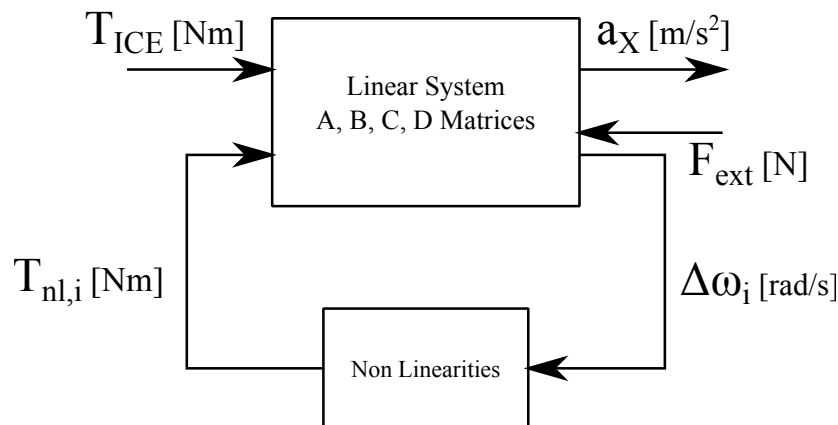
Fig. 6.1 Block diagram schematization of the model

The linear system block includes all linear contributions to the model (written in state space form in terms of its state, input and output matrices A, B, C, D).

The nonlinear effects are included by a feedback block that takes the relative speed (linear or rotational) across the nonlinear elements to determine the corresponding nonlinear efforts (forces or torques). Making reference to Fig. 6.2 the vehicle model is now described in detail.

6.2.1   Driveline

As mentioned before, driveability is an issue related mostly to the vehicle powertrain. An accurate modeling of the driveline is therefore required including all the components aimed at filtering the vibrations induced by the ICE.

The dual mass flywheel (DMFW), as an example, is the main filtering component in the overall driveline. Its assembly, characterised by a primary and a secondary inertia connected by different spans of arc springs including different dead bands, is thought to develop a proper nonlinear stiffness characteristic. This is required to be compliant both with the goal of transmitting the torque to the rest of the powertrain and to decouple the engine with the rest of the driveline. In addition, the springs are tuned soft enough to provide a low frequency resonance. Finally, Coulombian friction is introduced to contribute to the dissipations of the vibrational energy. For this reasons, the DMFW should be strictly included in a model for driveability analysis.

Half shafts are, together with the DMWF, the main compliances of the driveline, therefore governing the low frequency response of the system. Their modeling is trivial but fundamental.

Tires can be considered as dissipative components too as their dynamic characteristics can affect the dynamic behavior of the overall powertrain, as will be shown in next section.

Finally, the entire engine and transmission block should be considered in the modeling, together with its connection to the vehicle frame. During driving conditions the differential output torque is reacted by the engine mounting system, which transfer loads on the vehicle frame. It is therefore compulsory to investigate the interactions between the two from the dynamic point of view.

With reference to Fig. 6.2, the developed vehicle dynamic model for driveability analysis is presented.

The engine inertia and primary DMFW inertia are merged together in one flywheel (J_1). The clutch cover is merged with the secondary inertia of the DMFW (J_2). The DMFW nonlinear spring stiffness (Fig. 6.3a) is k_1 while damper c_1 models the viscous losses in parallel to it. The Coulombian friction is modeled with a hyperbolic tangent function:

$$T_{\text{DMFW,fric}} = C \cdot \tanh\left(\frac{\Delta\omega_{12}}{\omega_{\text{ref},1}}\right) \tag{6.1}$$

where $\Delta\omega_{12}$ is the relative angular speed between flywheels J_1 and J_2. C and $\omega_{\text{ref},1}$ have been identified from the experimentally measured hysteresis cycles of the DMFW characteristic.
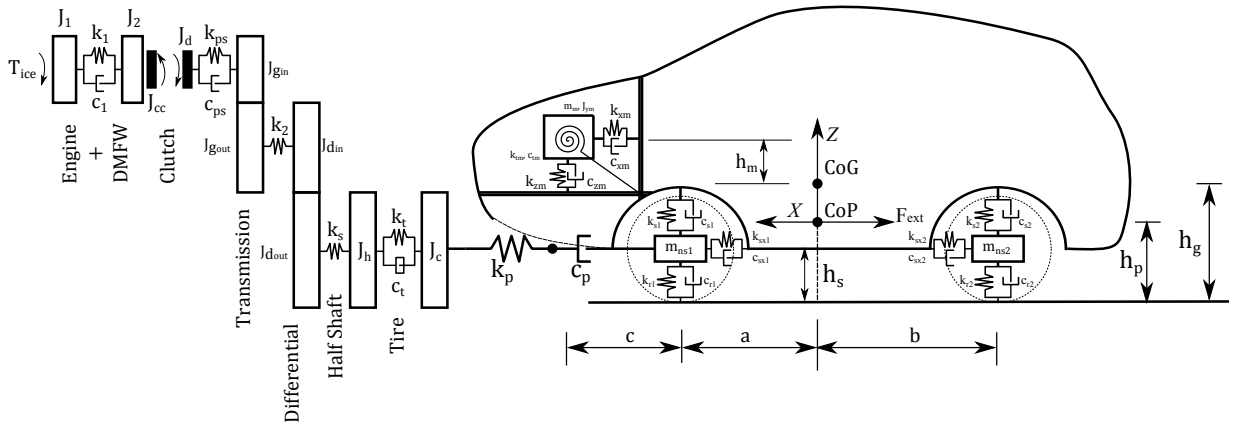
Fig. 6.2 Coupled torsional - longitudinal dynamic model.

The clutch torque T_c is modeled as a bilinear function of the relative angular speed ($\Delta\omega_{2d}$) between J_2 and J_d (clutch disc inertia), modulated by the axial load F of the clutch actuation systems:

$$T_c = nfFr_m \cdot f\left(\Delta\omega_{2d}\right) \tag{6.2}$$

where $f\left(\Delta\omega_{2d}\right)$ is a slip function described as:

$$f\left(\Delta\omega_{2d}\right) = \begin{cases} c_{c1}\Delta\omega_{2d} & \text{if } |\Delta\omega_{2d}| < \Delta\omega_0 \\ c_{c2} & \text{if } |\Delta\omega_{2d}| \geq \Delta\omega_0 \end{cases} \tag{6.3}$$

n is the number of surfaces in contact, f is the friction coefficient between the friction surfaces, r_m is the mean value of the disc radius, $\Delta\omega_0$ is a reference speed value and c_{c1} and c_{c2} are experimentally measured slip values. The clutch pedal position is translated into the actual axial load F by means of an experimental curve that characterizes the clutch actuation system. It is implemented in the model non linearities (Fig.6.1).
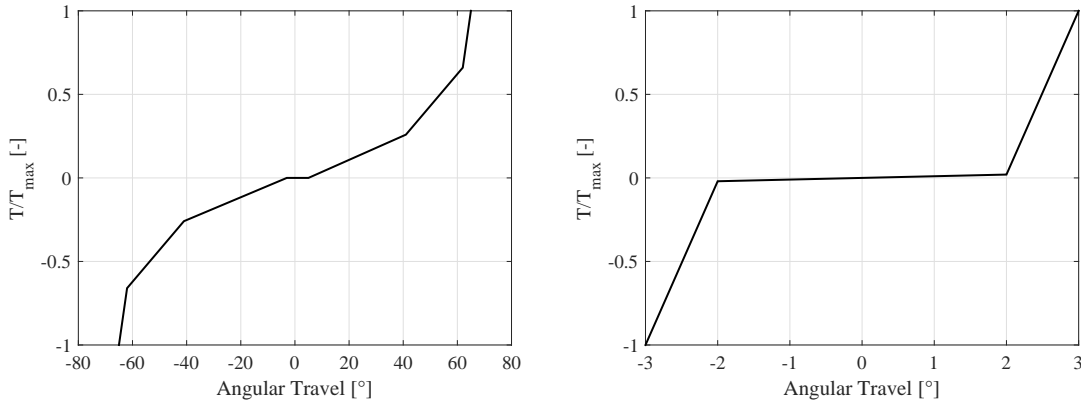
(a) Nonlinear DMFW stiffness characteristics.

(b) Nonlinear clutch stiffness characteristics.

Fig. 6.3 Nonlinear DMFW and clutch stiffness characteristics.

Clutch characteristics are modeled with the nonlinear spring k_{ps} (Fig. 6.3b) and viscous damper c_{ps}. A standard six gear manual transmission is considered with the active stage of reduction (two flywheels, J_{gin} and J_{gout}) according to the engaged gear. Final reduction is modeled as fixed transmission ratio with associated inertias J_{din} and J_{dout}. The transmission shaft stiffness is modeled by spring k_2.

The half shafts are modeled as springs with stiffness k_s. They connect the carrier of the differential to the wheel hub. The hub and tire belt inertias (J_h and J_c) are connected to the torsional stiffness and damping of the belt itself (k_t and c_t). The tire contact forces couple the torsional and longitudinal dynamic behavior. As described in [95] they are modeled as a series connection of a spring and a viscous damper to take slip and relaxation length into account. This behavior can be described by a first order differential equation in terms of the longitudinal contact force F_x as a function of the unsprung mass speed V_{us} and tire belt speed $\omega_c R$:

$$\frac{dF_x}{dt} + \frac{k_p}{c_p}F_x = V_{us} - \omega_c R \tag{6.4}$$

where k_p is the tire longitudinal stiffness and c_p is the longitudinal slip coefficient. The expressions for k_p and c_p are the following:

$$k_p = \frac{b_w \cdot F_z}{a_w}; \qquad c_p = \frac{b_w \cdot F_z}{V_x} \tag{6.5}$$

where b_w is the slope of the $\mu_x - \sigma$ curve of the tire (longitudinal adhesion vs longitudinal slip), F_z is the vertical load including the effect of the load transfer due to longitudinal accelerations, a_w is half length of the contact patch and V_x is the longitudinal vehicle speed.

The engine and transmission case is modeled as a rigid body with mass and polar moment of inertia (m_m, J_{ym}), connected to the sprung mass by means of *engine mounts* with linear longitudinal, vertical and torsional stiffness and damping characteristics (k_{xm}, k_{zm}, k_{tm} and c_{xm}, c_{zm}, c_{tm}). Yaw and roll engine mounts properties are neglected due to the absence of such generated motions in the model [96].

6.2.2 Chassis

.

The vehicle chassis is comprehensive of the vehicle frame and all the subcomponents attached to it (e. g. steering system, suspension systems). From the dynamic point of view, the frame can be considered as a flexible body, having its own stiffness and structural damping. However, where the driveability is concerned, the frequency range of interest is much smaller than the one related to the frame resonance frequencies. Therefore, the vehicle body is considered rigid with its own mass and inertia while the chassis components are attached to it by means of flexible connections.

Vertical suspension characteristics are modeled as a parallel connection of springs and dampers (k_{s1}, k_{s2} and c_{s1}, c_{s2}), connected to the sprung (m_s) and the unsprung masses (m_{ns1} and m_{ns2}). The sprung mass rotates in its pitch motion around the pitch centre (*CoP*). Longitudinal suspension characteristics are taken into account by linear spring and damper elements (k_{sx1}, k_{sx2} and c_{sx1}, c_{sx2}). They take into account the longitudinal compliance of the elastomeric bushings of the suspension arms and the bushings of the subframe. Vertical stiffnesses and dampings of the tires are modeled with springs k_{r1}, k_{r2} and dampings c_{r1}, c_{r2}. The road is considered dry and flat with no vertical irregularities.

Synchronizers are not included in the model because incorrect engagement maneuvers are not taken into account. For a given gear, the linear portion of the system is represented in state space in terms of its A, B, C, D matrices. The change between two different gears is simulated by changing these matrices according to the appropriate transmission ratio.

Nonlinear characteristics such as those of the DMFW are implemented as look up tables. Alternatively they are linearized with their local slope corresponding to a given torque level. Similarly, the tire characteristics are linearized considering a given vertical load and vehicle speed V_x.

6.2.3 Model Validation

The model validation is performed both in time and in the frequency domain, to verify that the model is robust enough to reproduce the desired phenomena in the relevant frequency range for driveability analysis (up to 30 Hz). To this end, the experimental acceleration (acquired by means of an AVL Data Acquisition System using a 3-axis accelerometer ASC 5521 with 0–5V analog input sampled at 100 Hz) is compared with the one predicted by the model. Two numerical results are considered: linearized and fully nonlinear. The former is a version of the model in which the nonlinear characteristics of the powertrain components are linearized on their local slopes or at a certain vehicle speed, the latter includes all the nonlinear contributions.

The experimental campaign has been performed by the industrial partner of the project. The description of the measurement procedures have not been provided due to confidentiality reasons.

(a) Tip in Tip out.

(b) Gearshift.

(c) Motoring and Full Load.

(d) Up: Motoring and Full Load (different time frame), Down: FFT of the numerical acceleration.
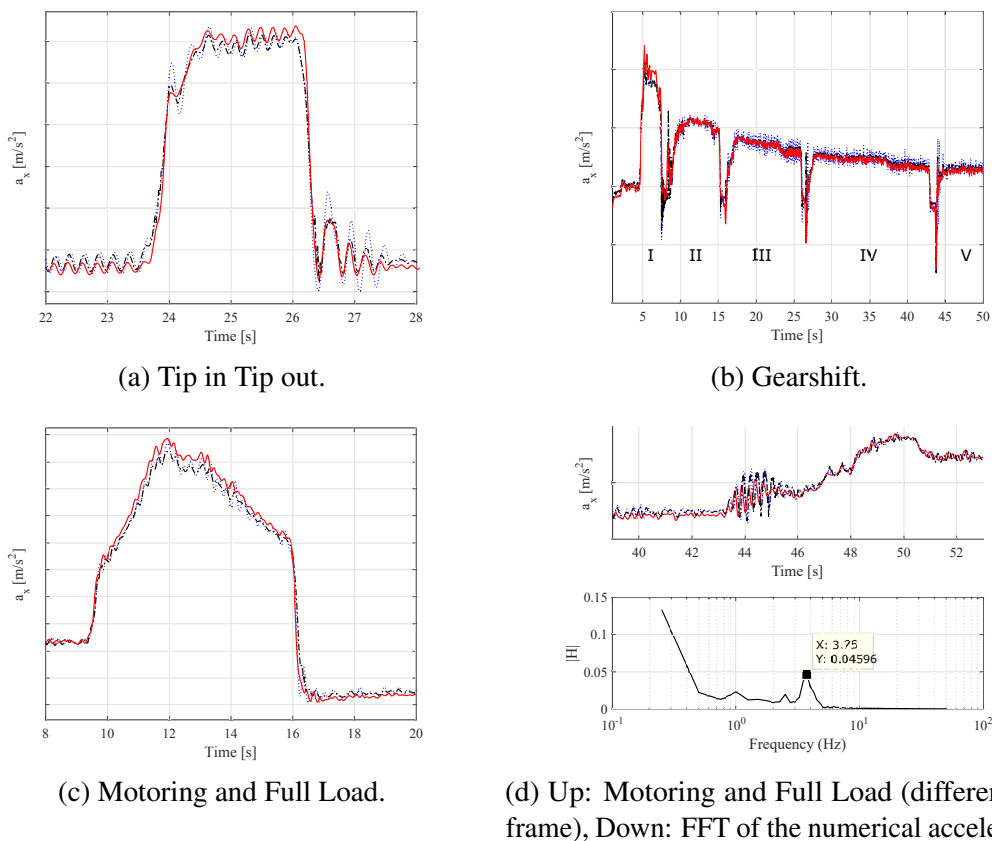
Fig. 6.4 Vehicle longitudinal acceleration, comparison between numerical and experimental results (dotted blue: numerical linear model, dashed dotted black: numerical nonlinear model, continuous red: experimental). y - axis ticks are omitted for confidentiality reasons.

Figure 6.4 presents a part of the time domain validation performed on the developed model, in which different manoeuvres have been considered. Fig. 6.4a shows the comparison between numerical and experimental longitudinal accelerations during a tip in - tip out manoeuvre performed in 2nd gear. Both the linear and the nonlinear model seem to present a good fit both in the tip in and in the tip out phase although the linear model shows a less damped response, justified by the fact that it does not account for the damping contributions of the nonlinear components. Oppositely, the nonlinear model is much more able to fit the experimental data.

A gearshift manoeuvre (Fig. 6.4b) has also been tested acquiring the longitudinal acceleration. The correlation between numerical and experimental results is good in these phases too, presenting the same behaviour regarding the linear and the nonlinear model.

Numerical and experimental longitudinal acceleration during a full load test in 2nd gear is compared in Figure 6.4c. Since the manoeuvre is less impulsive than a tip in - tip out, it does not produce large vibration oscillations. In this case the difference regarding the correlation between experimental and linear/nonlinear numerical results is marginal. Focusing on a different time frame (Fig. 6.4d), rather strong oscillations are instead observed. In this phase the engine is in the motoring condition and its torque contains a consistent amount of frequency contributions. If not properly attenuated, these can be transmitted to the powertrain and therefore to the driver. The model can be considered reliable also for these phases, but particular attention should be paid regarding the frequency of the oscillations at about 44 s of the simulation. A fast Fourier transform (FFT) of the numerical acceleration shows that this frequency is in between 3 and 4 Hz. As will presented in next section, these oscillations are ascribed to be the ones of the DMFW, which in these phases plays a fundamental role in providing the proper contributions in terms of vibration attenuation.

From the validation in the time domain, the model seems to be able to reproduce the relevant phenomena that involve driveability issues. The linearized version of the model behaves well even in the most critical manoeuvres, provided that the points of linearization are properly chosen (e.g. proper vertical load and vehicle speed to linearize the tire, proper slopes of nonlinear powertrain elements). A linear model is also useful for control purposes, maybe associated with its reduced order version. The nonlinear model, instead, provides a more accurate reproduction of the experimental data even though, in general, it presents a slightly less damped response, probably related to the difficulty of finding accurate damping values for lubricants.

The model's ability to reproduce the main frequency contributions of each modeled powertrain and chassis subcomponent is tested also in the frequency domain. To this end,

experimental tip in - tip out manoeuvres have been used to compute the frequency response function between input engine torque and output longitudinal acceleration, together with the numerical results. This manoeuvre is considered suitable for these purposes because ideally excites all the system modes.

The comparison is presented in Fig. 6.5, showing a good match up to about 10 Hz. For higher frequencies the input and output experimental signals are affected by a low coherence due to the 100 Hz sampling rate. For a more accurate comparison a higher sampling frequency should be adopted.
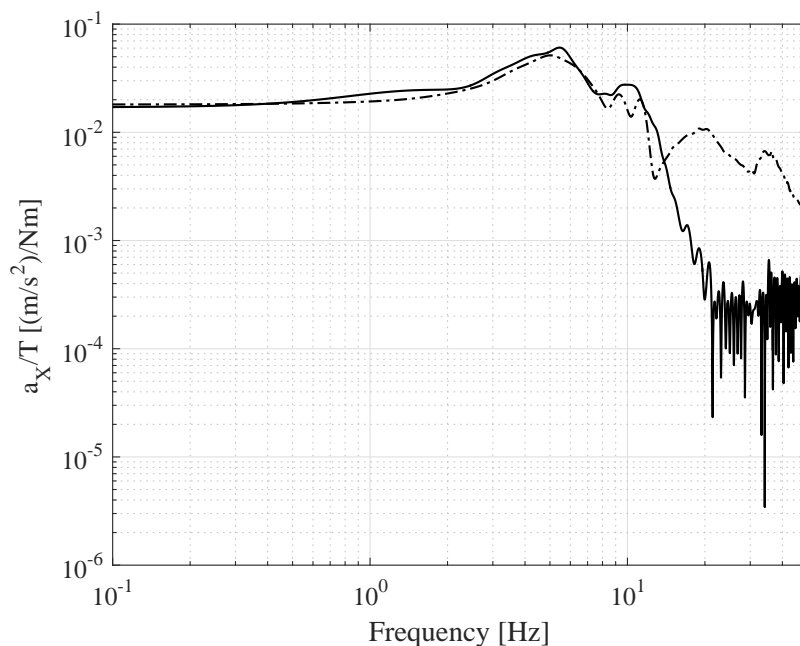
Fig. 6.5 Comparison between numerical (dashed dotted line) and experimental (continuous line) frequency response functions.

6.3   Driveability Analysis

Once the model is validated both in the time and frequency domains, it can be easily used for further investigations regarding the influence of each powertrain parameter on the vehicle driveability or control systems design for driveability enhancements.

Recalling the concept of driveability previously presented, understanding which powertrain parameters have more influence on the vibration filtering properties of the transmission, or how the tuning of certain components can improve the responsiveness of the system, is of fundamental importance.

In this section, a procedure for driveability analysis is presented, exploiting the main properties of linear dynamic systems. The linearized version of the model is therefore considered, choosing different points of linearization. Modal analysis is first performed to determine the natural frequencies of the system. Then, modal energy is computed to investigate the sensitivity of the system modes on the different powertrain parameters. In addition, the frequency response function between engine torque (input) and longitudinal acceleration (output) is studied. Time domain analysis on the linearized system is finally considered for driveability evaluation purposes.

6.3.1   Modal and Energy Analysis

The natural frequencies f_n of the system have been obtained through the computation of the eigenvalues of the linearized state matrix. The linearization point involves a very small vehicle speed (to avoid the presence of the tire damping c_p), a DMFW stiffness linearized around its low stiffness zone and a clutch stiffness consistent with the torque transmissible by the DMFW (Fig. 6.3).

(a) First 11 natural frequencies of the system plotted as a function of the mode they make reference to.
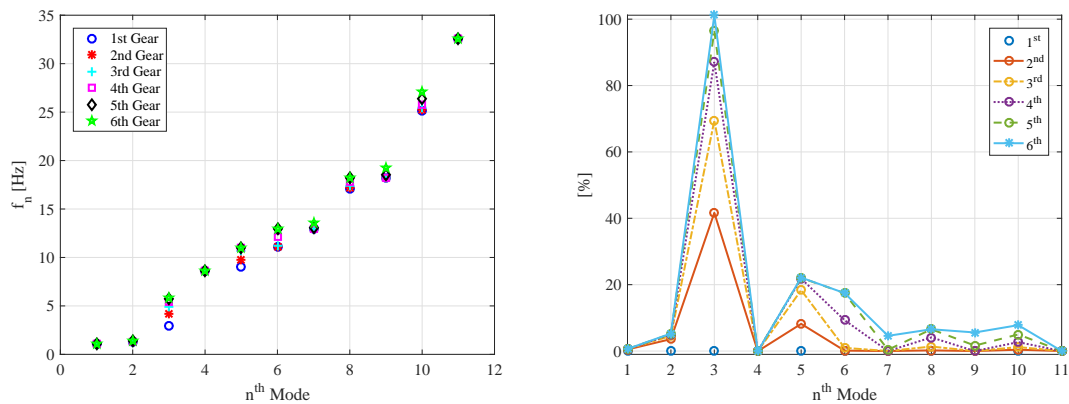
(b) Natural frequency variation of each mode with respect to its value computed in first gear engaged.

Fig. 6.6 Preliminary modal analysis regarding the influence of the engaged gear on the natural frequencies variation.

In Figure 6.6a, the first 11 natural frequencies of the system are plotted with respect to the mode they make reference to. Their sensitivity regarding the engaged gear is also presented. The natural frequencies of the system span between 1 and 35 Hz, verifying that the model is able to catch all the relevant frequency contributions from the driveability point of view. In addition, it can be seen that some modes have a frequency that is dependent

on the engaged gear. The feeling is that these modes are somehow related to powertrain components, but this statement should be verified.

Figure 6.6b presents the natural frequency variation of each mode with respect to its value computed in first gear engaged. The variations (percentages of increment p) are computed as:

$$p_{\mathrm{g}} = (f_{\mathrm{n},g}/f_{\mathrm{n},1} - 1) \tag{6.6}$$

where g is the actual engaged gear, $f_{\mathrm{n},g}$ is the vector of the system natural frequencies with engaged gear g and $f_{\mathrm{n},1}$ is the vector of the system natural frequencies with first gear engaged. The third mode is extremely sensitive with the engaged gear, with variations that reach 100 %. This mode should be investigated in more detail. The general trend is that of natural frequency increase with engaged gear increase (from 1st to 6th). The variations are, by the way, always below 20 %, which means that for any engaged gear, the frequency values of each mode increase of 10 - 20 % their values in case of first gear engaged.

This first analysis only provided the numerical values of the system natural frequencies and how they are affected by the engaged gears. The comprehension of which powertrain component vibrates the most at a certain mode of vibration is therefore strictly necessary.

The study of the system eigenvectors can actually be suitable to detect the amount of displacement (linear or rotational) related to each degree of freedom at each mode of vibration. However, since the model is somehow coupled in terms of linear and rotational degrees of freedom, the study of the eigenvectors of the system could lead to misunderstandings.

A more effective way can be to compute the potential energy u_{ij} stored in each spring i of the model at each mode of vibration j:

$$u_{ij} = \frac{\frac{1}{2}k_i \left(\psi_{i,j} - \psi_{i+1,j} \right)^2}{\frac{1}{2}\{\psi\}_j^T [K]\{\psi\}_j} \tag{6.7}$$

where matrix $[K]$ is the stiffness matrix of the linearized system and $\{\psi\}_j$ is the eigenvector associated to the j-th mode.

Figure 6.15 shows a colour map representation of the potential energy contributions of the different model springs in modes 1 to 11 considering 2nd, 3rd and 4th gear engaged. Whichever is the engaged gear, it is possible to identify 4 main mode clusters, characteristic of different groups of powertrain components. In cluster A the largest amount of potential energy is stored in the suspension springs $k_{\mathrm{s}1}$ and $k_{\mathrm{s}2}$. Since it spans between first and second system modes of vibration, and due to the fact that these modes have a frequency

not higher than 2 Hz (Fig. 6.6a), it can be stated that cluster *A* is relative to chassis modes in terms of vertical bounce and pitch motion. No effect of the engaged gear is, coherently, evidenced.

Following the same method, the next clusters can be identified. From Fig. 6.6b, it has been shown how the third mode was the most sensitive regarding the engaged gear. The colour maps here presented show that in the third mode of vibration, which spans between 3 and 5 Hz, the potential energy is stored mainly in the DMFW spring k_1, in the torsional engine mount spring k_{tm} and in the half shafts springs k_s. In addition, the effect of increasing the engaged gear is that of moving the majority of the stored potential energy from the half shafts (low gear) to the DMFW (higher gear). This cluster is named with the letter *B*, and it is relative to the coupling between rotational and linear motion of the powertrain/vehicle. The next sections will give more insights regarding the influence of this cluster on the time and frequency domain response of the vehicle acceleration.

Cluster *C* is dominated mainly by the engine mount dynamics in terms of longitudinal, vertical and torsional motion of the powertrain with respect to the chassis body. The relevant modes are in between the fourth and the sixth, spanning between 10 and 15 Hz.

Finally, cluster *D* involves modes between 7th and 10th. In this range of frequencies (15 - 30 Hz) the potential energy is mainly stored in the springs connecting the unsprung masses with the vehicle body (k_{sx1}, k_{sx2}) or with the ground (k_{r1}, k_{r2}). Definitely, this cluster is relative to the motions of the front/rear unsprung masses (i.e. wheel hop).

The energy analysis is a powerful tool to clearly identify which degrees of freedom of the system are involved at a certain mode of vibration. The subdivision in mode clusters allows an easy representation of which components are more influential in a certain frequency range.

Modes between the 3rd and 6th are relative to the 3 - 15 Hz range and belong to clusters *B* and *C*. As will be presented in next section, this is the most important range of frequencies from the driveability point of view because the main powertrain component systems responsible for guaranteeing vibrations attenuation and responsiveness are acting exactly here.

6.3.2   Frequency and Time Domain Analysis

As done in the previous section, a linearized version of the model is considered here too. In this case, the model written in state space form is used for the computation of the frequency

response function (FRF) between input engine torque and output longitudinal acceleration. A sensitivity analysis is performed regarding the influence of different parameters.

Fig. 6.7 Frequency response function between input engine torque and output vehicle longitudinal acceleration of the undamped system. Black FRF: 2nd gear, red FRF: 3rd gear, blue FRF: 4th gear.

Figure 6.7 presents the frequency response function between input engine torque and output longitudinal acceleration of the undamped system, considering different engaged gears (between 2nd and 4th). As observed from the previous analysis, the engaged gear affects mainly clusters B and C, since these two are relative to powertrain modes of vibration. In addition it is shown how the B cluster resonance moves to higher frequencies when higher gears are engaged. In the case of very low frequency content of the input torque the response is flat and dominated by the equivalent overall inertia:

$$G = \left. \frac{a_{\mathrm{x}}(\omega)}{T_{\mathrm{in}}(\omega)} \right|_{\omega=0} = \frac{\tau_{\mathrm{gb}} \cdot \tau_{\mathrm{d}}}{R \cdot m_{\mathrm{e}}} \qquad (6.8)$$

where τ_{gb} and τ_{d} are the transmission ratios of the gearbox and of the differential respectively, R is the effective rolling radius of the tire and m_{e} is the apparent (or equivalent) mass of the vehicle taking the translating masses and the rotating inertias into account. Since τ_{gb} decreases and m_{e} increases with higher engaged gears, the low frequency gain therefore moves to lower values. The equivalent mass of the vehicle can be computed simply by reporting the system inertias to the ground level, translating rotational into longitudinal

motion:

$$
\begin{aligned}
m_{\mathrm{e}} = {} & m + J_1 \left(\tau_{\mathrm{gb}}\tau_{\mathrm{d}}/R\right)^2 + J_2 \left(\tau_{\mathrm{gb}}\tau_{\mathrm{d}}/R\right)^2 + \left(J_{\mathrm{gin}} + J_{\mathrm{gout}}/\tau_{\mathrm{gb}}^2\right) \left(\tau_{\mathrm{gb}}\tau_{\mathrm{d}}/R\right)^2 + \\
& + \left(J_{\mathrm{din}} + J_{\mathrm{dout}}/\tau_{\mathrm{d}}^2\right) \left(\tau_{\mathrm{d}}/R\right)^2
\end{aligned}
\tag{6.9}
$$

Even though the study of the FRF considering the undamped system is helpful to show the system resonance frequencies and their relative interactions in a particular frequency range, it presents some limits because it does not allow to identify the real FRF, the one relative to the damped system. Also, it is expected that the torque to acceleration FRF would have a shape consistent with the aim of the overall powertrain: filter the vibrations and offer responsiveness.
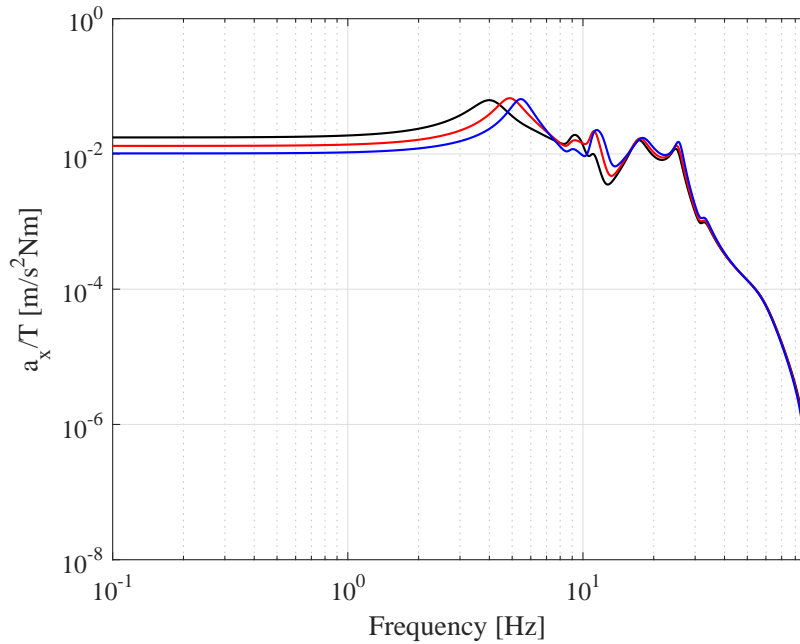
Fig. 6.8 Frequency response function between input engine torque and output vehicle longitudinal acceleration of the damped system. Black FRF: 2nd gear, red FRF: 3rd gear, blue FRF: 4th gear.

Figure 6.8 presents the FRF between input engine torque and output longitudinal acceleration of the damped system considering the same sensitivity of the engaged gear as in previous analysis. The model has been linearized considering the same linearization point exploited for the undamped system. In this case, to introduce a consistent amount of tire damping, the vehicle speed has been set to 20 km/h.

First of all, the presence of the components' damping reduces the resonance peaks amplitude and, in some cases, eliminates them. In addition, the same sensitivity regarding

the engaged gear is evidenced: the increase of the engaged gear reduces the low frequency gain while introducing response variations in *B* and *C* clusters. In particular, the mode related to *B* cluster seems to be the most sensitive to gear variation.

The FRFs present a low pass filter trend, with cut off frequency equal to the frequency of cluster *B*. This means that since the torque to acceleration FRF gives complete insights regarding the powertrain characteristics of a vehicle, it is shown how its filtering behaviour is exactly one of them.

Up to the first powertrain resonance (cluster *B*) the response is flat and dominated by the equivalent inertia. When the frequency content of the input increases, the powertrain components start to reduce the response of the system as, effectively, a low pass filter does. This has actually never been observed in the literature and represents one of the main contributions of this thesis work.
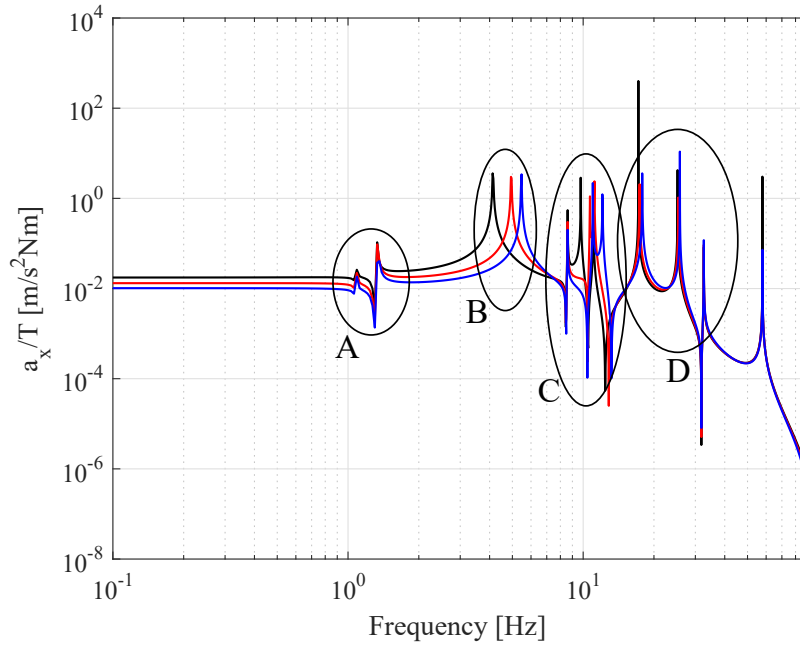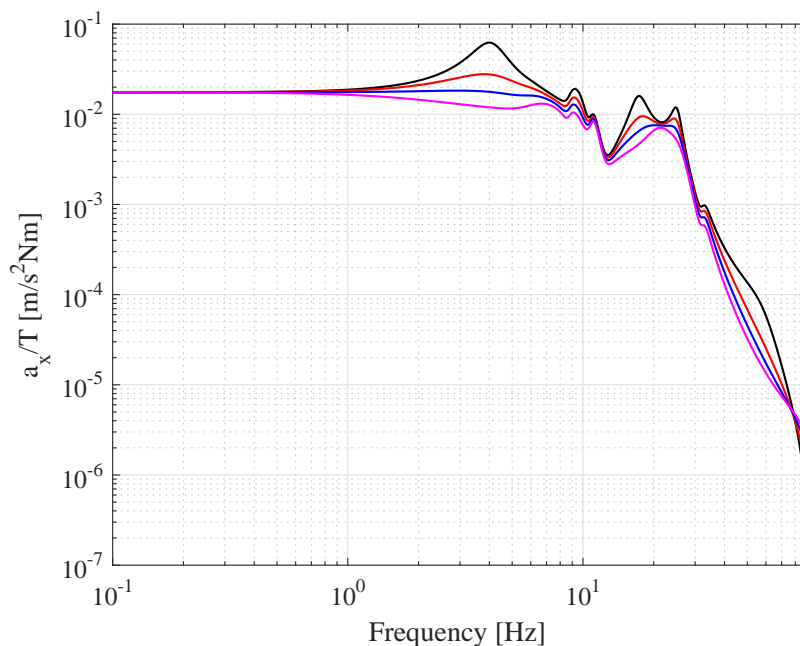

Fig. 6.9 Frequency response function between input engine torque and output vehicle longitudinal acceleration of the damped system. Black FRF: V = 20 km/h, red FRF: V = 50 km/h, blue FRF: V = 80 km/h, magenta FRF: V = 120 km/h.

Figure 6.9 presents the FRF between input engine torque and output longitudinal acceleration of the damped system considering different vehicle speeds to linearize the tire. Increasing the speed the curves show a more damped behaviour. This effect is caused by the tire ground contact model (Eq. 6.4). For low speeds, the damping is so high that its role in dissipating energy is negligible. When increasing the speed, the tire contact damping

c_p decreases, so its deformation increases with the effect of dissipating more energy and reducing the amplitude of the resonance peaks. Obviously, no effect of the vehicle speed on the low frequency gain is present.

Before switching to next section in which a sensitivity analysis will be performed on different powertrain parameters to qualitatively and quantitatively observe how they can affect and/or improve the vehicle driveability, it can be worthwhile to show some time domain simulations performed with the linearized model.
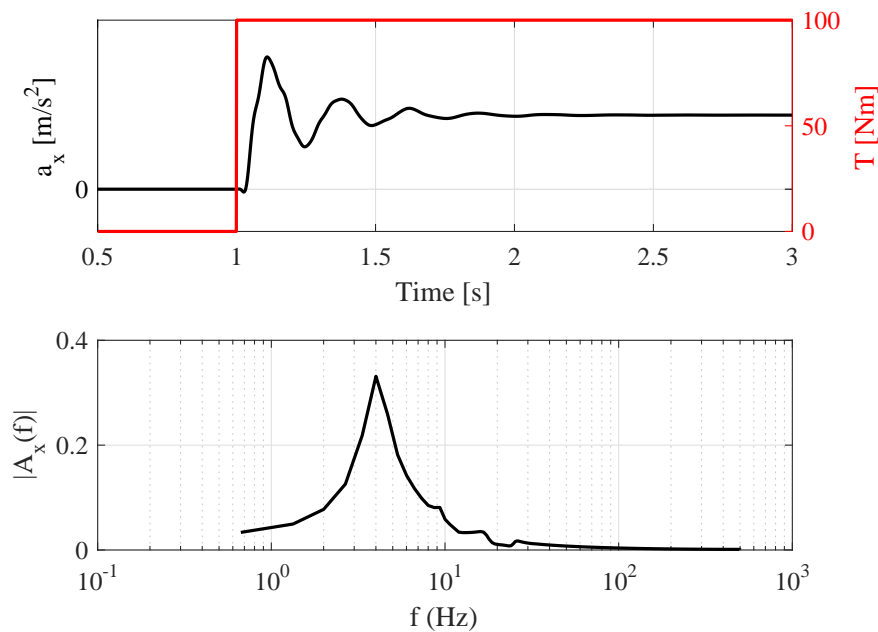
Fig. 6.10 Input torque (red scale) and longitudinal acceleration time response (black scale) of the linearized model (up) and FFT of the acceleration signal (down). 2nd gear engaged, V = 20 km/h.

Figure 6.10 shows the response of the linearized system (2nd gear, 20 km/h) after a step of the input torque. The longitudinal acceleration presents a main frequency content that the Fourier transform verifies to be of about 4 Hz, exactly inside the frequency range of cluster *B*. This is somehow verifying the consistent importance of the powertrain parameters which are involved in this cluster. In addition, as observed from the FFT of the acceleration response, other frequency contributions (although of small amplitude) are taking place, mainly between 9 and Hz. Thus, cluster *C* is also contributing in the overall system response.

It is therefore worthwhile to explain why the longitudinal acceleration response in these simulations is much different than the one present in Fig. 6.4. In this case the input torque does not hold all of its harmonic contributions, leading to a system response which is

purely a function of all the powertrain components vibrations. During the model validation, instead, the real input torque was feeding the model, with the consequence of generating an acceleration response which would also be a function of all its harmonic contributions.

Summarizing, the frequency domain analysis can be helpful for the evaluation of the system response since it perfectly reflects what would then be the time domain response, responsible for comfort issues. With the aim of driveability enhancements, a sensitivity analysis regarding the influence of the different powertrain components parameters on the torque to acceleration FRF can be performed, followed then by a time domain analysis of the longitudinal acceleration response for the computation of driveability evaluation indexes.

6.3.3   Sensitivity Analysis

The aim of this section is to achieve a clear comprehension of which powertrain parameters are mainly influencing the acceleration response of a vehicle.

Previous analyses have shown the central role played by the components belonging to clusters *B* and *C*, which are mainly the DMFW, the half shafts and the engine suspension. Therefore, the sensitivity analysis focuses on the aforementioned component's parameters that are more easily identifiable: their stiffnesses. It will be shown how these stiffnesses affect the resonant frequencies of the system and its torque to acceleration FRF.
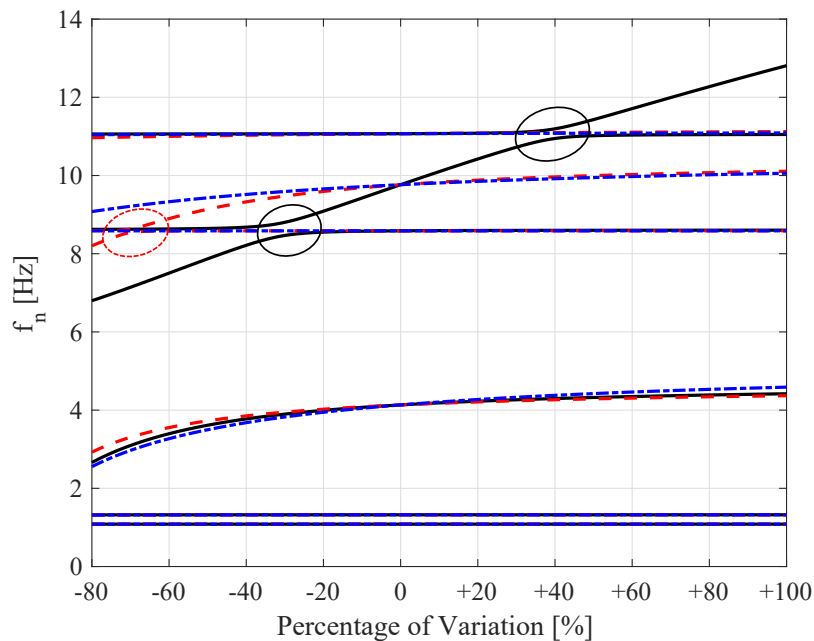
Fig. 6.11 First 6 natural frequencies of the systems as a function of the individual variation of the DMFW stiffness (continuous black), of the torsional engine mount stiffness (dashed red) and of the half shafts stiffness (dashed dotted blue). 2nd gear engaged.

Figure 6.11 shows the first 6 natural frequencies in 2nd gear as a function of the individual variation of DMFW stiffness (k_1, continuous black), of the torsional engine mount stiffness (k_{tm}, dashed red) and of the half shafts stiffness (k_s). As previously observed, the first two modes of the system are relative to the vertical bounce and pitch motion of the chassis. Therefore, since they are not influenced by the components under analysis, their natural frequencies remain constant for all the parameter ranges.

By converse, Fig. 6.15 showed how the third mode is affected exactly by the parameters under variation. This mode varies its frequency with stiffness variation, but it is interesting to note that all the parameters generate similar natural frequency variations.

Cluster C is comprehensive of modes related to the engine block. Therefore, the fourth, fifth and sixth modes will be coupled modes. Considering the DMFW stiffness variation, it is shown that fourth mode is influenced only for variations lower than −30 %. Conversely, sixth mode is insensitive to variations smaller than +40 %. In the middle, fifth mode increases its natural frequency only for DMFW stiffness variations in between the above mentioned percentages. The three natural frequencies never cross each other and a veering phenomenon occurs (shown with black circle).

The torsional engine mount stiffness variation does not generate veering (apart from the non - realistic case of $-70\,\%$ of reduction). The fifth mode increases its frequency with stiffness increase, fourth and sixth modes are almost not sensible.

The half shafts stiffness variation affects mainly the third mode (relative to cluster *B*) and the fifth (cluster *C*). No veering phenomena are observed.

(a) DMFW Sensitivity.

(b) Engine suspension sensitivity.

(c) Half shaft sensitivity.
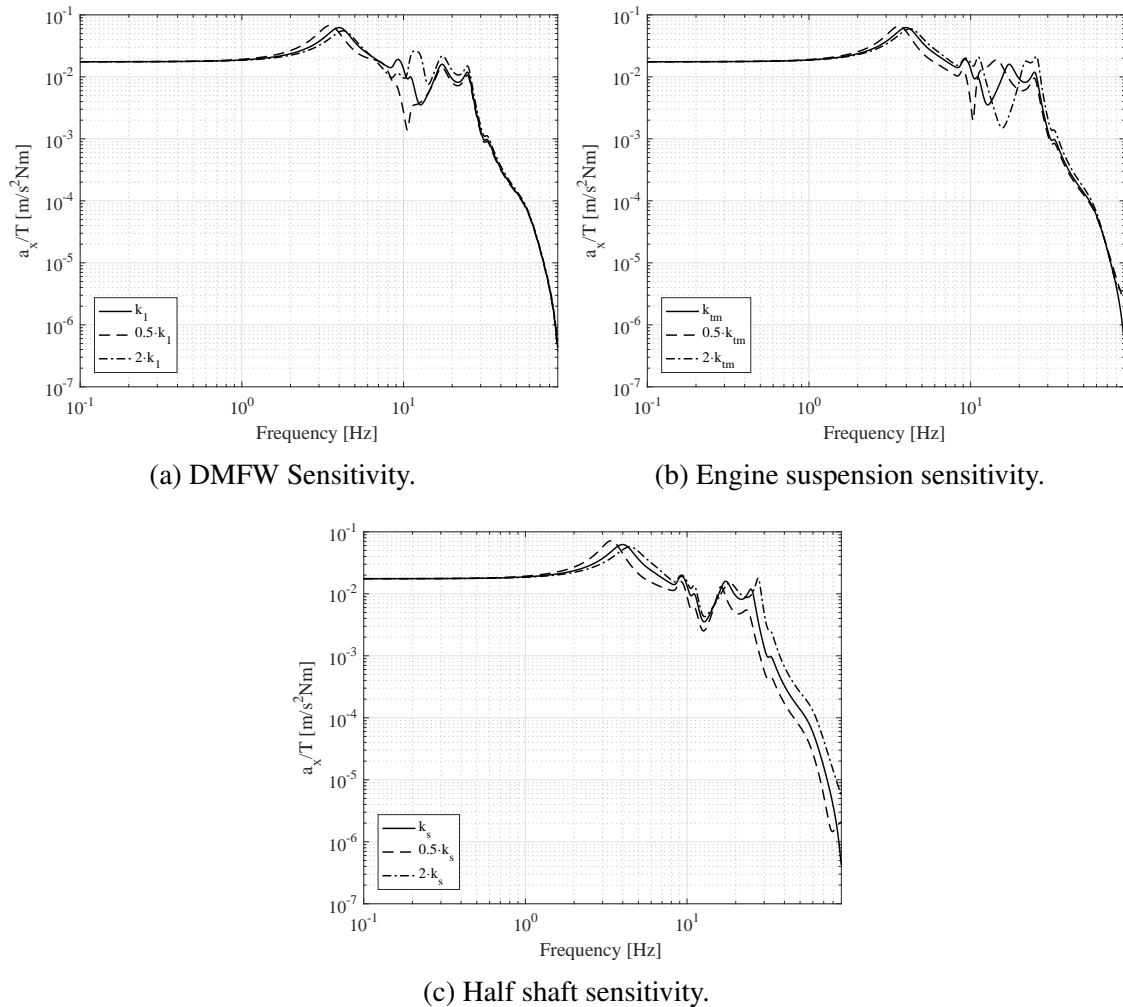
Fig. 6.12 Parameters sensitivity on frequency response function between input engine torque and output longitudinal acceleration.

Figure 6.12 shows the frequency response function between input torque and output longitudinal acceleration when DMFW, engine suspension and half shaft stiffnesses are varied. Nominal, half and twice their values have been considered while the other parameters are the same as the previous analysis (20 km/h, 2nd gear engaged). For all the parameters

considered, the main effects of the DMFW, engine mount and half shafts stiffness variation belongs to clusters *B* and *C*.

The general trend is that reducing the stiffnesses lowers the first powertrain natural frequency and improves the attenuation in the same range of frequencies. Increasing the stiffnesses above the nominal values reduces the attenuation in the same band and leads to larger amplitudes of the cluster C modes.

Additionally, doubling the DMFW and torsional engine mount stiffnesses, two peaks of the frequency response function are present between 6 and 15Hz. This confirms that the DMFW and the torsional engine mount modes intimately interact with each other, similar to a dynamic vibration absorber. High frequency modes (more than 30Hz) do not show any variation apart from the case of half shaft stiffness increase.

Up to now the attention has been focused mainly on the powertrain characterization via conventional system dynamics techniques. In the following, a method for evaluating the driveability of a vehicle is presented. It is mainly based on the computation of metrics of the longitudinal acceleration time history.

6.4   Driveability Evaluation

Vehicle driveability is a measure of the driver's complex subjective perception of the interactions between himself and the vehicle, associated with longitudinal acceleration aspects. It can include both issues related to the transmitted vibrations from the engine to the driver and aspects concerning the responsiveness of the vehicle itself. As underlined, in this subject a central role is played by the overall vehicle powertrain dynamics.

Several objective criteria can be considered for driveability assessments [97]:

- Dynamic response. The longitudinal chassis acceleration can be characterized as a 2nd order system response including natural frequency, overshoot, rising time.

- Peak to peak (PTP) acceleration. PTP acceleration can give a quantitative number of how much acceleration is felt by the driver during a tip in - tip out event.

- Jerk. The time derivative of the acceleration is able to measure the harshness, the severity and the asperity of a certain manouevre.

- Time delay. It is a measure of how long the vehicle takes to generate acceleration after the driver torque request.

- Energy spectral density. It is used to determine the magnitude of each vibration frequency involved during a certain manoeuvre.

- Vibration dose value. It is a quantity that describes the total amount of vibration felt by a human in contact with a vibrating surface.

Most of the car manufacturers make use of a commercial software for the evaluation of the driveability of their vehicles. AVL Drive is one of such software. It utilizes computational methods (such as neural networks) to process the acceleration data obtained from a certain manoeuvre. AVL is able to recognize different events that affect the drive quality during the same manoeuvre and, based on additional signals (such as vehicle speed, engine torque, accelerator position), triggers these events and give them a relative score.

Based on the criteria previously listed and on the events that AVL is actually measuring, it is possible to list a set of metrics obtainable from the longitudinal acceleration time history with which a driveability evaluation can be performed [98]. In the following, a description of the metrics is presented showing in which criteria a higher rating can be obtained.

- Response time. The response time is defined as the time that the acceleration takes to reach 0.5 m/s^2. The shorter the response time, the faster the vehicle response and therefore the driver feeling.

- Initial bump. The initial bump is the angle between the acceleration rise and the time axis. It has the meaning of acceleration gradient and the higher it is, the less the driver feels a sort of drag because of slow acceleration increase.

- Kick. The kick is defined as the maximum acceleration drop after the first peak achievement. The higher is the kick, the more the driver feels a rough variation in the acceleration response, which deteriorates his comfort.

- Stumble. The stumble is defined as the decrease of acceleration after the given torque requested. It is again a measure of the powertrain flexibility and therefore of the vehicle response.

- Vibration dose value (VDV). The VDV is a measure of the vibration "absorbed" by a human in contact with a vibrating surface and is expressed as:

$$VDV = \left(\int_{t_0}^{t_\mathrm{f}} a_\mathrm{w}^4(t)\, dt \right)^{1/4} \tag{6.10}$$

Fig. 6.13 Input torque (red scale) and longitudinal acceleration time response (black scale) of the linearized model. Different engaged gears, V = 20 km/h.

where a_w is the frequency weighted acceleration using a bandpass filter between 1 and 32 Hz while t_0 and t_f are the starting and final simulation time. The lower the VDV, the better the driver feeling.

Therefore, although AVL may be not available, a preliminary driveability evaluation can however be performed by computing the abovementioned indexes and giving them ratings. Then, by acting on the main parameters affecting the driveability, the same manoeuvre can be again simulated and the indexes computed. The improvements/worsening can be observed and objectively evaluated.

Recalling the acceleration response already presented in Fig. 6.10, its sensitivity regarding the main driveability indices for different engaged gears is now analyzed in more detail.

The input torque is given to the model as an impulsive step. Of course it is unrealistic, but for simulation purposes it is worthwhile to consider a system input capable of ideally exciting all the system frequencies.

In the case of a step input torque considering a vehicle speed of 20 km/h and different engaged gear, the acceleration time response presents a visible stumble and a consistent kick of about 2 m/s^2. The abovementioned indexes have been computed for the same manoeuvre in case of different engaged gears. The results are presented in Tab. 6.1.

Index	Unit	1st	2nd	3rd	4th	5th	6th
Response time	s	0.048	0.043	0.04	0.038	0.037	0.036
Bump	deg	87.60	88.49	88.33	88.71	88.59	88.41
Kick	m/s^2	1.529	2.12	2.144	1.74	1.39	1.2
Stumble	m/s^2	-0.12	-0.07	-0.04	-0.02	-0.007	-0.001
VDV	$m/s^{0.75}$	1.2379	1.1197	0.9192	0.7296	0.594	0.507

Table 6.1 Driveability indexes for a longitudinal acceleration step response in case of different engaged gears.

Considering the six longitudinal acceleration responses of Fig. 6.13, the general trend is the one already observed in Fig. 6.8, i.e. the first powertrain natural frequency increases with increased engaged gear. The steady state longitudinal acceleration, instead, reduces when engaging higher gears (Eq. 6.8). In addition, it is noticeable that the response time decreases when engaging a higher gear, a symptom of a stiffer powertrain system. This is also demonstrated by the bump, which slightly increases from 1st to 6th gear, and by kick and stumble, both reducing in higher gears.

This simplified analysis can be helpful for a fast evaluation of the driveability in the case of powertrain modifications. Considering the same model with modified powertrain parameters (e. g. DMFW stiffness, torsional engine mount stiffness, half shaft stiffness) the potential benefits of the modifications can be evaluated simply by re - computing these indexes.

The last section shown the central role of the DMFW, the engine suspension and the half shaft in the vibration transmissibility function of the powertrain. It has been presented how the reduction of the stiffness of these components can lead to a reduction of the first powertrain natural frequency, improving the vibration attenuation. Simply by reducing the DMFW and the engine mount torsional stiffness, the longitudinal acceleration step response is newly obtained.

Figure 6.14 shows the time domain sensitivity of the longitudinal acceleration step response when DMFW and torsional engine mount stiffness are varied. Nominal, 20 % less and 50 % less than their values are considered. When decreasing both the stiffnesses together, it is possible to notice a small increase of the stumble, together with a reduction of the initial bump. This, somehow, reduces the responsiveness of the vehicle under impulsive requests of torque. However, what is observed is a reduction of the system response first natural frequency which, instead, is good for improving the filtering behavior provided
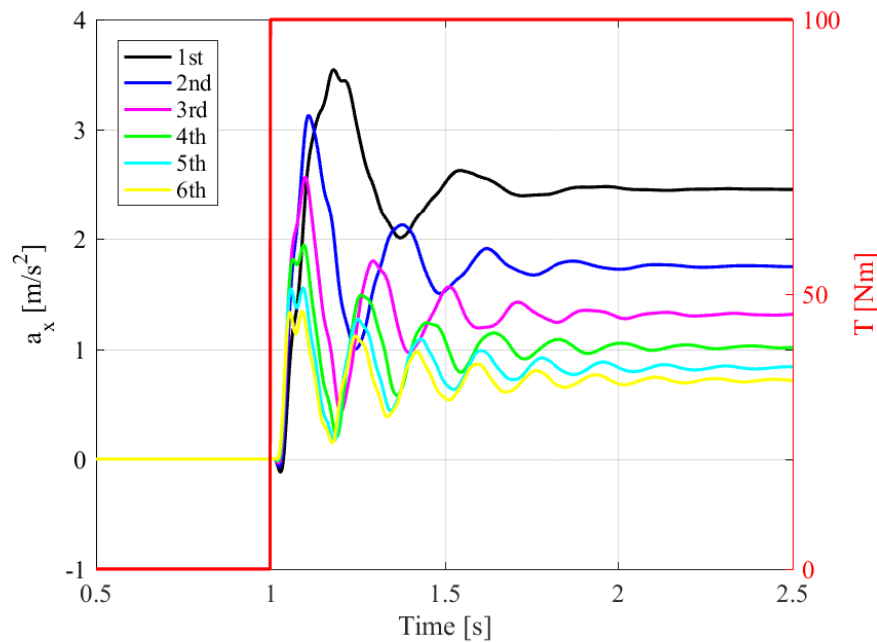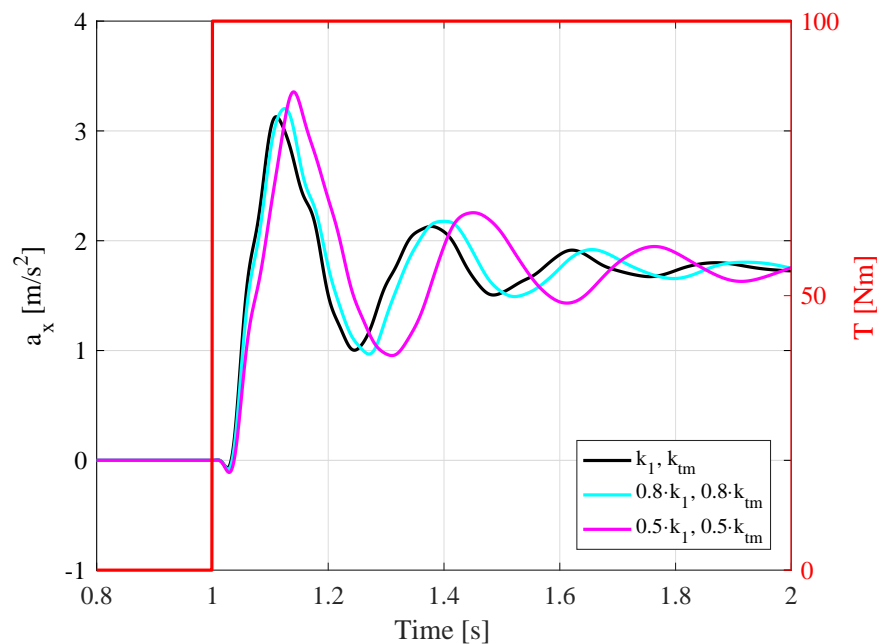
Fig. 6.14 Input torque (red scale) and longitudinal acceleration time response (black scale) of the linearized model. Sensitivity of DMFW and torsional engine mount stiffness, V = 20 km/h.

that additional damping is introduced. As a matter of fact, it is shown that the amplitude of the oscillations are larger than the case of nominal stiffnesses.

Finally, it is worthwhile to underline that the acceleration step response is representative of the behavior of the powertrain, but does not give insights where the powertrain filtering behavior is concerned. In addition, the engine torque is never as perfectly smooth as simulated in the previous analysis, but due to its internal construction always contains a consistent contribution of harmonics that have to be filtered out. The trend is to reduce as much as possible the first powertrain natural frequency to filter the vibrations and, as shown, adding viscous or Coulombian damping to attenuate them.
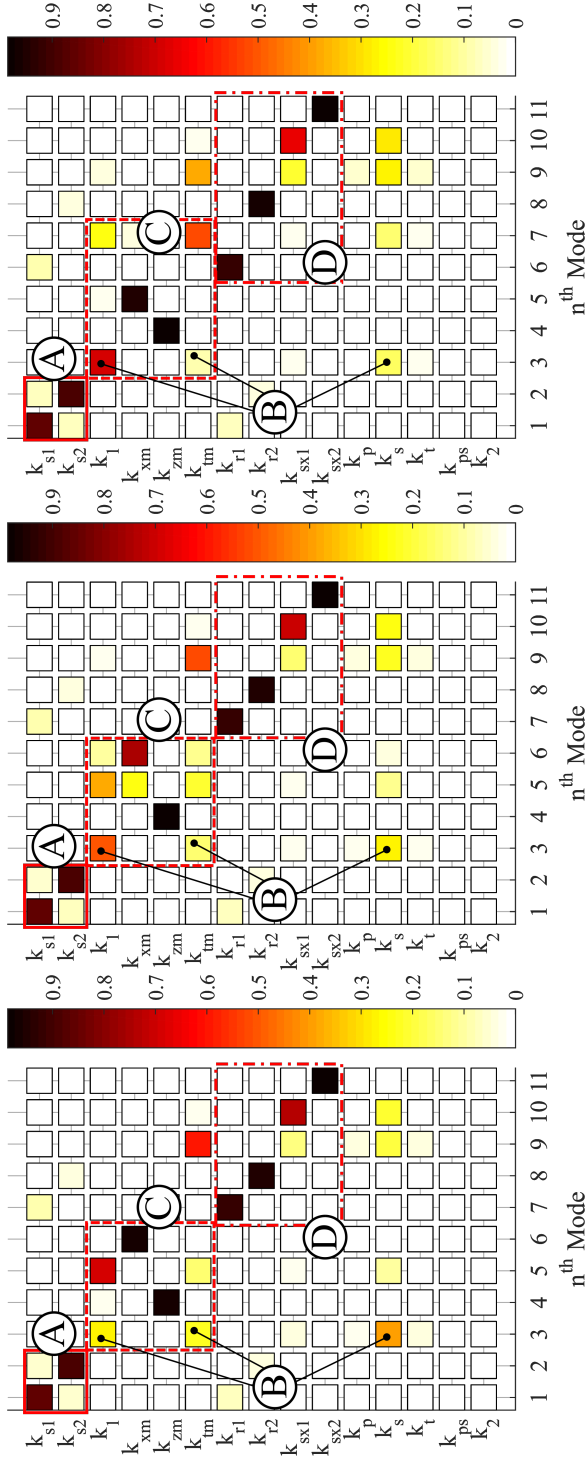
Fig. 6.15 Modal energy contribution of the different model springs in modes 1 to 11. 2nd gear (left), 3rd gear (center), 4th gear (right).

6.5 Driveability Perspectives with P4 Electric Motor

Previous sections showed that possible driveability enhancements could be reached by a fine tuning of the passive powertrain components. As an example, the reduction of the DMFW and engine mounts torsional stiffness leads to a reduction of the first powertrain natural frequency, improving the possibility of filtering out the vibrations coming from the engine. This action brings two main drawbacks, both related to the longitudinal acceleration time response. The first is related to its amplitude, which presents larger oscillations that should be better damped, the second is related to its responsiveness. An additional drawback can be related to the maximum deflection of the spring under maximum torque transmission, but this can be handled as it is already done in conventional DMFWs, i.e. letting additional sets of torsional springs work only in limited bands of angular displacements. Since the matter of damping can also be solved in practical applications, the responsiveness problem is the major one.

With the P4 architecture, an additional actuator is installed on the vehicle: the rear electric motor. Due to the high degree of controllability of electric machines and their small time delays, they are perfect candidates for improving the vehicle ability to quickly respond to driver commands.

With the aim of improving the driveability, passive and active components can be merged together exploiting their main characteristics:

- Tune the passive powertrain parameters in order to improve the vibration transmissibility function of the vehicle;

- Providing the same driver requested torque at the ground level, splitting it between the ICE and EMP4 and use the latter to improve the vehicle responsiveness.

Providing torque at the vehicle rear axle completely changes the acceleration response. In addition, the model should be modified in order to allow another input to be present. In the following, the modifications to the model considered until now are presented.

6.5.1 Vehicle Model Modifications

The model modifications regards, of course, the rear axle only. The model shown in Fig. 6.2 presents the presence of the rear unsprung mass only, allowed to have vertical and longitudinal degrees of freedom. What should be added is the presence of the rear tire - ground interaction (spring and damper connected in series), the rear wheel (tire hub and
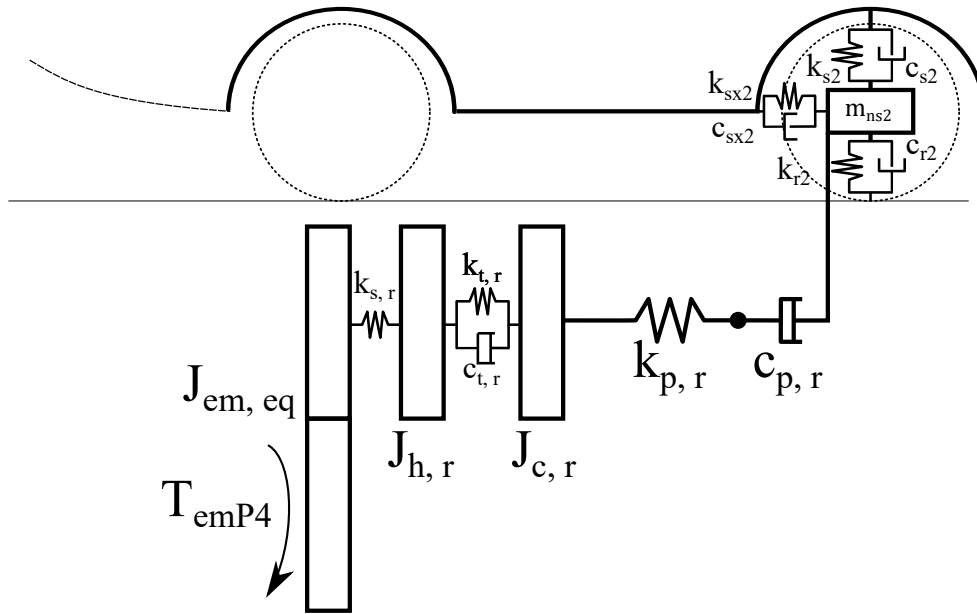
Fig. 6.16 Vehicle model modifications, introduction of the presence of the rear axle.

belt, two inertias connected by a parallel spring and damper representing the belt stiffness and damping properties), the half shafts (a torsional stiffness) and the rear transmission (two inertias).

The modified model is shown in Fig. 6.16. The nomenclature of the different components is the same as the one presented in Fig. 6.2 with an additional subscript r evidencing the rear axle position.

6.5.2 Frequency Domain Analysis

Once the four additional degrees of freedom (3 with mass and 1 massless related to the tire) are introduced into the model, a first check to be performed is to look at the frequency response function between input engine torque and output longitudinal acceleration. Since the system has been modified on the rear axle only, it is expected that such FRF would be very similar to the one of the original model, with main differences regarding the low frequency gain, in which the increased equivalent inertia can play a role.

Figure 6.17 shows the aforementioned FRF for the system without and with the presence of the rear axle. At low frequency, both the responses are flat but with a lower gain in the case when the rear axle is present. Recalling Eq. 6.9, an additional term should be taken into account:

$$J_{h,r}/R^2 + J_{c,r}/R^2 + J_{em,eq}\left(\tau_{em}/R\right)^2 \tag{6.11}$$
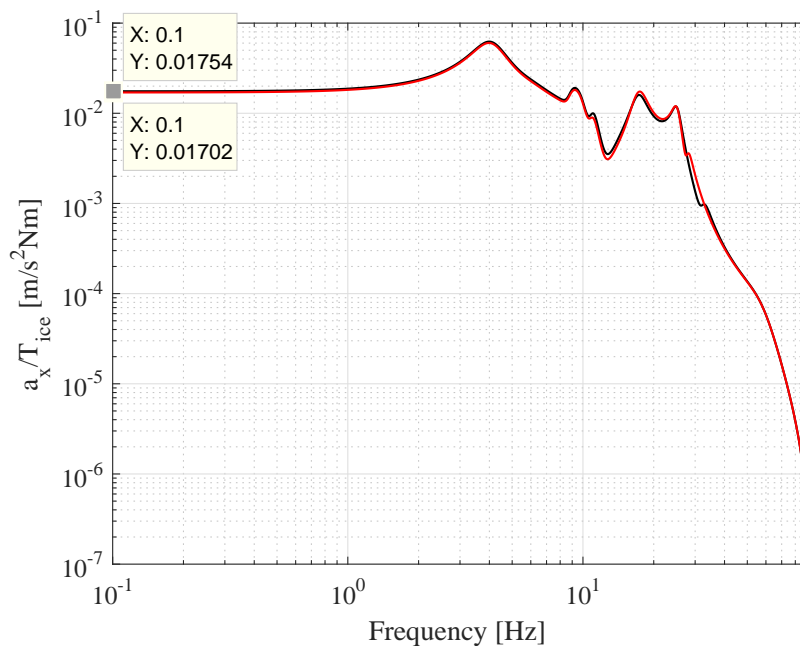
Fig. 6.17 FRF between input engine torque and output longitudinal acceleration for the model without (black line) and with the presence of the rear axle (red line). Effect of the additional inertia.

where τ_{em} is the total transmission ratio between electric motor and wheels, comprehensive of the differential ($\tau_{gb,r}\tau_{d,r}$). The introduction of this additional term leads to a reduction of the low frequency gain. Small variations are introduced in the frequency range between 10 and 30 Hz.

Similarly, the FRF between input electric motor torque and output longitudinal acceleration can be obtained, both for the undamped and for the damped system.

Figure 6.18 shows the effect of the damping in the different system components and presents the general frequency domain behavior of the system whenever the input comes from the rear axle electric motor. In general, it seems that a main resonance is present at about 30 Hz, while the resonances under 10 Hz seem to be almost completely damped out.

A last analysis is presented in Fig. 6.19 to compare the two system FRFs. The input torque position (front or rear axle) clearly affects the longitudinal acceleration response. In particular, the engine torque mostly excites the low powertrain frequencies while the rear electric motor torque generates resonances with larger amplitude in the 10 - 30 Hz range, characteristic of vehicle components which own these natural frequencies. However, it is noticeable that up to 10 Hz the response is close to flat, which means, as an example, that the longitudinal acceleration step response will present low amplitude oscillations at least if the input torque is not able to excite higher frequency modes.
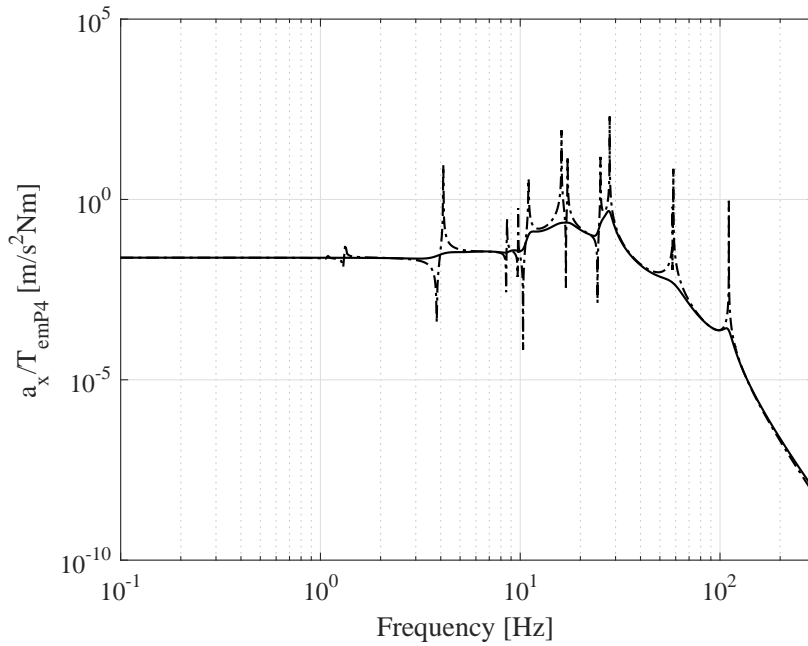
Fig. 6.18 FRF between electric motor input torque and output longitudinal acceleration for the undamped (dashed dotted line) and for the damped system (continuous line).

These characterstics can be effectively useful for further driveability improvements using the hybrid vehicle since in the low frequency range of electric motor torque actuation it can be used as a dissipative component to introduce damping torque in order to attenuate the longitudinal acceleration response as much as possible.

Therefore, the model has one control input (electric motor torque) and one disturbance input (engine torque). Since the linearized version of the model is considered, the output longitudinal acceleration will be the summation of the one related to the ICE input ($a_{x,ice}$) and the one related to the electric motor ($a_{x,emp4}$). Therefore, two frequency response functions should be considered:

- Engine torque to longitudinal acceleration frequency response function:

$$H_{ICE} = \frac{a_{x,ice}}{T_{ICE}} \tag{6.12}$$

- Electric motor torque to longitudinal acceleration frequency response function:

$$H_{EMP4} = \frac{a_{x,emp4}}{T_{EMP4}} \tag{6.13}$$
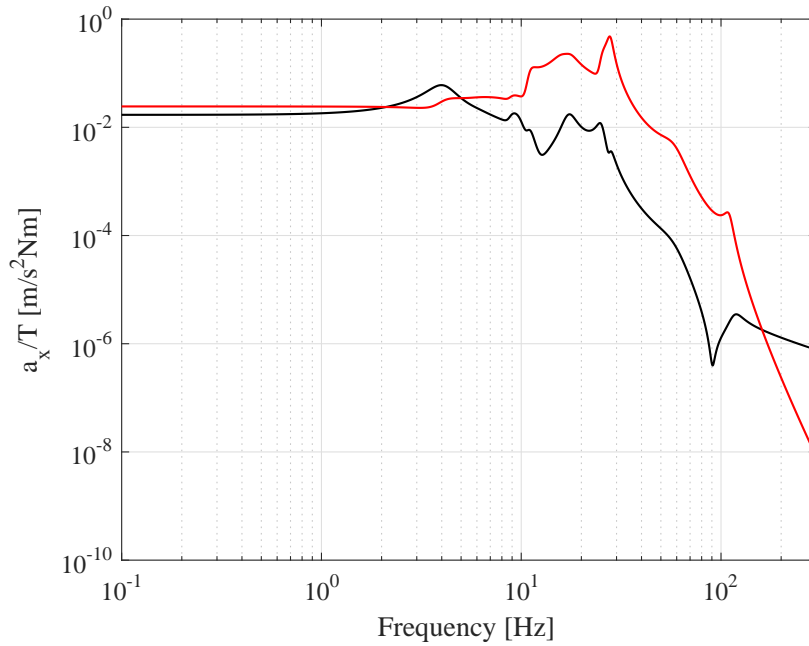
Fig. 6.19 FRF between input engine torque and output longitudinal acceleration (black line) and between electric motor input torque and output longitudinal acceleration (red line) for the damped system.

To obtain the final value of the vehicle longitudinal acceleration, the accelerations should be added:

$$a_x = a_{x,ice} + a_{x,emp4} = H_{ICE}T_{ICE} + H_{EMP4}T_{EMP4} \tag{6.14}$$

6.6 Chapter Summary and Future Works

This chapter analyzed the longitudinal dynamics of the vehicle where its vibratory behavior is concerned. The concept of driveability regards both the capability of the powertrain to attenuate the vibrations coming form the internal combustion engine, and its characteristic of fastly transmit to the wheels the torque requested by the driver. A complete 16 DOF nonlinear vehicle model has been built and validated through extensive experimental validations both in time and in frequency domain, verifying its ability to reproduce the relevant phenomena where driveability is concerned. The linearization of its nonlinear components allows a methodology for driveability analysis based on classical system dynamics theory to be developed. Modal analysis has showed the influence of the engaged gear on the variation of the natural frequency modes. Energy analysis underlined the

components which, during the vibration, stored the most potential energy. Four main mode clusters have been categorized to be relative to different subgroups of components (e. g. chassis, powertrain, unsprung masses). The frequency response function between input engine torque and output longitudinal acceleration showed the central role of the powertrain to be an equivalent mechanical filter which, over the first powertrain mode, starts to filter out the vibrations coming from the input. This result is even more evident considering the damped frequency response function and its variation with different vehicle speeds. A sensitivity analysis, focused on clusters B and C, provided interesting design criteria regarding parameters such as DMFW stiffness and engine mount torsional stiffness. The trend is that of reducing these stiffnesses to improve the attenuation of the acceleration response starting from low frequencies, paying attention during the maximum torque transmission regarding too high springs deflections.

If driveability enhancements are provided by passive components only, a compromise between different system dynamic characteristics should take place. As a matter of fact, reducing the stiffness of the main powertrain components leads to improvements of the transmissibility function of the powertrain but makes the powertrain softer, therefore reducing the responsiveness of the overall vehicle. To merge improved filtering behavior and improved responsiveness, the possibility to include an additional actuator coming from the hybrid architecture under analysis can lead to several advantages.

The total required torque at the ground level could be split between the thermal and electric motor. Since the proposed powertrain modifications (reduction of DMFW stiffness for example) improve the vibration transmissibility function but lead to a reduction of the vehicle responsiveness, part of the required torque can be provided by the electric motor with a proper control strategy so that response time can be reduced, stumble eliminated and bump increased, for example.

A simple solution to give more responsiveness to the vehicle is to subtract part of the required torque for traction to the ICE, giving it to the rear electric motor. Defining a value k as the ratio between the electric motor torque at the ground level (subscript g) and the required torque again at the ground level as:

$$k = \frac{T_{g,\text{EMP4}}}{T_{g,\text{req}}} = \frac{\tau_{\text{em}} T_{\text{EMP4}}}{T_{g,\text{req}}} \tag{6.15}$$

while coherently writing the ICE torque partialization $1 - k$ as:

$$1 - k = \frac{T_{g,\text{ICE}}}{T_{g,\text{req}}} = \frac{\tau_{\text{g}} \tau_{\text{d}} T_{\text{ICE}}}{T_{g,\text{req}}} \tag{6.16}$$

substituting Eqs. 6.15 and 6.16 into Eq. 6.14, the frequency response function between the required torque and the longitudinal acceleration is obtained:

$$H_{\text{req}} = \frac{a_{\text{x}}}{T_{\text{g,req}}} = \frac{(1-k)}{\tau_{\text{g}} \tau_{\text{d}}} H_{\text{ICE}} + \frac{k}{\tau_{\text{em}}} H_{\text{EMP4}} \tag{6.17}$$

Based on the two FRFs H_{ICE} and H_{EMP4}, with the goal of smoothing the longitudinal acceleration profile as much as possible, improving the vehicle responsiveness, the value k can be tuned as a function of the driver pedal position and of the vehicle speed for example, in order to obtain a mapped value for different driving conditions. Optimization techniques are the best candidate for performing this analysis.

Chapter 7

Conclusions

The recent and always more stringent regulations regarding passenger vehicles' emissions in the atmosphere (CO_2, PMs, CO, HC, NO_x), are pushing the car manufacturers to introduce modifications to their vehicles with the goal of increasing their overall efficiency. Standing in the field of ICE driven vehicles, possible improvements regard the engine (e.g. advanced injection systems and methods, downsizing, aftertreatment techniques) or the chassis (body weight reduction through the use of innovative materials, tires rolling resistance reduction, aerodynamic drag reduction). Hybrid electric vehicles are promising technologies that make use of more than one source of energy to provide traction to the wheels or allow part of the energy, that otherwise would be wasted in heat, to be recovered and stored for future use. The need for car manufacturers to study, analyze and introduce hybrid electric vehicles in the market requires the application of established methodologies helpful for the comprehension of the different phenomena and the possibility for system and component optimization. The main goal of this thesis work has been to develop accurate design tools and methodologies for the study of mild hybrid vehicle architectures.

When dealing with mild hybrid architectures, their main function is the recuperation of energy during vehicle braking phases. The selection of which architecture considered for the design can be based first on this characteristic. Therefore, the study of the influence of the electric machine position on the regenerative braking performance is the preliminary selection step. Another constraint regards the required chassis modifications to be introduced for making the system work. In order to avoid the complete powertrain and car body re - design, electric battery, power electronics and electric motor should find a place in the already existing vehicle structure. Therefore, a compromise between small modifications and low advantages in terms of hybrid functionalities is straightforward. To this end, two mild hybrid architectures are analyzed. In the first one the alternator is substituted with an

electric motor (named P1f), able to recover energy and provide traction power, while the second one considers the presence of an electric motor mounted on the rear axle of the vehicle (named P4).

The comparison between the two architectures is based on different energy analyses. The influence of the electric machine position, in addition to the dissipative components interposed between the motor and the wheels (transmission efficiency, clutch, engine over - running torque, belt efficiency, aerodynamic and rolling resistance) is evaluated by simulating several braking conditions, characterized by an initial vehicle speed and a deceleration. The results put in evidence the role played by the aerodynamic and rolling resistances, constituting the main source of dissipation when dealing with high speed braking maneuvers, and the one relative to the engine over - running torque, the most important dissipation in case of low deceleration braking maneuvers. Due to its proximity to the wheels, the P4 electric motor is able to recover the highest amount of available kinetic energy. However, showing the consistent dissipations introduced by the internal combustion engine due to its over - running torque, the analysis suggests the need for uncoupling the electric motor from the rest of the powertrain during braking and traction phases in order to optimize the energy recovery and the power dissipations.

Mild hybrid architectures can therefore be selected based on their capabilities to recover the highest amount of energy from the braking phases of the vehicle. However, once selected, it is worthwhile to test their functionalities by simulating their operations on conventional homologation cycles. To do this, two things are needed. The first is the actual characteristic of the electric motor in terms of a torque - speed map, efficiency, absorbed battery current and thermal behavior. The second is an energy management strategy, a criterion for selection of traction torque split between the prime movers.

In Chapter 3 a framework for the design of a single class of traction motors for mild hybrid electric vehicle has been presented. The goal has been that of optimize the mechanical characteristics of the electric machine based on the vehicle and on the functionalities that the vehicle is going to perform during its operation. Driving cycle analysis, as well as additional requirements like hill start, maximum speed, torque at maximum speed, have been considered for obtaining the required torque - speed map of the motor. The dimensions of the motor are firstly obtained through well established analytical linear techniques, and then validated using for numerical simulations. It has been showed how the adopted linear analytical model is too conservative, since it does not consider possible local iron saturations. The framework then involves the constant power region design of the motor. An electromagnetic dynamic model of the electric machine is developed and winding design as well as field weakening techniques are investigated. DC

and phase currents maps for each point of operation of the motor are obtained. Furthermore, the framework is completed by a thermal analysis. The different points of operation of the motor in its torque - speed map are simulated from the thermal point of view, and thermal resistance and time constants maps are identified.

The electric motor design framework proposed constitutes an important preliminary stage since it provides several parameters required for hybrid vehicles system level analysis, otherwise hardly accessible. The optimization regards its mechanical characteristics only and is addressed to a single class of motors in order to adapt the electric machine to the vehicle and the application, but additional design parameters are planned be involved (topological, geometrical parameters).

In Chapter 4 the modeling of the electric powertrain is completed by the introduction of the electric battery. It is implemented through the use of maps representing voltage, resistance, maximum charge and discharge current as a function of the state of charge. In parallel, the energy management strategy is responsible for the correct torque split between the internal combustion engine and electric motor based on the functional and component limitations of the electric powertrain. A simple rule based energy management strategy is studied with the goal of developing fast algorithms for easy implementation in real time applications. The architecture therefore exploits two working modes for traction phases: pure ICE and pure electric traction, while during the braking phases the priority is given to the regeneration of energy through P4 electric motor usage. The available electric motor torque at the level of the wheels is computed based on the status of the electric powertrain at each time instant. Specifically speaking, battery temperature, state of charge and maximum admissible current as well as electric motor temperature are all physical quantities that limit the electric machine use when their respective threshold values are reached. Furthermore, of very important interest for the designer would be to understand, based on the hybrid architecture under analysis, what is the best size of the electric battery that allows the powertrain to properly function in the established working conditions while introducing the smallest amount of additional mass to the system. From the simplest to the most complex, a set of four battery design methodologies have been presented and discussed, showing the central role played by the selected driving cycle, by the initial battery state of charge and by the maximum electric traction vehicle speed as influencing parameters affecting the capacity of the battery and the energy balance. It has been shown that for a proper and optimized sizing of the battery pack, a deep sensitivity analysis regarding different realistic driving cycles and battery initial status should be performed to provide the inputs for further investigations.

The need for fuel consumption reductions and analysis of the main working conditions requires powertrain design optimization, optimal energy management strategies and design of the electric battery to become primary subjects when dealing with hybrid electric vehicle architectures. However, several other implications, even uncoupled with the energetic ones, are born and need for proper analysis.

When extending the rear axle braking maneuvers to cornering conditions, an unavoidable oversteering effect is encountered due to the different adhesion conditions of the rear tires. As a matter of fact, the application of a rear axle braking torque that distributes torque equally between the left and right wheels due to the presence of an open differential, clearly leads to possible tire saturations that reduce their lateral capabilities. In Chapter 5 the amount of introduced yaw moment due to the reducing lateral capabilities of the tires is analytically computed and plotted as a function of the lateral acceleration and the applied rear axle braking torque. The yaw moment variation is furthermore limited considering the actual tires adhesion conditions and its computation, performed offline, could be helpful for further control strategies related to enhanced vehicle dynamics. The split between rear axle electric and passive braking is subsequently investigated with the goal of preserving vehicle stability while trying to recover the highest amount of energy. The need for a stability detector, a measurable or computable quantity highlighting possible losses of maneuverability, has been showed during braking in a turn maneuvers. The best candidate for having such role is the front/rear sideslip angles difference of the wheels, a parameter that is computed based on the knowledge of vehicle speed, yaw rate and steering wheels angle, quantities available in the actual vehicle's signals network. A possible braking split strategy involves the use of the electric braking until selectable thresholds on the stability detector are reached to increase the energy recovery, and consequent conventional braking split with rear electric braking to guarantee the stability. However, the analysis suggests the need for braking blending strategies between vehicle dynamics control systems (VDC systems) already present on board (such as ESP, ABS, TCS) and the presented braking split strategies to improve the vehicle maneuverability while maximizing the energy recovery.

In order to give more completeness to the thesis work, Chapter 6 is devoted to the study of the vibratory behavior of the vehicle powertrain (driveability) including the benefits that the presence of an additional actuator (rear axle electric motor) could bring regarding this subject. A nonlinear dynamic model of the powertrain and the vehicle has been developed and validated in the time and frequency domains. The model includes the presence of a dual mass flywheel, engine suspension, tire - ground contact, longitudinal and vertical motion of the unsprung masses while the linearization of the nonlinear components allows one to exploit linear system dynamics techniques, creating a framework for driveability

analysis. By means of modal and energy analysis, four main mode clusters have been showed and categorized to be relative to different subgroups of components as a function of their range of frequency (chassis, powertrain, unsprung masses). The frequency response function between input engine torque and output longitudinal acceleration showed the central role of the powertrain in the filtering behavior of the transmission and highlights how the reduction of dual mass flywheel and torsional engine mount stiffness is able to improve the acceleration response attenuation. Nevertheless, driveability enhancements could be achieved also by means of the additional electric motor positioned on the rear axle. The dynamic model has been modified including the presence of the rear transmission and tire - ground contact while the frequency response function between input rear electric motor torque and output longitudinal acceleration presents resonance peaks in the range of 10 - 50 Hz, characteristic of unsprung mass components. Therefore, if properly tuned, passive powertrain components could offer higher filtering performance, while rear axle electric motor, if used in parallel to the internal combustion engine, is able to improve the acceleration responsiveness of the vehicle, provided that the frequency of actuation is lower than 10 Hz in order to avoid higher amplitudes of the response.

A final remark relative to the overall system integration is therefore left. Proper optimizations of the powertrain components allow the mild hybrid electric architecture to reach substantial fuel consumption and emissions reductions in the order of 30 % with respect to the conventional ICE driven vehicles. However, systems level analysis should be extended towards all the other situations in which the hybrid vehicle is going to function. The system integration should regard both vehicle structure and control systems aspects. In order to reduce the time to market, minimal modifications on the chassis system should be carried out and, therefore, the architecture that offers the best compromise in terms of modifications and performance should be the one selected. Meanwhile, electric motor control strategies for efficiency optimization should be integrated together with the already existing systems of traction and vehicle dynamics control, in order to exploit the best performance of the hybrid powertrain in the wide working conditions in which the vehicle is going to function.

Bibliography

[1] UITP, 9 - 10.2010; Global Health Observatory (GHO). http://www.who.int/gho/urban_health/situation_trends/urban_population_growth_text/en.

[2] EU energy and transport in figures, Statistical Pocketbook 2010, p. 18.

[3] EIA - Energy Information Administration, International Energy Outlook, June 2006; UP 2014, Data Book.

[4] EU energy and transport in figures, Statistical Pocketbook 2012.

[5] REGULATION (EC) No 443/2009 OF THE EUROPEAN PARLIAMENT AND OF THE COUNCIL of 23 April 2009 setting emission performance standards for new passenger cars as part of the Community's integrated approach to reduce CO2 emissions from light-duty vehicles. Official Journal of the European Union, June 2009.

[6] E. Spessa, "Evolution of powertrain technologies and fuels for LD and HD vehicles", Sustainable Transport Systems: Energy and Environmental Issues, Slides of the course. 2016.

[7] S. Onori, L. Serrao, G. Rizzoni, Hybrid Electric Vehicles, SpringerBriefs in Control, Automation and Robotics, DOI 10.1007/978-1-4471-6781-5_1

[8] L. Guzzella, A. Sciarretta, Vehicle Propulsion Systems: Introduction to Modeling and Optimization (Springer, Berlin, 2013).

[9] J.M. Miller, Propulsion Systems for Hybrid Vehicles (The Institution of Electrical Engineers, London, 2003.

[10] A. Emadi, K. Rajashekara, S. Williamson, S. Lukic. Topological Overview of Hybrid Electric and Fuel Cell Vehicular Power System Architectures and Configurations. IEEE Transactions on Vehicular Technology, Vol. 54, n.3. May 2005.

[11] K.C. Bayindir, M.A. Gozukucuk, A. Teke. A comprehensive overview of hybrid electric vehicle: Powertrain con
figurations, powertrain control techniques and electronic control units. Energy Conversion and Management, Vol. 52, pp. 1305-1313. 2011.

[12] C. Mi, M. A. Masrur, D. W. Gao. Hybrid electric vehicles: principles and applications with practical perspectives. John Wiley & Sons. 2011

[13] A.A. Pesaran. Choices and requirements of batteries for EVs, HEVs, PHEVs, in NREL/PR- 5400-51474 (2011).

[14] J. Van Mierlo, G. Maggetto, "Vehicle Simulation Programme", Autotech, I Mech E, Birmingham, GB, 1995.

[15] K. L. Butler, M. Ehsani, P. Kamath, "A Matlab-Based Modeling and Simulation Package for Electric and Hybrid Electric Vehicle Design" IEEE Transaction on Vehicular Technology, Vol. 48, No. 6, pp. 1770 - 1778. 1999.

[16] T. Markel, A. Brooker, T. Hendricks, V. Johnson, K. Kelly, B. Kramer, M. O'Keefe, S. Sprik, K. Wipke, "ADVISOR: a systems analysis tool for advanced vehicle modeling", Journal of Power Sources, Vol.110, p. 255-266. 2002.

[17] A. Tonoli, N. Amati, E. Zenerino, "Dynamic modeling of belt drive systems: effects of the shear deformations", Journal of vibration and acoustics, 128(5), 555–567. 2006.

[18] G. Li, J. Ojeda, E. Hoang, M. Gabsi, and M. Lecrivain, "Thermal - Electromagnetic Analysis for Driving Cycles of Embedded Flux - Switching Permanent - Magnet Motors", IEEE Transactions on Vehicular Technology, vol. 61, no. 1, pp. 140–151, 2012.

[19] S. Guenther, S. Ulbrich, and W. Hofmann, "Driving Cycle - Based Design Optimization of Interior Permanent Magnet Synchronous Motor Drives for Electric Vehicle Application", International Symposium on Power Electronics, Electrical Drives, Automation and Motion (SPEEDAM), June 2014, pp. 25–30. 2014.

[20] P. Lindh, M. G. Tehrani, T. Lindh, J. - H. Montonen, J. Pyrhonen et al, "Multidisciplinary Design of a Permanent - Magnet Traction Motor for a Hybrid Bus Taking the Load Cycle into Account", IEEE Transactions on Industrial Electronics, vol. 63, no. 6, pp. 3397 - 3408, 2016

[21] T. Finken, K. Hameyer. "Design of electric motors for hybrid-and electric-vehicle applications." ICEMS. 2009.

[22] J. Wang, X. Yuan, K. Atallah, "Design Optimization of a Surface - Mounted Permanent - Magnet Motor With Concentrated Windings for Electric Vehicle Applications", IEEE Transactions on Vehicular Technology, vol. 62, no. 3, pp. 1053 - 1064. 2013.

[23] N. Bernard, R. Missoum, L. Dang, N. Bekka, H. Ben Ahmed, M. El - Hadi Zaim, "Design Methodology for High - Speed Permanent Magnet Synchronous Machines", IEEE Transactions on Energy conversion, vol. 31, no. 2, pp. 477 - 485. 2016.

[24] A. G. Sarigiannidis, M. E. Beniakar, A. G. Kladas, "Fast Adaptive Evolutionary PM Traction motor Optimization based on Electric Vehicle Drive Cycle", IEEE Transactions on Vehicular Technology, 2016.

[25] P. B. Reddy, A. M. El - Refaie, K. K. Huh, J. K. Tangudu, T. M. Jahns, "Comparison of Interior and Surface PM Machines Equipped With Fractional - Slot Concentrated Windings for Hybrid Traction Applications", IEEE Transactions on Energy Conversion, vol. 27, no.3, pp. 593 - 602. 2012.

[26] R. Yang, N. Schofield, A. Emadi, " Comparative Study Between Interior and Surface Permanent Magnet Traction Machine Designs", 2016 IEEE Transportation Electrification Conference and Expo (ITEC).

[27] J. Dong, Y. Huang, L. Jin, H. Lin, "Comparative Study of Surface - Mounted and Interior Permanent - Magnet Motors for High - Speed Applications", IEEE Transactions on Applied Superconductivity, vol. 26, no. 4, 2016.

[28] G. Pellegrino, A. Vagati, P. Guglielmi, B. Boazzo, "Performance Comparison Between Surface - Mounted and Interior PM Motors Drives for Electric Vehicle Application", IEEE Transactions on Industrial Electronics, vol. 59, no. 2, pp. 803 - 811

[29] G. Pellegrino, A. Vagati, B. Boazzo, P. Guglielmi, "Comparison of Induction and PM synchronous Motor Drives for EV Application Including Design Examples", IEEE Transactions on Industry Applications, vol. 48, no. 6, pp. 2322 - 2332. 2012.

[30] Z. Yang, F. Shang, I. P. Brown, M. Krishnamurthy, " Comparative Study of Interior Permanent Magnet, Induction and Switched Reluctance Motor Drives for EV and HEV Applications", IEEE Transactions on Transportation Electrification, vol. 1, no. 3, pp. 245 - 254. 2015.

[31] Y. Yang, S. M. Castano, R. Yang, M. Kasprzak, B. Bilgin, A. Sathyan, H. Dadkhah, A. Emadi, "Design and Comparison of Interior Permanent Magnet Motor Topologies for Traction Applications", IEEE Transactions on Transportation Electrification, vol. 3, no. 1, pp. 86 - 97. 2017.

[32] V. T. Buyukdegirmenci, A. M. Bazzi, P. T. Krein, " Evaluation of Induction and Permanent - Magnet Synchronous Machines Using Drive - Cycle Energy and Loss Minimization in Traction Applications", IEEE Transactions on Industry Applications, vol. 50, no. 1, pp. 395 - 403. 2014.

[33] T. J. Miller, Brushless Permanent - Magnet and Reluctance Motor Drives, Clarendon Press - Oxford, 1989.

[34] R. Krishnan, Permanent Magnet Synchronous and Brushless DC Motor Drives, CRC Press, 2010.

[35] Duane C. Hanselman, Brushless Permanent - Magnet Motor Design, 1994, McGraw - Hill.

[36] W. L. Soong, T. J. Miller, "Theoretical limitation to the field weakening performance of the five classes of brushless synchronous ac motor drive", IEEE Proceedings-Electric Power Applications, vol. 141, no. 6, pp 127 - 132. 1994.

[37] P. A. Hargreaves, B. C. Mecrow, and R. Hall, "Calculation of iron loss in electrical generators using finite element analysis", IEEE international electric machines and drives conference, 2011.

[38] D. Dorrell, M.-F. H., M. P., L. E., D. S., and V. G., "A review of the design issues and techniques for radial-flux brushless surface and internal rare-earth permanent-magnet motors", IEEE transactions on industrial electronics, vol. 58, no. 9, Sep. 2011.

[39] F. M. Gonzalez - Longatt, "Circuit Based Battery Models: A Review", Congreso Iberoamericano de estudiantes De Ingenieria Electrica. Cibelec. 2006.

[40] L. Gao, S. Liu, R. A. Dougal, "Dynamic Lithium - Ion Battery Model for System Simulation", IEEE Transactions on Components and Packaging Technologies, vol. 25, no. 3, pp. 495 - 505. 2002.

[41] M. Chen, G. A. Rincòn - Mora, "Accurate Electrical Battery Model Capable of Predicting Runtime and I - V Performance", IEEE Transactions on Energy Conversion, vol. 21, no. 2, pp. 504 - 511. 2006.

[42] H. He, R. Xiong, J. Fan, "Evaluation of Lithium - Ion Battery Equivalent Circuit Models for State of Charge Estimation by an Experimental Approach", Energies, vol. 4, pp. 582-598, 2011.

[43] X. Hu, S. Li, H. Peng, "A comparative study of equivalent circuit models for Li - ion batteries", Journal of Power Sources, 198 (2012) 359–367.

[44] H.P. Geering, Optimal Control with Engineering Applications (Springer, Berlin, 2007).

[45] L. Xu, M. Ouyang, J. Li, F, Yang, L. Lu, J. Hua, "Application of Pontryagin's Minimal Principle to the energy management strategy of plugin fuel cell electric vehicles", International Journal of Hydrogen Energy, 38 (24), 10104 - 10115, 2013.

[46] N. Kim, S. Cha, H. Peng, "Optimal Control of Hybrid Electric Vehicles Based on Pontryagin's Minimum Principle", IEEE Transactions on Control Systems Technology, vol. 19, no. 5, pp. 1279 - 1287. 2011.

[47] L. Serrao, S. Onori, A. Sciarretta, Y. Guezennec, G. Rizzoni, "Optimal energy management of hybrid vehicles including battery aging", IEEE American Control Conference (ACC), 2011.

[48] S. Stockar, V. Marano, G. Rizzoni, L. Guzzella, "Optimal Control for Plug - in Hybrid Electric Vehicle Applications", IEEE American Control Conference (ACC), 2010.

[49] L. Tang, G. Rizzoni, S. Onori, "Energy Management Strategy for HEVs Including Battery Life Optimization", IEEE Transactions on Transportation Electrification, vol. 1, no. 3, pp. 211 - 222. 2015.

[50] G. Paganelli, S. Delprat, T. M. Guerra, J. Rimaux, J. J. Santin, "Equivalent consumption minimization strategy for parallel hybrid powertrains", IEEE Vehicular Technology Conference (VTC), 2002.

[51] C. Musardo, G. Rizzoni, Y. Guezennec, B. Staccia, "A-ECMS: An Adaptive Algorithm for Hybrid Electric Vehicle Energy Management", European Journal of Control (2005) 11: 509 - 524.

[52] A. Sciarretta, L. Guzzella, "Control of Hybrid Electric Vehicles", IEEE Control Systems, vol. 27, no. 2, pp. 60 - 70. 2007.

[53] A. Sciarretta, M. Back, L. Guzzella, "Optimal Control of Parallel Hybrid Electric Vehicles", IEEE Transactions on Control Systems Technology, vol. 12, no. 3, pp. 352 - 363. 2004.

[54] W. Enang, C. Bannister, "Robust proportional ECMS control of a parallel hybrid electric vehicle", Proceedings of the Institution of Mechanical Engineers, Part D: Journal of Automobile Engineering 231.1 (2017): 99-119.

[55] O. Sundstrom, L. Guzzella, P. Soltic, "Optimal hybridization in two parallel hybrid electric vehicles using dynamic programming." IFAC Proceedings Volumes 41.2 (2008): 4642-4647.

[56] L. V. Pérez, G. R. Bossio, D. Moitre, G. O. Garcìa, "Optimization of power management in an hybrid electric vehicle using dynamic programming", Mathematics and Computers in Simulation 73.1 (2006): 244-254.

[57] A. Piccolo,L. Ippolito,V.Galdi,A.Vaccaro, "Optimization of energy flow management in hybrid electric vehicles via genetic algorithms", in Proceedings of the 2001 IEEE/ASME International Conference on Advanced Intelligent Mechatronics (2001).

[58] M. Salman, N. J. Schouten, N. A. Kheir "Control Strategies for Parallel Hybrid Vehicles" IEEE American Control Conference (ACC), 2000.

[59] B. Baumann, G.Washington, B. Glenn, G. Rizzoni, Mechatronic design and control of hybrid electric vehicles. IEEE/ASME Trans. Mechatron. 5(1), 58–72 (2000)

[60] T. Hofman, M. Steinbuch, "Rule - based energy management strategies for hybrid vehicles", Int. J. Electric and Hybrid Vehicles, vol. 1, no. 1, pp. 71 - 94, 2007.

[61] D. Bianchi, L. Rolando, L. Serrao, S. Onori, G. Rizzoni, N. Al-Khayat et al. "A rule-based strategy for a series/parallel hybrid electric vehicle: an approach based on dynamic programming", ASME 2010 Dynamic Systems and Control Conference (pp. 507-514). American Society of Mechanical Engineers.

[62] T. Hofman, D. Hoekstra, RM. Van Druten, and M. Steinbuch, "Optimal design of energy storage systems for hybrid vehicle drivetrains", Vehicle Power and Propulsion, 2005 IEEE Conference, pages 5 - pp. IEEE, 2005.

[63] O. Sundstrom, L. Guzzella, P. Soltic, "Optimal hybridization in two parallel hybrid electric vehicles using dynamic programming", IFAC Proceedings Volumes, 41(2):4642 - 4647, 2008.

[64] O. Sundstrom, L. Guzzella, P. Soltic, "Torque-assist hybrid electric powertrain sizing: From optimal control towards a sizing law", IEEE Transactions on Control Systems Technology, vol.18, no. 4, pp. 837 - 849, 2010.

[65] E. Tara, S. Shahidinejad, S. Filizadeh, E. Bibeau, "Battery storage sizing in a retrofitted plug-in hybrid electric vehicle", IEEE Transactions on Vehicular Technology, vol. 59, no. 6, pp. 2786 - 2794, 2010.

[66] YS Wong, KT Chau, CC Chan, "Battery sizing for plug-in hybrid electric vehicles", Journal of Asian Electric Vehicles, vol.4 no. 2, pp. 899 - 904, 2006.

[67] A. J. Markel, A. Simpson. Plug-in hybrid electric vehicle energy storage system design. National Renewable Energy Laboratory, 2006.

[68] M. Pourabdollah, N. Murgovski, A. Grauers, B. Egardt, "Optimal sizing of a parallel phev powertrain", IEEE Transactions on Vehicular Technology, vol. 62, no. 6, pp. 2469 - 2480, 2013.

[69] O. Sundstrom, A. Stefanopoulou, "Optimal power split in fuel cell hybrid electric vehicle with different battery sizes, drive cycles, and objectives", Computer Aided Control System Design, 2006 IEEE International Conference on Control Applications, 2006 IEEE International Symposium on Intelligent Control, 2006 IEEE, p. 1681 - 1688. IEEE, 2006.

[70] O. Sundstrom, A. Stefanopoulou, "Optimum battery size for fuel cell hybrid electric vehicle, Journal of fuel cell science and technology, vol. 4, no. 2, pp. 167 - 175, 2007.

[71] R. Rajamani, Vehicle Dynamics and Control. Second Edition. ISSN 0941-5122. Springer. 2012.

[72] K. Reif, "Brakes, Brake Control and Driver Assistance Systems", Springer. ISBN 978-3-658-03977-6. 2014.

[73] L. De Novellis, A. Sorniotti, P. Gruber, J. Orus, JM Rodriguez Fortun, J. Theunissen, J. De Smet, "Direct yaw moment control actuated through electric drivetrains and friction brakes: Theoretical design and experimental assessment", Mechatronics, vol. 26, pp. 1 - 15, 2015.

[74] M. Shino, M. Nagai, "Yaw-moment control of electric vehicle for improving handling and stability", JSAE Review, vol. 22, pp. 473 - 480. 2001.

[75] E. Esmailzadeh, A. Goodarzi, GR. Vossoughi, "Optimal yaw moment control law for improved vehicle handling", Mechatronics, vol. 13, pp. 659 - 675. 2003.

[76] F. Tahami, S. Farhangi, R. Kazemi, "A Fuzzy Logic Direct Yaw-Moment Control System for All-Wheel-Drive Electric Vehicles", Vehicle System Dynamics, vol. 41, no. 3, pp. 203 - 221. 2004.

[77] W. Xu, D. Wang, Y. Li, "The Laterall Stability Control of Vehicles Based on Sliding Mode Method", Proceeding of the IEEE International Conference on Information and Automation. 2014.

[78] J. Ghosh, A. Tonoli, N. Amati, "Improvement of Lap-Time of a Rear Wheel Drive Electric Racing Vehicle by a Novel Motor Torque Control Strategy", WCX 17: SAE World Congress. 2017.

[79] Y. Chen, JK. Hedrick, K. Guo, "A novel direct yaw moment controller for in-wheel motor electric vehicles", Vehicle System Dynamics, vol. 51, no. 6, pp. 925 - 942. 2013.

[80] RJ. Rieveley, BP. Minaker, "Variable Torque Distribution Yaw Moment Control for Hybrid Powertrains", SAE Technical Paper, 2007.

[81] M. Hancock, F. Assadian, "Impact of Regenerative Braking on Vehicle Stability", IET, 2006.

[82] P. Falcone, S. Khoshfetrat Pakazad, S. Solyom, "Predictive Approaches to Rear Axle Regenerative Braking Control in Hybrid Vehicles", IEEE Conference on Decision and Control, 2009.

[83] K. Bayar, J. Wang, G. Rizzoni, "Development of a vehicle stability control strategy for a hybrid electric vehicle equipped with axle motors", Proceedings of the Institution of Mechanical Engineers, Part. D, Journal of Automobile Engineering 266.6 (2012): 795 - 814.

[84] D. Kim, S. Hwang, H. Kim, "Vehicle Stability Enhancement of Four - Wheel - Drive Hyubrid Electric Vehicle Using Rear Motor Control", IEEE Transactions on Vehicular Technology, vol. 57, no. 2, pp. 727 - 735, 2008.

[85] JV. Alcantar, F. Assadian, "A Robust Stability Control System for a Hybrid Electric Vehicle Equipped with Electric Rear Axle Drive", SAE Int. J. Passeng. Cars - Mech. Syst. 9(2): 2016.

[86] J. Edelmann, M. Plochl, "Handling Characteristics and Stability of the Steady State Powerslide Motion of an Automobile", Regular and Chaotic Dynamics, vol. 14, no. 6, pp. 682 - 692, 2009.

[87] E. Velenis, E. Frazzoli, P. Tsiotras. "Steady-state cornering equilibria and stabilisation for a vehicle during extreme operating conditions." International Journal of Vehicle Autonomous Systems 8.2-4 (2010): 217-241. APA

[88] List, H. and Schoeggl, P., "Objective Evaluation of Vehicle Driveability," SAE Technical Paper 980204, 1998, doi:10.4271/980204.

[89] L. Castellazzi , A. Tonoli, N. Amati, A. Piu et al., "Vehicle Driveability: Dynamic Analysis of Powertrain System Components," SAE Technical Paper 2016-01-1124, 2016, doi:10.4271/2016-01-1124.

[90] L. Castellazzi, A. Tonoli, N. Amati, E. Galliera (2017): A study on the role of powertrain system dynamics on vehicle driveability, Vehicle System Dynamics, DOI: 10.1080/00423114.2017.1294699

[91] Couderc P, Callenaere J, Der Hagopian J, et al. Vehicle driveline dynamic behaviour: experimentation and simulation. J Sound Vibration. 1998;218(sv981808):133–157.

[92] Capitani R, Delogu M, Pilo L. Analysis of the influence of a vehicle's driveline dynamic behavior regarding the performance perception at low frequencies; 2001. (SAE Technical Paper; 2001-01-3333).

[93] Sorniotti A. Driveline modeling, experimental validation and evaluation of the influence of the different parameters on the overall system dynamics; 2008. (SAE Technical Paper; 2008-01-0632).

[94] Galvagno E, Morina D, Sorniotti A, et al. Drivability analysis of through-the-road-parallel hybrid vehicles. MECCANICA. 2013;48(2):351–366.

[95] Pacejka H, Besselink I. Tire and vehicle dynamics. 3rd ed. Oxford: Butterworth-Heinemann; 2012.

[96] Genta G, Morello L. The automotive chassis, Volume 2: system design. Dordrecht: Springer; 2009.

[97] Yard, M. Control and Drive Quality Refinement of a Parallel-Series Plug-in Hybrid Electric Vehicle. Master thesis, The Ohio State University, 2014.

[98] C. Jauch, K. Bovee, S. Tamilarasan, L. Güvenc, G. Rizzoni (2015). Modeling of the OSU EcoCAR 2 vehicle for Drivability Analysis. IFAC-PapersOnLine, 48(15), 300-305.